Soy Protein Nanoparticles as an Oral Delivery Vehicle for Nutraceuticals

by

Jing Zhang

A thesis submitted in partial fulfillment of the requirements for the degree of

Doctor of Philosophy

in

Food Science and Technology

Department of Agricultural, Food and Nutritional Science
University of Alberta

Abstract

The objective of this research was to explore the feasibility of using SPI nanoparticles to improve the absorption of vitamin B_{12} (VB_{12}) using *in-vitro* and *ex-vivo* models. The molecular interactions between soy proteins and VB_{12} were firstly studied and the results revealed that VB_{12} was bound to the interior of three-dimensional protein network mainly via hydrophobic interactions to form soy proteins-VB_{12} complexes. VB_{12}-loaded SPI nanoparticles with different particle size (30, 100 and 180 nm) and surface charge (-17, 22 and -40 mV) were obtained using a cold-gelation method by adjusting preparation conditions and applying surface coating with chitosan and sodium alginate. SPI nanoparticles exhibited uniform size distribution and spherical shape. SPI nanoencapsulation led to a slower VB_{12} release in simulated gastric and intestinal fluids. Surface coating retarded the release of VB_{12} from SPI nanoparticles. All the nanoparticles showed a low cytotoxicity and high cellular uptake efficiency in Caco-2 cells. Cellular uptake of nanoparticles was dependent on energy, particle concentration and incubation temperature, suggesting the active endocytosis pathways. The transport efficiency of VB_{12} across Caco-2 cell monolayers was significantly increased after nanoencapsulation, up to 3 times. 30 nm SPI nanoparticles demonstrated the highest VB_{12} transport efficiency compared with larger-sized and surface modified ones. The transcytosis of SPI nanoparticles (30-180 nm) was predominantly via clathrin-mediated and macropinocytosis pathways. In addition,

the caveolae-mediated transcytosis pathway was partially involved in the transport of 30 nm SPI nanoparticles. The transcytosis of chitosan modified SPI particles was involved in the clathrin-/caveolae-independent pathway, while that of alginate/chitosan modified nanoparticles was through the clathrin-/caveolae-mediated and macropinocytosis pathways. In addition to the transcellular pathways, all the nanoparticles could facilitate the paracellular transport of VB_{12} via tight junctions. Since 30 nm SPI nanoparticles showed the optimized VB_{12} transport efficiency, which were further applied on the *ex vivo* Ussing chamber test. The results indicated that 30 nm SPI nanoparticles enhanced the intestinal absorption of VB_{12}, up to 4 times. The findings in this study suggested that SPI nanoparticles could be a promising oral carrier for VB_{12}, which is recommended for further study via *in vivo* tests in the future.

Preface

Chapter 3 of this thesis has been published as J. Zhang, L. Liang, Z. Tian, L. Chen and M. Subirade, "Preparation and *In Vitro* Evaluation of Calcium-induced Soy Protein Isolate Nanoparticles and Their Formation Mechanism Study", *Food Chemistry,* vol 133, 390-399. M. Subirade and L. Chen were the supervisory authors. Chapter 4 of this thesis has been published as J. Zhang, Z. Tian, L. Liang, M. Subirade and L. Chen, "Binding Interactions of β‑Conglycinin and Glycinin with Vitamin B_{12}", *The Journal of Physical Chemistry B,* vol 117, 14018-14028. L. Chen was the supervisory author. In terms of contribution in these two chapters, I was responsible for design and performace of experiments, collection and analysis of research data, as well as the preparation of manuscript. Z. Tian helped me with the training of experimental instruments such as Zetasizer NanoS, UV-vis spectrophotometer and CD. L. Liang and M. Subirade contributed to the discussion of protein conformational change and the revision of manuscript. L. Chen contributed to the experimental design, data discussion, manuscript composition and revision.

Another manuscript was generated based on the data in Chapters 5 and 6, which was to be submitted soon as J. Zhang, D. Vine, C. Field and L. Chen. I was responsible for the experimental design, data collection and analysis as well as the manuscript composition. C. Field assisted with the cell culture training. D. Vine helped with *ex vivo* evaluation of intestinal absorption of VB_{12} and discussion of

the related data. L. Chen was the supervisory author, who impressively contributed to the experimental design, data discussion, manuscript composition and revision.

Dedication

This dissertation is dedicated to my beloved family for their motivation, love and support.

Acknowledgements

I would like to greatly thank my supervisor, Dr. Lingyun Chen for her guidance, help and support to my Ph.D research. I am extremely grateful to Dr. Chen for encouraging and inspiring all the way on my Ph.D study. Without her continuous support, my work could not have been done. Without her training, my academic writing and presentation delivery skills could not have been improved. I would like to thank my cosupervisor, Dr. Muriel Subirade, in the University of Laval, Quebec City. I sincerely appreciate the valuable opportunity of 6-month study in the University of Laval, provided by Dr. Chen and Dr. Subirade. I would like to thank Dr. Feral Temelli and Dr. Catherine Field for their constructive suggestions to my research project during committee meetings. I indeed learned a lot from Dr. Temelli course of Advanced Foods, which is very helpful to my research work. I would also thank Dr. Catherine Field for her solid training of Caco-2 cell culture work. And I greatly thank Dr. Donna Vine for her instruction and help with the *ex vivo* tests. I learned a lot during the every discussion of *ex vivo* study. I also would like to thank other committee members, Dr. Thavaratnam Vasanthan and Dr. Hongbo Zeng for their guidance and support during my Candidacy Exam. I sincerely thank the external examiner, Dr. Qingrong Huang, University of Rutgers, for his help with my thesis and final exam. I also greatly thank the examination Chair, Dr. Michael Gänzle, for taking care of my final exam.

My sincere thanks go to many brilliant scientists. I greatly thank Dr. Li Liang for the incredible guidance on the analysis of protein conformational change. Special thanks are dedicated to: Dr. Catherine, Dr. Qun Li and Susan for their kind assistant on Caco-2 cell culture work; Dr. Vine and Dr. Faye for their incredible instruction and help with *ex vivo* tissue experiments; Mr. Tian for his great help with HPLC. I thank Arlene Oatway and Dr. Mingxiong Chen for their help with TEM imaging and kind encouragement; Dr. Xuejun Sun and Ms. Geralidine Barron for their training on confocal imaging; Jinzhou Huang for his help with flow cytometer; Joan for her long term support to the cell culture work. Great thanks go to my sweet colleagues and friends, especially to Ruoxi, Annie, Fatemeh, Alex, and Dr. Song, for their kind support. Special thanks go to David, Linda and Adrienne Lloyd, Dr. David, Carole and Johanna Ibsen for their wonderful friendship, incredible support and caring.

My work could not have been done without the support of my family. They have been incredibly caring, understanding, encouraging and supportive. I really appreciate their love. My life would not have been complete without the amazing friends I have known.

I am grateful to the Natural Sciences and Engineering Research Council of Canada (NSERC) for generous financial support; Canada Foundation for Innovation (CFI) for equipment support; the China Scholarship Council (CSC) for providing 4-year scholarship; the Department of Agricultural, Food and Nutritional Science for providing a wonderful place for my research and study.

Table of Contents

List of Tables

List of Figures

List of Abbreviations

ADME	Absorption, deposition, metabolism and excretion
AL	Alginate sodium
ADM	Archer Daniels Midland Company
ATCC	American Type Culture Collection
BSA	Bovine serum albumin
CD	Circular dichroism
7S	β-Conglycinin
CLSM	Confocal laser scanning microscopy
CMCS	Carboxymethyl chitosan
6-COUM	Coumarin-6
Col	Colchicine
CPZ	Chlorpromazine hydrochloride
CS	Chitosan
CyD	Cytochalasin D
DAPI	4',6-diamidino-2-phenylindole
DLS	Dynamic light scattering
DMEM	Dulbecco's modified eagle medium
DMSO	Dimethyl sulfoxide
DPBS	Dulbecco's phosphate-buffered saline
EDC	N-(3-dimethylaminopropyl)-N-ethylcarbodiimide
EDTA	Ethylenediaminetetraacetic acid
FBS	Fetal bovine serum
EFSA	European Food Safety Agency
FA	Folic acid FA
FAE	Follicle-associated epithelia
FDA	US Food and Drug Administration
FIM	Foundation of Innovation Medicine
FLI	Flilipin III
FTIR	Fourier transform infrared spectroscopy
GI tract	Gastrointestinal tract
11S	Glycinin
GRAS	Generally Regarded as Safe
HBSS	Hank's balanced salt solution
HC	Haptocorrin
HEPES	4-(2-Hydroxyethyl)-1-piperazineethanesulfonic acid
HSA	Human serum albumin
IF	Intrinsic factor
k_q	Fluorescence quenching rate
K_{SV}	Stern-Volmer quenching constant
LDH	Lactate dehydrogenase

LDL	Low-density lipoprotein
β-LG	β-Lactoglobulin
M cell	Microfold cell
β-ME	β-Mercaptoethanol
MTT	Thiazolyl blue tetrazolium bromide
Nab-P	Nanoparticle albumin-bound paclitaxel
HAADF-STEM	High angle annual dark field- scanning transmission electron microscopy
HPLC	High performance liquid chromatography
NINT	National Institute of Nanotechnology
NSERC	Natural Sciences and Engineering Research Council of Canada
PDI	Polydispersity index
PEG	Poly(ethylene glycol)
Phe	Phenylalanine
pI	Isoelectric point
PIBCA	Poly(isobutyl cyanoacrylates)
PLA	Poly(lactic acid)
PLGA	Poly(lactic-co-glycolic acid)
PMS	Phenazine methosulfate
PQ	Partitioning quotient
PTA	Phosphotungstate
γ-PGA	Poly(γ-glutamic acid)
RP-HPLC	Reverse-phase high performance liquid chromatography
SGF	Simulated gastric fluid
SIF	Simulated intestinal fluid
SLNs	Solid lipid nanoparticles
SDS	Sodium dodecyl sulfate
SPI	Soy protein isolate
SPI-NP-1	Soy protein isolate nanoparticles with the size of 30 nm
SPI-NP-2	Soy protein isolate nanoparticles with the size of 100 nm
SPI-NP-3	Soy protein isolate nanoparticles with the size of 180 nm
TBA	Thiobarbituric acid
TEER	Transepithelial electrical resistance
TC-II	Transcobalamin II
TEM	Transmission electron microscopy
Trp	Tryptophan
Tyr	Tyrosine
XTT	2,3-Bis-(2-Methoxy-4-Nitro-5-Sulfophenyl)-2H-Tetrazolium-5-Carboxanilide
VB_{12}	Vitamin B_{12}

VD	Vitamin D
WGA	Wheat germ agglutinin

Chapter 1. Introduction and Thesis Objectives

1.1 Introduction

To date, oral delivery is still the preferred administration route of bioactive compounds, especially for chronic therapies where repeated administration is needed, nevertheless, many compounds exhibited low oral bioavailability due to poor solubility, permeability, and/or instability in GI tract (Hattori, et al., 1995; Bell, 2001; Galindo-Rodriguez, et al., 2005; Loveday & Singh, 2008). Nanoparticle-based delivery systems are able to prevent premature degradation of bioactive compounds, directly deliver them to the appropriate sites, and maintain their concentration at suitable levels for long periods of time (Alishahi, et al., 2011). Therefore, nanoparticles have great potential to enhance the efficacy and bioavailability of nutraceuticals. In the range of nutraceutical delivery, there have been substantial advances achieved in nanoparticle engineering to enhance the oral bioavailability of poorly water-soluble compounds such as β-carotene and vitamin D (VD) by increasing their solubility and stability in GI fluids (Livney, 2010). However, very little has been done on the enhancement of the uptake of hydrophilic nutraceuticals such as VB_{12}.

So far, only a few studies have been performed to prepare SPI nanoparticles for drug/nutraceutical delivery including curcumin and VD_3 by simple coacervation method (Teng, et al., 2012, 2013). Nonetheless, the utilization of ethanol, glutaraldehyde, dimethyl sulfoxide (DMSO), and

N-(3-dimethylaminopropyl)-N-ethylcarbodiimide (EDC) in preparation of SPI nanoparticles would limit their application in food products. Without using any toxic reagent, SPI nanoparticles have been produced using an ionic gelation method (Teng, et al., 2013), by which nutraceuticals can be encapsulated into SPI nanoparticles under mild conditions. SPI nanoparticles produced by this method could be applied in food products for nutraceutical delivery.

SPI contain hydrophilic charged and uncharged groups (-NH_2, -COOH, -OH and -SH) as well as hydrophobic groups (CH_3- and benzene rings), which provide a potential base for the development of electrostatic interactions, hydrogen bonds, hydrophobic interactions or van der Waal interactions with nutraceuticals. All these possible interactions confer that soy protein either alone or combined with other biopolymers are able to confine nutraceuticals in a three-dimensional protein network, so as to preserve their active form until release at their target site in the human body, for potentially improved absorption (Chen, et al., 2008; Chen & Subirade, 2009). Besides, the characteristics of nanoparticles (size, surface charge and hydrophobicity) would affect the biological properties of nanoparticles including the loading, release and permeability across small intestinal barriers; nevertheless, these have been less reported to a limited extent. Therefore, a fundamental understanding of the molecular interactions between SPI-nutraceuticals, and the impacts of preparation conditions on particle features (size, surface charge and hydrophobicity), subsequently the mechanisms of encapsulated nutraceutical release, uptake and transport are essential. Exploring

how particle features affect the intestinal absorption of nutraceuticals will consequently help us to further bioengineer particle properties in order to achieve optimal absorption of nutraceuticals.

1.2 Hypotheses and Objectives

Literature review of previous studies led to the following hypotheses of the present study:

(1). SPI can trap molecules of interest into their three-dimensional networks by developing hydrophobic interactions, hydrogen bonds, electrostatic interactions or van der Waal forces;

(2). SPI nanoparticles can be prepared by cold-gelation method and their features (size, surface hydrophobicity and charge) can be modulated by adjusting the cold gelation conditions (pH and calcium concentration);

(3). SPI nanoparticles can act as delivery vehicles to efficiently carry nutraceuticals across the small intestinal barriers so as to improve their absorption.

The overall objective of this research was to understand the mechanisms of SPI nanoparticle formation by cold-gelation method, and explore the feasibility of using SPI nanoparticle as oral delivery vehicles for nutraceuticals in order to improve the absorption of nutraceuticals through both *in-vitro* and *ex-vivo* tests. VB_{12} was selected as a model compound for hydrophilic nutraceutical.

The entire study was designed based on the following major objectives.

Objective 1:

To prepare SPI nanoparticles with different properties including size, surface charge and hydrophobicity using cold-gelation technique, and then investigate the particle formation mechanism (Chapter 3).

Objective 2:

To investigate the molecular interactions between two SPI fractions (7S and 11S) and VB_{12}, so as to explore the feasibility of using SPI nanoparticles to encapsulate VB_{12} (Chapter 4).

Objective 3:

To evaluate the impacts of particle properties (size and surface charge) on VB_{12} *in vitro* release in simulated GI fluids, particle uptake efficiency as well as associated mechanisms by Caco-2 cells (Chapter 5).

Objective 4:

To assess the impacts of particle properties (size and surface charge) on VB_{12} transport efficiency and related mechanisms across Caco-2 cell monolayers. The optimal particle was chosen and applied on Ussing Chamber test to investigate its intestinal absorption enhancement for VB_{12} (Chapter 6).

The outcome of this study will allow us to design an ideal oral carrier to improve the oral absorption of nutraceuticals. This work will open more exciting opportunities for their applications in the field of functional foods for nutraceutical delivery.

Chapter 2. Literature Review

2.1 Nutraceutical and Functional Food

2.1.1 Concepts and Benefits

Nutraceutical is a combined word of "nutrition" and "pharmaceutical", which was invented by Dr. Stephen L. DeFelice, founder and chairman of the Foundation of Innovation Medicine, Crawford, New Jersey in 1989 (Kalra, 2003). Health Canada defined a nutraceutical as a product isolated or purified from foods that is generally sold in medicinal forms not usually associated with food. It has a physiological benefit and/or provides protection against chronic disease (Health Canada, 1998). Meanwhile, a functional food is specified as a food to be similar in appearance to a conventional food, to be consumed as part of the usual diet, to be demonstrated to have physiological benefits, and/or to reduce the risk of chronic diseases beyond basic nutritional functions (Health Canada, 1998). The majority of functional food are of the same form of conventional foods, the intake amount and form are generally similar to foods that are consumed for regular dietary purposes (Siro, et al, 2008). In Japan, however, the functional food products have been presented in the form of capsules and tablets since 2001 (Ohama, et al. 2006).

Production of functional foods is being considered as the top priority in the worldwide food industry (Basu, et al. 2007). Examples include breakfast cereals enriched with β-glucan, which can lower low-density lipoprotein (LDL)

cholesterol and protect against cardiovascular disease (Jenkins, et al., 2002); vitamin D (VD) fortified milk and orange juice, which are routinely consumed to maintain bone growth and prevent VD deficiency (Holick, 2007); ω-3 fatty acids enriched eggs, which are used as a source of polyunsaturated fatty acids to reduce the risk of cardiovascular disease and enhance brain functions (Kris-Etherton, et al., 2003), etc. Increasing health consciousness, aging population and health care expenses have been the main stimulating elements for rapid global growth of the nutraceutical and functional food industry (Basu, et al., 2007; Hasler, 2000).

2.1.2 Challenges

To date, oral delivery is still the preferred administration route of bioactive compounds, especially for chronic therapies where repeated administration is required, nevertheless, many compounds exhibit low oral bioavailability owing to: (1) low mucosal permeability; (2) absorption restricted to a particular region of small intestine; (3) low solubility leading to a slow dissolution in the mucosal fluids and elimination of a large fraction of compounds from the gastrointestinal (GI) tract; and (4) instability during food processing (temperature, oxygen, light) or in the GI tract (pH, enzymes, presence of other nutrients), resulting in oxidation or degradation of an ingredient prior to its absorption (Bell, 2001; Galindo-Rodriguez, et al., 2005; Hattori, et al., 1995; Loveday & Singh, 2008). These limitations consequently restrict potential health benefits of bioactive molecules and the effectiveness of nutraceutical products (Bell, 2001). In this context, encapsulating

the bioactive compounds into nanoparticles is a promising solution to improve their oral bioavailability.

2.2 Vitamin B_{12}

Vitamin B_{12} (VB_{12}), is a water soluble vitamin, the largest and most complex molecule of all vitamins. It is made up of a central cobalt atom and a planar corrin ring (Figure 2-1) (Kozyraki & Cases, 2013). VB_{12} represents all potential methylcobalamin and adenosylcobalamin (Figure 2-1) (Kozyraki & Cases, 2013); whereas it is usually exclusively used for cyanocobalamin, which is a synthetic form of cobalamin and most commonly found in nutritional supplements.

VB_{12} plays an important role in brain and nervous system, as well as red blood cell formation. VB_{12} is also required for the metabolism of human cells, DNA synthesis and regulation, fatty acid synthesis and energy fabrication (Zittoun & Zittoun, 1999). VB_{12} cannot be synthesized in mammal cells, its existence in animal products such as red meat and eggs is attributable to bacterial fermentation-synthesis. Dietary ingestion of these products is the only natural source for humans (Kozyraki & Cases, 2013).

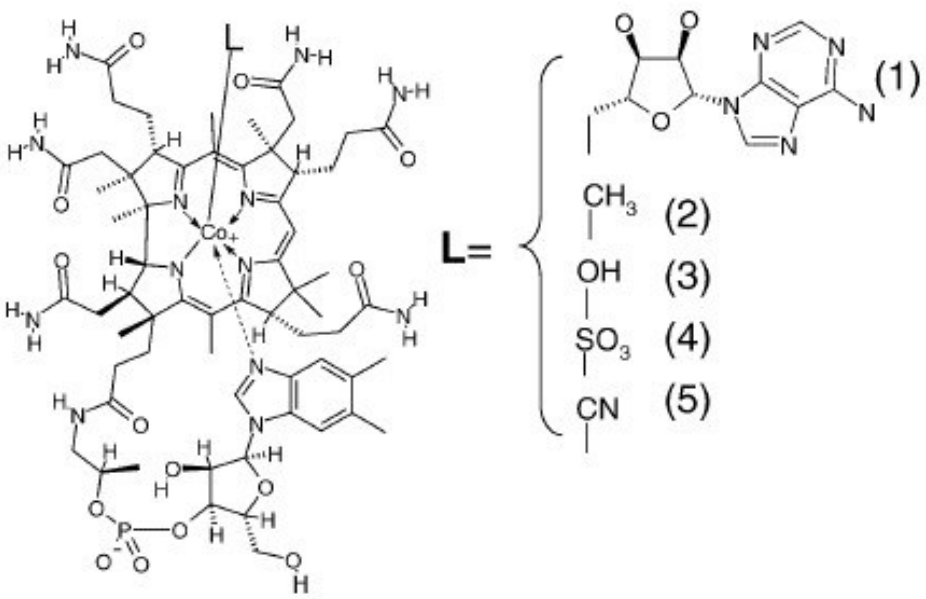

Figure 2-1. Structural formula of vitamin B_{12} (VB_{12}) and partial structures of VB_{12} compounds. The partial structures of VB_{12} compounds show only those portions of the molecule that differ from VB_{12}. 1: 5'-deoxyadenosylcobalamin; 2: methylcobalamin; 3: hydroxocobalamin; 4: sulfitocobalamin; 5: cyanocobalamin. Adapted from (Watanabe, 2007).

2.2.1 Absorption of VB_{12}

The absorption of VB_{12} is a complex and multistep process. It involves several gene products including carrier proteins, plasma membrane receptors and transporters, and occurs in several organs including salivary glands, stomach, pancreas and small intestine (Kozyraki & Cases, 2013). Firstly, dietary VB_{12}, which is usually bound to proteins in food, is released in the stomach under the effects of gastric acid and pepsin. The free VB_{12} then binds to haptocorrin (HC), which is a carrier produced by salivary glands and parietal cells in the stomach (Kozyraki & Cases, 2013). When the VB_{12}-HC complex reaches the duodenum, HC is degraded by pancreatic protease, the liberated VB_{12} then binds to intrinsic

factor (IF) produced by parietal cells (Allen, et al., 1978). In the distal ileum, after being recognized by specialized receptors on mucosal cells, IF-VB_{12} complex enters the blood and is directed to portal circulation. In the blood, VB_{12} binds to a plasma transporter, transcobalamin II (TC-II) and form TC-II /VB_{12} complex (Kozyraki & Cases, 2013). This complex is an active fraction and is delivered to cells in the body with blood circulation (Ermens, et al., 2003). Upon reaching the cells in the body, TC-II /VB_{12} complex is recognized by cell receptor and internalized into cells via endocytosis. Within the cells, TC-II is degraded within lysosome and free VB_{12} is finally released to the cytoplasm, where it can be utilized to form various coenzymes for cell metabolism (Nielsen, et al., 2012). An intensive fraction (50%) of VB_{12} is stored in the liver and can be recycled by enterohepatic circulation. The VB_{12} in the liver can be secreted in bile and transported into duodenum via an IF-dependent route (Kozyraki & Cases, 2013). Nevertheless, a dysfunction at any one of these organs and processes may lead to VB_{12} deficiency.

2.2.2 VB_{12} Deficiency and Treatment

In human body, a variety of symptoms may occur when serum VB_{12} concentration is slightly below the normal concentration such as fatigue, depression and impaired memory (Tomczykiewicz, et al., 1998). Severe VB_{12} deficiency can cause irreversible damage, mainly to the brain and nervous system (Kuo, et al., 2009; Tomczykiewicz, et al., 1998). VB_{12} deficiency could also

possibly result in life-threatening anemia (Ray & Cole, 2005). Vegans and the elderly are at a high risk of VB_{12} deficiency. Amongst strict vegans, VB_{12} deficiency is mostly induced by avoidance of meat diets. Taking supplement will be beneficial for this group. In the elder, its deficiency is mainly attributed to food-cobalamin malabsorption (60-70%) (Andrès, et al., 2004). This malabsorption is caused by atrophic gastritis, *Helicobacter pylori* infection and long term ingestion of antacids and biguanides. Those individuals are in need of VB_{12} supplementation as well. Besides, pernicious anemia accounts for approximately 15-25% of VB_{12} deficiency in the elder (Dali-Youcef & Andrès, 2009), which can be treated by intramuscular injection. In contrast with injection, oral administration is of increasing interest because it is not only efficient and convenient, but less irritative and cost-effective.

The efficacy of traditional VB_{12} supplementation is limited, a very high daily dose is required in order to reach normal serum VB_{12} concentration (Berlin, et al., 1968). For instance, it is shown that daily intake of 1000 μg cyanocobalamin is needed to provide effective therapeutic effects for VB_{12} deficiency of all causes (Nyholm, et al., 2003). Only approximately 1% of the initial dosage can be absorbed in the intestine of patients with pernicious anemia (Kuzminski, et al.,1998). In order to address the challenge and achieve enhanced bioavailability of VB_{12}, a modified and more effective delivery system is in demand. It is proposed that novel compound carriers can carry VB_{12} directly across the GI barriers and bypass the original complex pathway during absorption, which may

remarkably improve the effectiveness of VB_{12} supplementation.

2.3 Protein-Nutraceutical Interactions

Natural proteins have great capacity of binding various ligands (Saifer & Goldman, 1961). In protein-ligand complexes, proteins provide protecting, stabilizing, encapsulating and/or controlled releasing mechanisms to the bound compounds. As a result, the complexes can improve the solubility of hydrophobic compounds, protect the sensitive compounds against oxidation or degradation, and/or provide means of stimulated-induced release and targeted delivery (De Wolf & Brett, 2000; Liang & Subirade, 2012; Liang, et al, 2008; Liang, Tremblay-Hébert, & Subirade, 2011). Commonly used ligand-binding proteins in research database include: β-lactoglobulin (β-LG), human serum albumin (HSA) and bovine serum albumin (BSA) (Belatik, Hotchandani, Bariyanga, & Tajmir-Riahi, 2012; Pérez & Calvo, 1995). The most important and common functionality of these animal proteins is that they serve as transporters for a variety of compounds (Pérez & Calvo, 1995). For instance, β-LG has been studied extensively and reported as a useful transporter for retinol (Pérez & Calvo, 1995), fatty acids (Pérez & Calvo, 1995), and vitamin D_2 (Wang, et al., 1997). Binding to β-LG not only protected retinol from degradation caused by heat, oxidation and irradiation (Loveday & Singh, 2008), but also improved the uptake of retinol in the intestine (Pérez & Calvo, 1995). Lipoproteins, as another example are bound to carotenes in many vegetables, cyanobacteria, animals and crustaceans.

Interestingly, it was observed under the observational and experimental conditions that people with higher levels of plasma lipoproteins were able to take up more carotenoids from the diet and circulated more carotenoids through the blood (Casso, et al., 2000; Vogel, et al., 1997). The versatile functionalities of natural proteins and relevant research suggest the development of protein-nutraceutical complexes is a promising approach to incorporate bioactive compounds in functional foods (De Wolf & Brett, 2000).

2.3.1 Characterization of Protein Binding Properties

Fluorescence quenching is an established technique for measuring binding affinities of a protein to a ligand (Belatik, et al., 2012; Lakowicz, 2009). It refers to the decrease of the quantum yield of fluorescence from a fluorophore induced by various molecular interactions with a quencher molecule (Lakowicz, 2009). The triggered interactions include hydrophobic interactions, hydrogen bonding, van der Waal interactions, electrostatic interactions and/or covalent bonding (Kroll, et al., 2003). Fluorescence quenching can occur by different mechanisms including dynamic quenching and binding-related quenching, which can be differentiated by their different reliance on temperature, viscosity or preferably by lifetime measurement (Hou, et al., 2008). In dynamic quenching process, higher temperatures lead to a faster diffusion and consequently a greater extent of collisional quenching. Whereas, binding-related quenching refers to fluorophore-quencher complex formation, where higher temperatures result in

dissociation of the weakly bound complex and consequently a lower extent of static quenching (Hou, et al., 2008). While analyzing emission spectra of proteins in the presence and absence of nutraceuticals at different temperatures, their quenching mechanisms can be determined by the linear Stern-Volmer equation (Lakowicz, 2009):

$$\frac{F}{F_0}=1+k_q*\tau_0*[Q]=1+K_{sv}*[Q] \quad (2\text{-}1)$$

where F_0 and F represent the fluorescence intensities in the absence and presence of a nutraceutical, respectively, k_q is the quenching rate constant of the bimolecular, K_{SV} is the dynamic quenching constant, τ_0 is the average lifetime of a fluorophore without quencher being equal to 10^{-8} s, and [Q] is the concentration of a nutraceutical (Lakowicz, 2009).

Eq. (2-1) is normally used to identify whether or not the quenching is caused by dynamic collision or formation of a binding complex. Accordingly, Stern-Volmer quenching constant (K_{SV}) and fluorescence quenching rate (K_q) can be obtained. For dynamic quenching, K_q is less than or close to 2.0×10^{10} $M^{-1}s^{-1}$ and the K_{SV} increases with temperature. As for binding-related quenching, K_q is much higher than 2.0×10^{10} $M^{-1}s^{-1}$ and the K_{SV} decreases with temperature due to the dissociation of weakly bound complexes (Lakowicz, 2009).

The binding parameters including binding constant and the number of nutraceutical binding sites per protein have been frequently calculated using double logarithm regression model (Eq.2-2) (Hou, et al., 2008; Li, et al., 2012; Van De Weert, 2010):

$$\lg(\frac{F_0}{F}-1)=\mathrm{n}\lg K_a+n\lg[Q] \quad (2\text{-}2)$$

where F_0 and F represent the fluorescence intensities in the absence and presence of a nutraceutical, respectively, K_a is binding constant, n is the number of binding sites per protein molecule, and [Q] is the concentration of nutraceutical.

By plotting $\lg(\frac{F_0}{F}-1)$ against $\lg[Q]$, the binding constant K_a and the number of binding sites (n) can be obtained. Eq. (2-2) is used when the formed binding complex is non-fluorescent. As well the concentration of free nutraceutical entered in Eq. (2-2) is assumed to be equal to the added nutraceutical concentration [Q]. This assumption is only valid when the nutraceutical concentration is in excess, at least by a factor of 10 above that of the protein concentration (Stan, et al., 2009; Van De Weert, 2010). Otherwise, the concentration of nutraceutical entered in Eq. (2-2) is not the added nutraceutical concentration [Q], but rather the free nutraceutical concentration $[Q]_{free}$ (Van De Weert, 2010). It can be calculated by the Eq. (2-3):

$$[Q]_{free}=[\mathrm{Q}]-\{n\left(1-\frac{F}{F_0}\right)\times[\mathrm{P}]\} \quad (2\text{-}3)$$

where [P] is the concentration of the protein.

After combining Eq. (2-2) with Eq. (2-3), Eq. (2-4) can be obtained (Bi, et al., 2004; Van De Weert, 2010):

$$\lg(\frac{F_0}{F}-1)=\mathrm{n}\lg K_a+n\lg\left[\frac{[Q]-(F-F_0)[P]}{F_0}\right] \quad (2\text{-}4)$$

According to Eq. (2-4), n can be calculated from the slope of linear regression of the curve $\lg(\frac{F_0}{F}-1)$ against $\lg\left[\frac{[Q]-(F-F_0)[P]}{F_0}\right]$ and K_a is deduced from the intercept of the linear regression.

K_a varies as the compounds of interest differ. It was reported that K_a of β-LG was from as little as 1.5×10^2 M^{-1} for 2-heptanone to as high as 5×10^7 M^{-1} for retinol. The binding affinity of a protein for a compound can be reflected by its binding constant value K_a. Higher K_a indicates a stronger binding capacity. For instance, the binding affinity of β-LG for VD_2 is 10-fold greater than that of retinol, suggesting that β-LG may be a better carrier of VD_2 than of retinol (Wang, et al., 1997).

2.4 Nanoparticles as Oral Delivery Vehicles for Nutraceuticals

Nanoparticles are defined as colloidal carriers with a diameter ranging from 10 to 1000 nm (des Rieux, et al., 2006). Nanoparticles can be encapsulated with bioactive ingredient and are divided into two fundamental categories: nanocapsules and nanospheres. Nanocapsules have a core/shell structure, where the bioactive ingredients are confined within the inner core and surrounded by a solid polymeric wall (des Rieux, et al., 2006). Nanospheres have a uniform matrix structure with the ingredient dispersed within the polymeric matrix or near the surface (Couvreur, et al., 1995). The term “nanoparticles” is commonly used for both forms.

2.4.1 Advantages of Nanoparticles in Nutraceutical Delivery

Delivery of nutraceuticals requires protective mechanisms that perserve the activity until the time of consumption so as to be delivered to the physiological target within the organism (Kim & Cho, 2006). Nanoparticles are promising vehicles to effectively deliver nutraceuticals to human small intestine.

Nanoparticles can dramatically prolong the formulation residence time by decreasing the influence of intestinal clearance mechanisms and by increasing their surface area to interact with the biological support (Brannon-Peppas, 1995; Kawashima, 2001). In addition, they can effectively cross the epithelial lining of the small intestine due to their small size and are readily to be taken up (Desai, et al.,1997; Lamprecht, et al., 2004). Furthermore, the physicochemical characteristics (e.g. size, surface charge, surface hydrophobicity), controlled release properties (e.g. delayed, prolonged, triggered), and biological behavior (e.g. targeting, bioadhesion, cellular uptake) of nanoparticles (Galindo-Rodriguez, et al., 2005) can be modulated by the use of various fabrication materials. Last but not least, the particle surface can be modified by adsorption or chemical grafting of molecules such as poly(ethylene glycol), poloxamers, lectins and chitosan so as to achieve the optimal absorption (des Rieux, et al., 2006).

Although food scientists and industries have embraced nanotechnology in the progress of nutraceutical delivery, most research on nanoparticle delivery systems have been focused on drug delivery in the pharmaceutical field; their application in food sciences is still in the early stage (Chau, et al., 2007).

2.4.2 Nanoparticle Preparation Techniques

There are two basic approaches to prepare nanoparticles. The first one is the "top-down" approach, which involves physically machining materials to nanoscale by employing mechanical forces such as grinding, milling, etching and lithography (Sanguansri & Augustin, 2006). This approach involves size reduction by applying a mechanical force such as compression, impact and shear. The second one is the "bottom-up" approach by which nanoparticles are produced by self-assembly of smaller molecules in the presence of certain chemical reagents (Chen, et al., 2006; Shimomura & Sawadaishi, 2001; Whitesides & Grzybowski, 2002). Self-assembly depends on the balance between the attraction and repulsion forces of a pair of molecules. These forces can be affected by many factors including temperature, pH, concentration, ionic strength of the systems, the mechanical forces (pressure, shear and ultrasound) or magnetic field strength (Sanguansri & Augustin, 2006). Usually, nanoparticles are produced by a combination of the two theories together.

2.4.2.1 Nanoemulsion

Great interest has been shown in food and other industries in the use of nanoemulsions as delivery systems for non-polar functional ingredients, such as lipophilic bioactive lipids, drugs, flavors, antioxidants, and antimicrobial agents (Hu, et al., 2004; Kesisoglou, et al., 2007; McClements, 2010; Weiss, et al., 2008). Nanoemulsions are non-equilibrium systems and thereby cannot be formed

spontaneously. The formation normally requires energy input from either mechanical devices or chemical potential of the components (Solans, et al., 2005).

Nanoemulsions are usually prepared by either high or low energy emulsifications. High-energy approaches use mechanical devices capable of producing strong disruptive forces to break up oil and water phases and produce oil droplets (Silva, et al., 2012). High-pressure homogenization is the mostly used emulsifying technique (Solans, et al., 2005). During high-pressure homogenization, the mixture is pumped through a restrictive valve under very high pressure. The high shear stress induces the formation of very fine droplets (Quintanilla-Carvajal, et al., 2010; Sanguansri & Augustin, 2006). Particle size can be controlled by varying homogenization conditions (pressure and number of passes) and solution composition (oil-to-water ratio, emulsifier-to-water ratio) (Matalanis, et al., 2011). Lutein, an antioxidant, has a low oral bioavailability due to its poor solubility in water. Its nanoemulsion was successfully produced by using the high-pressure homogenization technique, and was demonstrated to have enhanced dissolution and bioavailability (Mitri, et al., 2011). Though high-energy methods are effective in reducing droplet sizes, they may not be suitable for encapsulating some unstable molecules such as proteins and peptides because their bioactive properties may be destroyed during the high-energy and high sheer processes.

In the case of low-energy approaches, nanoemulsion can be formed spontaneously during mixing of oil-water-emulsifier systems as a result of phase transitions produced during the emulsification process (Anton, et al., 2008;

Bouchemal, et al., 2004; Chu, et al., 2007; Uson, et al., 2004). The emulsification is carried out either at constant temperature and changing the composition (Uson, et al., 2004) or at constant composition and changing the temperature (Rang & Miller, 1999; Shinoda & Saito, 1968).

Nanoemulsions normally have far better stability to gravitational separation than conventional emulsions or suspensions. As the Brownian motion effects dominate gravitational forces in the relatively small particle size (McClements, 1999; Tadros, et al., 2004). They also tend to remain stable against droplet flocculation and coalescence due to stronger repulsion forces. Since the range of the attractive forces acting between the droplets decreases as the particle size decreases. However, that the attractions between the steric repulsion is less dependent on particle size (McClements, 1999; Tadros, et al., 2004). Owing to the smaller particle size and higher surface-to-volume ratio, lipophilic compounds in nanoemulsions can be transported more easily through epithelial cell membranes, which results in increased bioavailability than conventional emulsions (Acosta, 2009; Huang, et al., 2010). Hence, food-grade nanoemulsions may be highly useful in increasing the bioactivity of poorly absorbed lipophilic components. Nevertheless, it is difficult to remove the oil phase and obtain particles with a narrow size distribution using the emulsion methods (Ko & Gunasekaran, 2006). Furthermore, nanoemulsion systems often need great amount of oil or emulsifier contents, or the use of organic cosolvents such as ethanol. Therefore, a better balance between the benefits of bioactive compounds and the potential side effects

such as obesity and cardiovascular diseases associated with the high lipid content needs to be achieved by alternative fabrication approaches (Huang, et al., 2010).

2.4.2.2 Ionic Complexation and Gelation

Electrostatic interactions have been utilized in numerous studies in preparation of nanoparticles in order to overcome the undesirable effects of organic solvents (Anal, et al., 2008; Ye, et al., 2006). As proteins contain both acidic and basic amino acids, proteins can carry both positive charges when environmental pH values are lower than their isoelectric points (pIs), and negative charges when environmental pH values are higher than their pIs. This unique property makes proteins able to interact with polysaccharides with opposite charged and form nanoparticles via attractive interactions (Elzoghby, et al., 2011). For examples, sodium caseinate can interact with polyanionic gum arabic at pHs 5.4-3.0 to form nanoparticles with 100-200 nm in diameter (Ye, et al., 2006). Similarly, sodium caseinate can interact with polycationic chitosan at pHs 4.8-6.0 to form 250-350 nm nanoparticles (Anal, et al., 2008). pH and ionic strength determine the number of charges that are present on these polymers and consequently determine the intensity of the electrostatic interactions as well as the formation of protein-polysaccharides complexes (Park, et al., 1992). Besides, at pH values that are above the pIs, negatively charged proteins can interact with cations such as Ca^{2+} to form nanoparticles. Particles properties including size, surface charge and internal structures are determined by the solution pHs, the

added calcium concentration and so on (Giroux & Britten, 2011; Giroux, et al., 2010).

In the preparation of whey proteins nanoparticles, soluble polymers were produced by heating whey protein dispersions at low ionic strength and neutral pH. After cooling to room temperature, whey nanoparticles were formed by acidification of diluted polymer dispersions followed by neutralization of pH and addition of Ca^{2+} (Abbasi, et al., 2014; Giroux & Britten, 2011; Giroux, et al., 2010). The whey protein nanoparticles have been used to encapsulate hydrophobic aroma with a high loading efficiency and improved aroma retention (Giroux & Britten, 2011). Soy protein isolate (SPI) nanoparticles have also been produced by this method and applied to the encapsulation of vitamin D_3 (VD_3) (Teng, et al., 2013). Chitosan was also introduced into SPI solutions before the addition of calcium in order to achieve better controlled release properties (Teng, et al., 2012).

The preparation of nanoparticles based on electrostatic interactions not only helps preserve the stability and activities of bioactive compounds as it involves only aqueous solvents and the encapsulation is achieved in mild processing conditions, but is a simple and cost-effective process.

2.4.2.3 Supercritical Fluid Technique

This is a new technique, where the compounds and polymers are solubilized in a supercritical fluid such as carbon dioxide, followed by the solution being expanded through a nozzle. The supercritical fluid is evaporated in the spraying

process and the solute particles eventually precipitate (Pinto Reis, et al., 2006). This technology has branched a number of modified processes by using different nucleation and growth mechanisms of particles precipitation (Yeo & Kiran, 2005). The derived processes include the rapid expansion of supercritical solutions (Matson, et al., 1987), the supercritical anti-solvent (Dixon, et al., 1993), the supercritical-assisted atomization (Kerč, et al., 1999), the carbon dioxide-assisted nebulization with a bubble dryer® (Sievers, et al., 2003) and the particles from gas-saturated solutions (Rodrigues, et al., 2004). Different supercritical fluid processes are used to serve several purposes: (1) to incorporate an active compound in a slow-dissolving matrix so as to achieve sustainable release (Jung & Perrut, 2001; Perrut & Clavier, 2003); (2) to stabilize fragile molecules and (3) to incorporate the active ingredients so as to enhance solubility and bioavailability of poorly soluble compounds by use of fast-dissolving hydrophilic excipients (Jo, et al., 2002; Kikic, et al., 2000).

Supercritical carbon dioxide fluid holds several unique characteristics and physicochemical properties. It is non-toxic, non-flammable, and has the extraction power tuned by temperature and pressure, as well as a higher mass transfer rate than conventional organic solvents. Therefore, it has been used as a green solvent in nanoparticle generation (Chiu & Tan, 2001), e.g. the encapsulation of insulin inside poly(ethylene glycol)/poly(L-lactide) (PEG/PLA) nanoparticles (Elvassore, et al., 2001). Nevertheless, the supercritical fluid technique is faced with many challenges. To begin with, this process requires a high initial capital investment for

high pressure equipment which is essential for the elevated operating pressures. In addition, it is a challenge to dissolve strong polar substances in supercritical carbon dioxide fluid (Pinto Reis, et al., 2006).

In one word, various techniques have been developed to prepare nanoparticles and each bears both its strengths and limits. The physicochemical properties of the active ingredients and coating materials, as well as their interactions need to be taken into account when select the preparation method to maximize the overall properties of the nanoparticle systems.

2.5 Oral Bioavailability of Nanoparticles for Nutraceutical Delivery

Bioavailability is defined as a measure of the extent of a therapeutically active component that reaches the systemic circulation and is available at the site of action (Huang, et al., 2010). The biological barriers to oral delivery of nanoparticles involve the harsh gastric juice, the mucus layer that lines a majority of the GI tract and the epithelial lining (Gamboa & Leong, 2013). The oral bioavailability of nanoparticles for nutraceutical delivery is determined by many factors mainly including: (1) stability in GI tract; (2) permeability across the mucus layer of small intestine; and (3) permeability across the intestinal epithelial lining.

2.5.1 Enhancement of Stability in GI Tract

Some vulnerable compounds such as bioactive peptides and vaccines are not stable in the stomach due to the harsh gastric juice of acidic pH (pH 1.0-3.5) and digestive enzymes such as pepsin (Campbell, 2009; Marieb & Hoehn, 2010). (Marieb & Hoehn, 2010). Properly encapsulating them inside polymer nanoparticles could isolate them from gastric juices so as to maintain their bioactivity when traveling through the stomach. Take insulin as an example, it can be degraded in stomach (Hamman, et al., 2005), however, after encapsulating it into alginate/chitosan nanoparticles, approximately 50% was retained in the gastric environment for up to 24 h (Sarmento, et al., 2007).

When nutraceuticals are carried to the small intestine from stomach by nanoparticles, a plethora of enzymes in intestinal fluids would be an additional stumbling block for nanoparticles (Bedine, 2000). For instance, the duodenum of the small intestine contains degradative enzymes such as amylase, trypsin, and lipase (O'Neill, et al., 2011), leading to degradation of starch, proteins, and fats, respectively. Nanoparticles could protect the encapsulated ingredient against harsh intestinal environment and deliver it to the target absorption site. For example, in order to improve its oral bioavailability, insulin was encapsulated into chitosan/poly(γ-glutamic acid) (CS/γ-PGA) nanoparticles by an ionotropic gelation method (Sonaje, et al., 2010). Freeze-dried CS/γ-PGA nanoparticles exhibited intactness in pHs 2.0-7.2. The freeze-dried nanoparticles were then filled in an enteric-coated capsule. Upon oral administration, this capsule could

prevent the loaded nanoparticles from contact with gastric juice and liberate them rapidly in the proximal segment of rat small intestine. Subsequently, nanoparticles could adhere and penetrate into the local mucus layer (Sonaje, et al., 2009). The permeated nanoparticles could transiently open the tight junction between epithelial cells and at the same time nanoparticles were disintegrated due to pH-sensitivity. The released insulin was then able to pass through the epithelial lining through the opened tight junctions and entered into systemic circulation (Lin, Sonaje, et al., 2008; Sonaje, et al., 2009). Subsequently, the relative bioavailability of insulin was significantly improved (Sonaje, et al., 2010).

2.5.2 Enhancement of Permeability: Mucoadhesion and Permeation

Upon oral administration, nutraceuticals encounter a mucus layer while traveling the GI tract, which, together with a compact epithelial cell lining, compose a mucus barrier in the GI tract. The mucus layer is mainly composed of high molecular weight anionic glycoproteins, mucins, which are continuously produced by goblet cells in the intestinal epithelium (Atuma, et al., 2001). Mucins, enzymes, electrolytes and water give the cohesive and adhesive nature of the mucus layer (Allen & Garner, 1980; Kompella & Lee, 2001), making it a protecting barrier to prevent penetration of particles/pathogens to the epithelial surface (Schachter & Williams, 1982).

The thickness of mucus layer varies depending on the extent of digestive activity. For example, in human, its average thickness is about 170 μm in the gut, 10

μm in the ileum and 100 μm in the colon (Allen, 1989; Kerss, 1982). Nutraceuticals need to overcome this barrier to be absorbed through the gut wall and translocated into general circulation. Nanoparticles have the potential to adhere to the mucus layer thanks to their small size and diverse physicochemical properties. They can direct nutraceuticals to interact with mucus layer and facilitate their passage through the intestinal epithelium, which subsequently leads to higher nutraceutical concentration and longer residence time at the site of absorption and thereby more effective absorption (Florence, 2005; Mikos, et al., 1991).

The adhesion and interactions between nanoparticles and the mucus layer are driven by hydrogen bonding, van der Waal interactions, polymer chain interpenetration, hydrophobic forces, and electrostatic/ionic interactions (Lai, et al., 2009). The transport of nanoparticles across the mucus layer is greatly influenced by particle size (Acosta, 2009; Yun, et al., 2012). The mesh-pore spacing of mucus gel, ranging from 50 to 1800 nm limits the big particles to cross the intestinal mucosal barrier (Lai, et al., 2010). It has been reported that particles larger than 1000 nm cannot pass through this mucus barrier (Szentkuti, 1997), whereas particles less than 200 nm can diffuse through effectively (Primard, et al., 2010). Among the nanoparticles within the scale of 1000 nm, smaller particles also exhibited faster penetration across the mucus layer (Szentkuti, 1997). For example, the penetration time of hydrophobic latex nanospheres through the mucus gel layer decreased from 30 to 2 min by reducing particle size from 415 to 4 nm (Szentkuti, 1997).

Apart from reducing particle size, the addition of bioadhesive polymers over the surface of nanoparticles, such as chitosan, lectins and poly(acrylic acids), is the other approach to enhance their adhesion to the mucus layer (Acosta, 2009; Gabor, et al., 2004; Lehr, et al., 1992; Takeuchi, et al., 1996). For example, poly(isobutyl cyanoacrylates) (PIBCA) nanoparticles coated with mucoadhesive chitosan showed up to 44-fold higher attachment to rat intestinal mucosa compared to uncoated PIBCA nanoparticles. This significant improvement in mucoadhesion is due to the electrostatic interactions between the positively charged chitosan-coated nanoparticles and the negatively charged mucus. However, too strong an electrostatic interaction may lead to entrapment of particles within the porous mucus layer and impair the transport of the nanoparticles and nutraceuticals (Florence, 2005; Hussain, et al., 2001). Therefore, a balanced charge density is crucial in designing effective nanoparticle delivery systems.

2.5.3 Enhancement of Permeability: Transport across Epithelium

Upon penetrating through the mucus gel layer, nanoparticles encounter the underlying epithelial cell layer in GI lumen. This second barrier controls the absorption of exogenous substances and protects against the invasion of pathogenic microorganisms (Lavelle, 2001). The diverse lipid and protein composition of epithelial cell membrane makes the control of bioactive compounds absorption highly selective and site-specific (Janmey, 1995). Moreover, the space between epithelial cells is small (approximately 1 nm) because of tight junctions, making the

epithelium a highly compact barrier that is difficult to pass through (Förster, 2008). Once nanoparticles pass through the mucus layer and reach the surface of epithelial cells, they have to cross this epithelial lining so as to enhance the transport efficiency of nutraceuticals. Nanoparticles, as delivery vehicles, help nutraceutical transport across the intestinal epithelium via three main pathways (Figure 2-2): (1) paracelluar transport, where nanoparticles pass through the space between cells; (2) transcellular transport by enterocytes, where nanoparticles are internalized into cytoplasm, travel through the cell interior and released to the basolateral side, including passive (diffusion) and active (endocytosis) transport; (3) transcellular transport by M cells, where lymphatic uptake takes place (des Rieux, et al., 2006). These mechanisms involve different physicochemical and biological interactions between nanoparticles and epithelial cells. Therefore, designing nanoparticles with favorable physicochemical characteristics have been intensively investigated in order to regulate their transport pathways.

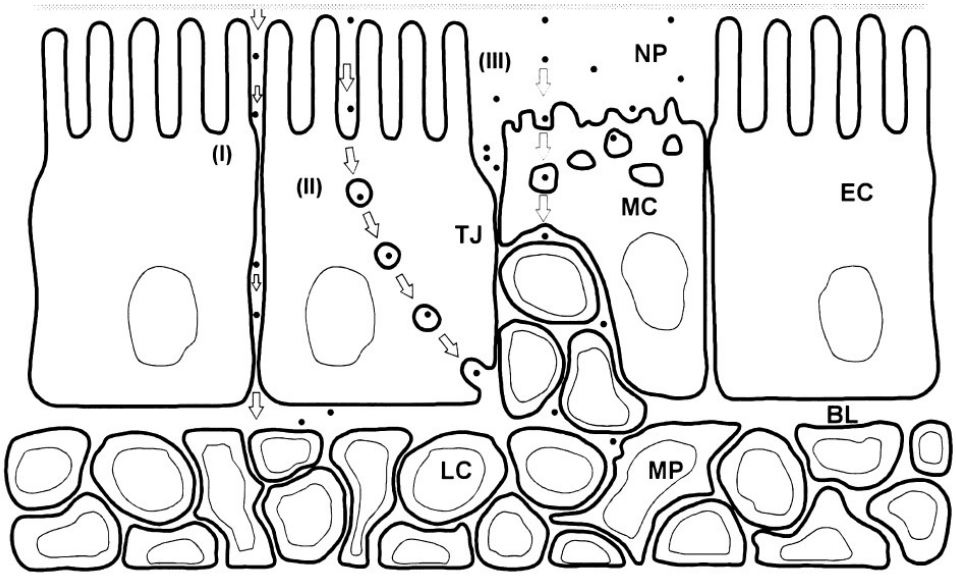

Figure 2-2. Transport pathways of nanoparticles through intestinal epithelial cells: (I) paracellular transport through tight junction, (II) transcellular transport by enterocytes and (III) transcellular transport by microfold cells (MC). TJ: tight junctions; EC: enterocytes; MC: microfold cells; LC: lymphocytes; MP: macrophages; BL: basal lamina. Adapted from (Jung, et al., 2000).

2.5.3.1 Paracellular Pathway

Paracellular transport refers to the transfer of nanoparticles across an epithelium through the tight junctions (Figure 2-2). Paracellular transport results from passive diffusion under the control of tight junctions (Yun, et al., 2012). Tight junctions share similar biophysical properties with ion channels. Paracellular transport is dependent on particle size, surface charge and concentration as well solution pH (Tang & Goodenough, 2003); however, it is not affected by hydrogen bonding capacity and lipophilicity (Jung, et al., 2000).

The dimension of the intercellular space is approximately 1 nm. The average size of aqueous pores created by epithelial tight junctions is around 0.7-0.9 nm at the jejunum, 0.3-0.4 nm at the ileum, and 0.8-0.9 nm at the colon in the human intestine (Tomita, et al., 1988). Consequently, these solutes with a molecular radius exceeding 1.5 nm (approximately 3.5 kDa) cannot be transported through this space (Rubas, et al., 1996).

Paracellular transport can be enhanced by coating the nanoparticles with polymers that may open the tight junctions, such as chitosan (Schipper, et al., 1997), poly(acrylate) (Lehr, et al., 1990), lectins and starch (Björk, et al., 1995). These polymeric nanoparticles were reported to enhance oral absorption of compound incorporated such as insulin, heparin and endotoxins via the paracellular pathway (Chen, et al., 2009; Sonaje, et al., 2010; 2011). With these polymers binding to the epithelial cells, the tight junctions may be reversibly interrupted by structural reorganization of tight junction-associated protein OZ-1 and cytoskeletal F-actin (chitosan) (Ma, et al., 2005). The enhanced transport may also be caused by a reduction of free extracellular Ca^{2+} concentration (polyacrylate) (Lehr, et al., 1990).

Considering tight junctions comprise only about 0.01% of the total absorption surface area of the intestine, the transport of nanoparticles across intestinal epithelia via paracellular route is greatly restricted by the tiny intercellular space as well as the tightness of junctions (Pappenheimer, 1987). The mechanisms for increasing the paracellular permeability of nanoparticles has been

widely investigated using *in vitro* cell models such as Caco-2 cell line; nonetheless, their relevance for the *in vivo* situation remains unknown (Jung, et al., 2000).

2.5.3.2 Transcellular Pathway by Enterocytes and Microfold cells

Enterocytes and M cells are the main sites where nutrient absorption takes place in the small intestine. Absorptive enterocytes make up more than 90% of the total epithelial surface whereas M cells represent approximately 1% and are only within Peyer's patches (Giannasca, et al., 1999). M cells are distinguished from enterocytes by their unique morphological properties, including (1) the underdeveloped microvillous and glycocalyx structures; (2) the presence of apical microfolds; (3) the increased intracellular vacuolization and (4) the absence of mucus (Sanderson & Walker, 1993). Transcellular transport, or transcytosis, across enterocytes is the most promising pathway for nanoparticles to pass through the intestinal epithelium and enter the blood stream. It is owing to not only the large surface area as a result of the presence of villi and microvilli but the multiple mechanisms participating during nanoparticle uptake. Transcytosis refers to the transport of a compound from one side of a cell to the other side by crossing the interior of the cell; the process involves a succession of complicated and iterative molecular sorting events (Mellman, 1996). With the aim of achieving efficient absorption of nutraceuticals via nanoparticle delivery, endocytosis efficiency of nanoparticles can be enhanced by modeling the physicochemical

properties of the particles. The process of transcytosis of nanoparticles has been extensively studied and used to design optimal delivery systems.

The first step of transcellular transport of nanoparticles is endocytosis. It refers to membranous vesicles containing nanoparticle(s) being pinched from the apical side of a cell and engulfed into the cytoplasm (Jung, et al., 2000). Endocytosis occurs via various mechanisms; great insights have been provided on the effects of nanoparticles with different physicochemical properties on endocytosis mechanism and efficiency. The endocytosis routes include passive and active mechanisms. Passive endocytosis is driven by the concentration gradient between the two sides of the cell membrane and is energy-independent. Active endocytosis, on the other hand, is the internalization of a compound against its concentration gradient and is energy-dependent. Active endocytosis includes (1) phagocytosis, a pathway mostly being used to remove microorganisms, cell debris and even apoptotic cells, and (2) pinocytosis (Beloqui, et al., 2012; Chung, et al., 2012; des Rieux, et al., 2006). The latter can be further categorized into:

(a) macropinocytosis, referring to the formation of a membranous vesicle (0.5-5 μm in diameter) filled with a large volume of extracellular fluid and molecules/nanoparticles (Sahay, et al., 2010).

(b) clathrin-mediated endocytosis, a mechanism involving the package of a cargo into vesicles from invagination of cell membrane with the assistance of the triskelion protein clathrin (Bareford & Swaan, 2007). This mechanism often leads

to intracellular processing, i.e. degradation of the cargo by lysosome within the cytoplasm (Galindo-Rodriguez, et al., 2005).

(c) caveolae-mediated endocytosis. Caveolae are flask-shaped invaginations (50-100 nm) that cover over 10% of endothelial cell membrane (Bareford & Swaan, 2007). This mechanism avoids the lysosomal pathway; therefore, it is the most promising pathway for transporting sensitive nutraceuticals across the intestinal barrier (del Pozo-Rodriguez, et al., 2009).

(d) receptor-independent endocytosis, or adsorptive endocytosis that occurs resulting from not specific ligand-receptor interactions, but electrostatic forces, hydrogen bonding or hydrophobic interactions between nanoparticles and cell membrane (Junginger, 1996). This pathway can lead to either intracellular processing or a transcytotic transport of the engulfed particles (Jung, et al., 2000).

Particle size is one of the most important determinants in endocytosis. On one hand, it significantly influences the endocytosis efficiency. It is reported that the internalization of Herceptin-colloidal gold nanoparticles ranging from 2-100 nm was highly size-dependent; the most efficient uptake was observed in nanoparticles with a diameter of 25-50 nm (Jiang, et al., 2008). On the other hand, particle size greatly affects the endocytosis mechanisms taken by the nanoparticles. For example, Hillaireau & Couvreur (2009) reported that larger solid particles (0.75-20 μm) could be internalized via phagocytosis. Moreover, Lai, et al., (2008) discovered that the entry of negatively charged polymer nanoparticles with the diameter of 43 nm was internalized via clathrin-mediated

endocytosis, while that of 24 nm was by clathrin- and caveolae-independent pathways. As for receptor-independent endocytosis, as receptors are not needed in this process, it is believed that the uptake of nanoparticles depends primarily on the size and other surface properties (Mohanraj & Chen, 2007). Studies on this theory, however, remain insufficient.

Apart from particle size, surface properties are another crucial factor determining the efficiency and mechanism of endocytosis. First of all, positively charged nanoparticles usually demonstrate higher uptake efficiency compared to their neutral and negatively charged equivalents. This is owing to the electrostatic forces between the particles and the negatively charged epithelial cell surface (Zhao, et al., 2011). Positively charged nanoparticles, such as chitosan and poly-lysine nanoparticles, could be internalized via clathrin-mediated endocytosis with some fraction utilizing macropinocytosis (Harush-Frenkel, et al., 2007; Rappoport, 2008; Sahay, et al., 2010) or by adsorptive endocytosis through non-specific interactions (Davda & Labhasetwar, 2002; Huang, et al., 2002). In addition, surface modification of nanoparticles can also affect the uptake mechanism. Wang, et al. (2013) observed that surface modification of PLGA nanoparticles with chitosan could alter their internalization from caveolae-mediated pathway to macropinocytosis and clathrin-mediated endocytosis. Moreover, surface hydrophobicity plays a role in regulating cellular uptake as well. The greatest particle uptake by Peyer's patches was observed in the nanoparticles with the highest surface hydrophobicity (Eldridge, et al., 1990).

Last but not least, the transport of nanoparticles can be affected by the cooperation of surface charge and hydrophobicity of nanoparticles as well as the *in vitro* and *in vivo* model being used (des Rieux, et al., 2006). It is reported that neutral or negatively charged and hydrophobic PLGA nanoparticles showed higher uptake by Peyer's patches (Shakweh, et al., 2005). However, positively charged and hydrophilic chitosan nanoparticles demonstrated higher uptake by mucus-covered enterocytes (Acosta, 2009).

2.5.4 Evaluation Models

Several screening methods including *in vitro* and *ex vivo* models are currently used as prediction tools for nanoparticle absorption in small intestine.

2.5.4.1 In Vitro Caco-2 Cell Model

Caco-2 cell monolayers have been widely used for evaluating the transport efficiency and associated mechanisms of nanoparticles across the small intestinal epithelium (Yin Win & Feng, 2005; Zabaleta, et al., 2012). When cultured on permeable insert of Transwell chambers (Figure 2-3), Caco-2 cells are able to spontaneously differentiate and polarize in 21 days. They form a continuous monolayer that exhibits the phenotype of mature enterocytes, including the presence of microvilli, tight junctions, dome formation, and production of brush border enzymes and transporters (Hidalgo, et al., 1989). The apical and basolateral chamber represents the intestinal lumen and the blood stream, respectively.

Caco-2 cell model enables the studies of both apical-to-basolateral (absorption) and basolateral-to-apical (secretion) transport.

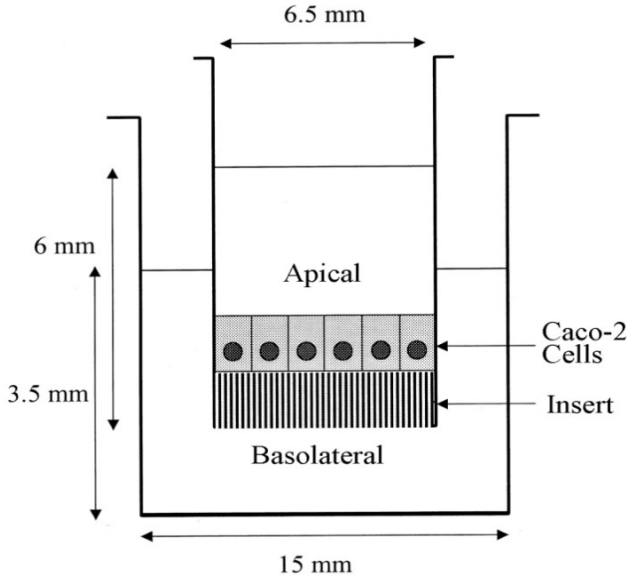

Figure 2-3. Transwell chamber system. Caco-2 cells are seeded on insert and they form a continuous monolayer epithelium in 21 days. Monolayer is continuous and thus separates the chamber into lower (basolateral) and upper (apical) compartments. Adapted from (Postgård, et al., 2002).

Indicators such as the permeability of hydrophilic molecules PEG 4000 or transepithelial electrical resistance (TEER) have been used to monitor the integrity of Caco-2 cell monolayers (Barthe, et al., 1999). The transport of PEG 4000 across well-formed Caco-2 cell monolayers is negligible. Any increment of PEG 4000 transport is indicative of cell damage or openingof the tight junctions (Barthe, et al., 1999). In terms of TEER value, it varies from laboratory to laboratory mainly depending on passage number of Caco-2 cells, and the higher values were reported in the older passages (Delie & Rubas, 1997).

Caco-2 cells retain many morphological and functional properties of the enterocytes. However, Caco-2 cell monolayers are devoid of mucin-producing goblet cells, hence the influence of mucus layer on the intestinal epithelium are excluded. In this case, mixed cultures of Caco-2 cells with mucin-producing cells such as HT-29 cells have been applied to overcome this limitation (Walter, et al., 2000; Wikman-Larhed & Artursson, 1995). Furthermore, the tight junctions formed in the Caco-2 cell lines appear to be tighter than those in enterocytes; a fact that may affect the permeability of nanoparticles via paracellular pathway (Artursson, Ungell, & Löfroth, 1993; Lennernäs, Palm, Fagerholm, & Artursson, 1996). Additionally, the expression of transporters can be highly different compared to the expression in human intestine. Therefore, predicting the nanoparticles absorption requires further *ex vivo* tests.

2.5.4.2 Ex Vivo Ussing Chamber Model

To increase the predictive value of *in vitro* studies, the sections of small intestinal tissues mounted in the Ussing chamber (Figure 2-4) can be used for the evaluation of the mucosa adhesion and permeability of nanoparticles for nutraceuticals delivery (Agüeros, et al., 2009; Dube, et al., 2010; Lennernäs, et al., 1996). Nanoparticles are added to the donor chamber and its accumulation in the receiver chamber is recorded as a function of time. The nanoparticles can be given from either mucosal or serosal surface, which allows evaluation of the directional flux from mucosal-to-serosal or from serosal-to-mucosal side. This model allows

the analysis of several pieces of tissues at the same time; therefore, it offers the possibility of running Peyer's Patch and Peyer's Patch-free tissues in parallel.

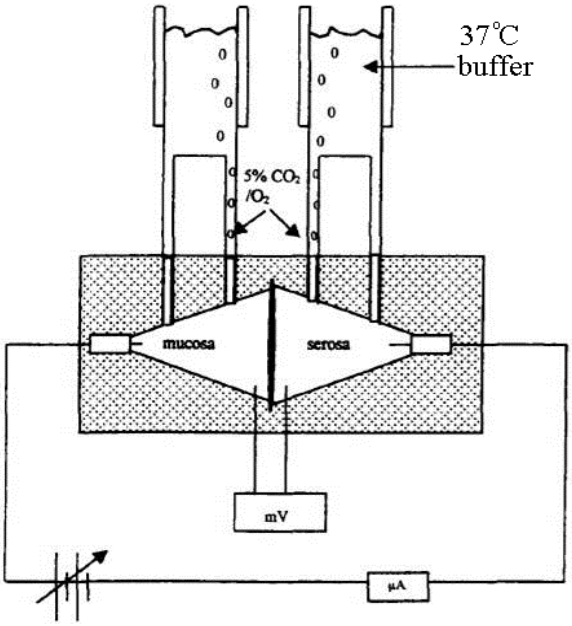

Figure 2-4. Ussing Chambers: intestinal tissue is mounted in a flux chamber; nanoparticles are added either in mucosal chamber or serosal chamber to measure mucosal-to-serosal or serosal-to-mucosal flux. The electrical resistance can be monitored. Adapted from (Barthe, Woodley, & Houin, 1999).

This model is rapid and useful for targeting transport at specific sections of intestine. Additionally, it allows the measurement of the electrical parameters of the mucosa during the experimental tests. Electrodes in the mucosal and the serosal bathing solutions can measure the potential difference and the current flow across the tissue resulting from the inorganic ion flow across the epithelium. The tissue viability and integrity can be monitored by recording the short-circuit current and TEER value (Yeh, et al., 1994). It is essential to check these two parameters during

the tests to make sure the tissues remain intact and functioning well. Nevertheless, these parameters have been barely monitored in many studies. Besides, the incubation time has to be carefully considered (Levine, et al., 1970; Plumb, et al., 1987). Furthermore, the intestinal mucosa is very metabolically active, thus adequate supply of energy source such as glucose or glutamine is needed (Barthe, et al., 1999).

One general issue with all the *in vitro* and *ex vivo* systems is that the effect of physiological factors such as gastric emptying rate, GI transit rate, GI pHs, etc. are excluded in the data analysis (Barthe, et al., 1999); therefore, the efficacy of nanoparticles for nutraceuticals delivery should be validated by *in vivo* test.

2.6 Protein-based Nanoparticles

2.6.1 Advantages of Food Protein as a Potential Delivery Vehicle

Various synthetic polymers have been widely used to prepare nanoparticles for drug delivery. Among them, PLA and PLGA are most commonly used due to their superior biodegradability and regulatory physiochemical properties (Allémann, et al., 1993; Allémann, et al., 1996; Cheng, et al., 2007; Krause, et al., 1985; Nobs, et al., 2003). However, they cannot be used in food for nutraceutical delivery, as they are not generally recognized as safe (GRAS) for consumption in large quantities (Chen, et al., 2006). Food proteins are one of the promising materials for nutraceutical delivery as they are not only GRAS but can interact with

nutraceuticals via various interctions (e.g. hydrophobic interactions, electrostatic interactions, hydrogen bonding, disulfide bonding, and van der Waal forces). In addition, their three-dimensional protein networks may enable them to reversibly bind of active compounds, to protect them in a matrix and to specifically target to the site of action (Chen, et al., 2006; Elzoghby, et al., 2011).

Unique functional properties possessed by proteins include water holding capacity, forming, gelation and emulsion, which allow them to be an ideal material for nanoencapsulation (Chen, et al., 2006). Their amphiphilic property allows them to encapsulate both hydrophobic and hydrophilic nutraceuticals (Chen, et al., 2006). In addition, food proteins have high nutritional values, desirable absorption in the body, low toxicity of the end degradation products and extraordinary binding capacity to various ingredients (Liu, et al., 2005). Moreover, many modifications can be performed on proteins, owing to their consistent primary structures that allow them to form complexes with adhesion enhancers or ligands for cell targeting and controlled release, such as polysaccharides, lipids, and other biopolymers. Some protein delivery systems such as hydrogels, emulsions and microparticles have been intensively studied over the years, yet protein-based nanoparticles are relatively new in the food industry in spite of their potential to improve the bioavailability of nutraceuticals (Chen, et al., 2008).

2.6.2 Animal Protein-Based Nanoparticles

A variety of animal proteins such as whey proteins and albumin have emerged as versatile nanocarriers mainly for therapeutic and diagnostic agents. Whey protein nanoparticles have been applied to encapsulate zinc chloride and date palm pit extract (Bagheri, et al., 2013; Gülseren, et al., 2012; Girard, et al., 2002). Albumin nanoparticles demonstrated a high binding capacity to various compounds due to their multiple binding sites, suggesting they can be used as a promising carrier for bioactives (Kratz, 2008). However, most of albumin nanoparticles have been extensively developed for drug delivery, especially for targeting delivery of anticancer drugs to tumor tissues (Kratz, 2008; Park, 2012). The most successful and advanced nano-product is Abraxane® which was first approved by the FDA in 2005 and since then has been approved in 41 countries so far for the treatment of metastatic breast cancer (Petrelli, et al., 2010).

Animal protein-based nanoparticles, however, cannot achieve a sustainable release owing to their hydrophilic nature and rapid solubilization in aqueous environments (Elzoghby, et al., Samy, & Elgindy, 2012). Therefore, chemical crosslinkers (e.g. glutaraldehyde and formaldehyde) are usually used to harden protein nanoparticles; nevertheless, the application of the nanoparticles in foods may be limited due to the presence of residual crosslinkers as well as the risk of formation of toxic products by reaction with the tissues during *in vivo* biodegradation (Muzzarelli, 2009).

2.6.3 Plant Protein-Based Nanoparticles

In contrast to hydrophilic animal proteins, hydrophobic plant proteins such as zein and lectins have been used to prepare nanoparticles as well (Ezpeleta, et al., 1996; Lai & Guo, 2011). Zein, an alcohol-soluble protein, is regarded as GRAS and food grade ingredient by FDA. Zein nanoparticles have been applied to encapsulate: (1) fish oil and docosahexaenoic acid (DHA), with enhanced oxidative stability (Torres, et al., 2010; Zhong, et al., 2009); (2) 5-fluorouracil, with targeted delivery to liver (Lai & Guo, 2011); and (3) doxorubicin, with enhanced cytotoxicity in breast cancer cells through sustained release (Perumal, et al., 2009). Lectins are carbohydrate-binding proteins, which are nonenzymatic, non-immunogenic and highly specific for sugar moieties (Van Damme, et al., 1998). Lectins can specifically bind to glycosylated proteins and lipids (glycan) in cell membranes; therefore, as a result, they have been extensively used as coating materials over various nanoparticles. For example, lectin-coated nanoparticles can bind to intestinal epithelial cells so as to stimulate the cellular uptake, the transport of across enterocytes and the translocation into blood circulation (Russell-Jones, et al., 1999). In addition, lectin-coating can protect peptides and proteins from *in vivo* digestion after oral administration (Gabor, et al., 2004). However, such applications of lectins in food areas for nutraceutical delivery have been barely studied.

Studies on plant protein nanoparticles in food areas are very limited, yet they hold great promise in nutraceutical delivery. On the top of unique properties discussed above, these particles have strong structures without the need of toxic

chemical cross-linkers as a result of hydrophobic nature of plant proteins (Ezpeleta, et al., 1996). In addition, compared with animal proteins, plant proteins are less expensive and may reduce the risk of spreading diseases such as bovine spongiform encephalitis (mad cow disease) (Ezpeleta, et al., 1996; Lai & Guo, 2011). It should be noticed that organic solvents may be needed during the preparation of some plant proteins which could limit their application in the food industry.

2.7 Soy Proteins

Soybean is rich in proteins (40-50%), lipids (20-30%) and carbohydrates (26-30%) (Petruccelli & Anon, 1995). Soy proteins are abundant, renewable, inexpensive and biodegradable. They are composed of albumins (10%) and globulins (90%). The globulins are composed of 2S (15%), 7S (34%), 11S (41.9%) and 15S (9.1%) proteins, based on their sedimentation rates when dissolved in a pH 7.6 and 0.5 M ionic strength buffer (Fukushima, 1991).

Functionalities of soybean proteins are determined by the composition and structure of the major components. Soy proteins have demonstrated significant effects on reducing serum cholesterol, low density lipoprotein cholesterol and triglyceride levels due to the presence of isoflavones in the product (Anderson, et al., 1995). On the basis of this research, FDA granted a health claim that “25 grams of soy protein a day, as part of a diet low in saturated fat and cholesterol may reduce the risk of heart disease.”

2.7.1 Soy Protein Isolate

Soy protein isolate (SPI) refers to highly refined soybean proteins, with a minimum protein content of 90% on a moisture-free basis, which has been claimed as a GRAS substance by FDA in 1979. It is composed almost exclusively of two globular protein fractions differentiated by sedimentation coefficient: 7S (β-conglycinin) and 11S (glycinin) (Saio & Watanbe, 1978; Wolf, et al., 1961). 7S (180 to 210 kDa) is a glycosylated hetero-trimer and constituted randomly of three different subunits: α (≈67 kDa), α′ (≈71 kDa), and β (≈50 kDa), which are stabilized by non-covalent bonds. The α and α' subunits are composed of two different domains: the core region (418 residues) and the extension region (α, 125 residues; α′, 141 residues) (Maruyama, et al., 1998), whereas the β subunit contains only the core region (416 residues). The core region is well preserved in each subunit, which contributes to the thermal stability of 7S. The extension region in 7S, on the other hand, demonstrates a strong acidic nature and 57.3% sequence identity (Shutov, et al., 1996). It also possesses high solubility and emulsifying ability. 11S (309 to 363 kDa) is a hexamer composed of intermediary subunits, in which one acidic subunit (A, 38 kDa) and one basic subunit (B, 20 kDa) are linked by a single disulfide bridge. The disulfide bonds between the subunits can perform non-covalently and provide a hexamer that can be dissociated by urea, guanidinium or sodium dodecylsulphate (Shewry, 1995). The mass fractions of acidic subunits are around 60%, which confer excellent emulsifying properties to 11S (Liu, et al., 1999). Similarl to 7S, 11S has certain thermal stability. Their function differs

owing to structural differences. Nevertheless, both fractions contain antiparallel β-sheet and random coil as major secondary structures and low levels of α-helix (Fukushima, 1968). Their molecules are fairly folded tertiarily, which form the water-impenetrable hydrophobic region. Hydrophobic interactions play an important role in stabilizing the internal structures of 7S and 11S. Their molecules are usually proteinase-resistant before the internal structure is disrupted. The initial velocity of the proteinase hydrolysis is proportional to the degree of their disruption (Fukushima, 1968).

2.7.2 SPI-based Nanoparticles

SPI has been used as a coating material to fabricate microparticles encapsulated with various compounds such as orange oil, flavors, α-tocopherol and so on (Charve & Reineccius, 2009; Kim & Morr, 1996; Nesterenko, et al., 2012). Besides, some of SPI microparticles were produced with the combination of SPI with other proteins or polysaccharides (Augustin, et al., 2006; Mendanha, et al., 2009; Yu, et al., 2007). The combination provides better protection and oxidative stability for fish oil, as well as better drying properties (Augustin, et al., 2006). If these nutraceuticals can be incorporated into nanoparticles, more favorable functions would be achieved, considering nanoparticles contribute to higher solubility, better tissue permeability, prolonged retention time and more efficient cellular uptake of the entrapped compounds (Chen, et al., 2006). However, to date, only a handful of studies have been done to prepare SPI nanoparticles

(Teng, et al., 2012, 2013). Recently, SPI nanoparticles encapsulated with curcumin, were produced by a simple coacervation-crosslinking-evaporation process (Teng, et al., 2012). These nanoparticles exhibited satisfactory curcumin encapsulating ability and desirable stability at high concentrations. Nonetheless, ethanol and glutaraldehyde were involved in the preparation process, which would limit the application of these nanoparticles in the food products (Teng, et al., 2012). Prior to the preparation of nanoparticles, SPI was conjugated with folic acid (FA) using simple coacervation method (Teng, et al., 2013). FA possesses positively charged lysine residues on the backbone, as a result, SPI nanoparticles conjugated with FA showed snaller particle size and lower zeta-potential of -36 to -42 mV, depending on the conjugation degree, suggesting higher dispersion stability. The encapsulation and loading efficiency of the conjugated particles were significantly higher than the non-conjugated ones ($p < 0.05$) (Teng, et al., 2013). FA conjugation also led to enhanced cellular uptake by at most 93% in Caco-2 cells. However, the utilization of reagents such as DMSO, EDC and ethanol in nanoparticles preparation would limit their applications in food products. In another study, SPI nanoparticles and carboxymethyl chitosan/SPI nanoparticles (CMCS/SPI) were produced by a simple ionic gelation method (Teng, et al., 2013), without using any organic reagent. In comparison with CMCS nanoparticles, CMCS/SPI nanoparticles showed better particle forming capability and increased loading efficiency of VD_3. In addition, compared to SPI nanoparticles, CMCS/SPI nanoparticles demonstrated significantly higher encapsulation efficiency, reduced

release of VD_3 in simulated gastric fluid, and increased release under simulated intestinal condition (Teng, et al., 2013). In comparison to simple coacervation method, ionic gelation method used in this study is a green and non-toxic method which may be used for SPI nanoparticle preparation so as to achieve their application food industry for nutraceutical delivery. However, their biological properties and cytotoxicity need to be studied by *in vitro* and *in vivo* tests.

2.8 Safety Concerns and Prospects of Nanoparticles-based Functional Foods

Nanotechnology offers many opportunities for the development of food ingredients, additives as well as innovative delivery systems for bioactive compounds (Chaudhry, et al., 2007). Although there has not been scientific evidence suggesting toxicity of nanoparticles is a major hazard to human health so far; the potential risks of nanoparticles being consumed with food products cannot be neglected (Nel, et al., 2006).

As a consequence of the small size and large surface area per mass/volume, nanoparticles can penetrate more easily into different tissues and cells, and be potentially more hazardous to the body than the same ingredient in natural form (Nel, et al., 2006). However, it remains to be determined whether the unique physicochemical properties of nanoparticles would result in unpredictable harmful effects (Chau, et al., 2007).

Currently, there are still some gaps preventing risk inspectors for establishing the safety for many possible food related applications of nanotechnology. The routine monitoring of the physicochemical state of nanoparticles in food matrices is still not applicable due to the complexity food matrices, which consequently increases the uncertainty in the exposure assessment. Nanoparticles have the potential to pass through GI, blood-brain, placenta and blood-milk barriers, which may lead to undesirable accumulation of nanoparticles in different tissues/organs (Martirosyan, et al., 2012), therefore, the development of real-time tracking technique of nanoparticles in biological fluids, tissues and organs is in demand. Also, the possible interactions between the nanoparticles with other food components may alter the physicochemical properties of nanoparticles and may in turn influence their behaviors in the human body (Sanguansri & Augustin, 2006). However, these interactions have been barely studied so far. Besides, the hazard assessment of pro-inflammatory potential of nanoparticles needs to be evaluated as well, as the inflammation itself is related with some diseases, such as cancer, diabetes and bowel diseases (Martirosyan, et al., 2012).

To date, the potential toxicity of nanoparticles has been explored frequently by assessing the impacts of nanoparticles on cell viability using *in vitro* cell culture models and the bio-distribution of nanoparticles in different tissues/organs using animal models; however, more comprehensive toxicological research on the nanoparticle-based food products is needed in the future. The health, safety and environmental impacts should be addressed before applying nanoparticles in food

products in order to minimize potential side effects (Sanguansri & Augustin, 2006). In addition, regulatory standards should be developed in terms of adding nanoparticles into food (Rashba & Gamota, 2003). As nanoparticle-based food products are supposed to be administrated daily over years, preparation of nanoparticles with food-grade or GRAS materials/solutions and green techniques could minimize the adverse effects (Bernkop-Schnürch, 2013).

Chapter 3. Preparation, Formation Mechanism and *In Vitro* Evaluation of Calcium-induced Soy Protein Isolate Nanoparticles[1]

3.1 Introduction

To date, oral delivery is still the preferred administration route of bioactive compounds, especially for chronic therapies where repeated administration is required, nevertheless, many compounds exhibit low oral bioavailability due to poor solubility, permeability, and/or instability in the gastrointestinal (GI) tract. Nanoparticles are promising vehicles that may allow efficient delivery of bioactive compounds to human small intestine for an improved absorption because they can dramatically prolong the formulation residence time by decreasing the influence of intestinal clearance mechanisms and by increasing their surface area to interact with the biological support (Kawashim, 2001; Peppas, 1995). Moreover, they are small enough to cross the epithelial lining of the gut and are readily taken up by cells (Desai, et al., 1997; Lamprecht, et al., 2004), thus permitting the delivery of bioactive molecules to their target sites in the body. Although various nano-vehicles have been designed for intelligent, modulated, and selective delivery of drugs to specific areas in order to maximize drug action and minimize side effects, many of

[1]A version of this chapter has been published in Food Chemistry (2012), 133: 390-399.

these nanoparticles areprepared from synthetic polymers (Guo, et al., 2011; Tang, et al., 2010, Malik et al., 2000), which cannot be used in foods that require "generally regarded as safe" (GRAS) materials.

Among GRAS ingredients, food grade proteins are especially interesting for nanoparticles preparation as delivery vehicles. Food proteins possess unique functional properties including their ability to form gels and emulsions, offering the possibility of developing delivery systems for both lipophilic and hydrophilic bioactive compounds (Chen & Subirade, 2006; Picot & Lacroix, 2003). Additionally, food proteins can bind a wide range of bioactive molecules into their polypeptide structures (Chen & Subirade, 2008), which creates possibilities for a better protection of the bioactive molecules until release at the functional site. Moreover, the nanoparticle surfaces can be modified to enhance affinity to certain organs/tissues for improved target delivery due to availability of a diversity of reactive groups on protein chains. Over the past decade, gelatin (Shutava et al., 2009), β-lactoglobulin (Chen & Subirade, 2005), and bovine serum albumin (BSA) (Jun, et al., 2011), have already been made into nanoparticles. However, effort to develop plant protein based nanoparticles has been less extensively investigated, even though plant proteins are more affordable and acceptable to consumers. The few examples include gliadin and zein (Arangoa, et al., 2001; Patel, et al., 2010).

SPI is widely used in the food industry owing to its excellent gelling property. It is composed almost exclusively of two globular protein fractions differentiated by their sedimentation coefficient: 7S (β-conglycinin) and 11S (glycinin). Both

fractions can form heat-induced or cold-induced gels (Saio & Watanabe, 1978; Renkema, et al., 2001). For cold gelation, the matrix formation involves a two-step process. During the preheating step, proteins are unfolded and polymerized into soluble aggregates, followed by a cooling step and subsequent addition of cationic ions, resulting in the formation of a bulk gel system. SPI based microparticles have been prepared using a cold gelation method in our previous work (Chen & Subirade, 2009). These microparticles demonstrated potential as oral delivery vehicles for both water and lipid soluble bioactive compounds. By decreasing the particle size to nanometer range, a novel SPI delivery system can be developed with the pursue of improving the absorption of bioactive compounds which exhibit low bioavailability. However, research to develop SPI nanoparticles using cold gelation has never been reported. As the features of nanoparticles (size, surface properties, etc.) determine their biological behavior and efficiency as delivery systems (Sundar, et al., 2010), a fundamental understanding of the impact of processing conditions on particle features, subsequently the mechanism of particle formation is necessary.

This study is the first stage of the project focusing on preparation and *in-vitro* evaluation of calcium-induced SPI nanoparticles. The impacts of processing conditions on particle features were systematically investigated. The SPI nanoparticle formation mechanism was explored based on an investigation of protein conformational changes during the nanoparticle formation process using three combined techniques, including Fourier transform infrared spectroscopy (FTIR), circular dichroism (CD) and fluorescence spectroscopy. Nanoparticle

dissociation behavior in the presence of dithiothreitol (DTT), urea, sodium dodecyl sulfate (SDS) and ethylenediaminetetraacetic acid (EDTA) was also studied to investigate the driving forces (disulfide bond, hydrogen bond, and hydrophobic interaction) contributing to nanoparticle formation. The cytotoxicity and cellular uptake of the prepared nanoparticles were evaluated *in vitro* using Caco-2 cells.

3.2 Materials and Methods

3.2.1 Materials

SPI PRO-FAM® 646 was kindly provided by Archer Daniels Midland Company (ADM, Decatur, IL, USA), containing 94.4% protein on a dry basis as determined by combustion with a nitrogen analyzer (Leco Corporation, St. Joseph, MI, USA) calibrated with analytical reagent grade EDTA and caffeine using a conversion factor of 6.25. D_2O, NaOD, DCl, Rose Bengal, 3-(4,5-dimethyltiazole-2-*yl*)-2,5-diphenyltetrazolium bromide (MTT), dimethyl sulfoxide (DMSO) and 4',6-diamidino-2-phenylindole (DAPI) were purchased from Sigma-Aldrich (Oakville, ON, Canada). Concanavalin A and Alexa Fluor® 594 conjugate, Eagle's minimum essential medium (EMEM), fetal bovine serum (FBS), Trypan-blue, Trypsin-EDTA, sodium pyruvate, 4-(2-hydroxyethyl)-1-piperazineethanesulfonic acid (HEPES) and 1% penicillin-streptomycin solution were purchased from Invitrogen (Burlington,

Canada). Caco-2 cells (HTB®-37™) were purchased from the American Type Culture Collection (ATCC). All other chemicals were of reagent grade.

3.2.2 Nanoparticle Preparation

SPI powder (10 mg/ml) was hydrated in deionized water and stirred for 30 min at 23 °C. The pH of the suspensions was raised to pH 12 using 0.5 M NaOH and the suspensions were allowed to stand for 30 min. The alkaline treated SPI solutions were heated at 85 °C for 30 min in tightly closed tubes using a water bath to induce SPI unfolding and disrupt large particles. The solutions were then cooled to 23 °C for 30 min and their pH values were adjusted back to 7, 8, and 9 with 0.5 M HCl. The final protein concentration was diluted to 6 mg/ml. $CaCl_2$ was added to a final concentration of 2.5, 5, 10 and 15 mM in the protein solutions to induce particle formation. The final suspensions exhibited pH values in the range of 6.8-8.8 as the addition of $CaCl_2$ decreased the pH and the final protein concentration was diluted to 5 mg/ml. The prepared suspensions were stored at 23 °C overnight prior to visual and turbidity analysis. The turbidity of the formed suspensions was measured using a UV-Vis spectrophotometer (Jasco V-530, Japan) at 600 nm. The protein nanoparticles were deemed "formed" when the suspensions turbidity value increased by at least 50% and without precipitation upon addition of calcium. The turbidity values of 2.5-15 mM $CaCl_2$ solutions at pH 7-9 were measured as blank controls.

3.2.3 Nanoparticle Characterizations

The size and zeta-potential of the nanoparticles were measured at 23 ^{o}C respectively by dynamic light scattering and laser Doppler velocimetry using a Zetasizer NanoS (model ZEN1600, Malvern Instruments Ltd., UK). Their suspensions were diluted in 0.01 M phosphate buffer (the same pH as the original suspension) to a suitable concentration before analysis.

The morphology or inner core structure of pretreated SPI and SPI nanoparticles was observed by a JEOL 2200FS Transmission Electron Microscope (TEM) (JEOL Ltd., Tokyo, Japan) at 200 kV equipped with a Schottky field emission gun and an in-column omega type energy filter. For sample preparation, one drop of the prepared suspensions was placed on TEM grids coated with carbon films. The extra suspensions were blotted with filter paper after 1 min when enough particles were adsorbed on grids. The samples were air dried before imaging. The morphology of pre-treated SPI and SPI nanopaticles was observed using zero-loss TEM mode, which filtered out all the inelastic electrons to enhance the image contrast. The inner structure of the nanoparticles, whereas, was characterized using high angle annual dark field scanning transmission electron microscopy (HAADF-STEM) imaging. A 0.7 nm probe with beam dose 1.6 x 10^{-2} electron/nm^2 was used for all HAADF imaging. By adjusting the camera length, the collection angle of HAADF detector was optimized to capture the best contrast of the area of interest.

Surface hydrophobicity (S_o) of pre-treated SPI and SPI nanoparticles was evaluated by the Rose Bengal method (Lukowski., et al., 1992). Briefly, a fixed amount of Rose Bengal (20 μg/ml) was added to the pre-treated SPI or SPI nanoparticle suspensions at different concentrations (15-35 μg/ml). Rose Bengal underwent partitioning between the dispersion medium and the protein or particle surface. At each concentration the partitioning quotient (PQ) was calculated according to: PQ = (amount of Rose Bengal bound on the surface of nanoparticle or protein) / (amount of Rose Bengal in dispersion medium). From the results of the above calculations, profiles were constructed for PQ as a function of the total particle or protein surface area. The plots obtained were found to be linear and the corresponding slopes for all concentrations tested were taken as a measure of S_o value.

3.2.4 Nanoparticle Stability Test

The influence of pH on SPI nanoparticle stability was evaluated by adjusting suspension pH to 2-9 using 0.1 M NaOH or HCl. The final protein concentration was diluted to 2.5 mg/ml. Samples were stored at 23 ^{o}C overnight prior to size and zeta-potential analysis using the Zetasizer NanoS. The storage stability of SPI nanoparticles was also investigated by measuring particle size and suspension turbidity after storage at 4 ^{o}C for 7, 14 and 21 days.

3.2.5 Protein Solubility and Conformation Study

The formation of a stable protein solution was a prerequisite for nanoparticle formation. The solubility of the native and the pre-treated SPI was evaluated by dispersing SPI powders (5 mg/ml) in deionized water adjusted to pH 7 using 0.5 M HCl or NaOH. The dispersions were stirred for 1 h at 23 ^{o}C and then centrifuged at 12,000 × g for 30 min. The protein concentration of supernatants was determined according to the Bradford method using BSA as the standard (Bradford, 1976). Percent protein solubility was calculated according to: protein solubility (%) = (amount of protein in supernatant / amount of protein added) × 100.

Protein conformational changes before and after nanoparticle formation were characterized using FTIR, CD and fluorescence spectroscopy. The FTIR spectra were determined at 23 ^{o}C using a Magna 560 Nicolet spectrometer (Madison, WI, USA) equipped with a mercury-cadmium-telluride detector in the wave number range of 400 to 4000 cm^{-1} during 128 scans with 4 cm^{-1} resolution. D_2O was used to prepare native SPI, pre-treated SPI and SPI nanoparticle dispersions (5 mg/ml), and 0.5 M NaOD or DCl was used to adjust pD. To ensure a complete H/D exchange, samples were prepared 2 days before and kept at 4 °C in a sealed nitrogen environment prior to infrared measurements. Samples were placed between two CaF_2 windows separated by a 23 μm polyethylene terephthalate film spacer. To study the amide I region (1700-1600 cm^{-1}), known as amide I′ in D_2O of the protein, subtraction and Fourier self-deconvolutions were performed using the software provided with the spectrometer (*Ominic* software). Band narrowing was

achieved with a full width at half of 24 cm^{-1} and with a resolution enhancement factor of 2.5 cm^{-1}.

The CD spectra were recorded on a J-710 spectropolarimeter (Jasco Co., Tokyo, Japan) at both far-UV (190-250) and near-UV (250-320) regions. Path lengths were 0.1 cm for far-UV region and 2 cm for near-UV region. Ellipticity was recorded at a speed of 100 nm/min, 0.2 nm resolution, 20 accumulations and 1.0 nm bandwidth. The samples (5 mg/ml) used were pre-treated SPI and SPI nanoparticles prepared at pH 8 in the presence of 0, 2.5 and 5 mM calcium. The concentration of samples was diluted to 12.5 μg/ml in 0.01 M sodium phosphate buffer (pH 8). Buffer background was subtracted from the raw spectra.

Protein intrinsic fluorescence emission spectra were measured using a Cary Eclipse Fluorescence spectrophotometer (Varian Inc., Palo Alto, CA, USA). The spectra were recorded from 290 to 500 nm with an excitation wavelength of 280 nm. Spectral resolution was 5 nm for excitation and 10 nm for emission. Samples experienced the same dilution as indicated in CD spectra measurement.

3.2.6 Nanoparticle Dissociation Test

To better understand the driving forces of SPI nanoparticle formation, SPI nanoparticle dissociation behavior was studied. Nanoparticle dispersions were mixed with an equal volume of each dissociating reagent (DTT, urea, SDS, or EDTA) at various concentrations. The mixed solutions were adjusted to pH 7 and left to stand overnight. The suspension turbidity was determined with a UV-Vis

spectrophotometer at 600 nm. The impact of dissociate reagents on the nanoparticle visual appearance and morphology was observed using a camera (Kodak Easyshare Z812, USA) and a TEM (Hitachi H-7000, Tokyo, Japan), respectively. For TEM observation, the samples were prepared by coating a copper grid with a thin layer of nanoparticle suspension. After negative staining with 1% phosphotungstic acid, excess liquid was blotted from the grid. Samples were then air dried and examined using a TEM at an accelerating voltage of 100 kV.

3.2.7 *In Vitro* Cytotoxicity and Cellular Uptake of the SPI Nanoparticles

For MTT assay, Caco-2 cells (passages 26) were seeded at 5×10^4 cells/well into 96-well plates (Costar, Corning, NY, USA) in the EMEM medium, supplemented with 10% FBS, 1 mM sodium pyruvate, 2.23 mg/ml of $NaHCO_3$, 2.38 mg/ml HEPES and 100 IU/ml penicillin-100 μg/ml streptomycin solution. The cells were allowed to recover for 24 h at 37 °C in the incubator. The medium in each well was then replaced with SPI nanoparticle suspension diluted with EMEM medium to obtain SPI concentrations of 0.3125, 0.625, and 1.25 mg/ml. EMEM medium without nanoparticles was used as a control. After 24 and 48 h incubation, the cell viability was evaluated by MTT assay as follows: aliquots (10 μl) of MTT solution (10 mg/ml in PBS) were added to each well and the plates were incubated for 4 h at 37 °C, followed by removal of the medium and addition of 100 μl DMSO to each well. After 30 min incubation at 37 °C, the plates were read at 570 nm using

a microplate reader (GENios, Tecan, Männedorf, Switzerland). Results are expressed as percentage of cell growth with respect to the control wells.

Confocal laser scanning microscopy (CLSM) was used to observe the uptake of nanoparticles in Caco-2 cells. For a better observation, nanoparticles were labeled with Courmarin 6 (6-COUM). Briefly, 1.5 ng/ml 6-COUM was added in pre-treated SPI solution at pH 9, where the dye is chemically stable. After stirring for 3 h under dark environment, the solution was adjusted to pH 8 followed by addition of 5 mM calcium to induce nanoparticle formation. The 6-COUM labeled SPI nanoparticles were dialyzed in dark at 4 °C against 5 L of PBS (0.01M, pH7.4), the PBS being replaced every 6 h nearly for 48 h until no 6-COUM was detected in solution by a Fluorescence spectrophotometer (λ_{ex} = 495 nm, λ_{em} = 525 nm). The PBS used for dialysis was accumulated to determine the amount of 6-COUM not loaded on nanoparticles. The amount of 6-COUM was calculated based on a standard calibration curve constructed by measuring the fluorescent emission intensity of the 6-COUM at different concentrations (0.1-1.5 ng/ml). The amount of 6-COUM loaded on nanoparticles is equal to the amount of 6-COUM added minus the amount of 6-COUM not loaded on nanoparticles.

Caco-2 cells (5×10^4 cells/well) used for the uptake study were seeded onto the coverslip in 6-well plates (Costar, Corning, NY, USA), and allowed to recover for 24 h at 37 °C. Both 6-COUM loaded SPI nanoparticles (0.3125 mg/ml) and free 6-COUM (used as a control) were added to each well and incubated for 12 h. Then the cells were washed twice with PBS, and their membranes were stained with

0.0005% (w/v) Alexa Fluor® 594-Concanavalin A conjugate in PBS for 10 min. The residual dye was removed after washing, then the cells were fixed with an ice-cold solution of 3.7% formaldehyde for 30 min. Afterwards, the cells were washed 3-time to remove the residual formaldehyde. The slides with seeded cells were covered with the mounting medium containing 1 µg/ml DAPI to stain the cell nuclei and closed with cover glasses. Cells were then observed with a CLSM 510 Meta (Carl Zeiss, Jena, Germany) equipped with a diode at 405 nm of excitation, an Argon laser (providing the excitation at 488 nm) and a helium/neon laser (providing the excitation at 543 nm). An oil immersion objective (40×) was used to visualize samples. Images were processed with ZEN 2009 LE software (Carl Zeiss MicroImaging GmbH, Oberkochen, Germany).

3.2.8 Statistical Analysis

All experiments were performed in triplicate samples in at least three independent batches. Results were expressed in tables as mean ± standard deviation. Error bars on figures represented standard deviations. Statistical differences between samples were performed by comparison of means using ANOVA. The level of significance used was $p < 0.05$.

3.3 Results and Discussion

3.3.1 Pretreatment for SPI

A well dissolved SPI solution is important for nanoparticle preparation. Normally the commercially available SPI powders form turbid, incompletely dissolved suspensions when dispersed in deionized water. Previous research suggests that incubation of proteins (e.g. SPI, egg albumin and hemoglobin) at an acidic or alkaline pH followed by readjustment of pH back to neutrality could improve protein solubility and other functionalities (Jiang, et al., 2009; Liang & Kristinsson, 2007; Kristinsson & Hultin, 2004). Additionally, soy protein hydrothermal cooking and alkaline treatment can work synergistically to dramatically decrease insoluble particles (Wang, et al., 2006). Our preliminary research indicated that heating a SPI solution to 85 ^{o}C for 30 min at pH 12 and then adjusting pH back to neutrality can significantly improve protein solubility. The solubility at pH 7 increased from 12.3 ± 0.5% to 95.0 ± 0.9% after this treatment (data not shown). SPI may be partially hydrolyzed to induce this higher solubility.

FTIR is a powerful tool used to monitor the protein secondary structural changes during denaturation, aggregation and gelation by analyzing the amide I (the so-called amide I' deuterated peptide groups) vibration of the polypeptide chain (primarily the C=O stretching vibration) (Lefèvre & Subirade, 1999). Through proper fitting of the amide I' band of the original FTIR spectrum of a protein, the conformation of the protein (*i.e.*, helix, sheet or turn) can be obtained.

As shown in Figure 3-1 (a), native SPI molecule showed several bands: 1692 cm^{-1} (β-sheets/turns), 1678 cm^{-1} (turns or sheets), 1659 cm^{-1} (turns), 1646 cm^{-1} (α-helix + unordered structures), 1630 and 1619 cm^{-1} (β-sheets), and 1607 cm^{-1} (vibration of amino acid residues) (Liu et al., 2009; Byler & Susi, 1986; Boye, Ma, Ismail, & Alli, 1996). The bands at 1678 and 1619 cm^{-1} were associated with the aggregation process (Liu, et al., 2009). Strong absorptions at 1692, 1678, 1630 and 1619 cm^{-1} were observed in Fig. 3-1 (a), indicating β-sheets dominated the secondary structures in native SPI. This is in agreement with previous report that native SPI secondary structures consisted of about 60% β-sheets (Hwang & Damodaran, 1996). After the thermal treatment at 85 ^{o}C for 30 min at pH 12, only minor absorptions remained (Figure 3-1 (b)), indicating a denaturation of SPI protein and a loss of most protein secondary structures during this process. When the pH was adjusted back to 8, the spectrum showed a band redistribution (Figure 3-1(c)), however, dissimilar to that of the native one. These results indicate that SPI was irreversibly denatured during the alkaline/heat treatment processes and that a reorganization of secondary structures occurred when pH was adjusted back to 8. It is supposed that more hidden reactive side chains on protein molecules were exposed during protein unfolding, which could facilitate particle formation.

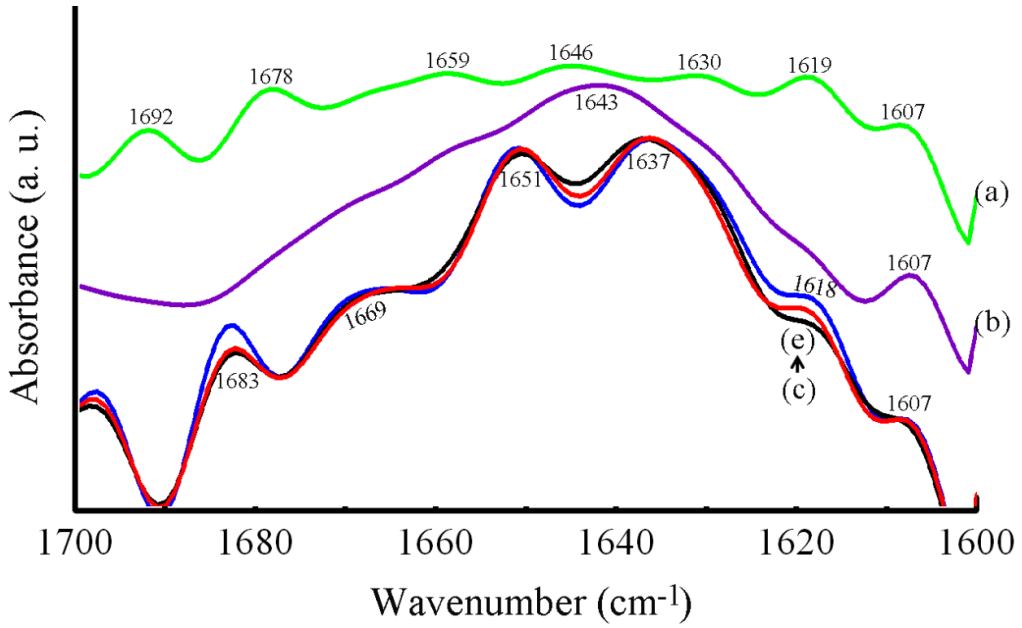

Figure 3-1. Deconvoluted FTIR spectra of (a) native SPI at pD 8; (b) alkaline treated SPI at pD 12 for 30 min; (c) alkaline/heat treated SPI after adjusting pD back to 8 (pre-treated SPI); SPI nanoparticles in the presence of (d) 2.5 and (e) 5 mM $CaCl_2$. The samples were prepared with 5 mg/mL protein. (a.u.-arbitrary units).

3.3.2 Nanoparticle Formation

After pre-treatment, 2.5, 5, 10 and 15 mM $CaCl_2$ were added to 5 mg/ml transparent SPI solutions at pH 7, 8, and 9 to induce particle formation at 23 ^{o}C. The suspensions with turbidity value increasing by at least 50% and without any apparent precipitation were deemed as "potential nanodispersion". Upon addition of 2.5 mM $CaCl_2$, nanodispersions were formed at pH 7 or 8. Addition of 5 mM $CaCl_2$ induced nanodispersion formation at pH 8 or 9, whereas at pH 7, a pronounced precipitation was observed. A pH of 9 was required for nanodispersion

formation when the $CaCl_2$ concentration was increased to 10 mM. Increasing the $CaCl_2$ concentration to 15 mM resulted in large precipitates regardless of the pH value and protein concentration. These "potential nanodispersions" were chosen for further characterization.

3.3.3 Nanoparticle Characterization

3.3.3.1 Particle Size

The size and polydispersity index (PDI) of the particles in "potential nanodispersions" were measured and summarized in Table 3-1. Particles with various sizes of 28-179 nm were obtained in all the "potential nanodispersions" by modulating preparation conditions. A PDI range of 0.23-0.29 was observed for all samples. This suggests that these prepared nanoparticles had an acceptable homogeneity (Dragicevic-Curic, et al., 2010). Previous research reported that size distribution was an important parameter impacting both biocompatibility and biodistribution of nanoparticles *in-vivo* (Lodhia, et al., 2010). Calcium concentration played an important role in determining SPI nanoparticle size. For a given pH, increasing calcium concentration resulted in larger particle diameters. For example, at pH 8, when $CaCl_2$ concentration was increased from 2.5 to 5 mM, the particle size increased from 28 to 101 nm, respectively. The other factor impacting nanoparticle size was the solution pH. Higher pH values favored the

formation of smaller nanoparticles. For instance, at 5 mM $CaCl_2$, particle size decreased from 101 to 71 nm when the pH increased from 8 to 9.

Table 3-1. Impact of preparation conditions on the size and zeta-potential of the SPI nanoparticles.

$CaCl_2$ (mM)	pH	Diameter (nm)	PDI	Zeta-potential (mV)
2.5	7	60 ± 3	0.28 ± 0.00	-11.7 ± 0.3
	8	28 ± 1	0.27 ± 0.00	-14.3 ± 0.7
5	8	101 ± 2	0.29 ± 0.00	-8.8 ± 0.6
	9	71 ± 3	0.23 ± 0.03	-11.0 ± 0.3
10	9	179 ± 3	0.27 ± 0.00	-7.5 ± 0.6

Note: Results were expressed as mean ± standard deviation.

3.3.3.2 Nanoparticle Morphology and Inner Structure

The zero loss TEM micrographs confirmed that SPI nanoparticles were successfully prepared in all opaque solutions upon the addition of calcium, whereas no nanoparticles were observed in the pre-treated SPI solutions (Figure 3-2 (a)). The formed nanoparticles had a spherical shape and a uniform size distribution (Figure 3-2 (b)). The inner structure of the formed nanoparticles was observed by HAADF-STEM (Figure 3-2 (c-d)). An interesting inner structure was observed for nanoparticles treated with calcium, however, such a structure was not observed for the pre-treated SPI. Calcium probably induced protein molecule aggregation by shielding the electrostatic repulsion between the charged protein molecules, and/or acted as a bridge between the negatively charged carboxylic groups on neighboring

protein molecules. The uniqueness this inner structure may allow these nanoparticles to efficiently encapsulate bioactive compounds for their target or controlled delivery.

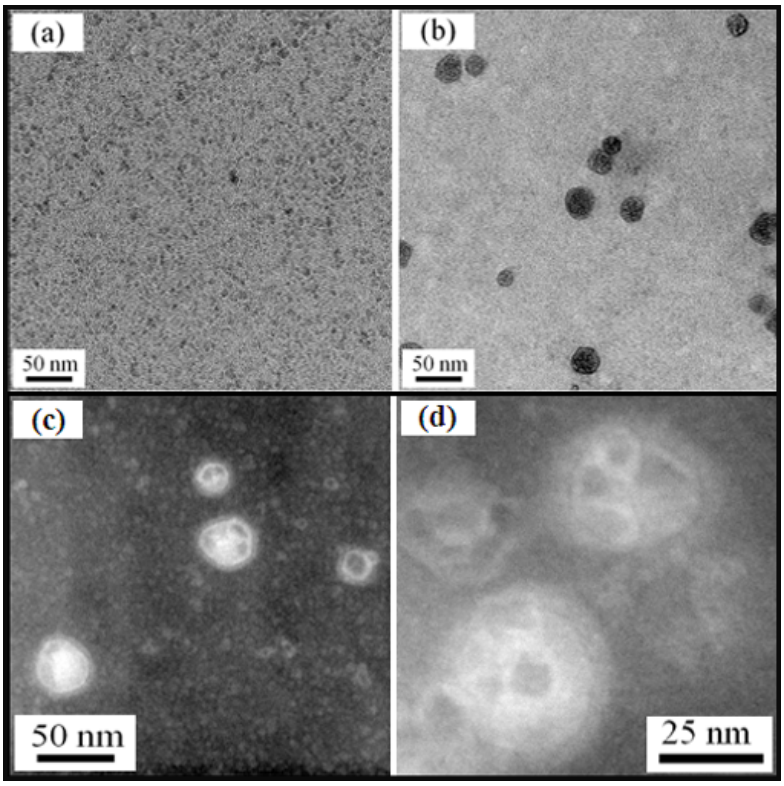

Figure 3-2. Zero loss images-TEM images of (a) pre-treated SPI and (b) SPI nanoparticles; HADDF-STEM images of (c) and (d) the inner structure of SPI nanoparticles. The samples were prepared with 5 mg/ml protein in the (a) absence and (b-d) presence of 5 mM $CaCl_2$ at pH 8.

3.3.3.3 Surface Charge and Hydrophobicity

Nanoparticle stability depends on a balance of repulsive and attractive forces between nanoparticles when they approach one another; this can be used to predict the long-term stability of a nano-dispersion. As demonstrated in Table 3-1, SPI

nanoparticles exhibited a zeta-potential within the range of -7.5 to -14.3 mV. Although the extent of change was rather small, the trend was obvious. Increasing the pH or decreasing calcium concentration enhanced nanoparticle surface charge.

The Rose Bengal partitioning experiment was conducted to study the surface hydrophobicity of the SPI before and after nanoparticle formation. For pre-treated SPI, a higher pH enhanced SPI molecule surface hydrophobicity, with the S_o value increasing from 101 to 153 cm^2/ml when pH was raised from 7 to 9 (Table 3-2). This could be attributed to stronger repulsions among protein molecular chains at a higher pH. This causes partial unfolding of SPI protein that would lead to exposure of non-polar amino acids and an increase in surface hydrophobicity. After the addition of calcium (Table 3-2), the S_o values decreased greatly, indicating a significant decrease in the nanoparticle surface hydrophobicity. Hydrophobic interactions may have been developed among protein aggregates to contribute to nanoparticle formation, causing the non-polar amino acids to be buried in the interior of SPI networks, leading to decreased SPI surface hydrophobicity.

Table 3-2. The degree of surface hydrophobicity (S_0, cm^2/ml) of pretreated SPI (0 mM $CaCl_2$) and SPI nanoparticles prepared with 2.5, 5 and 10 mM $CaCl_2$ at 5 mg/mL protein concentration.

pH	$CaCl_2$ (mM)			
	0	2.5	5	10
7	101 ± 2	42 ± 1	P	P
8	147 ± 1	89 ± 2	14 ± 3	P
9	153 ± 0	97 ± 3	35 ± 7	20 ± 3

Note: P meant precipitation; results were expressed as mean ± standard deviation.

3.3.4 Nanoparticle Stability

The pH stability of the SPI nanoparticles was tested by measuring their size and zeta-potential in various pH solutions (pH 2-9) to determine the pH ranges where these nanoparticles can be utilized (Table 3-3). SPI nanoparticles demonstrated good stability at the pH 2-3 and 7-9 ranges, since proteins are positively or negatively charged when the pH is deviated from its isoelectric point (pI near 4.5) (Table 3-3). Within the pH range of 4-6, the zeta-potential of nanoparticles was reduced to around zero (Table 3-3), leading to severe precipitation. A strategy such as coacervation with another polyelectrolyte could be applied to enhance the surface charge of the SPI nanoparticles within these pH ranges to improve their stability (Santipanichwong, Suphantharika, Weiss, & McClements, 2008). The storage stability of SPI nanoparticles was also investigated after storage at 4 ^{o}C for 7, 14 and 21 days. Results showed that storage time had no significant effect ($p > 0.05$) on nanoparticle size and dispersion turbidity, indicating that nanoparticles remained stable during storage for 21 days at 4 ^{o}C.

This experiment demonstrated that SPI nanoparticle characteristics such as size, inner structure, surface charge and hydrophobicity can be modulated by controlling the preparation conditions including environmental pH and calcium concentration. Nanoparticles with stability near neutrality are of particular interest for their practical use in industrial applications.

Table 3-3. The influence of pH on the size and zeta-potential of SPI nanoparticles in presence of 2.5 and 5 mM $CaCl_2$. The nanoparticles were prepared with 5 mg/ml protein concentration at pH 8.

pH	Size (nm)		Zeta-potential (mV)	
	2.5 mM $CaCl_2$	5 mM $CaCl_2$	2.5 mM $CaCl_2$	5 mM $CaCl_2$
2	33.9 ± 2.4	82.8 ± 1.3	16.9 ± 0.9	17.3 ± 2.3
3	45.9 ± 5.6	99.4 ± 1.4	18.7 ± 0.6	19.3 ± 1.5
7	100.8 ± 14.7	146.0 ± 13.3	-10.3 ± 0.4	-9.5 ± 2.1
8	32.7 ± 7.2	119.0 ± 35.1	-15.8 ± 1.1	-10.8 ± 2.3
9	29 ± 10.2	76.0 ± 0.5	-19.1 ± 0.2	-11.4 ± 1.7

Note: All the samples formed precipitates at pH 4-6.

3.3.5 Protein Conformational Changes during the Nanoparticle Formation Process

3.3.5.1 FTIR Study

The infrared deconvoluted spectra of the amide I′ band region of the pre-treated SPI and the SPI nanoparticls prepared at the calcium concentration of 2.5 and 5 mM are presented in Figure 3-1 (c-e). The spectrum of the pre-treated SPI was composed of six bands located at 1683, 1669, 1651, 1637, 1618, and 1607 cm^{-1}. Components located at 1683 and 1618 cm^{-1} were assigned to β-sheets (Bandekar, 1992), whereas the peak at 1651 cm^{-1} was attributed to the presence of small amounts of α-helix in pre-treated SPI (Arrondo, Muga, Castresana, & Goni, 1993). The weak band at 1669 and 1607 cm^{-1} could represent peptide group segments in

the turns (Byler & Susi, 1986) and the vibration of the amino acid residues (Maltais, Remondetto, & Subirade, 2008). SPI nanoparticles showed a similar pattern of bands as those of pre-treated SPI, however, the band intensity at 1683 and 1618 cm^{-1} changed. Upon addition of 5 mM calcium, the band attributed to the anti-parallel β-sheet (Bandekar, 1992) at 1683 cm^{-1} was increased significantly, suggesting that antiparallel β-sheet was involved in the process of calcium induced nanoparticle formation. The band at 1618 cm^{-1} was assigned to the intermolecular β-sheet structure caused by aggregation via hydrogen bonding (Lefèvre & Subirade, 2000). With increasing calcium concentration up to 5 mM, this band increased gradually. Calcium may shield the surface charge of SPI molecules to decrease electrostatic repulsive forces between them. Subsequently, the protein can aggregate by forming an antiparallel β-sheet structure stabilized by hydrogen bonding. These aggregates could be the basic units for nanoparticle network formation.

3.3.5.2 Far- and Near-UV CD

CD spectroscopy is an established and a valuable technique for studying protein structure, dynamic and folding due to its sensitive ability to detect very small alterations in protein secondary and tertiary structural changes (Wallace & Janes, 2003). The far-UV CD spectra of pre-treated SPI and SPI nanoparticles prepared with 2.5-5 mM calcium at pH 8 are presented in Figure 3-3 (A). The spectrum of the pre-treated SPI showed a negative peak at 207 nm with a shoulder

around 218 nm. After adding 2.5 mM calcium, the peak showed a red shift to 210 nm with the same ellipticity and a shoulder around 225 nm. Interestingly, addition of 5 mM calcium induced three peaks at 208, 218 and 225 nm, respectively. These features implied a highly ordered structure, most probably of α/β type structure (Allaoua & Wang, 2001). In addition, the spectrum showed a significant decrease in negative ellipticities for all wavelengths of the far-UV CD spectrum, accompanied by a red shift of λ_{max} from 207 nm to 210 or 208 nm, which is a characteristic of secondary structure conformation change (Allaoua & Wang, 2001). The spectra were processed with CDPro software to calculate the conformation proportion of α-helix, β-sheet, β-turn and random coil in SPI molecular chains (Figure 3-3 (B)). In the pre-treated SPI, the α-helix and β-sheet percentage was 17.9 and 27.2%, respectively. After the introduction 2.5 or 5 mM calcium, the percentage of α-helix decreased and that of β-sheet increased. For example, when 5 mM calcium was added, the content of α-helix decreased to 12.6% and β-sheet increased to 29.9%. Although the change is not statistically significant, its trend is consistent with the results of FTIR in Figure 3-1(c-e). Therefore, it could be concluded that calcium induced a progressive increase in the proportion of β-sheet structures at the expense of a-helix structures.

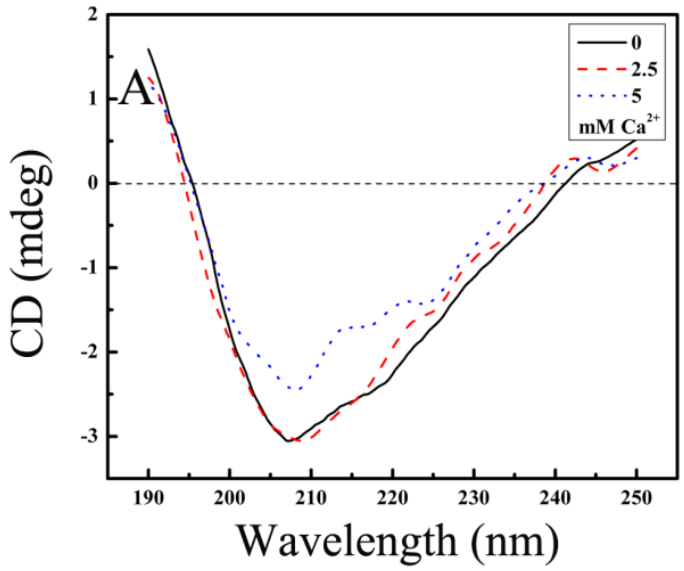
A
0
2.5
5
mM Ca2+
CD (mdeg)
Wavelength (nm)
2
1
0
-1
-2
-3
190
200
210
220
230
240
250

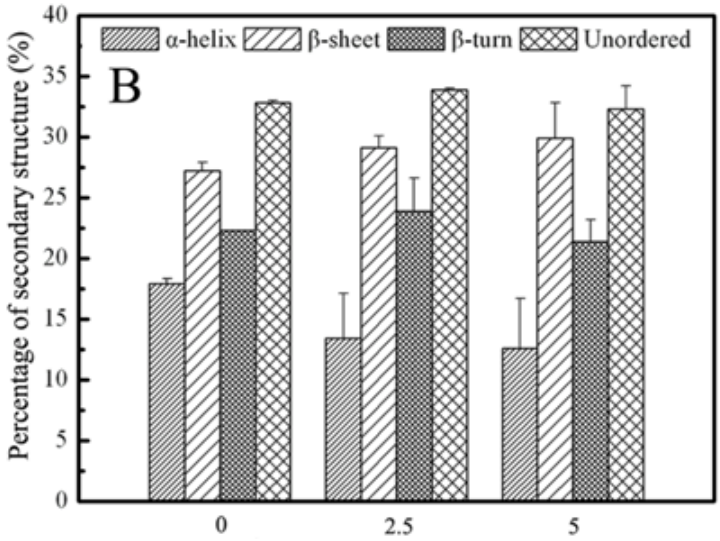
B
α-helix
β-sheet
β-turn
Unordered
Percentage of secondary structure (%)
40
35
30
25
20
15
10
5
0
0
2.5
5

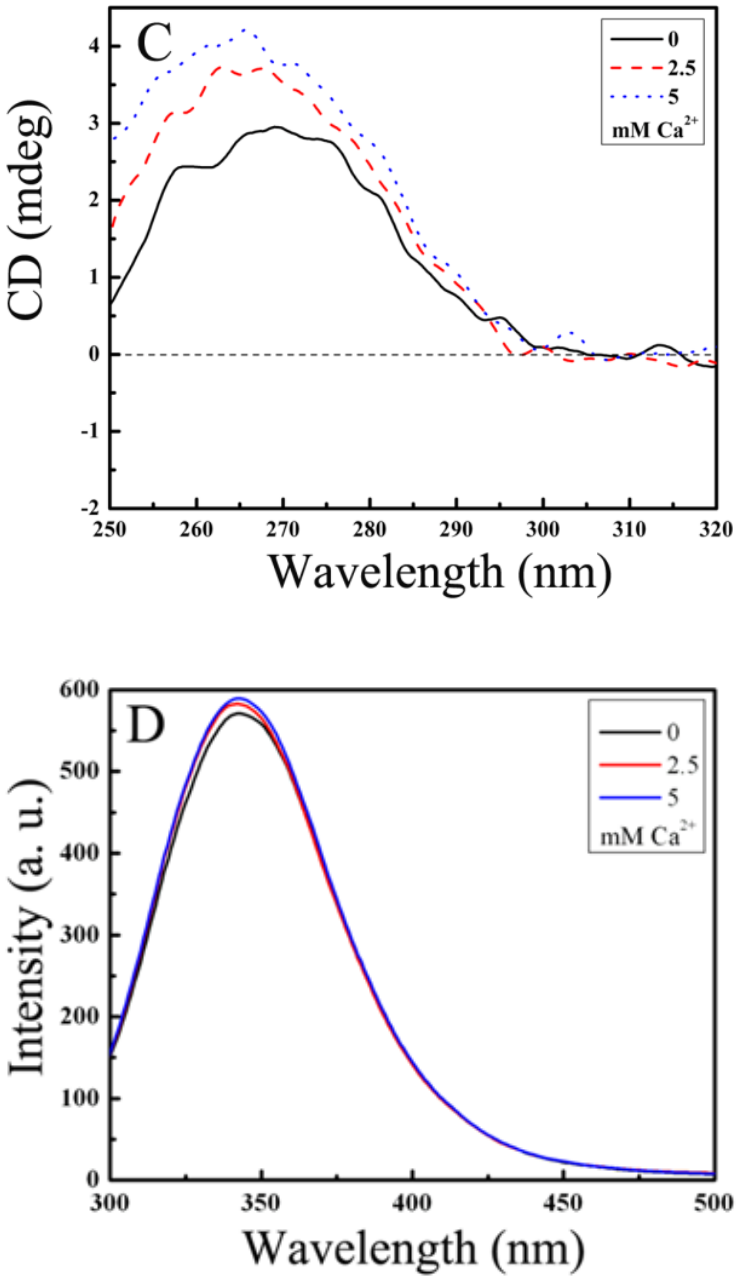

Figure 3-3. (A) Far UV-CD, (B) percentage of secondary structure (%) calculated from Far-UV CD spectra, (C) near UV-CD and (D) intrinsic emission fluorescence spectra of pretreated SPI (0 mM Ca^{2+}) and SPI nanoparticles in the presence of 2.5 and 5 mM $CaCl_2$. The samples were prepared with 5 mg/ml protein at pH 8, and then diluted to 12.5 μg/ml with pH 8, 0.01 M sodium phosphate buffer.

Figure 3-3 (C) showed the near-UV CD spectra of pre-treated SPI and SPI nanoparticles prepared 2.5 and 5 mM calcium at pH 8. The CD spectra in the region of 250-320 nm are attributed to aromatic amino acids. The real shape and magnitude of the near-UV CD spectrum of a protein are determined by the number of each type of aromatic amino acid present, their mobility, the nature of their environment (hydrogen-bonds, polar groups and polarisability), as well as their spatial disposition in the protein (Kelly, et al., 2005). The near UV-CD spectrum of the pre-treated SPI showed a broad positive distribution range from 250 to 300 nm, comprised of four maxima at 257, 266, 277 and 281 nm, with a shoulder at 295 nm, which are attributed to phenylalanine (Phe), tyrosine (Tyr) and tryptophan (Trp), respectively (Kelly, et al., 2005). The addition of calcium led to a remarkable increase in the ellipticities and a slight blue shifting of peaks in the region of 260-280 nm. The near-UV CD data show that SPI tertiary conformation changes took place after calcium addition. These may involve electrostatic interaction changes caused by calcium shielding of surface charges, resulting in re-organization of the protein secondary and tertiary structures. As the protein molecular chain rearranged, the microenvironment of the aromatic amino acid would change accordingly.

3.3.5.3 Fluorescence Spectra

Intrinsic fluorescence spectra with an excitation frequency of 280 nm tracked the protein conformational changes of Trp and Tyr residues triggered by unfolding

or folding of the SPI polypeptide chains. The wavelength of maximum emission of Trp and Tyr residues is sensitive to the polarity of their local environment. The Trp and Tyr content of the SPI sample used for this study is 1.1 and 3.8 g/100 g protein, respectively. As shown in Figure 3-3 (D), the fluorescence spectrum of the pre-treated SPI presented a broadband at λ_{max} of 343 nm. Addition of 2.5 or 5 mM calcium led to an increase in Trp and Tyr fluorescence intensity and a slightly blue-shifted wavelength of maximum emission (both from 343 to 342 nm). Previous study indicated that fluorescence intensity increased and the λ_{max} shifted to a shorter wavelength as the environmental polarity of a fluorophore decreased (Liang, et al., 2008). Although the calcium-induced blue shift at λ_{max} of SPI fluorescence is not significant, the simultaneous increase in fluorescence intensity in this study suggests the aromatic amino acids in protein chains was changing to a more "non-polar" environment (Wu, et al., 2009).

In summary, both FTIR and far-UV CD results confirmed that calcium could induce the development of β-sheet structures in pre-treated SPI to form aggregates. The near-UV CD and the fluorescence spectra results suggest that the microenvironment of the aromatic amino acid residues became more “non-polar” as the protein molecular chain was rearranged.

3.3.6 Nanoparticle Dissociation Test

In order to pursue a further understanding of the interactions involved in the nanoparticle formation, dissociation reagents were added to nanoparticle

dispersions, such as, DTT, urea and SDS. These dissociation reagents can disrupt covalent disulfide bonds, hydrogen bonds, and hydrophobic interactions, respectively. Solution turbidity was monitored at different concentrations of the dissociation reagents. As shown in Figure 3-4, although the turbidity showed nearly no change with increasing DTT concentrations, it decreased sharply with increasing urea or SDS concentrations. As can be seen from the TEM images (Figure 3-5), the formed nanoparticles remained unchanged in the presence of 40 mM DTT, but were disrupted in the presence of either 1 M urea or 0.05% SDS. This confirms that the main driving forces involved in nanoparticle formation and stabilization are hydrogen bonding and hydrophobic interaction, rather than disulfide bonding. Ren, et al., (2009) also concluded that protein aggregates and a part of monomeric subunits of 7S and 11S, as structural units, interacted with each other to form heating-induced protein particles in soy milk primarily through hydrogen bonding and hydrophobic interactions. In addition, EDTA was used as a chelating agent to identify whether calcium was necessary to maintain the stability of the nanoparticles as EDTA can prevent interactions between calcium and carboxyl groups of the protein chains. The result indicates that calcium is critical to maintain nanoparticle stability, since after adding 5 mM or more of EDTA, a pronounced precipitation occurred for SPI nanoparticles (Figure 3-6). As a divalent cation, calcium acts to shield negative charges on polypeptide chains and serves as a salt-bridge to enable polypeptide chains to approach one another. In this process, calcium favors the development of β-sheet structures to form SPI aggregates

stabilized by hydrogen bonding. These aggregates could then be associated to form nano-networks via hydrophobic interactions. The aromatic amino acid residues may subsequently be buried inside the SPI network surrounded by a more "non-polar" microenvironment.

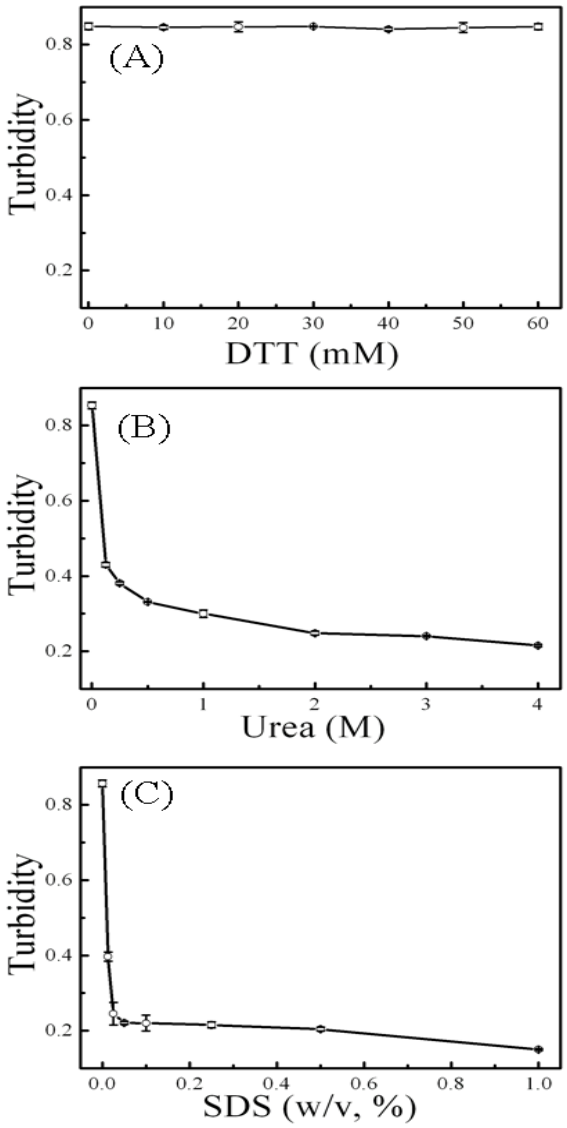

Figure 3-4. The influence of dissociation reagents of (A) DTT, (B) urea and (C) SDS on the turbidity of the nanoparticle dispersions. The nanoparticles were prepared with 5 mg/ml protein in the presence of 5 mM $CaCl_2$ at pH 8.

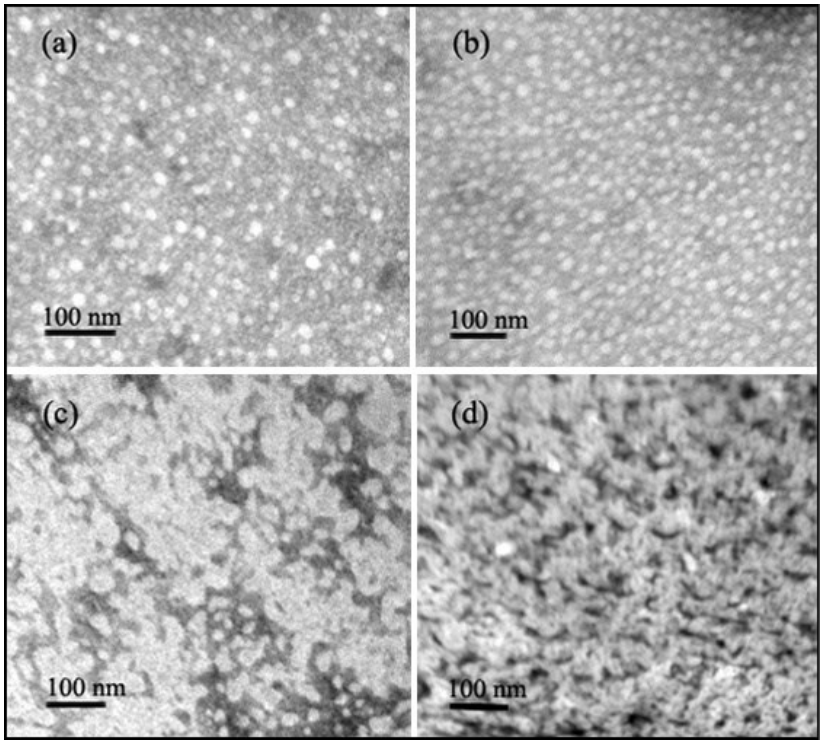

Figure 3-5. TEM photographs of dissociation reagents on the morphology of the nanoparticle dispersions (a: SPI nanoparticles, SPI nanoparticles in the presence of b: 40 mM DTT, c: 1 M urea and d: 0.05% SDS). The nanoparticles were prepared with 5 mg/ml protein in the presence of 5 mM $CaCl_2$ at pH 8.

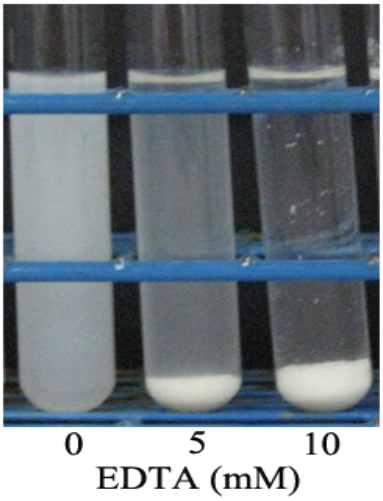

Figure 3-6. Visual appearance of SPI nanoparticle dispersion in the presence of 0, 5 and 10 mM EDTA. The nanoparticles were prepared with 5 mg/ml protein in the presence of 5 mM $CaCl_2$ at pH 8.

3.3.7 *In Vitro* Cytotoxicity and Cellular Uptake of SPI Nanoparticles

The toxicity of nanoparticles was evaluated by MTT assay. The viability of Caco-2 cells after incubation with SPI nanoparticles for 24 and 48 h was demonstrated in Figure 3-7. Cellular viability was maintained at levels near 100%, even at high nanoparticle concentration (1.25 mg/ml) and after a long-time exposure (48 h). This result suggests that SPI nanoparticles were nearly non-toxic to cell proliferation at all the concentrations tested, which is quite favorable for their applications. This could be attributed to the hydrophilic nature and good biocompatibility of soy protein.

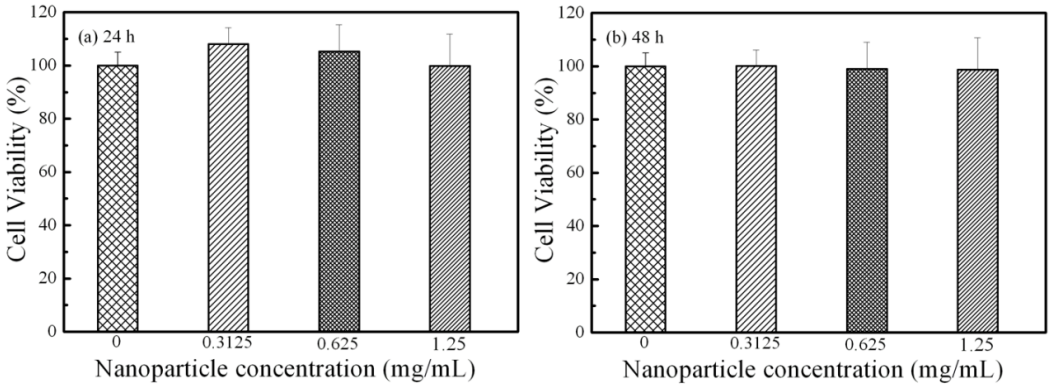

Figure 3-7. Percentage of cell viability evaluated by MTT assay on Caco-2 cells treated with increasing concentrations of SPI nanoparticles in EMEM medium for (a) 24 h and (b) 48 h.

Figure 3-8 showed confocal microscopic images of Caco-2 cells after 12 h incubation with (a) free 6-COUM and (b) 6-COUM-loaded SPI nanoparticles at 37 °C. No green fluorescent signal was observed for Caco-2 cells treated with free 6-COUM, which was in agreement with the fact that raw 6-COUM marker could

not be directly internalized by the cells or its leaking rate was low within the time scale of fluorescent observation (Win & Feng, 2005). However, strong green signals were observed in Caco-2 cells after incubation with 6-COUM labeled SPI nanoparticles for 12 h, and the signals were mainly located between the membrane and the nuclei. This result demonstrates that the SPI nanoparticles can be taken up by Caco-2 cells and accumulated in the cell cytoplasm.

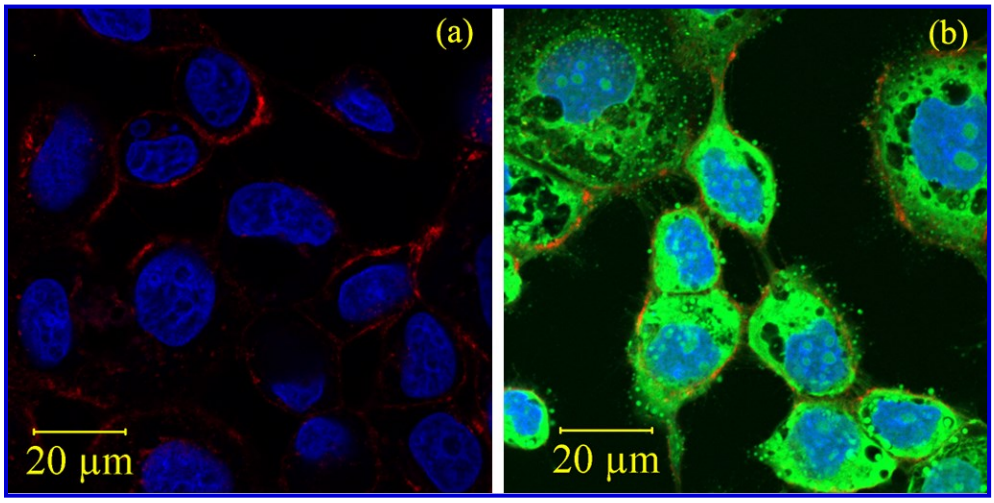

Figure 3-8. Confocal microscopy images of Caco-2 cells after 12 h incubation with (a) 6-COUM and (d) 6-COUM-labeled SPI nanoparticles at 37°C. The cell apical membranes were stained with Concanavalin A and Alexa Fluor® 594 conjugate (red), the nucleus were stained with DAPI (blue) and the SPI nanoparticles were labeled by 6-COUM (green). The nanoparticles were prepared with 5 mg/ml protein in the presence of 5 mM $CaCl_2$.

3.4 Conclusions

SPI nanoparticles (28-179 nm) were successfully prepared by adopting a cold gelation method with a minor modification. A primary alkaline/heat

treatment improved SPI solubility and enabled protein unfolding to expose reactive amino acids, followed by a cooling step and the adjustment of pH to neutrality or slightly alkaline conditions. Calcium was then added to induce a nano-scale network formation. The obtained nanoparticles demonstrated spherical shape and uniform size distribution. Nanoparticle characteristics such as size, surface charge and hydrophobicity could be modulated by modifying environmental pH and calcium concentration. A protein conformation study and the nanoparticle dissociation test both suggested that calcium shields the negative charges on polypeptide chains and serves as a salt-bridge to facilitate SPI aggregation. These aggregates were then associated to form SPI nano-networks via hydrophobic interactions. In vitro study suggests that SPI nanoparticles were non-toxic and mainly distributed in the cytoplasm when uptaken into Caco-2 cells. Considering that these SPI nanoparticles were prepared at ambient temperature without using toxic reagents, they would provide a promising opportunity to serve as novel delivery systems for heat labile ingredients (bioactive peptides, vitamins, etc.) for pharmaceutical or food applications.

Chapter 4. Binding Interactions of β-Conglycinin and Glycinin with Vitamin B_{12}[2]

4.1 Introduction

Vitamin B_{12} (VB_{12}), also called cobalamin, is a water soluble vitamin primarily available in red animal products. It plays an important role in brain and nervous system, as well as red blood cell formation. VB_{12} is also required for the metabolism of human cells, DNA synthesis and regulation, fatty acid synthesis and energy fabrication (Zittoun & Zittoun, 1999). In the human body, when VB_{12} is insufficient, a variety of symptoms like fatigue, depression and poor memory may occur (Nardone & Tezzon, 2010). Severe VB_{12} deficiency can potentially cause serious and irreversible damage, mainly to the brain and nervous system. It also causes symptoms of mania and psychosis (Kuo, et al., 2009; Nardone & Tezzon, 2010). Vegetarians and the elderly are at a high risk of VB_{12} deficiency. It is reported approximately 20% of the elder suffer VB_{12} deficiency, and more than 60% of VB_{12} deficiency is caused by food-cobalamin malabsorption (Andres, et al., 2004). This deficiency, according to Ray and Cole (2005), could very possibly result in severe neurological damage and life-threatening anemia (Ray & Cole, 2005). Amongst strict vegans, VB_{12} deficiency is primarily induced by avoidance of meat in the diet. Those individuals, consequently, have to require medical

[2] A version of this chapter has been published in The Journal of Physical Chemistry B (2013), 117: 14018-14028.

supplement. Intramuscular injection is a well-established way to treat VB_{12} deficiency, however, new administration routes such as oral and nasal administration are attracting more interest owing to their convenience.

Food-grade proteins are potential carriers for bioactive compounds. Soy protein is considered a top priority due to its high nutritional value, good digestibility and excellent functional properties, which include gelation and emulsifying capabilities. Beta-conglycinin (7S) and glycinin (11S) are two major fractions of soy protein, attributing to about 30% and 40%, respectively, of the total weight (Maruyama, et al., 1998; Miriani, et al., 2011). 7S (180 to 210 kDa) is a glycosylated hetero-trimer and constituted randomly by three different subunits: α (≈67 kDa), α′ (≈71 kDa), and β (≈50 kDa), which are stabilized by non-covalent bonds. The α and α' subunits are composed of two different domains: the core region (418 residues) and the extension region (α, 125 residues; α′, 141 residues) (Maruyama, et al., 1998), whereas the β subunit contains only the core region (416 residues). The core region is well preserved in each subunit and it contributes to the thermal stability of 7S. The extension region in 7S, on the other hand, demonstrates a strong acidic property and 57.3% sequence identity (Shutov, et al., 1996), and possesses good solubility and emulsifying ability. 11S (309 to 363 kDa) is a hexamer composed of intermediary subunits, in which one acidic subunit (A, 38 kDa) and one basic subunit (B, 20 kDa) are linked by a single disulfide bridge. The disulfide bonds between subunits could perform non-covalently to give a hexamer that can be dissociated by urea, guanidinium or sodium dodecylsulphate (Shewry,

1995). The mass fractions of acidic subunits are around 60%, which confer excellent emulsifying properties to 11S (Liu, et al., 1999). 11S also demonstrates certain thermal stability. Both 7S and 11S contain antiparallel β-sheet and random coil as major secondary structures, as well as low level of α-helix (Fukushim, 1968). Their molecules are fairly folded tertiarily, which forms the water-impenetrable hydrophobic region. Hydrophobic interactions play an important role for stabilizing the internal structures of 7S and 11S. Their molecules are usually proteinase-resistant before the internal structure is disrupted. The initial velocity of the proteinases hydrolysis is proportional to the degree of their disruption (Fukushim, 1968).

7S and 11S contain hydrophilic charged and uncharged groups (-NH_2, -COOH,-OH and -SH) as well as hydrophobic groups (CH_3- and benzene rings) which provide a potential base for the development of electrostatic interactions, hydrogen bonds, disulfide bonds and hydrophobic interactions with small molecules such as VB_{12}. All these possible interactions confer that soy protein either alone or in combination with other biopolymers are able to confine nutraceuticals in a three-dimensional protein network, so as to preserve their active form until release at their target site in human body for potentially improved absorption (Chen, et al., 2008; Chen & Subirade, 2009).

This study aims to explore the feasibility of using soy protein as a carrier for VB_{12} to improve its absorption. An investigation of VB_{12} binding to soy protein at molecular level is an important initial step in achieving the overall objective. In

spite of the high potential, protein binding of VB_{12} has seldom been investigated, expect for some limited work focusing on human serum albumin (HSA), bovine serum albumin (BSA) and lysozyme (Hou, et al., 2008; Li, et al., 2012; Li, Zhang, et al., 2011). The interaction of VB_{12} with soy protein has never been reported. In this study, the molecular interactions of VB_{12} with 7S and 11S were systematically studied using fluorescence and far-UV CD spectroscopic techniques. This study would provide a theoretical foundation for developing VB_{12} fortified soy protein products.

4.2 Materials and Methods

4.2.1 Materials

Soybeans were purchased from a local supermarket (Edmonton, AB, Canada). Ethylenediaminetetraacetic acid (EDTA), caffeine, sodium bisulfite and VB_{12} were purchased from Sigma-Aldrich (Oakville, ON, Canada). All other chemicals were of reagent grade.

4.2.2 7S and 11S Extraction

The 7S and 11S proteins were extracted according to previous research with minor modifications (Liu, Lee, & Damodaran, 1999). Briefly, dehulled and milled soybean flour was treated with *n*-hexane/ethanol (10:1, v/v) to remove the oil. The defatted flour was dispersed in 15 volumes of distilled water at the pH of 7.5

adjusted by 2 M NaOH and then stirred for 4 h at 4 ^{o}C. The slurry was centrifuged at 10,000 × *g* for 15 min at 20 ^{o}C (Beckman Coulter, Avant® J-E, Harbor Boulevard, Fullerton, California, USA). Dry sodium bisulfite (0.98 g/L) was then added to the supernatant; the pH of the mixture was changed to 6.4 with 2 M HCl and kept at 4 ^{o}C overnight. The precipitate (11S) was obtained after centrifugation at 12,000 × *g* for 20 min and the supernatant was kept for 7S extraction. The 11S pellet was washed 4 times, resuspended in distilled water at pH 8.0 and then lyophilized. To prepare 7S, the supernatant accumulated above was treated with 0.25 M NaCl and the pH value was adjusted to 5.0. The mixture was stirred for 4 h at 4 ^{o}C and then centrifuged at 12,000 × *g* for 20 min. The supernatant was diluted with 2 times volume of distilled water at pH 4.8 and centrifuged at 10,000 × *g* for 15 min. The pellet (7S) was washed 4 times, resuspended in distilled water at pH 8.0 and lyophilized. The protein contents in 7S and 11S powder (dry basis) were 98.7 (± 0.1)% and 97.0 (± 0.2)% (w/w), respectively, as determined by combustion with a nitrogen analyzer (Leco Corporation, St. Joseph, MI, USA) calibrated with analytical reagent grade EDTA and caffeine using a conversion factor of 6.25.

4.2.3 Sample Preparation

Stock solutions were prepared by dissolving 7S and 11S in sodium phosphate buffer (0.01 M, pH 7.4) to obtain a concentration of 100 μM, measured by spectrophotometer (Jasco V-530, Japan) using a molar extinction coefficient of ε_{280nm} = 16640 M^{-1} cm^{-1} (7S, NCBI Accession No. AAT40424) and ε_{280nm} = 38040

M^{-1} cm^{-1} (11S, NCBI Accession No. AAT40405). VB_{12} stock solution was prepared daily by dissolving VB_{12} with sodium phosphate buffer (0.01 M, pH 7.4) to a concentration of 5 mM. Samples were prepared by mixing 7S or 11S with VB_{12} stock solutions in varying proportions. The samples were incubated for around 2 h at room temperature prior to analysis.

4.2.4 Fluorescence Spectra Measurement

Fluorescence spectra were collected from a Cary Eclipse fluorescence spectrophotometer (Varian Inc., Palo Alto, USA) equipped with a 1.0 cm quartz cell and thermostatted bath. The excitation wavelength was fixed at 295 nm with the emission spectra and recorded from 296 to 500 nm. The excitation and emission slit widths were set up at 5 and 10 nm, respectively. The fluorescence emission sodium phosphate buffer (0.01 M, pH 7.4) background was subtracted from the raw spectra.

4.2.5 Fluorometric Titration Measurement

Five milliliter solutions with appropriate concentration of 7S and 11S were titrated by successive addition of a 5 mM VB_{12} stock solution to give a final solution with a concentration of 10 μM protein and 0-50 μM VB_{12}. The fluorescence spectra were recorded at four different temperatures (292, 298, 304 and 310 K).

4.2.6 UV-Vis Absorbance Measurement

The UV absorbance spectra of 7S or 11S in the presence of 0-40 μM VB_{12} and 10 μM VB_{12} alone were collected using a UV-Vis spectrophotometer (Jasco V-530, Japan) from 200 to 600 nm. Sodium phosphate buffer (0.01 M, pH 7.4) background was subtracted from the raw spectra.

4.2.7 Synchronous Fluorescence Spectra

Synchronous fluorescence spectra of 7S and 11S (10 μM) in the absence and presence of VB_{12} (0-40 μM) were recorded by scanning simultaneously the excitation and emission monochromator. The wavelength interval ($\Delta\lambda$) was set at 15 and 60 nm, respectively. Sodium phosphate buffer (0.01 M, pH 7.4) background was subtracted from the raw spectra.

4.2.8 Three Dimensional Fluorescence Spectra

Three dimensional fluorescence spectra of 7S or 11S (10 μM) in the absence and presence of 20 μM VB_{12} were measured with a Shimadzu spectrofluorophotometer (RF-5301 PC, Shimadzu Corporation, Tokyo, Japan). The excitation wavelength was set from 220 to 370 nm with an increment of 5 nm, and the emission wavelength was recorded from 220 to 520 nm at a scanning rate of 8000 nm/min. The slit of excitation and emission was 5 and 3 nm, respectively.

4.2.9 Far-UV CD Measurement

The far - UV CD spectra (185 - 250 nm) of 7S or 11S were recorded at a VB_{12} concentration of 0-40 μM from a J-710 spectropolarimeter (Jasco Co., Tokyo, Japan). The concentration of 7S or 11S was fixed at 10 μM. Path length was 0.1 cm. Ellipticity was recorded at a speed of 100 nm/min, a resolution of 0.2 nm, an accumulation of 20 and a bandwidth of 1.0 nm. Sodium phosphate buffer (0.01 M, pH 7.4) background was subtracted from the raw spectra. Results were expressed in terms of mean residue ellipticity and the secondary structures were determined via CDPro software package of CONTINLL program (http://lamar.colostate.edu/~sreeram/CDPro/), a server for analyzing protein secondary structure from CD spectroscopic data.

4.2.10 Statistical Analysis

All experiments were performed in triplicate samples in three independent batches. Statistical analysis was performed using Student's *t*-test and differences were judged to be significant at $p < 0.05$.

4.3 Results and Discussion

4.3.1 Influence of VB_{12} on Fluorescence Spectra of 7S and 11S

The intrinsic fluorescence of protein is mainly due to the aromatic amino acids including tryptophan (Trp), tyrosine (Tyr) and phenylalanine (Phe) residues. Fluorescence is a useful technique for analyzing the interactions between the proteins and ligands as the photophysical character of the fluorophore is sensitive to the polarity of its local surrounding (Liang, et al., 2008). A slight alteration of the protein microenvironment caused by protein conformational transition, biomolecule binding and the presence of a denaturant can lead to changes in its intrinsic fluorescence (Hou, et al., 2008). The impact of VB_{12} on the fluorescence spectra of soy protein was shown in Figure 4-1. The experiment was conducted at pH of 7.4 and temperature of 292 K with both protein concentrations fixed at 10 μM. The excitation wavelength was fixed at 295 nm, where only Trp generates a fluorescence emission. The Trp fluorescence intensity in both 7S and 11S decreased and simultaneously the λ_{max} shifted to a shorter wavelength as the concentration of VB_{12} steadily increased from 0 to 40 μM. Such ε_{max} shift indicates that the fluorescence chromophore (Trp) of both proteins changed to a more hydrophobic microenvironment (Pan, et al., 2011). Moreover, the decrease of fluorescence intensity with a blue-shift is indicative of the occurrence of fluorescence quenching of 7S/11S induced by interacting with VB_{12}. Theoretically, there are several potential causes of quenching including the inner-filter effect,

collisional quenching and binding-related quenching. The latter is further subdivided into ground-state complex formation, excited-state quenching in the complex (e.g. energy transfer), or structural changes around the fluorophores (Lakowicz, 2009; Van de Weert & Stella, 2011). Therefore, the detailed mechanism of soy protein fluorescence quenching induced by VB_{12} was investigated.

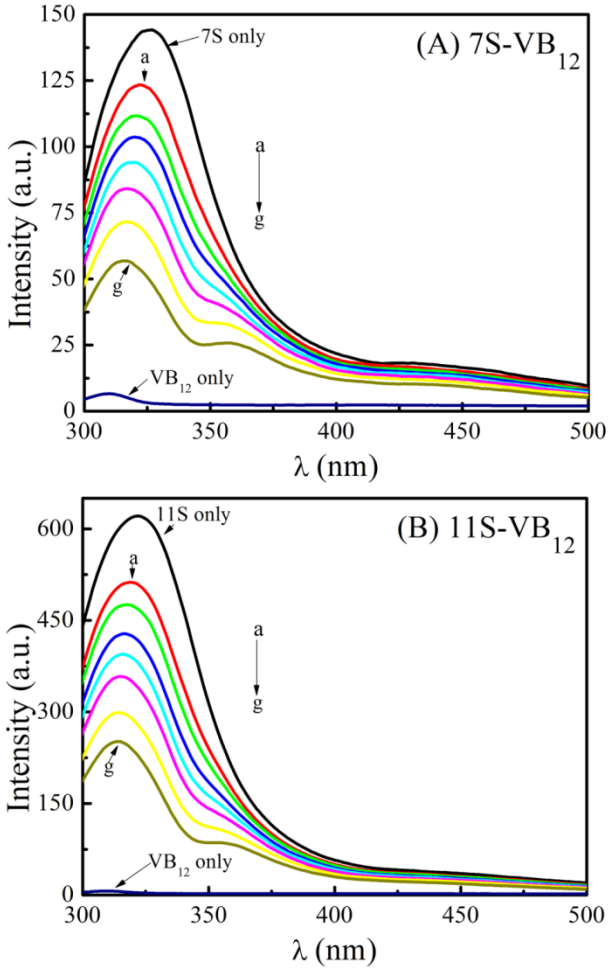

Figure 4-1. Fluorescence emission spectra of (A) 7S-VB_{12} and (B) 11S-VB_{12} systems and 10 μM VB_{12} alone in 0.01 M, pH 7.4 sodium phosphate buffer at 292 K with λ_{ex} = 295 nm. c(7S) = c(11S) = 10 μM; a-g: c(VB_{12}) = 10, 15, 20, 25, 30, 40 and 50 μM, respectively.

4.3.2 The Inner-Filter Effect

The inner-filter effect refers to the absorption (or optical dispersion) of light at the excitation or emission wavelength by the compounds present in the solution (Van de Weert & Stella, 2011). When a ligand is added to a protein solution, if the absorption of ligand at the excitation wavelength were strong, less light would reach the center of solution and consequently the fluorescence intensity of protein would be reduced. Its absorption at the emission wavelength of the fluorophore would reduce the emitted light that reaches the detector, which causes a decrease in the protein fluorescence intensity as well (Van de Weert & Stella, 2011). Therefore, the inner-filter effect of VB_{12} on the fluorescence intensity of both proteins was evaluated. The UV-Vis absorbance spectra of (A) 7S and (B) 11S in the presence of 0-40 μM VB_{12} and (C) VB_{12} alone at the concentrations of 0-40 μM were shown in Figure 4-2. The gradual enhancement of UV-Vis absorption with the increase of VB_{12} concentration was observed. In addition, the absorption value of VB_{12} at excitation or emission wavelength that was much larger than 0.1 indicates the occurrence of the inner-filter effect (Van de Weert & Stella, 2011). Its strong absorbance at 295 nm would reduce the amount of excitation radiation that reaches the Trp, simultaneously it can absorb some radiation emitted by the Trp at 334 nm leading to a decreased fluorescence intensity. Therefore, the influence of inner-filter effect of VB_{12} on protein fluorescence quenching has to be removed before conducting analysis of the quenching mechanism. The correction of fluorescence intensity can be achieved by measuring the absorbance value at the

excitation and emission wavelengths for each concentration of VB_{12} (including protein without VB_{12}) and then multiplying the observed fluorescence intensity value (Van de Weert & Stella, 2011):

$$F_{corr} = F_{obs} * 10^{\wedge(Aex+Aem)/2} \quad (4\text{-}1)$$

where F_{corr} *and* F_{obs} are the corrected and measured fluorescence values, respectively. A_{ex} and A_{em} are the absorption values at the excitation and emission wavelength (in a 1 cm path-length cuvette), respectively.

The corrected fluorescence intensity (corr) was generated from the observed fluorescence intensity (obs) according to Eq. (4-1). The plots of normalized fluorescence area (F/F_0) of both corr and obs *versus* VB_{12} concentration were displayed in Figure 4-3. The F/F_0 values of corr and obs decreased with the increasing VB_{12} concentration, and the former was slower than the latter suggesting that the fluorescence quenching of both proteins was partly caused by the inner-filter effect of VB_{12}. However, an evident reduction in F/F_0 values of corr was still observed after removal of the inner-filter effect, which was probably caused by either collisional or binding-related quenching (Van de Weert & Stella, 2011). Therefore, the specific quenching mechanism between 7S/11S and VB_{12} was studied in the next step.

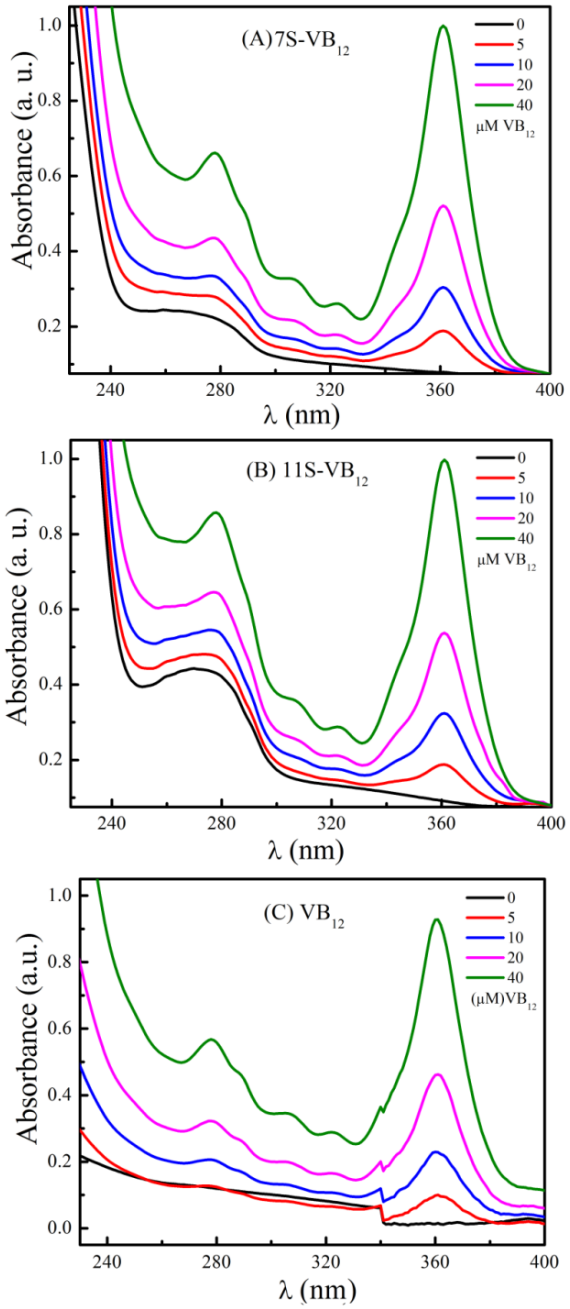

Figure 4-2. The UV-Vis absorption spectra of (A) 7S and (B) 11S in the presence of 0-40 μM VB_{12} and (C) 0-40 μM VB_{12} alone in 0.01 M, pH 7.4 sodium phosphate buffer at 292 K. c(7S) = c(11S) = 10 μM.

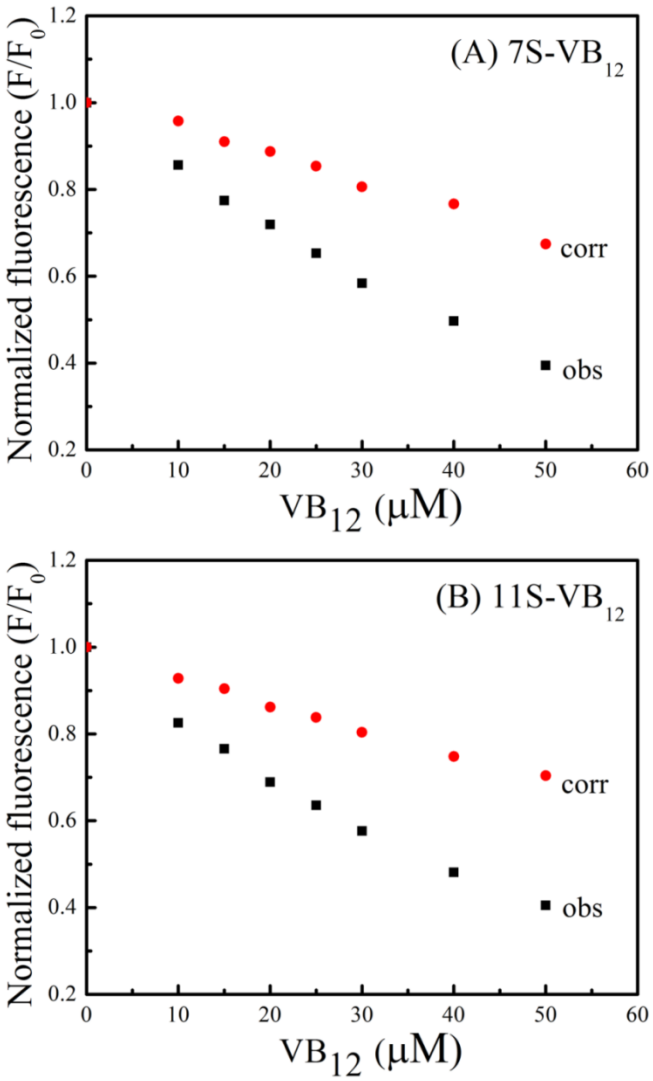

Figure 4-3. Effect of the inner-filter effect on the normalized fluorescence (F/F_0) of (A) 7S and (B) 11S with increasing VB_{12} concentration. c(7S) = c(11S) = 10 μM.

4.3.3 Collisional Quenching

Collisional quenching refers to the situation in which the quencher diffuses to the fluorophore during the lifetime of the excited state upon contact to cause a decrease in the fluorescence intensity. Collisional quenching can be estimated

using the Stern-Volmer equation and subsequently Stern-Volmer quenching constant (K_{SV}) and fluorescence quenching rate (k_q) can be obtained. If k_q were around 2.0×10^{10} $M^{-1}s^{-1}$, the reduced fluorescence intensity would be caused by collisional quenching (Lakowicz, 2009). With the assumption of a non-fluorescent complex formation, the experimental data after correction for the inner-filter effect were analyzed by the Stern-Volmer equation (Eq. (4-2)) (Ding, et al., 2010):

$$F_{corr\ 0}/F_{corr} = 1 + K_{SV} \times [VB_{12}] = 1 + k_q \times \tau_0 \times [VB_{12}] \quad (4\text{-}2)$$

where $F_{corr\ 0}$ and F_{corr} are the corrected fluorescence emission intensities in the absence and presence of quencher (VB_{12}), respectively. K_{SV} is the Stern-Volmer quenching constant, k_q is the fluorescence quenching rate constant of 7S/11S, and τ_0 is the lifetime of the fluorophore without quencher being equal to 10^{-8} s (Hou, et al., 2008).

The plots of $(F_{corr\ 0}/F_{corr} - 1)$ *versus* $[VB_{12}]$ were displayed in Figure 4-4. A good linear Stern-Volmer plot (R^2=0.9732 or 0.9977) was observed for both 7S and 11S. This suggests that only a single class of Trps within 11S or 7S was quenched and they were all equally accessible to VB_{12} (Lakowicz, 2009). The values of k_q were calculated to be 0.66×10^{13} and 0.79×10^{13} $M^{-1}s^{-1}$ for 7S and 11S at 292 K, respectively (Table 4-1), which are much larger than the collisional quenching constant 2.0×10^{10} $M^{-1}s^{-1}$. This result suggests that the collisional quenching played a negligible role in the quenching interaction between the 7S/11S and VB_{12} (Diarrassouba, et al., 2013; Van De Weert, 2010). It is well recognized that K_{SV} values in collisional quenching process increases with the elevation of temperatures,

as higher temperatures lead to a faster diffusion and thus a larger extent of collisional quenching (Lakowicz, 2009). Then K_{SV} values at four different temperatures (292, 298, 304 and 310 K) were determined and the results were demonstrated in Table 4-1. Raising temperature from 292 to 298 K or from 304 to 310 K led to a significant increase of *Ksv* in 7S-VB_{12} system, however, no significant increase was observed from 298 to 304 K ($p > 0.05$). Increasing temperature did not induce a significant increase of K_{SV} in 11S-VB_{12} system except for from 298 to 304 K ($p > 0.05$). It again confirms that collisional quenching was negligible in the quenching interaction between 7S/11S and VB_{12}. Therefore, the fluorescence quenching of 7S/11S was caused by binding-related changes (Van de Weert & Stella, 2011). In order to collect further proof of formation of a ground-state complex of 7S-VB_{12} or 11S-VB_{12}, an investigation of the occurrence of an energy transfer between protein and VB_{12} was performed.

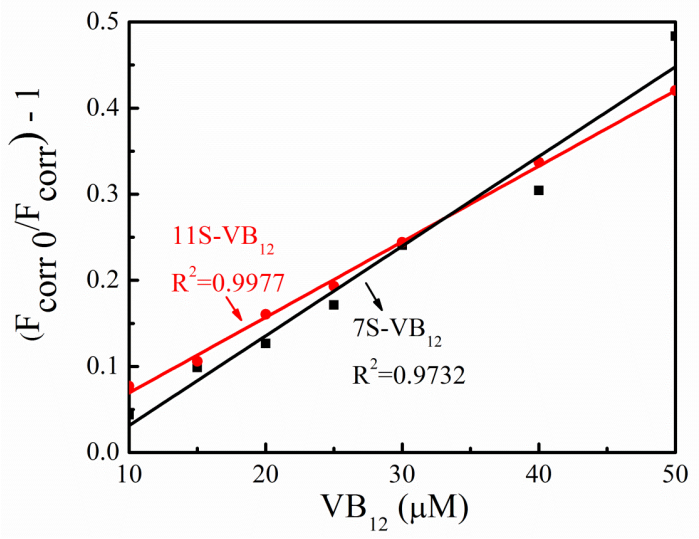

Figure 4-4. Stern-Volmer plots for the quenching of 7S/11S after correction of the inner-filter effect by 0-50 μM VB_{12} at 292 K; c(7S) = c(11S) = 10 μM.

Table 4-1. Stern-Volmer quenching constant K_{SV} and fluorescence quenching rate constant k_q of 7S-VB_{12} and 11S-VB_{12} at different temperatures, as per Eq. (4-2).

Samples	T (K)	K_{SV} (10^5 M^{-1})	R^A	S.D. (10^5)^B	k_q (10^{13} $M^{-1}s^{-1}$)
7S	292	0.707[a]	0.973	0.163	0.707[a]
	298	1.245[b]	0.990	0.050	1.245[b]
	304	1.258[b]	0.984	0.088	1.258[b]
	310	1.439[c]	0.990	0.079	1.439[c]
11S	292	0.793[a]	0.998	0.048	0.793[a]
	298	0.815[a]	0.991	0.058	0.815[a]
	304	1.057[b]	0.995	0.058	1.057[b]
	310	0.948[b]	0.988	0.122	0.948[b]

R^A is the correlation coefficient for K_{SV} values; S.D.^{B} is the standard deviation for K_{SV} values; [a-c] means the significantly difference at $p < 0.05$ in the same column.

4.3.4 Energy Transfer between 7S/11S and VB_{12}

The formation of 7S-VB_{12} or 11S-VB_{12} complexes may lead to the transfer of some of the excited energy fluorescence from the donor (7S/11S) to the acceptor (VB_{12}) (Van De Weert, 2010). A donor chromophore, initially in its electronic excited state, may transfer energy to an acceptor chromophore through non-irradiative dipole-dipole coupling (Helms, 2008). Measurements of energy transfer efficiency can be used to determine the distance between 7S/11S and VB_{12}. Energy transfer probably occurs when the following three factors are satisfied: (1) the donor can generate the fluorescence light; (2) the fluorescence emission spectrum of the donor and UV-Vis absorption spectrum of the acceptor have

adequate overlap; and (3) the distance between the donor and acceptor (r) is less than 8 nm (Förster, 1965). The energy transfer efficiency (E) is determined not only by the distance r, but also by the critical energy transfer distance (R_0). According to this theory, the binding distance r between 7S/11S and VB_{12} can be calculated by Eq. (4-3) (Jayabharathi, et al., 2011):

$$E = R_0^6 / (R_0^6 + r^6) \quad (4\text{-}3)$$

where E is the energy transfer efficiency, R_0 is the critical distance at which the efficiency of transfer is 50%. R_0 can be calculated by Eq. (4-4) when the wavelength is expressed in nm and J(λ) is in units of $M^{-1}cm^{-1}nm^4$ (Lakowicz, 2009):

$$R_0^6 = 8.79\times10^{-5} [\kappa^2 n^{-4} \varphi J(\lambda)] \text{ in } Å^6 \quad (4\text{-}4)$$

where κ^2 is the space factor of orientation, n is the refractive index of the medium, φ is the fluorescence quantum yield of the donor. In the present case, $\kappa^2 = 2/3$, n = 1.336 and φ = 0.15. J(λ) is the overlap integral of the fluorescence emission spectrum of 7S or 11S and the absorption spectrum of VB_{12} calculated from Figure 4-5. The overlap integral J(λ) for a donor-acceptor pair is defined according to Eq. (4-5) (Feng, et al., 1998):

$$J(\lambda) = \Sigma F(\lambda)\varepsilon(\lambda)\lambda^4 d\lambda / \Sigma F(\lambda)d\lambda \quad (4\text{-}5)$$

where F(λ) is the corrected fluorescence intensity of 7S/11S in the wavelength from λ to λ + Δλ and ε(λ) is the extinction coefficient of VB_{12} at λ.

The energy transfer efficiency (E) can also be obtained by using Eq. (4-6):

$$E = 1 - F_{corr}/F_{corr\ 0} \quad (4\text{-}6)$$

The overlap of the fluorescence emission spectrum of 7S or 11S and the UV-Vis absorption spectrum of VB_{12} was shown in Figure 4-5. J values together with *E*, R_0 and r calculated according to Eqs. (4-3)-(4-6), were presented in Table 4-2. The r values slowly decreased while *E* increased with the increasing concentration of VB_{12}. In addition, r is within the range of 1 to 10 nm, suggesting that energy transfer takes place (Lakowicz, 2009; Van De Weert, 2010). The result of $0.5R_0 < r < 1.5R_0$ (except for VB_{12} at the concentration of 10 μM) suggests high possibility of energy transfer from 7S or 11S to VB_{12} (Bi, et al., 2005). This can also explain the efficient quenching of Trp fluorescence (Figure 4-1) upon binding of VB_{12}. Moreover, it demonstrates that all the conditions of energy transfer theory are achieved: (i) 7S or 11S can produce fluorescence light (Figure 4-1); (ii) sufficient overlap is observed between the fluorescence spectra of 7S or 11S and the UV-Vis spectra of VB_{12} (Figure 4-5); (iii) the r value in both systems is less than 8 nm (Förster, 1965). The results highly support the binding of VB_{12} to 7S/11S through energy transfer leading to the formation of ground-state nanocomplexes. Hence, it is applicable to further determine their parameters such as the binding constant and number of binding sites of VB_{12} to soy protein (Diarrassouba, Liang, Remondetto, & Subirade, 2013).

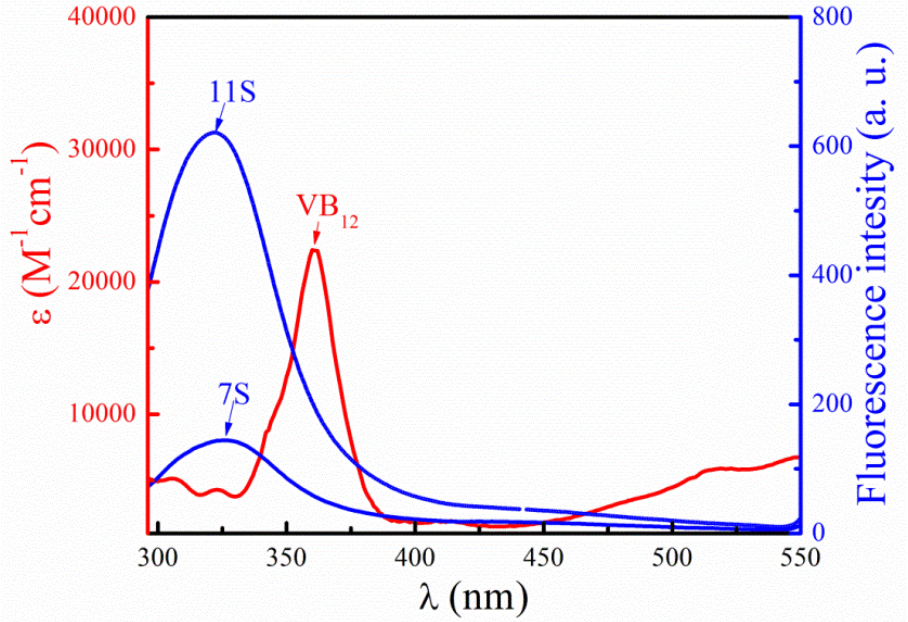

Figure 4-5. Overlap integral for energy transfer from donor 7S/11S to VB_{12} acceptor in 0.01 M, pH 7.4 sodium phosphate buffer at 292 K. c(7S) = c(11S) = 10 μM; λex = 295 nm.

Table 4-2. Energy efficiency transfer and distance between the donor 7S/11S and acceptor VB_{12}, as per Eqs. (4-3)-(4-6).

Protein	VB_{12} (uM)	E (%)	J (10^{14} $M^{-1}cm^{-1}nm^4$)	R_0 (nm)	r (nm)
7S	10	6.44	1.214	3.794	5.927
	20	11.23	1.220	3.798	5.359
	30	19.41	1.228	3.801	4.819
	40	23.34	1.239	3.807	4.642
	50	32.59	1.257	3.816	4.308
11S	10	8.86	1.116	3.741	5.517
	20	13.82	1.119	3.743	5.078
	30	19.62	1.122	3.745	4.737
	40	25.21	1.129	3.749	4.493
	50	29.60	1.131	3.750	4.332

4.3.5 Binding Constant and the Number of Binding Sites

It was indicated that binding-related quenching was the dominant mechanism involved in their interaction. Therefore, it is possible to determine the binding constant for a non-fluorescence complex (Diarrassouba, et al., 2013). When small molecules bind independently to a set of equivalent sites on a macromolecule, the binding constant K_a and the number of equivalent binding sites (n) can be calculated by the modified double logarithm regression equation (Van De Weert, 2010):

$$lg(F_{corr\ 0}/F_{corr} - 1) = nlgK_a + nlg\{[VB_{12}] - n(1 - F_{corr}/F_{corr\ 0})[P]\} \quad (4\text{-}7)$$

within Eq. (4-7), free VB_{12} concentration is defined as:

$$[VB_{12}]_{free} = [VB_{12}] - n(1-F_{corr}/F_{corr\ 0})[P] \quad (4\text{-}8)$$

where, n is the average binding number for one 7S/11S molecule, K_a is the binding constant, $[VB_{12}]$ is the total VB_{12} concentration and $[P]$ is the total 7S/11S concentration.

This modified Eq. (4-7) is more accurate than the original Hill equation $lg[(F_{corr\ 0}/F_{corr} - 1)] = nlgK_a + nlg[VB_{12}]$, where the free ligand concentration is considered to be equal to the total ligand concentration. By plotting the $lg(F_{corr\ 0}/F_{corr} - 1)$ against $lg\{[VB_{12}] - n(1 - F_{corr}/F_{corr\ 0})[P]\}$, the values of K_a and n at various temperatures were obtained and listed in Table 4-3. The n values were 1.422, 0.9634, 0.9441 and 0.9359 for 7S and 1.075, 0.994, 0.928 and 1.174 for 11S measured at 292, 298, 304 and 310 K, respectively. The decrease in the binding number was probably due to the dissociation of weekly-bound complex induced by

higher temperatures, which again supports the conclusion that a binding-related quenching occurred between soy protein and VB_{12}. Interestingly, the K_a values of 7S were all larger than those of 11S at the same temperature, demonstrating that 7S had a stronger binding affinity to VB_{12} than that of 11S (Charbonneau & Tajmir-Riahi, 2010) . 7S was also demonstrated to have a stronger binding affinity to carbonyl compounds such as 2-nonanone previously, thus it had a stronger off-flavor binding ability (Damodaran & Kinsella, 1981).

Table 4-3. Binding parameters of 7S-VB_{12} and 11S-VB_{12} at different temperatures as per Eqs. (4-7)-(4-8).

Samples	T (K)	K_a ($M^{-1}10^4$)	S.D. (10^4) [B]	R [A]	n
7S	292	1.252	0.085	0.985	1.422
	298	1.313	0.059	0.994	0.963
	304	1.296	1.022	0.981	0.944
	310	1.496	0.091	0.989	0.936
11S	292	0.952	0.04	0.995	1.075
	298	0.865	0.07	0.994	0.994
	304	1.037	0.06	0.992	0.928
	310	1.273	0.12	0.976	1.174

R[A] is the correlation coefficient for K_a values; S.D.[B] is the standard deviation for K_a values.

4.3.6 The Nature of Binding Forces

The signs and magnitudes of the thermodynamic parameters including enthalpy change (ΔH^{Θ}) and entropy change (ΔS^{Θ}) for protein reactions account for the main forces contributing to protein stability. If the ΔH^{Θ} does not differ

significantly over the temperature series tested, its value and that of ΔS^{Θ} can be determined from the van't Hoff equation (Ghosh, et al., 2009):

$$\ln K_a = -\Delta H^{\Theta}/RT + \Delta S^{\Theta}/R \quad (4\text{-}9)$$

where K_a is the binding constant at each corresponding temperature in Table 4-3 and R is the gas constant (8.31446 $Jmol^{-1}K^{-1}$). The enthalpy change (ΔH^{Θ}) can be obtained from the slope of the van't Hoff equation. Meanwhile, the Gibbs energy change (ΔG^{Θ}) can be evaluated from the thermodynamic equation (Ghosh, et al., 2009):

$$\Delta G^{\Theta} = -\mathrm{RT}\ln K_a = \Delta H^{\Theta} - T\Delta S^{\Theta} \quad (4\text{-}10)$$

In general, if $\Delta H^{\Theta} > 0$ and $\Delta S^{\Theta} > 0$, the main force is hydrophobic interactions; $\Delta H^{\Theta} < 0$ and $\Delta S^{\Theta} < 0$ are caused by van der Waal forces and hydrogen bond formation in low dielectric medium; $\Delta H^{\Theta} \approx 0$ (slightly positive or negative) and $\Delta S^{\Theta} > 0$ are characteristics of electrostatic interactions between ionic species in aqueous solution (Ross & Subramanian, 1981); $\Delta H^{\Theta} << 0$ and $\Delta S^{\Theta} > 0$, however, are arisen from both hydrophobic and hydrogen bond interactions, and hydrophobic interactions are predominant (Li, et al., 2012).

Table 4-4 displayed thermodynamic parameters of 7S-VB_{12} and 11S-VB_{12} complexes, calculated according to Eqs. (4-9)-(4-10) at four temperatures (292, 298, 304 and 310 K) under which 7S and 11S cannot be thermally denatured. The ΔG^{Θ} values were negative for both proteins indicating that the interaction process was spontaneous (Pan, et al., 2011). The positive ΔH^{Θ} and ΔS^{Θ} values indicate hydrophobic interactions played a major role in the formation of 7S-VB_{12} and

11S-VB_{12} complexes (Ross & Subramanian, 1981). As demonstrated in Figure 2-1, VB_{12} contains multiple functional groups including hydrophobic groups such as corrin ring and benzene ring, which could probably develop hydrophobic interactions with the hydrophobic groups or domain in soy proteins.

Table 4-4. Thermodynamic parameters of 7S-VB_{12} and 11S-VB_{12} at different temperatures, as per Eqs. (4-9)-(4-10).

Samples	T (K)	ΔH (kJ mol^{-1})	ΔG (kJ mol^{-1})	ΔS ($Jmol^{-1}K^{-1}$)
7S	292	6571	-22.906	100.810
	298		-23.484	
	304		-23.929	
	310		-24.774	
11S	292	13.274	-44.600	197.440
	298		-45.278	
	304		-46.649	
	310		-48.092	

4.3.7 Protein Conformation Study

In this section, the protein secondary conformation change upon VB_{12} binding was investigated using far-UV CD spectroscopy as a major tool. Synchronous fluorescence spectroscopy and three-dimensional fluorescence spectroscopy were used to monitor the alteration of protein tertiary structure.

4.3.7.1 Far-UV CD Analysis

As displayed in Figure 4-6 (A) and (B), both proteins exhibited nearly similar far-UV CD spectrum patterns. A positive peak was observed at 192.5 nm for 7S and 195 nm for 11S, meanwhile a negative peak appeared at 210 nm for 7S and 209 nm

for 11S, respectively. Such spectra indicate that both β-sheet and α-helix structures exist in 7S and 11S (Matsuo, et al., 2004). With the increase of VB_{12} concentration, the mean residue ellipticity at 192.5 nm for 7S decreased gradually, whereas that at 195 nm for 11S remained almost unchanged. Minor shifts of the peaks were observed as well, for example, the positive peak shifted to 194.5 nm in 7S and to 193.5 nm in 11S when the concentration of VB_{12} increased to 40 uM. Meanwhile, the mean residue ellipticity at 210 nm for 7S and 209 nm for 11S continuously increased with a blue-shift to 208 and 208.5 nm, respectively. All these changes illustrate that the interaction with VB_{12} induced the alteration of soy protein secondary structures. CONTINLL software was then used to calculate the secondary structure content of each protein. The results in Table 4-5 show that 7S is composed of 6.7% α-helix, 37.0% β-sheet, 19.5% β-turn and 36.9% unordered structure, while 11S is composed of 9.5% α-helix, 33.9% β-sheet, 18.7% β-turn and 37.8% unordered structure. These results are in accordance with previous reports that both 7S and 11S contain antiparallel β-sheet and random coil as major secondary structures, as well as low levels of α-helix (Fukushim, 1968; Sze, et al., 2007). With an increase in the concentration of VB_{12}, the contents of β-sheet and β-turn increased in both proteins at the expense of unordered structure. For instance, when the amount of VB_{12} was up to 40 μM, the β-sheet and β-turn contents in 7S elevated from 37.0 to 43.0% and from 19.5 to 26.8%, respectively, meanwhile, that of unordered structure decreased from 36.6 to 22.2%. The percentage of α-helix in 7S slightly increased as well. It is evident that binding of VB_{12} changed the

conformation of soy proteins, and therefore altered the local microenvironment around the intrinsic fluorophore leading to a more organized conformation as secondary structure content of 7S/11S increased at the expense of unordered structure. These secondary structural changes upon VB_{12} binding might lead to protein fluorescence quenching to a certain degree depicted in Figure 4-3 after correction of the inner-filter effect. In this case, the calculated values of binding distance r in 7S-VB_{12} and 11S-VB_{12} systems would be slightly larger than those listed in Table 4-2 (Guo, et al., 2010).

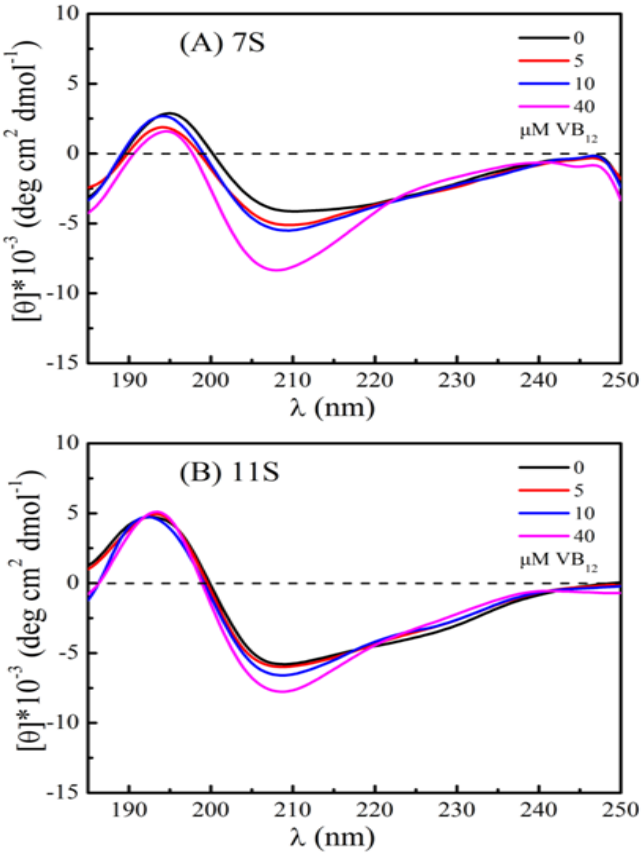

Figure 4-6. Far-UV CD spectra of (A) 7S-VB_{12} and (B) 11S-VB_{12} systems in 0.01 M, pH 7.4 sodium phosphate buffer at 292 K. c(7S) = c(11S) = 10 μM; c(VB_{12}) = 0, 5, 10 and 40 μM.

Table 4-5. The percentage of secondary structures (%) of 10 μM 7S and 11S in the absence and presence of increasing amount of VB_{12}.

	VB_{12} (μM)	α-helix (%)	β-sheet (%)	β-turn (%)	Unordered structure (%)
7S	0	6.7	37.0	19.5	36.9
	5	7.1	35.5	20.4	36.9
	10	7.3	35.9	20.1	36.7
	40	7.9	43.0	26.8	22.2
11S	0	9.5	33.9	18.7	37.8
	5	8.2	35.6	19.8	36.4
	10	8.2	38.0	21.9	31.8
	40	9.0	41.0	24.2	25.9

4.3.7.2 Three-Dimensional Fluorescence Spectroscopy

The three-dimensional fluorescence spectroscopy has become a popular technique in recent years. It provides solid information about protein tertiary conformational change when there is a shift at the excitation or emission wavelength around the fluorescence peak, or appearance of a new peak or disappearace of an existing peak. The tertiary conformational and micro-environmental changes of the two proteins were monitored by measuring their three-dimensional spectra in the absence and presence of VB_{12}, as indicated in Figure 4-7. The corresponding parameters are listed in Table 4-6. Peak A or a is the Rayleigh scattering peak ($\lambda_{ex}=\lambda_{em}$); peak B or b mainly represents the spectral characteristic of Trp and Tyr residues; and peak C or c is mainly caused by $\pi \rightarrow \pi^*$

transition of characteristic polypeptide backbone structure (C=O) of protein. The fluorescence intensity of peak B or b and C or c showed a significant decrease, but to different degrees after VB_{12} binding. Moreover, the λ_{em} of peak B or b expressed a slight blue-shift (Table 4-6), which is in accordance with the fluorescence results (Figure 4-1). The maximum of emission would shift to the lower wavelength (blue-shift) when aromatic amino acids move from a hydrophilic surrounding to a hydrophobic one, i.e. from the aqueous media to protein interior (Miriani, et al., 2011). It seems that interacting with VB_{12} induces a minor folding of protein tertiary conformation, which eventually leads Trp or Tyr residues of soy protein polypeptide chains to a more hydrophobic microenvironment.

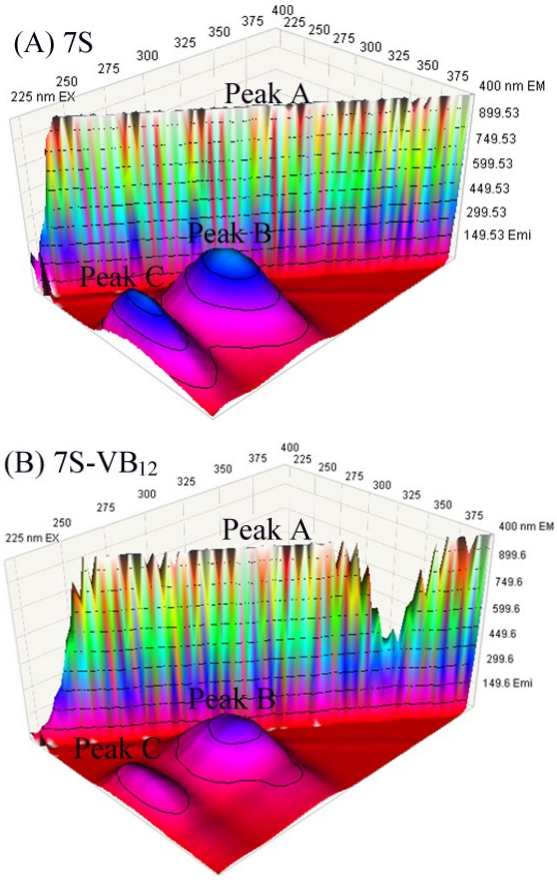

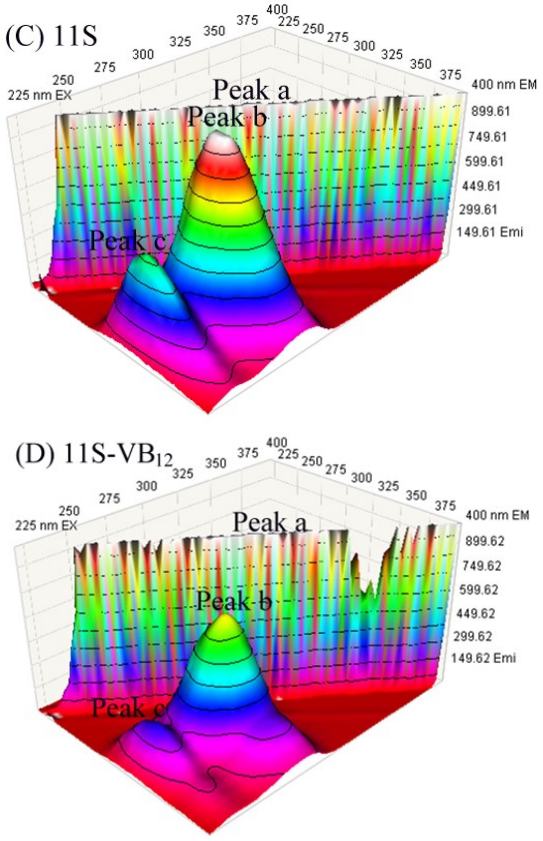

Figure 4-7. Three-dimensional fluorescence spectra of (A) 7S, (B) 7S-VB_{12}, (C) 11S and (D) 11S-VB_{12} in 0.01 M, pH 7.4 sodium phosphate buffer at 292 K.

Table 4-6. Three-dimensional fluorescence spectral characteristic parameters of 7S, 11S, 7S-VB_{12} and 11S-VB_{12} systems.

		Protein		Protein-VB_{12}		
	Peak	Peak position $\lambda_{ex}/\lambda_{em}$ (nm/nm)	Intensity F_0	Peak position $\lambda_{ex}/\lambda_{em}$ (nm/nm)	Intensity F	F_0/F
7S	A	225/225→ 400/400	-	225/225→ 400/400	-	-
	B	280/333	367	282/331	233	1.6
	C	230/318	324	228/319	137	2.4
11S	a	225/225→ 400/400	-	225/225→ 400/400	-	-
	b	280/331	1016	280/330	720	1.4
	c	233/331	490	234/332	263	1.9

4.3.7.3 Synchronous Fluorescence Spectroscopy

Synchronous fluorescence spectroscopy is another valuable tool to detect tertiary conformational change of a protein as it avoids complicated labeling with an extrinsic dye. This technology provides information about the molecular surroundings in the vicinity of a chromophore at low concentrations under physiological conditions (He, et al., 2005). It is used to monitor the possible shift in the wavelength of the maximum emission corresponding to the changes of the polarity around the chromophore molecule (Yuan, et al., 1998). When the λ_{max} value between excitation wavelength and emission wavelength is fixed at 15 and 60 nm, the synchronous fluorescence gives characteristic information of Tyr and Trp residues, respectively (Congdon, et al., 1993). Figure 4-8 showed the synchronous fluorescence spectra of 7S/11S with different concentrations of VB_{12} when $\Delta\lambda$ was set at 15 nm. No noticeable shift was observed suggesting that the polarity around Tyr residues stayed at the same level. In other words, the interaction of 7S/11S with VB_{12} did not occur around the vicinity of Tyr residues. Interestingly, an obvious blue-shift of Trp fluorescence in both 7S (from 339 to 333 nm) and 11S (from 339 to 334 nm) was observed upon the addition of VB_{12} when $\Delta\lambda$ was set at 60 nm in Figure 4-9. It is consistent with the results of fluorescence quenching (Figure 4-1) and three-dimensional fluorescence spectroscopy (Table 4-6). The blue-shift indicates that the polarity around Trp residues decreased (Klajnert & Bryszewska, 2002). This result supports the assumption that interaction of VB_{12} with two

proteins induces the folding of polypeptide chains around Trp residues to avoid outer polar environment, leading to a more hydrophobic surrounding.

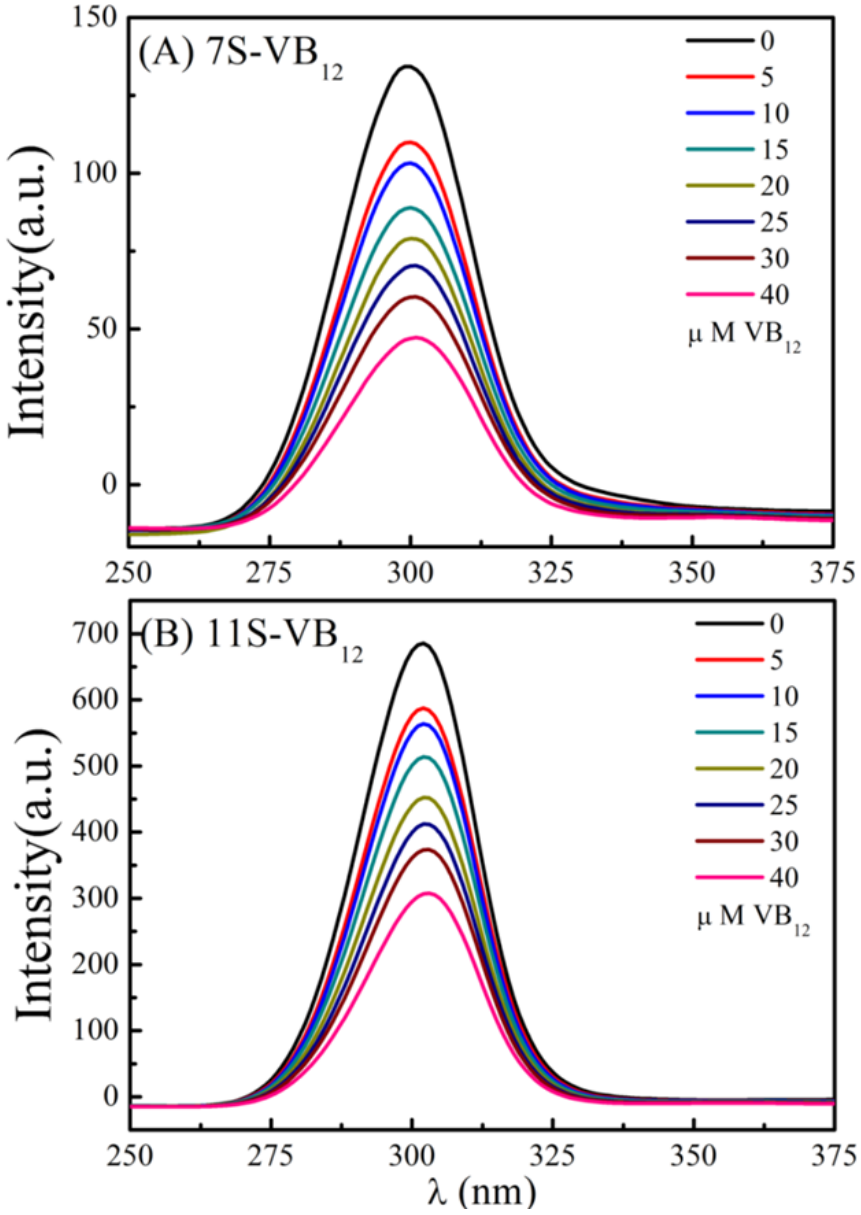

Figure 4-8. Synchronous fluorescence spectra of (A) 7S-VB_{12} and (B) 11S-VB_{12} systems in 0.01 M, pH 7.4 sodium phosphate buffer at 292 K with $\Delta\lambda = 15$ nm. c(7S) = c(11S) = 10 μM; c(VB_{12}) = 0, 5, 10, 15, 20, 25, 30 and 40 μM.

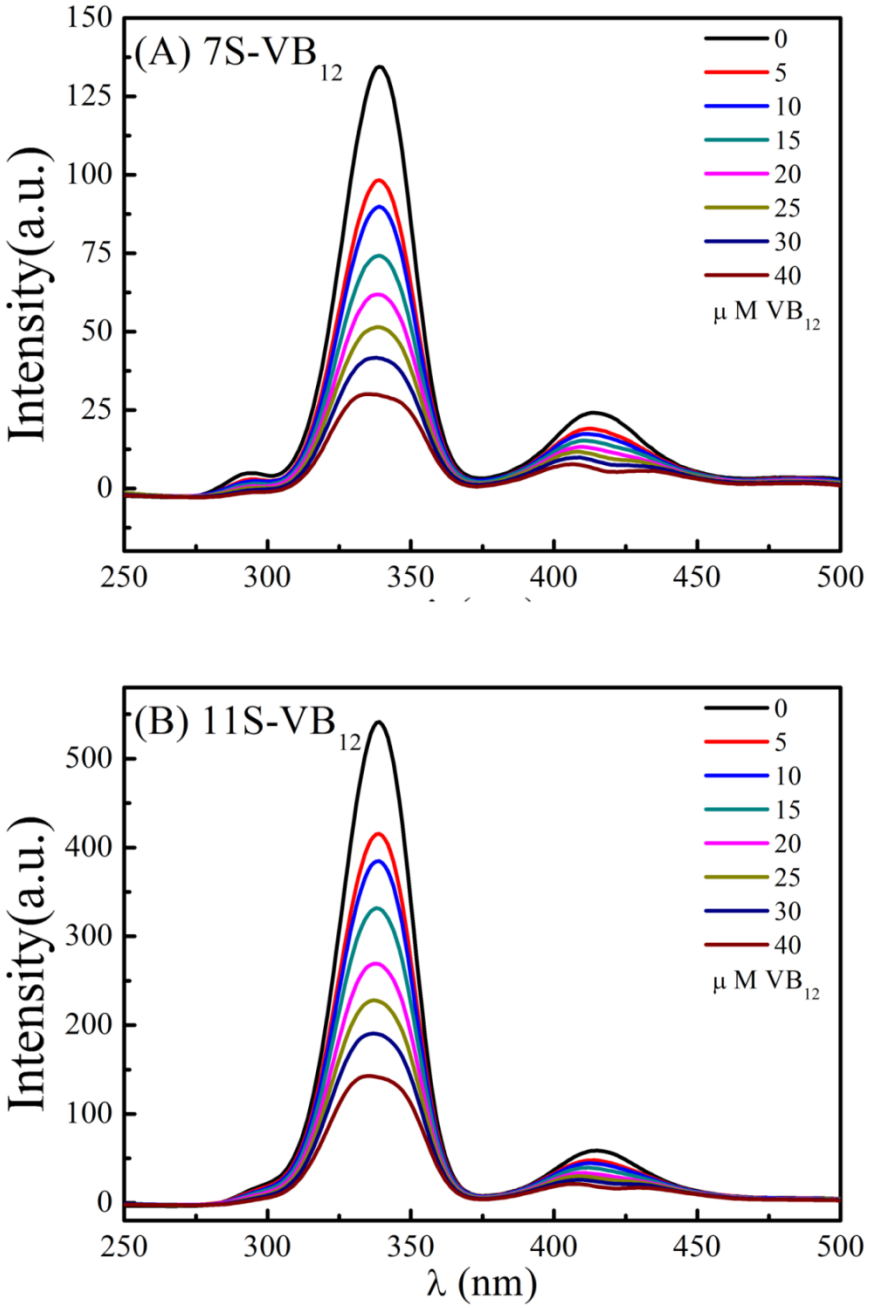

Figure 4-9. Synchronous fluorescence spectra of (A) 7S-VB_{12} and (B) 11S-VB_{12} systems in 0.01 M, pH 7.4 sodium phosphate buffer at 292 K with $\Delta\lambda$ = 60 nm. c(7S) = c(11S) = 10 μM; c(VB_{12}) = 0, 5, 10, 15, 20, 25, 30 and 40 μM.

4.4 Discussion

It has been reported that Trp residues in 7S are located in the N-terminal extension regions of the α subunit (Trp_{28} and Trp_{125}) (http://www.uniprot.org/uniprot/P13916) and of the α′ subunit (Trp_{28}, Trp_{125} and Trp_{126}) (http://www.uniprot.org/uniprot/P11827) that are rich in hydrophilic and negatively charged amino acids (Maruyama, et al., 2001). Trp residues in 11S are located in a more hydrophobic environment as suggested by the observations that 11S has a higher λ_{max} and higher value of the fluorescence emission intensity (Figure 4-1). Binding of VB_{12} to both proteins disrupted the protein original balanced environment, leading to the folding of the polypeptide chains around Trp residues to avoid the outer polar environment; consequently they were folded into a more hydrophobic environment. Therefore, their Trps emission spectra were blue-shifted in Figure 4-1. Simultaneously, VB_{12} were kept in the interior of 7S and 11S three-dimensional network mainly through hydrophobic interactions. Nevertheless, it is still difficult to deduce the exact binding site and domain of Trp residues as more than one Trp residues exist in both proteins. Therefore, more detailed proteomic work is needed to reveal which portion of proteins would be involved in these binding interactions.

Introducing a special carrier to nutraceutials normally aims to increase their solubility, stability or bioavailability (Liang, et al., 2008; Puyol, et al., 1991; Wang, et al., 1997). For example, β-lactoglobulin (β-LG) has been studied extensively and

reported as good transporters for retinol (Puyol, et al., 1991), fatty acids (Puyol, et al., 1991) and vitamin D_2 (Wang, et al., 1997). Such binding reported is to not only protect nutraceuticals from degradation caused by heat, oxidation or irradiation, but also improve their uptake in the intestine. Binding constants of β-LG vary as the compounds of interest differ, from as little as 1.5×10^2 M^{-1} for 2-heptanone to as high as 5×10^7 M^{-1} for retinol (Liang, et al., 2008; O'Neill & Kinsella, 1987). In this study, the binding constants of 7S and 11S to VB_{12} were 1.252 (± 0.085) × 10^4 and 0.952 (± 0.04) × 10^4 M^{-1} at 292 K (Table 4-3), respectively, indicating both proteins have a good affinity to VB_{12}. This is probably due to the highly compact internal structures of soy protein which may confine VB_{12} tightly into their three-dimensional network. Such a high binding affinity together with the interior location suggests that soy protein can be a good carrier for VB_{12} to potentially improve its bioavailability. This statement however needs to be verified by future *in vitro* and *in vivo* investigations.

4.5 Conclusions

This research has revealed good binding of VB_{12} to both soy β-conglycinin and glycinin to form 7S-VB_{12} and 11S-VB_{12} complexes respectively. Such complexing induced a more organized protein conformation with increased β-sheet and β-turn component and a more folded tertiary structure. It is deduced that VB_{12} was bound in the interior of the three-dimensional protein network mainly stabilized by hydrophobic interactions. The binding constant and number to VB_{12}

were 1.252 (± 0.085) × 10^4 and 1.422 for 7S and 0.952 (± 0.04) × 10^4 M^{-1} and 1.075 for 11S at 292 K, respectively. The results suggest that soy proteins have potential to be used as a carrier of VB_{12} to improve its bioavailability after oral administration.

Chapter 5. Impact of Particle Size and Surface Charge on the Release, Cell Uptake and Uptake Mechanism of Vitamin B_{12}-loaded Soy Protein Isolate Nanoparticles[3]

5.1 Introduction

To date, oral delivery is still the preferred administration route of bioactive compounds, especially for chronic therapies, where repeated administration is required. Nevertheless, many compounds exhibit low oral bioavailability due to: (1) low mucosal permeability, (2) low solubility leading to slow dissolution in the mucosal fluids and elimination of a large fraction of the compounds from the gastrointestinal (GI) tract, (3) restricted absorption to a region of the GI tract, and (4) instability during food processing (temperature, oxygen, light) or in the GI tract (pH, enzymes, presence of other nutrients), resulting in oxidation or degradation of an ingredient prior to its absorption (Bell, 2001; Galindo-Rodriguez, et al., 2005; Hattori, et al., 1995; Loveday & Singh, 2008). All of these factors limit the bioactivities and potential health benefits of nutraceuticals (Bell, 2001).

The oral bioavailability of nanoparticles for nutraceutical delivery is determined by many factors, including particle stability in the GI tract and uptake

[3] A version of this chapter is to be submitted for publication.

efficiency by intestinal epithelial cells (Acosta, 2009; Bernkop-Schnürch, 2013). Nanoparticles can protect the incorporated compounds against the harsh fluids (enzymes and acidic pH value) in GI tract and release them at the time of absorption (Bernkop-Schnürch, 2013; Sarmento, et al., 2007; Sonaje, et al., 2010). When nanoparticles reach small intestine, direct uptake is yet another method improving the bioavailability of active ingredients, especially for the compounds that are soluble in water but have low permeability, such as VB_{12} (Acosta, 2009). The uptake efficiency of incorporated ingredient in nanoparticles is determined by the physicochemical characteristics of particles, such as the particle size and surface charge (Lee, Nir, & Papahadjopoulos, 1993). Smaller particles normally demonstrate increased cellular uptake, due to their larger surface area-to-volume ratio (Jiang, et al., 2008; Jin, et al., 2009). Positively charged nanoparticles have more efficient cellular uptake because of their high affinity to the negatively charged epithelial cell membrane (He, et al., 2010).

Particle surface can be modified by a variety of polymers in order to achieve controlled release and improved nutraceutical absorption. Chitosan and alginate are the most commonly used polymers due to their biocompatible, biodegradable and mucoadhesive properties (Behrens, et al., 2002; Issa, et al., 2005; Rajaonarivony, et al., 1993; Sarmento, et al., 2007). An effective nanoparticle delivery system requires optimal combination of numerous variables to achieve the most efficient oral bioavailability of the nutraceutical of interest. A thorough understanding of the

influence and underlying mechanisms of these factors is of great importance to the development of effective nanocarriers.

Soy protein isolate (SPI) is a good candidate for nanoencapsulation due to its multiple functional properties of emulsion, gelation, foaming, film-forming and organoleptic properties (Franzen & Kinsella, 1976; Kinsella, 1979; Renkema, et al., 2001). SPI nanoparticles have been prepared by the processes of simple coacervation, followed by crosslinking and evaporation. SPI nanoparticles exhibited satisfactory encapsulating properties of curcumin and a desirable stability at high concentrations, due to the balanced composition of amino acids (Teng, et al., 2012). By this method, folic acid (FA, a carrier) conjugated SPI nanoparticles have been prepared (Teng, et al., 2013). The conjugation of FA led to significantly higher encapsulation and loading efficiencies, faster release of curcumin (in PBS/Tween-20 buffer) and higher cellular uptake by Caco-2 cells. However, the utilization of the reagents including ethanol/glutaraldehyde (Teng, et al., 2012), as well as dimethyl sulfoxide/N-(3-dimethylaminopropyl)-N-ethylcarbodiimide/ethanol (Teng, et al., 2013) in the preparation of these nanoparticles would restrict their applications in food. Without using any toxic reagent, SPI nanoparticles have been successfully prepared by a cold-gelation method in Chapter 3 by this method, VD_3 was incorporated inside SPI nanoparticles and carboxymethyl chitosan/SPI (CMCS/SPI) nanoparticles (Teng, et al., 2013). The molecular interactions between soy protein and VB_{12} have been investigated in Chapter 4. It demonstrated

that VB_{12} was bound into the three-dimensional network of soy protein, where the complexes of soy protein-VB_{12} were formed via hydrophobic interactions. The formation of these complexes suggested soy protein could play a potential role in encapsulation, protection and delivery of bioactive compounds in functional foods (De Wolf & Brett, 2000; Liang & Subirade, 2012; Liang, et al., 2008; Liang, et al., 2011).

The objective of this study was, therefore, to investigate the impacts of particle characteristics (size, surface charge/modification) on particle release and uptake properties. Caco-2 cell monolayer was used as an *in vitro* model to mimic the small intestinal epithelium. Cytotoxicity of SPI nanoparticles was tested using a XTT assay by measuring the activity of mitochondrial dehydrogenase in Caco-2 cells after being incubated with nanoparticles (Meshulam, et al., 1995). The effects of particle concentrations, incubation time and temperature on the cellular uptake efficiency were also evaluated in order to explore the particle uptake mechanisms. Two endocytic inhibitors including colchicine (COL) and cytochalasin D (CyD) were used to block clathrin- and/or caveolae-mediated endocytosis and macropinocytosis, respectively. Finally, the correlation of particle features with associated uptake mechanisms was discussed.

5.2 Materials and Methods

5.2.1 Materials

SPI PRO-FAM® 646 was kindly provided by Archer Daniels Midland Company (ADM, Decatur, IL, USA), containing 94.4% protein on a dry basis as determined by combustion with a nitrogen analyzer (Leco Corporation, St. Joseph, MI, USA) calibrated with analytical reagent grade EDTA and caffeine using a calculation factor of 6.25. Dimethyl sulfoxide (DMSO), cyanocobalamin (VB_{12}), coumarin 6 (COUM-6), 4', 6-diamidino-2-phenylindole (DAPI), colchicine (COL), 2,3-bis-(2-methoxy-4-nitro-5-sulphenyl)-(2H)-tetrazolium-5-carboxanilide (XTT) based toxicology assay kit with 1% phenazine methosulfate (PMS), and cytochalasin D (CyD) were purchased from Sigma-Aldrich (Oakville, ON, Canada). Wheat germ agglutinin (WGA)-Alexa Fluor® 555 conjugate, Dulbecco's modified eagle medium (DMEM), fetal bovine serum (FBS), trypsin-EDTA, 4-(2-hydroxyethyl)-1-piperazineethanesulfonic acid (HEPES) and 1% antibiotic-antimycotic were purchased from Invitrogen (Burlington, ON, Canada). Cobalt reference standard solution, low molecular chitosan and sodium alginate were purchased from Fisher Scientific (Toronto, ON, Canada). Caco-2 cells (HTB®-37™) were purchased from the American Type Culture Collection (ATCC, Manassas, VA, USA). Cell culture plates including 96-well, 48-well and 6-well are purchased from Costar (Corning, NY, USA). All other chemicals were of reagent grade.

5.2.2 Preparation of SPI Nanoparticles and VB_{12} Loading

5.2.2.1 SPI Treatment and Labeling

Pretreated SPI solution was prepared according to the procedure described in Section 3.2.3 (Chapter 3). For a better observation, a portion of pre-treated SPI was labeled with COUM-6. Briefly, 1 μg/ml COUM-6 in DMSO was added to pre-treated SPI solution at pH 9, where the dye is chemically stable. After stirring overnight in a dark environment at 4 °C, the solution was dialyzed in the dark at 4 °C against 5 L of phosphate buffered saline (PBS) (0.01 M, pH 7.4), the PBS being replaced every 6 h for 6 days until no COUM-6 was detected in solution by a Fluorescence spectrophotometer (SpectraMax M3, Sunnyvale, CA, USA) at λ_{ex}=458 nm and λ_{em}=505 nm. The amount of COUM-6 was calculated based on a standard calibration curve constructed by measuring the fluorescence emission intensity of the COUM-6 at different concentrations (0.1-1.5 μg/ml) using pre-treated SPI as the reaction medium.

5.2.2.2 Preparation of VB_{12}-loaded Nanoparticles

VB_{12} (10 μg/ml) was introduced into two pre-treated SPI solutions of pH 8 and pH 9 and left to react at room temperature overnight, followed by the addition of $CaCl_2$ dropwise to induce nanoparticle formation. The extra unbound VB_{12} was removed using dialysis tube with molecular weight cutoff of 2 kDa at 4 °C against 5 L of PBS (0.01 M, pH 7.4), which was replaced every 6 h for 4 days until no free

VB_{12} was detected in the outer solution by Atomic absorption spectrometer. VB_{12} loaded SPI nanoparticles were collected after dialysis. As hydrophobic interactions played a key role in the formation of SPI nanoparticles and binding complexes of soy protein-VB_{12}, disrupting hydrophobic interactions by SDS would dissociate nanoparticles resulting in the release of VB_{12} Thus, 0.05% SDS (w/v) was applied in each nanosuspension in order to release VB_{12} by dissociating nanoparticles. The amount of loaded VB_{12} was measured by Atomic absorption spectrometer using cobalt reference standard solution to make a standard curve of [Co] vs. Absorbance. The loading capacity (LC, %) and efficiency (LE, %) were calculated according to (Borges, et al., 2006):

$$\text{LC (\%)} = \frac{\text{VB}_{12}(\mu\text{g}) \text{ in nanoparticles}}{\text{nanoparticles } (\mu\text{g})} \times 100\%$$

$$\text{LE (\%)} = \frac{\text{VB}_{12} \ (\mu\text{g}) \text{ in nanoparticles}}{\text{VB}_{12} \ (\mu\text{g}) \text{ added}} \times 100\%$$

5.2.2.3 Surface Modification of VB_{12}-loaded SPI Nanoparticles

Surface modifications of SPI nanoparticles with chitosan and sodium alginate were performed by layer-by-layer assembly method with a minor modification (Bagre, et al., 2013; Ye, et al., 2005). Low molecular weight chitosan (<5 kDa) was dissolved in 1% aqueous acetic acid (v/v) to obtain 1% chitosan solution (w/v), which was then diluted to 0.2% using deionized water. Positively charged nanoparticles were obtained upon quickly introducing the negatively charged SPI

nanoparticles (freshly prepared) into the positively charged chitosan solution (0.2%) at different ratios (Bagre, et al., 2013). The positively charged nanoparticles of similar size to the original SPI nanoparticles, were successfully produced when the ratio of SPI original nanoparticles to 0.2% chitosan solution was 9:1 (v/v).

Solution of sodium alginate was prepared in phosphate buffered saline (1%, w/v, pH 9). Alginate coating on optimized chitosan nanoparticles was performed by quickly introducing alginate solution into the optimized chitosan modified nanoparticles (freshly prepared) at different ratios (Bagre, et al., 2013). The negatively charged nanoparticles, of similar size range as the original SPI nanoparticles, were successfully produced when the ratio of SPI nanoparticles to sodium alginate (1%) came to 1:1.

5.2.3 Characterization of Nanoparticles

The size and zeta-potential of nanoparticles were determined by dynamic light scattering (DLS) and laser Doppler velocimetry using Zetasizer Nano ZS (Malvern Instruments Ltd., UK) at 20 ^{o}C. Each measurement was made in triplicate on 3 independently prepared samples.

The surface morphology of nanoparticles was observed by transmission electron microscopy (TEM, Hitachi H-7000, Tokyo, Japan). Briefly, a drop of 1% phosphotungstic acid (PTA, w/v) was dipped on the carbon-coated copper grid for 1 min, then a drop of nanoparticle solution was added to react with 1% PTA for 45 s,

the extra solution was drawn off using filter paper. The samples were allowed to air dry thoroughly before TEM observation at an accelerating voltage of 140 kV.

5.2.4 *In Vitro* Release of VB_{12}

Release profiles of VB_{12} from nanoparticles were performed using a dialysis tube (cut-off 2 kDa) (Bagre, Jain, & Jain, 2013). Two concentrated media were used: (1) simulated gastric fluid (SGF): pH 1.2, 0.02 M HCl with 0.2% pepsin (w/v) (Chen & Subirade, 2006); and (2) simulated intestinal fluid (SIF): pH 7.4, 0.02 M PBS with 2000 unit/ml trypsin (Lin, et al., 1993). Three batches were tested for each medium. For each batch, 50 ml VB_{12}-loaded nanoparticles (freshly prepared) were mixed with 50 ml of pre-warmed SGF and SIF at 37 °C in a dialysis tube, which was then immersed in solutions with pH 1.2 HCl or pH 7.4 PBS (1 L, 0.01 M). VB_{12} was used as a control. The water bath system was kept at 37 °C and shaken at 100 rpm. At appropriate time intervals, 2 ml of sample was withdrawn from the dialysis tube and replenished with corresponding release medium at different time intervals. Digestive enzymes were inactivated by heating the samples at 95 °C for 3 min. Subsequently, 10 µl 10% SDS (w/v) was added to 2 ml collected sample and subjected to 10-min ultrasonication to dissociate nanoparticles, leading to VB_{12} release. The medium was subjected to centrifugation at 10,000 g for 5 min and the supernatant was collected. The amount of VB_{12} remaining in the dialysis tube was analyzed by Atomic absorption spectrometer using a cobalt reference

standard solution to make a standard curve of [Co] vs. Absorbance. The cumulative release percentage (%) of VB_{12} was calculated according to:

$$VB_{12}\ release(\%) = \frac{\text{total loaded } VB_{12} - \text{remaining } VB_{12}}{total\ loaded\ VB_{12}} * 100\%$$

5.2.5 Cell Viability

5.2.5.1 XTT Assay

Caco-2 cells of passages between 20-40 were used. The cells were cultured in DMEM-20, supplemented with 20% FBS, 1% non-essential amino acids, 1% antibiotic-antimycotic and 25 mM HEPES. Cells were cultured in a humidified atmosphere containing 5% CO_2 at 37 ^{o}C and the medium was renewed every other day.

For XTT colorimetric assay, Caco-2 cells (passages 26) were seeded at 5×10^4 cells/well into a 96-well plate in the EMEM-20. The cells were allowed to recover for 24 h at 37 °C in the incubator. The medium in each well (200 µl/well) was then replaced with SPI nanoparticle suspension diluted with Hank's balanced salt solution buffer (HBSS, pH 7.4) to obtain SPI concentrations of 0.625, 1.25, and 2.5 mg/ml. HBSS treatment without nanoparticles was used as a negative control. After 6 h incubation, cells were washed twice with 200 µl of HBSS after removal of nanoparticles. Then, 50 µl of 1 mg/ml XTT with 1% PMS mixture was added to each well. The microplates were incubated for 2 h at 37 °C in the dark to

develop formazan product and read at 450 nm. The absorbance at 690 nm was read as background. Cell viability (%) was calculated according to:

$$\text{Cell viability (\%)} = 100\% * \frac{A_{450nm\ 1} - A_{690nm\ 1}}{A_{450nm} - A_{690nm}}$$

where $A_{450nm\ 1}$ and A_{450nm} referred to the absorbance values at 450 nm with the treatment of nanoparticles and HBSS buffer respectively. $A_{690nm\ 1}$ and A_{690nm} represented the absorbance values at 690 nm with the treatment of nanoparticles and HBSS buffer respectively.

For cell counting, the cells were cultured in a T-25 flask, until they came to 80% confluence. The same samples and treatments as indicated in XTT assay were then applied to Caco-2 cells. After 6 h, cells were trypsinized after the removal of nanoparticles, harvested and suspended in 5 ml of DMEM-10. HBSS treatment without nanoparticles was used as a negative control. The number of living cells after each treatment was counted by a TC 10^{TM} Automated Cell Counter (Bio-Rad, Singapore) and the data were expressed as number of living cells per ml.

5.2.6 Endocytosis of Nanoparticles and Mechanism Studies

5.2.6.1 Confocal Laser Scanning Microscopy (CLSM) Study

Caco-2 cells (5×10^5 cells/well) used for the uptake study were seeded onto the coverslip in 6-well plates and incubated until 100 % confluence was reached. The cells were washed and equilibrated with HBSS buffer (pH 7.2) at 37 ^oC for 30 min; the buffer was then replaced with 1.5 ml COUM-6 labeled nanoparticle

suspensions (containing 1.25 mg/ml SPI nanoparticles in HBSS) and further incubated for 6 h at 37 ^{o}C. The intreaction of nanoparticles with Caco-2 cells observed under the CLSM was illustrated in 3.2.7 (Chapter 3).

5.2.6.2 Flow Cytometry

Caco-2 cells (5×10^5 cells/well) were seeded in 6-well plates. Upon reaching confluence, the culture medium was replaced by HBSS and pre-incubated at 37 ^{o}C for 30 min. After equilibration, 1.5 ml of COUM-6 labeled nanoparticle suspensions (containing 1.25 mg/ml SPI nanoparticles in HBSS) were added and incubated for 4 h. After removal of nanoparticles, cells were trypsinized, harvested and suspended in FCS washing buffer. Thereafter, the cells were analyzed by a Flow cytometry using FACSCalibur (Becton Dickinson, San Jose, CA, USA). The fluorescence intensity was recorded and analyzed by FCS Express 4 Flow Cytometry (De Novo Software, Los Angeles, CA, USA).

5.2.6.3 Spectrofluorimetry Study

Caco-2 cells (1×10^5 cells/well) were seeded in 48-well plates. Upon reaching confluence, the culture medium was replaced by HBSS and pre-incubated at 37 ^{o}C for 30 min. After equilibration, cellular uptake of nanoparticles was started by exchanging HBSS buffer with 0.4 ml of COUM-6 labeled nanoparticle suspensions (0.625-2 mg/ml in HBSS). The incubation of nanoparticles with cells at 37 ^{o}C lasted for 0.5-4 h. The experiment was terminated by gently washing cell

monolayers 3 times with HBSS buffer, 0.4 ml HBSS buffer was then added to each well. Cells were lysed with 0.4 ml Triton X-100 (1% in 0.4 M NaOH). The lysis was analyzed using a microplate reader (SpectraMax M3, Sunnyvale, CA) with the excitation wavelength at 458 nm and emission wavelength at 505 nm. The cells containing the nanoparticles lysed directly received the same treatment and were used as the corresponding overall. The cells incubated with HBSS were used as a control. Results of cellular uptake efficiency were expressed according to (Yin Win & Feng, 2005):

$$\text{Cellular uptake of SPI nanoparticles (\%)} = 100\% \times \frac{FI_1 - FI_2}{FI_3 - FI_4}$$

where FI_1: the fluorescence intensity (FI) of the lysed cell solution after removing nanoparticles; FI_2: FI of the lysed cell solution after removing HBSS; FI_3: FI of lysed cell solution without removing nanoparticles; and FI_4: FI of the lysed cell solution without removing HBSS.

5.2.6.4 Metabolic and Endocytosis Inhibition

To study potential cellular uptake pathways of nanoparticles, cells were pre-treated with metabolic and endocytosis inhibitors including sodium azide (100 mM), COL(5 μg/ml) and CyD (10 μg/ml) for 30 min (Beloqui, Solinís, Gascón, del Pozo-Rodríguez, des Rieux, & Préat, 2013). Following incubation with the nanosuspensions for a further 4 h, the cells were washed three times with HBSS to eliminate traces of nanoparticles left in the wells. Subsequently, 0.4 ml of HBSS was added to the wells after the removal of nanoparticles. Then 0.4 ml of 1%

Triton X-100 in 0.4 M NaOH was added to all the wells. The fluorescence intensity (FI) of the lysis was analyzed using a microplate reader (SpectraMax M3, Sunnyvale, CA, USA) with the excitation wavelength at 458 nm and emission wavelength at 505 nm. The cells containing the nanoparticles lysed directly received the same treatment and were used as the corresponding overall. Controls were prepared without the inhibitor pre-incubation at 37 ^{o}C. The cell uptake efficiency was calculated as indicated in Section 5.2.6.3.

5.2.7 Statistical Analysis

All experiments were performed in triplicate samples in at least three independent batches. The results were expressed as mean ± standard deviation (SD). Student's t-test was used for comparisons between two samples and one-way ANOVA for more than two samples.

5.3 Results and Discussion

5.3.1 Preparation and Characterization of Nanoparticles

VB_{12} was encapsulated upon the formation of SPI nanoparticles induced by calcium as described in Chapter 3. It was shown that VB_{12} was confined in the 3-dimensional network of soy protein mainly via hydrophobic interactions as indicatd in Chapter 4. Non-encapsulated VB_{12} was removed by dialysis (cut-off 2 kDa) against deionized water at 4 ^{o}C for 4 days. After dialysis, particles with

similar surface charge of around -17 mV and different diameters of approximately 30, 100 and 180 nm were obtained as determined by Zetasizer (Table 5-1), which were coded as SPI-NP-1, SPI-NP-2 and SPI-NP-3, respectively. The impacts of particle size on VB_{12} loading capacity and efficiency were also summarized in Table 5-1. The loading capacity and efficiency significantly elevated when particle size increased from 30 to 100 nm ($p < 0.01$), however, they stayed almost at the same amount when particle size increased from 100 to 180 nm ($p > 0.05$). For example, the loading efficiency was 10.28 ± 0.02% in SPI-NP-1, whereas it increased to 13.05 ± 0.06% in SPI-NP-2 and 13.47 ± 0.02% in SPI-NP-3.

Table 5-1. Characterization of VB_{12}-loaded SPI nanoparticles.

Sample	Code	Size (nm)	PDI	Zeta-potential (mV)	Loading capacity (%)	Loading efficiency (%)
SPI nanoparticles	SPI-NP-1	30 ± 1^{a}	0.27 ± 0.02	-17.9 ± 0.7^{a}	0.021 ± 0.002^{a}	10.28 ± 0.02^{a}
	SPI-NP-2	99 ± 4^{b}	0.29 ± 0.03	-17.2 ± 0.2^{a}	0.026 ± 0.006^{b}	13.05 ± 0.06^{b}
	SPI-NP-3	181 ± 3^{c}	0.31 ± 0.04	-16.3 ± 0.2^{a}	0.030 ± 0.002^{b}	13.47 ± 0.02^{b}

$^{a\,b\,c}$ means significant difference at $^{**}p<0.01$; PDI means polydispersity index.

Table 5-2. Characterization of chitosan and alginate modified VB_{12}-loaded SPI nanoparticles.

Sample	Code	Size (nm)	PDI	Zeta-potential (mV)
SPI nanoparticles	SPI-NP-2	100 ± 4^{a}	0.31 ± 0.04	-17.23 ± 0.21
Chitosan modified SPI nanoparticles	CS-SPI-NP-2	101 ± 7^{a}	0.35 ± 0.06	21.90 ± 1.00
Alginate/chitosan modified SPI nanoparticles	AL-CS-SPI-NP-2	104 ± 8^{a}	0.42 ± 0.10	-39.90 ± 2.40

$^{a\,b\,c}$ means significant difference at $^{**}p<0.01$; PDI means polydispersity index.

In order to obtain nanoparticles with different surface charge, but the same size, positively charged chitosan and negatively charged alginate were used to modify SPI-NP-2 nanoparticle surface (Bagre, et al., 2013; Li, et al., 2008). SPI-NP-2 nanoparticle was selected because of its higher cellular uptake efficiency compared with SPI-NP-1 and SPI-NP-3 nanoparticles, as indicated in Section *5.3.4.2*. Positively charged nanoparticles were prepared by quickly introducing freshly prepared SPI-NP-2 nanoparticles into chitosan solution (0.2 % in HAC) at different ratios. When the ratio of SPI-NP-2 nanoparticles to chitosan solution came to 9:1 (v/v), CS-SPI-NP-2 nanoparticles were obtained with positive surface charge of 22 mV while still maintaining the original size of around 100 nm (Table 5-2). Afterwards, alginate coating was applied over the surface of CS-SPI-NP-2 nanoparticles by quickly introducing 1% alginate sodium solution (w/v, pH 9) into the freshly prepared CS-SPI-NP-2 suspension at different ratios. The negatively charged AL-CS-SPI-NP-2 nanoparticles (-44 mV) with a similar size range as the original CS-SPI-NP-2 nanoparticles were successfully produced, when their ratio was 1:1 (Table 5-2).

The TEM images of VB_{12}-loaded nanoparticles after dialysis and surface modification were shown in Figure 5-1. The images demonstrated that all the nanoparticles had a spherical shape, smooth surface and uniform size distribution. The mean size of the nanoparticles can be calculated based on their diameter in the TEM images (Akbari, et al., 2011), and that was smaller than those analyzed by DLS analyzer in Tables 5-1 and 5-2. The SPI-NP-2 nanoparticle, for example, had a

mean size around 70 nm in Figure 5-1 (B); its mean size was around 100 nm measured by DSL in Table 5-1. The smaller size observed by TEM imaging was due to the shrinkage of the nanoparticles during air drying prior to TEM observation (Pan, et al., 2007; Xing, et al., 2010).

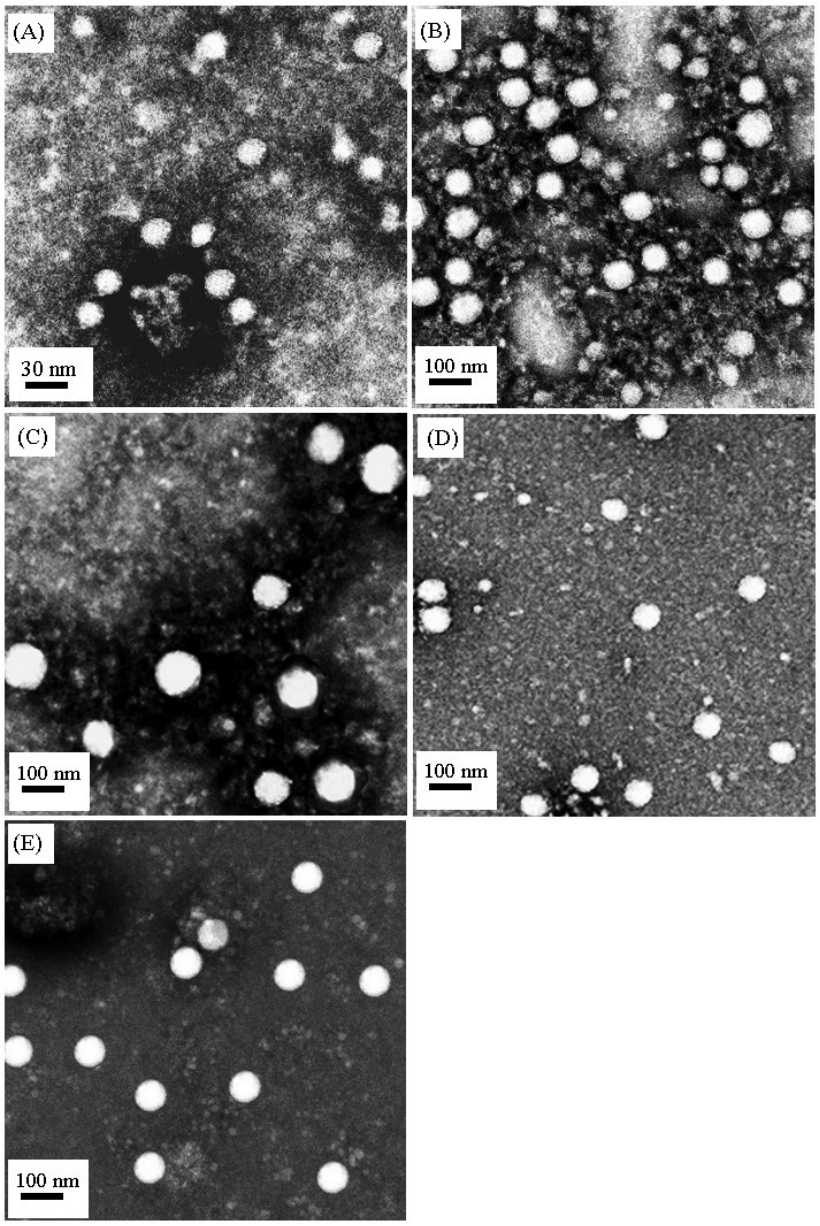

Figure 5-1. TEM images of VB_{12} loaded SPI nanoparticles of (A) SPI-NP-1, (B) SPI-NP-2, (C) SPI-NP-3, (D) CS-SPI-NP-2 and (E) AL-CS-SPI-NP-2.

5.3.2 *In Vitro* Release Profile of VB_{12}

Particle features, such as size and surface composition, are of great importance in controlling the degradation of nanoparticles and release of encapsulated compounds (Dunne, et al., 2000; Panyam, et al., 2003). In the present study, the effects of these parameters on VB_{12} release in simulated GI fluids were evaluated. The results were displayed in Figure 5-2.

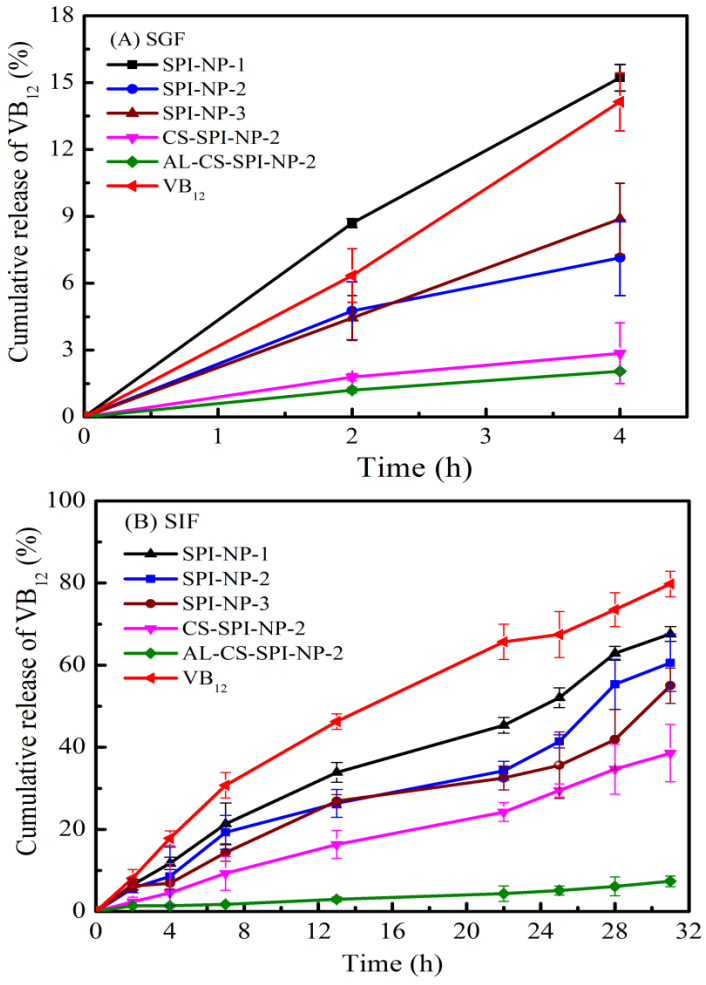

Figure 5-2. The impacts of particle size and surface charge on the diffusion of VB_{12} from dialysis tubing at (A) pH 1.2 with 0.1% pepsin (SGF) and (B) pH 7.4 with 1000 unit/ml trypsin (SIF) at 37 °C.

In SGF, SPI nanoparticles displayed a slower VB_{12} diffusion from the dialysis tubing (cut-off, 2 kDa), except SPI-NP-1 (Figure 5-2 (A)). At 4 h, it was observed that around 14% VB_{12} diffused out of the dialysis tubing. The pore size of dialysis tubing is 2 kDa, which is slightly higher than the molecular weight of VB_{12} (1.3 kDa), and thus leading to a slow diffusion of VB_{12} in 4 h. VB_{12} release was remarkably slowed down by applying chitosan/alginate coatings (Figure 5-2 (A)). At 4 h, the release of VB_{12} decreased from 7.1 ± 1.7% (SPI-NP-2) to 2.9 ± 1.4% (CS-SPI-NP-2) and 2.0 ± 0.1% (AL-CS-SPI-NP-2). Diffusion and matrix degradation are two important mechanisms contributing to the release of encapsulated compounds from food protein matrices (Chen, et al., 2010). It is well-known that pepsin cleaves the peptide bonds between hydrophobic amino acids including phenylalanine (Phe), tryptophan (Trp) and tyrosine (Tyr) (Lien, et al., 2012). The content of Phe, Trp and Tyr in the SPI sample used in this study is 5.2, 1.1 and 3.8 g/100g protein, respectively. During SPI nanoparticle preparation, Ca^{2+} was added to shield the negative charges on polypeptide chains and then to facilitate their association so as to form nanoparticles. During these processes, some of the hydrophobic groups were buried inside SPI nanoparticles as indicated in Chapter 3. Consequently, pepsin could not access these peptides bonds to break down nanoparticles and thus leading to a slower release after nanoencapsulation. As chitosan and alginate are resistant to pepsin digestion (Li, et al., 2007; Teng, et al., 2013), they acted as barriers to the diffusion of VB_{12}, thus leading to a slower release from CS-SPI-NP-2 and Al-CS-SPI-NP-2 than that from SPI-NP-2 (Figure

5-2 (A)). The faster VB_{12} release from CS-SPI-NP-2, compared with AL-CS-SPI-NP-2, was probably due to the higher solubility of chitosan at pH 1.2 (George & Abraham, 2006). In addition, the strong electrostatic interactions between chitosan and alginate would slow down VB_{12} diffusion across nanomatrices, thus resulting in an obviously reduced release in AL-CS-SPI-NP-2 nanoparticles (Bagre, et al., 2013).

In SIF, the release profiles of VB_{12} in the medium of 0.01 M PBS, pH 7.4 with 1000 unit/ml trypsin were displayed in Figure 5-2 (B). All the particles demonstrated a slower release in contrast to VB_{12} alone. At 31 h, 68 ± 2%, 61 ± 7% and 55 ± 4% VB_{12} were released from SPI-NP-1, SPI-NP-2 and SPI-NP-3 nanoparticles respectively, in contrast to 80 ± 8% VB_{12} itself diffusion from the dialysis tubing. Smaller-sized SPI nanoparticles demonstrated a moderately rapid VB_{12} release in 22-31 h in Figure 5-2 (B), which was possibly due to their larger surface area (per unit mass or volume) for the penetration of release medium and the attack of trypsin (Dunne, et al., 2000; Panyam, et al., 2003; Yin Win & Feng, 2005). Similarly, surface modification with chitosan and chitosan/alginate created a remarkable reduction in VB_{12} release. It decreased from 61 ± 7% in SPI-NP-2 to 39 ± 7% in CS-SPI-NP-2 and 7 ± 1% in AL-CS-SPI-NP-2. Trypsin is known to cleave peptide bonds mainly at the carboxyl site of basic amino acids lysine (Lys) or arginine (Arg), except when either is followed by proline (Pro) (Lien, et al., 2012). The content of Lys and Arg in the SPI sample used in the present study is 7.5 and 6.3 g/100g protein, respectively. In this case, trypsin could break down

SPI nanoparticles leading to the liberation of VB_{12}. However, the presence of Pro in SPI nanoparticles (5.2 g/100g protein) would probably prevent the action of trypsin to some degree. This thus led to a lesser VB_{12} release after nanoencapsulation. In addition, some of trypsin cleaving sites on SPI nanoparticles were masked by surface coatings of chitosan and alginate, thus leading to a slower release after surface modification.

To sum up, in SGF, SPI-NP-2 and SPI-NP-3 slowed down the release of VB_{12}, thus they can preserve VB_{12} to certain extent. In SIF, a slower release of VB_{12} was observed for all three SPI nanoparticles compared to VB_{12} alone. CS- and CS-AL- modified nanoparticles further slowed down the release of VB_{12}.

5.3.3 Cytotoxicity of Nanoparticles

The toxicity of nanoparticles was evaluated by XTT assay, which is more efficient and accurate than the traditional MTT assay, because live cells reduce XTT to form a water-soluble formazan product and eliminate the need for a solubilization step in MTT assay (Lien, et al., 2012; Meshulam, et al., 1995). During the assay, the yellow tetrazolium salt XTT is reduced to a highly colored formazan dye by mitochondrial dehydrogenase in metabolically active cells (Meshulam, et al., 1995). This conversion only happens in the living cells, because the intact mitochondrial membrane and cell membrane has active dehydrogenase and these enzymes are inactivated shortly after cell death. Therefore, the

amount/intensity of the formazan produced is proportional to the number of viable cells (Meshulam, et al., 1995; Scudiero, et al., 1988).

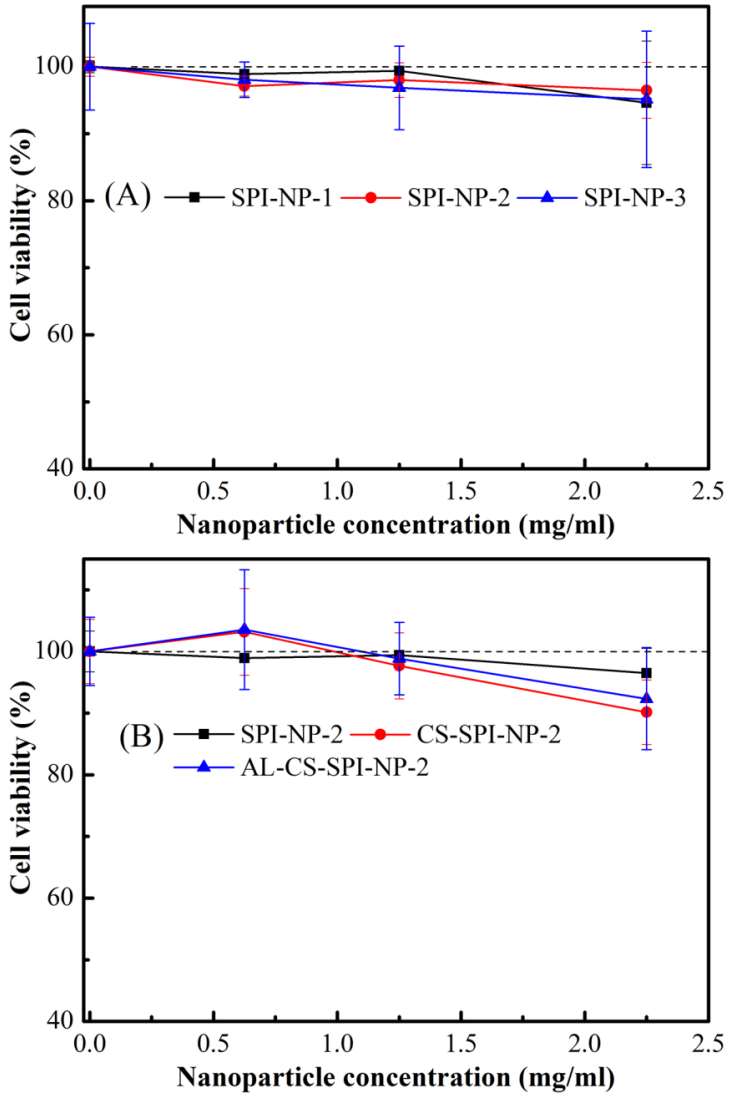

Figure 5-3. The impacts of nanoparticles (A) size and (B) surface charge on Caco-2 cell viability in 6 h at 37 °C, analyzed by XTT assay.

The influence of nanoparticles at various concentrations on cell viability was evaluated by incubating nanoparticles with Caco-2 cells at 37 °C for 6 h before

performing the XTT assay (Figure 5-3). It showed that the cell viability was over 90%, even at a high particle concentration (2.25 mg/ml), indicating that all the nanoparticles had low cytotoxicity on Caco-2 cells at these conditions. The number of living cells was also recorded before and after nanoparticle treatment. The results revealed that nanoparticle treatment did not induce a significant change of living cell number, compared with the cells without particle treatment ($p > 0.05$, data not shown). This high cell viability could be attributed to the hydrophilic nature and good biocompatibility of SPI, giving SPI nanoparticles good potential to be used in food or pharmaceutical industries. Alternative cytotoxicity evaluation can be performed in the future, in order to monitor the effects that SPI nanoparticles may have on biological tissues. For instance, oxidative stress in cells can be measured by glutathione assay and thiobarbituric acid assay (Lewinski, et al., 2008); cell membrane integrity can be detected using trypan blue-light microscopy examination and lactate dehydrogenase assay (Han, et al., 2011).

5.3.4 *In Vitro* Cellular Uptake Profiles

The Caco-2 cell line derived from human colon adenocarcinoma experiences enterocyte differentiation into the polarized absorptive cell monolayers in culture. Confluent Caco-2 cell monolayers form tight junctions and electrical properties that are similar to those of intestinal epithelium (Hidalgo, et al., 1989). This cell line, therefore, has been widely applied as a representative *in vitro* model for evaluating the uptake and transport of nanoparticles across the small intestinal

epithelium and for determining the underlying mechanism responsible for drug delivery (He, et al., 2010; Yin Win & Feng, 2005). Nanoparticles can theoretically cross the intestinal epithelium using a paracellular pathway from tight junctions and a transcellular pathway from epithelial cell membrane (des Rieux, et al., 2006). The transport efficiency of nanoparticles via a paracellular pathway is quite low. It is seriously limited by the surface area of tight junctions (< 1% of mucosal surface area) and the tightness of the junctions (pore diameter < 1 nm) (Jung, et al., 2000). The transcellular pathway is the most promising route for the transcytosis of nanoparticles considering the abundant surface membrane area. The multiple endocytic pathways could potentially participate in the uptake of nanoparticles. This pathway thus has been the most explored. The uptake of nanoparticles by enterocytes is the first step of the transcellular pathway.

5.3.4.1 Cellular Distribution of Nanoparticles

Confocal laser scanning microscopy (CLSM) was used to study the association of nanoparticles with Caco-2 cells. SPI was labeled with green dye COUM-6 after the heating treatment, but before the formation of nanoparticles, the labeling ratio of COUM-6 to SPI was $(0.75 \pm 0.06) \times 10^{-4}$ (w/w). The bio-distribution of COUM-6 labeled nanoparticles was observed under CLSM (Figure 5-4 (B)-(F)) and COUM-6 itself was used as a negative control (Figure 5-4 (A)). No green fluorescent signal was detected after the COUM-6 treatment indicating that this dye alone could not be internalized by Caco-2 cells in 6 h (Yin et

al., 2005). Nevertheless, strong green signals were observed at the periphery of cell nuclei after being incubated with nanoparticles (Figure 5-4 (B)-(F)). Moreover, the brighter green signals were observed with the treatment of SPI-NP-2 and CS-SPI-NP-2 nanoparticles, whereas the darker signals were observed with the treatment of SPI-NP-3 and AL-CS-SPI-NP-2 nanoparticles. It hinted that particle size and surface charge played an important role in the association of SPI nanoparticles with Caco-2 cells.

In order to further locate nanoparticles, the cell membrane was stained with WGA-Alex Fluor® 555 conjugate prior to CLSM observation. Then three-dimensional analysis of the optical sections (z-axis) of the cell monolayer was performed to localize the distribution of nanoparticles (Figure 5-5). It demonstrated that most of nanoparticles were distributed in the cytoplasm; and only a few of them were associated with the cell membrane. No nanoparticles were detected inside of the cell nuclei, which is beneficial for avoiding genetic mutations. The extranuclear localization of nanoparticles could also explain their relative safety as indicated by XTT assay.

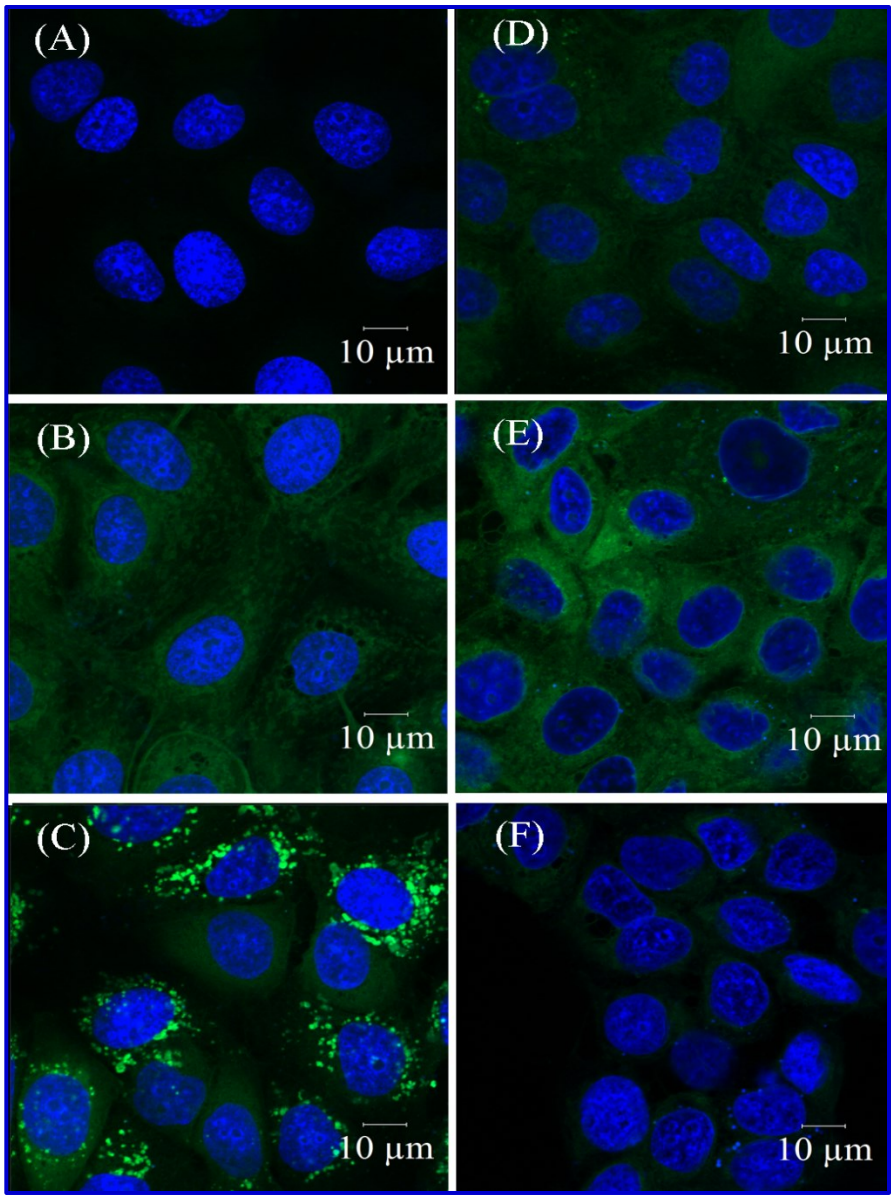

Figure 5-4. CLSM images of Caco-2 cells after incubation with (A) COUM-6, COUM-6 labeled SPI nanoparticles (B) SPI-NP-1, (C) SPI-NP-2, (D) SPI-NP-3, (E) CS-SPI-NP-2 and (F) AL-CS-SPI-NP-2 at 37 °C for 6 h. Nanoparticles were labeled with COUM-6 (green), and cell nuclei were stained with DAPI (blue).

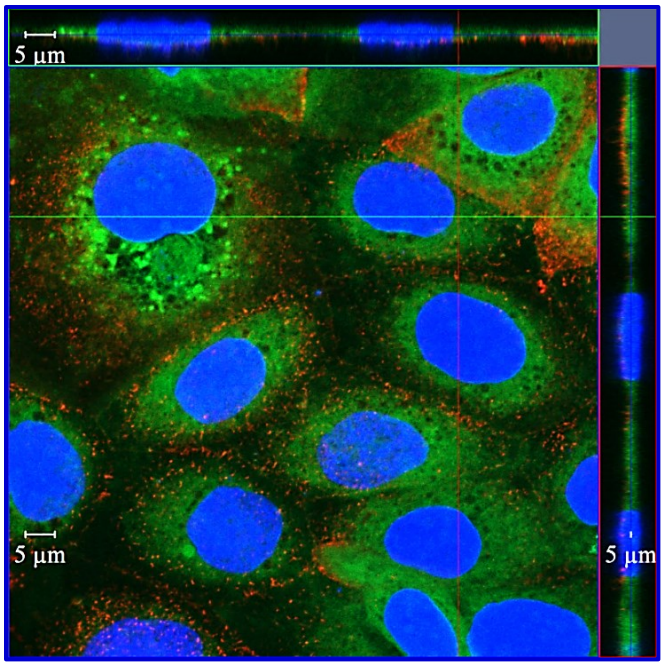

Figure 5-5. Localization of SPI nanoparticles within Caco-2 cells after incubation with CS-SPI-NP-2 nanoparticles at SPI particle concentration of 1.25 µg/ml, 37 ^{o}C for 4 h. Green: nanoparticles; blue: cell nuclei; red: cell membrane stained with WGA-Alex Fluor® 555 conjugate.

5.3.4.2 Effect of Nanoparticle Size and Surface Charge

The cellular uptake of nanoparticles discussed above includes two parts: firstly, the nanoparticles attach onto the cell surface and second, they become internalized inside of Caco-2 cells. The three-dimensional CLSM images in Figure 5-5 demonstrated that most nanoparticles were internalized into Caco-2 cells and only a few of them were attached onto the surface of the cell membrane. Physicochemical properties, such as particle size and surface charge, played a key function in the uptake of nanoparticles (He, et al., 2010). In this study, SPI was stained firstly with

COUM-6 before manufacturing the nanoparticles with varying size and surface charge. The impacts of these parameters on SPI nanoparticles uptake efficiency by Caco-2 cells were evaluated in Figure 5-6.

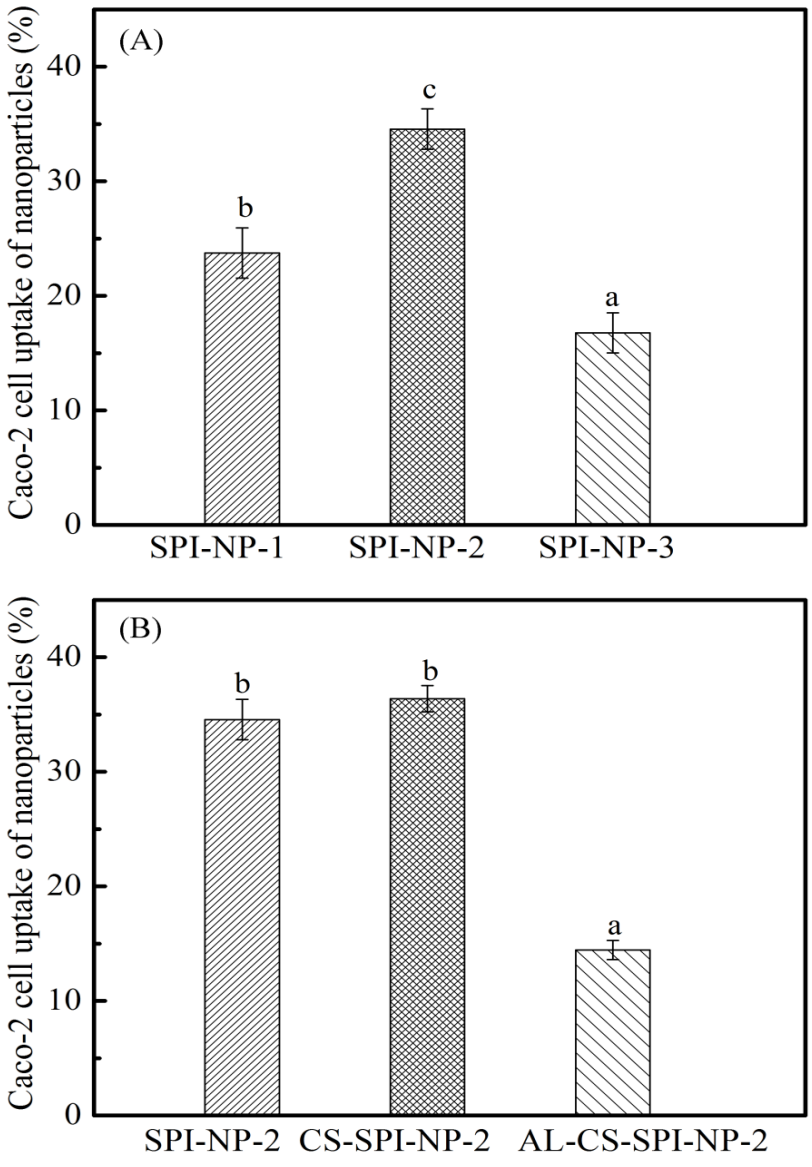

Figure 5-6. Effect of (A) particle size and (B) surface charge on cellular uptake efficiency of SPI nanoparticles by Caco-2 cells in 4 h at 37 ^{o}C. Each sample contained 1.25 mg/ml SPI nanoparticles. Significant difference was expressed as ^{a,b,c} at $p < 0.05$.

It was observed that the uptake efficiency of SPI nanoparticles by Caco-2 cells was size-dependent, in general, when their surface charge was fixed at -17 mV (Figure 5-6 (A)). Their uptake efficiency was in the order of 100 nm (SPI-NP-2) > 30 nm (SPI-NP-1) >180 nm (SPI-NP-3). One relevant study also indicated that 100 nm nanoparticles had a greater uptake efficiency than that of 50, 200, 500 and 1000 nm particles (Yin Win & Feng, 2005). Nanoparticles with larger size needed stronger driving forces and additional energy in the cellular internalization process (He, et al., 2010). Therefore, cellular uptake of SPI nanoparticles significantly decreased from 100 to 180 nm. The significant reduction in cellular uptake of particles from 100 to 30 nm (p<0.01) may, however, be due to the different pathways of nanoparticles being accumulated into the cells (Couvreur & Puisieux, 1993; Huang, Ma, Khor, & Lim, 2002). Besides, nanoparticles of less than 50 nm could directly pass through paracellular spaces instead of being internalized through cell membranes (Yin Win & Feng, 2005). Consequently, fewer nanoparticles were accumulated inside Caco-2 cells, resulting in the lower uptake efficiency of 30 nm nanoparticles. Their transport pathways were to be investigated in the next study.

The cellular uptake efficiency of nanoparticles with both positive and negative surface charges was studied, with their size fixed at 100 nm. A similar uptake efficiency of SPI nanoparticles was observed after surface modification with chitosan (CS-SPI-NP-2) (Figure 5-6 (B)). The uptake of CS-SPI-NP-2 nanoparticles may be due to the electrostatic interactions between the

positively-charged nanoparticles and the negatively-charged Caco-2 cell membrane (Behrens, et al., 2002). Normally, the positively charged nanoparticles demonstrated a higher cellular uptake than that of neutral or negatively charged nanoparticles (Danhier, et al., 2012; Foged, et al., 2005). However, the comparable uptake efficiency of SPI-NP-2 and CS-SPI-NP-2 nanoparticles observed in this study suggested that SPI nanoparticles alone had some advantages, such as unique surface composition and a hydrophilic/hydrophobic balance, which may contribute to their efficient uptake (Nam, et al., 2009). The high uptake efficiency of negatively charged SPI nanoparticles may be caused by certain peptides from proteins that activated the uptake mechanisms in Caco-2 cells (Luo, et al., 2013). Besides, the surface carboxyl groups on nanoparticles have been reported to play a vital role in the cell internalization of particles (Dausend, et al., 2008; He, et al., 2010; Luo, et al., 2013). Since the chitosan-based or chitosan modified nanoparticles were the effective carriers for various drugs or macromolecules, due to its mucoadhesion and absorption enhancement properties (Behrens, et al., 2002; Issa, et al., 2005; Rajaonarivony, et al., 1993; Sarmento, et al., 2007), the similar uptake efficiency of SPI-NP-2 nanoparticles as CS-SPI-NP-2 nanoparticles suggested that SPI nanoparticles would probably be a promising and effective carrier as well. Besides, the negatively charged particles are more beneficial for drug/nutraceutical delivery compared with the positively charged ones. Because positively charged particles could interact with cell membranes and serum

proteins strongly and thus leading to toxic and immunogenic problems (Bajaj, et al., 2009).

In contrast, alginate/chitosan modified nanoparticles (AL-CS-SPI-NP-2) had the lowest uptake efficiency (Figure 5-6 (B)), compared with CS-SPI-NP-2 and SPI-NP-2 nanoparticles. It was caused by the strong repulsion forces between negatively charged AL-CS-SPI-NP-2 nanoparticles and negatively charged apical membranes of Caco-2 cells. This energy barrier would consequently prevent AL-CS-SPI-NP-2 nanoparticles from approaching and adhering to cells, hence resulting in the lowest uptake efficiency (He, et al., 2010).

In order to further confirm the impacts of particle size and surface charge on their uptake efficiency, the Flow cytometry was used to record the fluorescence intensity of nanoparticles inside the Caco-2 cells. The nanoparticles were incubated with Caco-2 cells for 4 h, the unbound nanoparticles were washed 3 times using HBSS buffer. The cells were then trypsinized, centrifuged and washed 3 times to further remove the surface attached nanoparticles. Then the Caco-2 cells were re-suspended with FCS buffer for Flow cytometry measurement. The relative fluorescence intensity of nanoparticles with varying particle size and surface charge inside Caco-2 cells was shown in Figure 5-7 (A) and (B), respectively. The fluorescence intensity increased as the FL I-H peak shifted from left to right and vice versa. Accordingly, the fluorescence intensity increased in the order of SPI-NP-2 > SPI-NP-1> SPI-NP-3 and CS-SPI-NP-2 > SPI-NP-2> AL-CS-SPI-NP-2. It further confirmed that internalization of nanoparticles was

size and surface-charge dependent. Additionally, 100% of the Caco-2 cells were involved in the uptake of nanoparticles after 4 h as their FL I-H spectra were away from 10^1 in Figure 5-7.

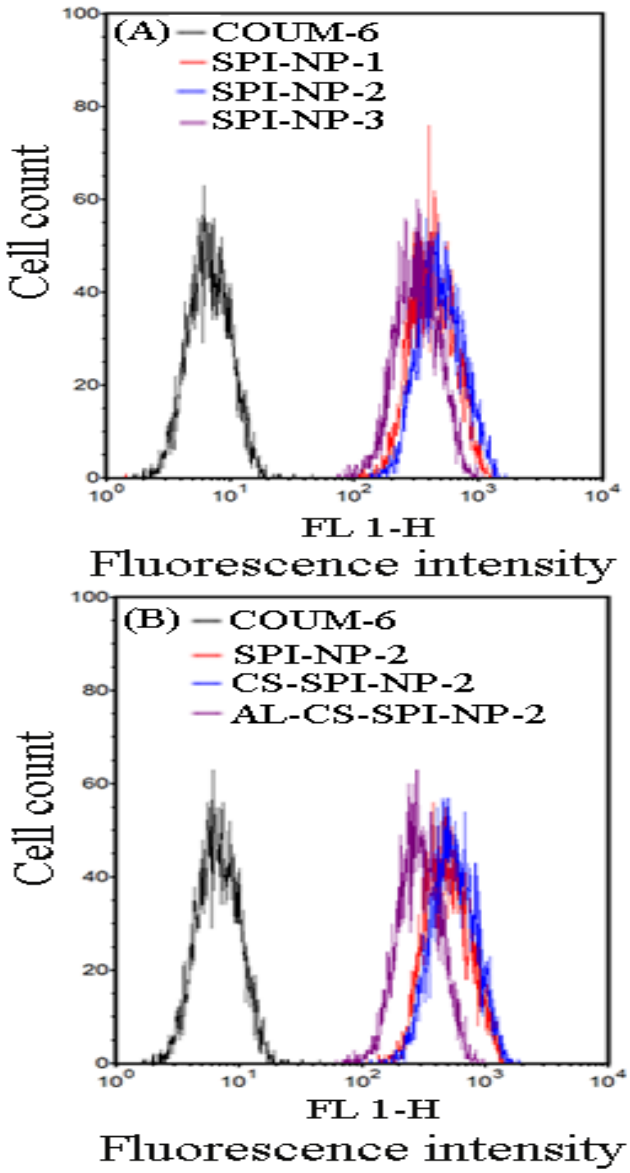

Figure 5-7. Fluorescence intensity of COUM-6 and COUM-6 labelled SPI nanoparticles in Caco-2 cells. The fluorescence intensity of COUM-6 was excited at the wavelength of 488 nm and the emission was collected in the 515-545 nm signal range (FL1-H).

The effects of temperature, time and particle concentration on nanoparticle association with cells would provide information on cellular uptake pathways by which nanoparticles enter into cells (Yin Win & Feng, 2005). These parameters were studied next.

5.3.4.3 Effect of Temperature

A temperature block was carried out at 4 °C where the metabolic activity of the cells and the fluidity of cell membrane are reduced, leading to restriction of the energy-dependent transcellular processes (He, et al., 2010; Liu, et al., 2010). Consequently, the amount of cell-associated nanoparticles at 4 °C would be attributed to the physical adhesion and the passive diffusion of nanoparticles (Jiang, et al., 2013).

There was a significant decrease in the uptake of nanoparticles by Caco-2 cells at 4 °C ($p < 0.001$), with the uptake being reduced to 8.8-21.4% of that seen at 37 °C (control, Figure 5-8). These results suggested that an energy-dependent endocytic process could be responsible for up to 78.6-91.2% of the uptake of nanoparticles. Physical adhesion and passive diffusion probably were responsible for the remaining uptake of nanoparticles (Jiang, et al., 2013). The percentage of nanoparticles physically adhering to the Caco-2 cell membrane would be less than 8.8-21.4%, after the deduction of the portion of nanoparticles being diffusing into the Caco-2 cells. It again suggested that most of the nanoparticles were

accumulated inside the Caco-2 cells, which was in good agreement with the findings in Figure 5-5.

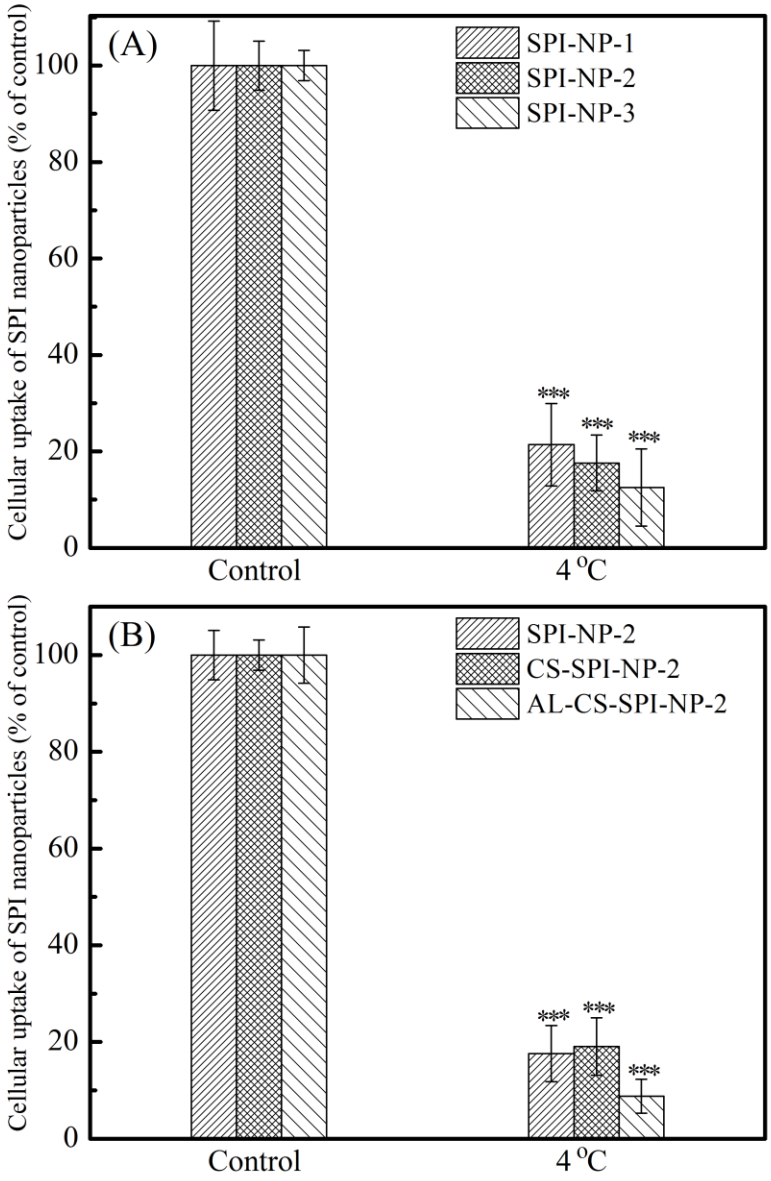

Figure 5-8. The effects of the temperature block at 4 °C on Caco-2 cell uptake efficiency of SPI nanoparticles with different (A) size and (B) surface charge. Nanoparticles containing 1.25 mg/ml SPI were incubated with Caco-2 cells for 4 h at 37 °C (control) and 4 °C. *** means the significant difference at $p < 0.001$ in comparasion to the corresponding control.

5.3.4.4 Effect of Incubation Time and Particle Concentration

It was noticed that cellular association with nanoparticles increased gradually during the first 4 h and then became saturable beyond 4 h, as the curves showed a the plateau effect (Figure 5-9). It suggested that the uptake of nanoparticles was a saturation process. The combination of linear uptake (< 4 h) and saturable uptake (> 4 h) hinted that the cellular uptake of SPI nanoparticles was accomplished by the processes of macropinocytosis and receptor-mediated endocytosis, respectively (Catizone, et al., 1993; Panyam, et al., 2003).

Moreover, the cellular uptake efficiency of SPI nanoparticles was relatively high in comparison with the most widely applied poly(lactic-co-glycolic) acid (PLGA) nanoparticles, which were negatively charged (Yin Win & Feng, 2005). After incubation nanoparticles of 100 nm with Caco-2 cells for 2 h at 37 °C, the cellular uptake efficiency of PLGA nanoparticles was 17% (Yin Win & Feng, 2005), while that of SPI-NP-2 nanoparticles was 23% (Figure 5-9). It again indicated that SPI nanoparticles would be a promising carrier for poorly absorbed compounds to cross the intestinal epithelial barrier. The data in Figure 5-9 also showed the uptake of nanoparticles was in the increasing order of SPI-NP-2 > SPI-NP-1 > SPI-NP-3 and CS-SPI-NP-2 ≥ SPI-NP-2 > AL-CS-SPI-NP-2 during the same time interval, which again confirmed that their uptake was size and surface charge dependent.

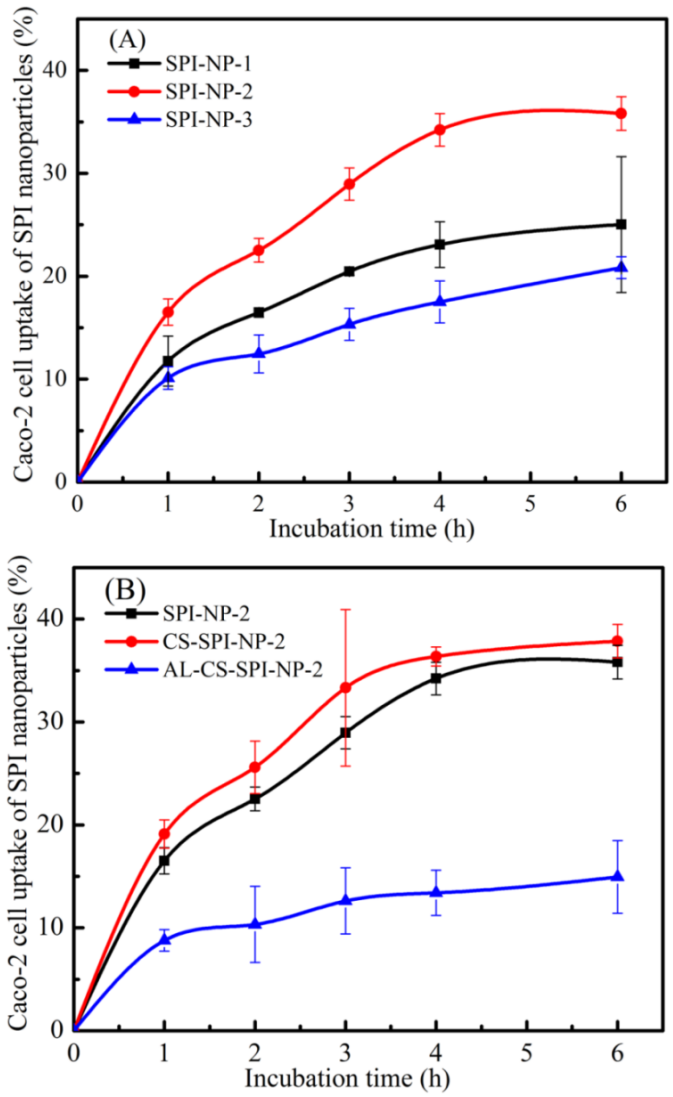

Figure 5-9. Time courses for Caco-2 cellular uptake efficiency of SPI nanoparticles with different (A) size and (B) surface charge at the concentration of 1.25 mg/ml at 37 ^{o}C.

The association of nanoparticles with Caco-2 cells versus the concentrations of nanoparticles was shown in Figure 5-10. It was a concentration dependent process and the saturation was reached at 1.75 mg/ml. The amount of SPI

nanoparticles associated with Caco-2 cells increased with particle concentration from 0 to 1.75 mg/ml, however, only a marginal increase was observed when the concentration was increased from 1.75 to 2.25 mg/ml. It again suggested that the cellular uptake of the nanoparticles was in part through macropinocytosis and in part through receptor-mediated endocytosis (Catizone, et al., 1993; Panyam, et al., 2003). At each concentration point, the order of cellular uptake of nanoparticles was SPI-NP-2 > SPI-NP-1 > SPI-NP-3 and CS-SPI-NP-2 ≥ SPI-NP-2> AL-CS-SPI-NP-2.

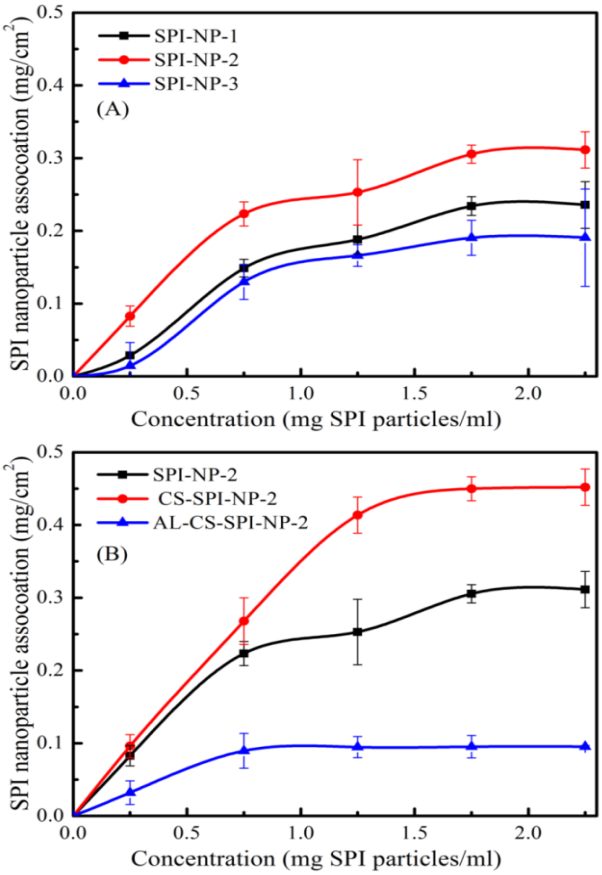

Figure 5-10. The effect of nanoparticles concentration on their cellular association, nanoparticles with (A) different size and (B) surface charge were incubated with Caco-2 cells for 6 h at 37 ^{o}C.

5.3.4.5 Effect of Metabolic Inhibitor

NaN_3 is a metabolic inhibitor, which blocks the production of ATP in cells and inhibits the endocytosis of nanoparticles (Bajaj, et al., 2009). The significant decrease of cellular uptake of SPI nanoparticles in the presence of NaN_3 was observed in Figure 5-11. It indicated the uptake of these nanoparticles by Caco-2 cells mainly occurred through energy-dependent endocytosis (He, et al., 2010). In addition, no complete inhibition under the NaN_3 treatment could be possibly explained by the use of glucose in the culture media (Behrens, et al., 2002).

Taken together, the cellular uptake behavior of SPI nanoparticles was saturable, temperature-, time-, concentration-dependent indicating that their uptake mechanisms by Caco-2 cells were dominantly by the energy-dependent endocytosis (Lu, et al., 2005), this is the focus in the following part.

5.3.5 Uptake Mechanism

Understanding the endocytosis process of nanoparticles could allow researchers to bioengineer a highly specialized delivery system so as to achieve optimized uptake efficiency. Energy dependent uptake by enterocytes is divided into: clathrin-mediated endocytosis, caveolae-mediated endocytosis, clathrin-/caveolae-independent endocytosis, and macropinocytosis (Beloqui, et al., 2013; Chung, et al., 2012; des Rieux, et al., 2006; Desai, et al., 1996). By clathrin-mediated endocytosis, the cargo is packaged into vesicles from

invagination of the cell membrane with the assistance of the triskelion protein clathrin (Bareford & Swaan, 2007; McMahon & Boucrot, 2011). The clathrin coated pits are around 120 nm in diameter (Conner & Schmid, 2003) and occupy 1-2% of membrane surface area and only last for 1 min (Bareford & Swaan, 2007). Clathrin-mediated endocytosis leads to an intracellular pathway in which endosomes fuse with lysosomes, which degrade their contents. Caveolae are flask-shaped invaginations with a diameter of 50-100 nm, covering more than 10% of the endothelial cell membrane (Bareford & Swaan, 2007). Caveolae-mediated endocytosis avoids the lysosomal degradation and thus it is the most promising pathway for transporting of some sensitive compounds across the intestinal barrier (del Pozo-Rodriguez, et al., 2009). Macropinocytosis is the invagination of highly ruffled regions of cell membrane to form a pocket, which pinches off into the cell to form a vesicle (500-5000 nm in diameter) filled with a large volume of extracellular fluid and molecules/particles within it (Sahay, et al., 2010). The filling of the pocket occurs in a non-specific manner induced by electrostatic and hydrophobic interactions, etc. (Bareford & Swaan, 2007).

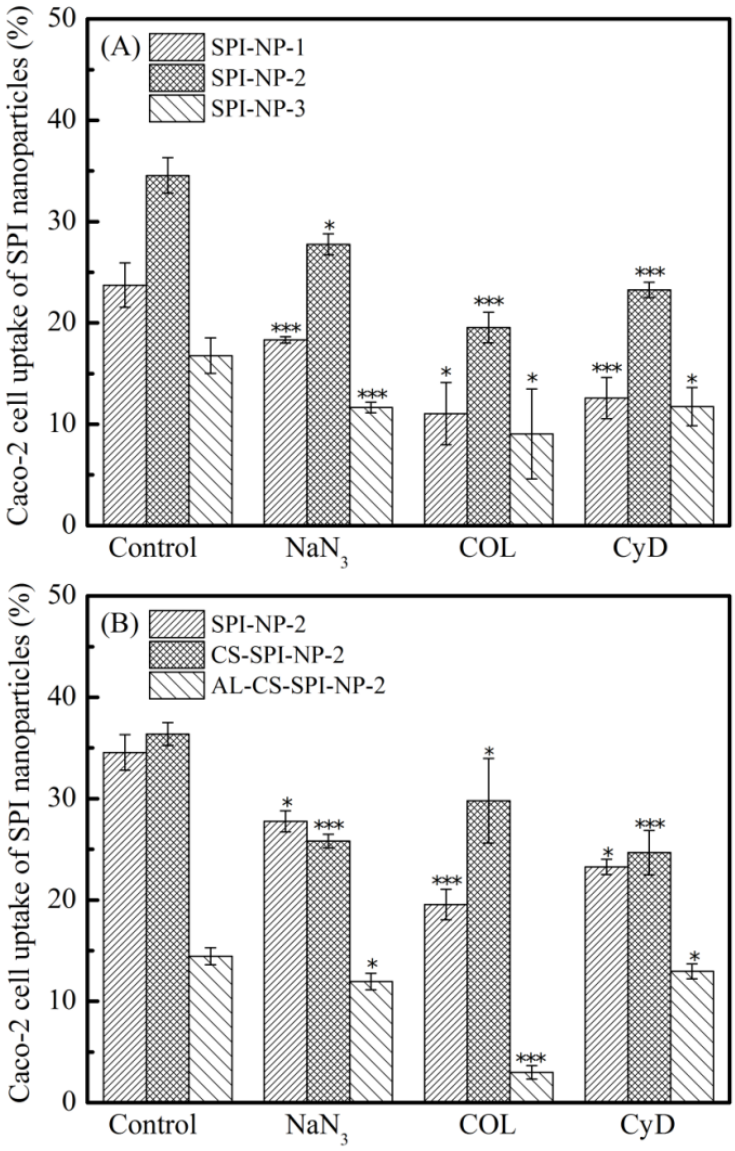

Figure 5-11. The effects of inhibitors on Caco-2 cell uptake efficiency of SPI nanoparticles with different (A) size and (B) surface charge. *: $p < 0.05$; **: $p < 0.01$; ***: $p < 0.001$ (compared to the control of each type).

Exclusion of specific endocytosis mechanisms by endocytosis inhibitors is a powerful technique to interpret the internalization mechanism of nanoparticles.

Two endocytic inhibitors including COL and CyD were pre-incubated with Caco-2 cells for 30 min. COL, an inhibitor of caveolae-mediated and/or clathrin-mediated endocytosis, inhibits actin polymerization and rearrangement for the formation and invagination of coated pits and caveosomes (He, et al., 2010). The presence of COL caused a remarkable decrease in cellular uptake of SPI nanoparticles as shown in Figure 5-11 (A). It suggested the clathrin- and/or caveolae-mediated endocytosis was involved in the cellular uptake of SPI nanoparticles. CyD is an inhibitor of macropinocytosis/phagocytosis and acts by blocking the actin polymerization (Lien, et al., 2012). Caco-2 cells are considered to be non-phagocytic cells (Harley, et al., 1997). Therefore, the inhibition of cellular uptake by CyD only reflects the block of macropinocytosis. Indeed, the addition of CyD caused a significant decrease in the uptake of SPI nanoparticles (Figure 5-11 (A)) suggesting cellular association with nanoparticles was regulated by macropinocytosis as well. No remarkable differences were noticed in the uptake pathways of nanoparticles with a diameter of 30-180 nm. As all SPI nanoparticles were produced using the same materials, their uniform uptake pathways may hint that the size of particles in this range may play a much lesser role in determining their entry route than the chemical composition of nanomaterials (Sahay, et al., 2010).

In addition to particle size, other physicochemical properties of surface charge and composition may play a role in controlling cellular entry of nanoparticles. Caco-2 cells pre-incubated with CyD and COL led respectively to 25% and 32% cellular uptake of CS-SPI-NP-2 nanoparticles. It demonstrated that

macropinocytosis probably played a more important role in the internalization of CS-SPI-NP-2 nanoparticles than the clathrin-/caveolae-dependent pathways. This finding was in accordance with a previous result that showed the entry of chitosan nanoparticles to Caco-2 cells occurred predominantly by adsorptive endocytosis (macropinocytosis), through the non-specific interactions between nanoparticles and cell membranes and in part by a clathrin-mediated process (Davda & Labhasetwar, 2002; Huang, et al., 2002). Still 43% of the CS-SPI-NP-2 nanoparticles were taken up by Caco-2 cells even after the removal of the inhibition produced by both CyD (25%) and COL (32%). This indicated that the endocytosis of CS-SPI-NP-2 nanoparticles was predominantly regulated by clathrin-/caveolae-independent pathways. As indicated above, the uptake of SPI-NP-2 nanoparticles was controlled by macropinocytosis and the clathrin- and/or caveolae-dependent pathways. It reflected that chitosan modification altered the cellular entry of nanoparticles, which was observed in other particles as well (Wang, et al., 2013). For example, surface modification of PLGA nanoparticles with chitosan converted their internalization from a caveolae-mediated pathway to macropincytosis and clathrin-mediated endocytosis by MDCK cells (Wang, et al., 2013). Evidently, multiple uptake pathways have been documented in the cellular uptake of chitosan modified nanoparticles, however, their uptake pathways varied (Davda & Labhasetwar, 2002; Harush-Frenkel, et al., 2007; Nam, et al., 2009; Rappoport, 2008; Sahay, et al., 2010; Wang, et al., 2013).

Similarly, the cellular uptake of AL-CS-SPI-NP-2 nanoparticles significantly decreased upon treatment with Col ($p < 0.001$) and CyD ($p < 0.05$), where 79% reduction was caused by COL, while only 10% reduction was caused by CyD. It suggested that the internalization of AL-CS-SPI-NP-2 nanoparticles by Caco-2 cells was predominantly regulated by clathrin- and/or caveolea-mediated endocytosis pathways and in part by macropinocytosis. However, more specific inhibitors such as flilipin III and chlorpromazine hydrochloride are needed in order to further identify the detailed pathway, which will be applied in the next study.

The multiple endocytosis pathways of SPI nanoparticles together with their high cellular uptake efficiency indicated that SPI nanoparticles have a great potential to improve the intestinal absorption of VB_{12}. Besides, the multiple pathways may allow us to further optimize SPI nanoparticles with preferential targeting sites and improved absorption of the compound encapsulated.

5.4 Conclusions

In this study, SPI nanoparticles of varying size and surface charge were produced by modulating preparation conditions and modifying particle surface. Nanoencapsulation led to a slower VB_{12} diffusion from the dialysis tubing in the SGF and SIF. All the particles exhibited a low cytotoxicity on Caco-2 cells. SPI nanoparticles were effectively internalized by Caco-2 cells into the cytoplasm via multiple endocytosis pathways, including clathrin- and/or caveolae-mediated endocytosis and macropinocytosis. In addition, chitosan and chitosan/alginate

modified particles led to a reduced VB_{12} release in SGF and SIF, compared with SPI particles without surface modification. However, SPI nanoparticles exhibited comparable and higher uptake efficiency, compared with chitosan ($p > 0.05$) and alginate/chitosan ($p < 0.001$) modified particles, respectively. The findings suggested that SPI nanoparticles would be a promising and effective carrier for VB_{12}.

Chapter 6. Impact of Particle Size and Surface Charge on the Transport Properties of Vitamin B_{12}-loaded SPI Nanoparticles and Associated Mechanisms[4]

6.1 Introduction

Nutraceuticals are frequently supplemented in functional foods in order to achieve enhanced health benefits. However, the efficacy of some compounds such as VB_{12} is limited due to the short residence time in GI tract and the poor permeability across the intestinal barriers. Intestinal barriers mainly consist of a mucus layer and a compact epithelial cell lining (Atuma, et al., 2001). Nanoparticles have the potential to adhere to mucus layer by non-specific interactions and pass through this barrier to interact with intestinal epithelia (Lin, et al., 2007; Lin, et al., 2007). Nanoparticles could help nutraceuticals across intestinal epithelial lining, mainly via paracellular and active transcellular routes (des Rieux, et al., 2006). Active transcellular pathways are divided into phagocytosis and pinocytosis. The latter includes macropinocytosis, clathrin-mediated endocytosis, caveolae-mediated endocytosis and clathrin/caveolae independent endocytosis (Beloqui, et al., 2013; Chung, et al.,

[4] A version of this chapter is to be submitted for publication.

2012). The size and surface physicochemical properties of nanoparticles severely affect their transport efficiency (Galindo-Rodriguez, et al., 2005; He, et al., 2010; Perumal, et al., 2008; Yin, et al., 2007).

So far, few studies have been done to improve the oral bioavailability of VB_{12} by using nanoparticle as a carrier. One study recently evaluated the preparation of VB_{12} nanoparticles by ionic gelation of N, N, N-trimethyl chitosan with tripolyphophate anions (de Britto, et al., 2012). Nevertheless, the biological properties of the nanoparticles including cellular uptake, transport and transport mechanisms have not been explored. Though the enhanced permeability of VB_{12} across Caco-2 cell monolayers and rat intestinal barriers was achieved by encapsulating VB_{12} into poly(acrylic acid)-cysteine microparticles using spray drying, the microparticles were made from synthetic polymers making them non-applicable in food products, because of safety concerns (Sarti, et al., 2011). Soy proteins could be one of the candidates for preparing VB_{12} nanoparticles due to their biodegradable, biocompatible, and high-nutritional properties as well as excellent functional properties including gelation, emulsion and foaming capacity (Elzoghby, et al., 2012). Soy protein isolate (SPI) nanoparticles have been produced recently for the encapsulation of vitamin D_3 and curcumin (Teng, 2012, 2013), but not for the encapsulation of VB_{12}.

In this thesis research, the molecular interactions between soy protein and VB_{12} were explored. The findings suggested that VB_{12} was bound into the three-dimensional network of soy protein, where the binding complexes of soy

protein-VB_{12} were formed mainly through hydrophobic interactions as described in Chapter 4. VB_{12}-loaded SPI nanoparticles with various particle sizes and surface charges were prepared in the Chapter 5. The impacts of particle features on the release, cytotoxicity and uptake properties were systematically studied. The results showed that encapsulating VB_{12} in SPI nanoparticles led to a slower release of VB_{12} in simulated GI fluids and higher cellular uptake efficiency, compared with non-encapsulated ones; however, the intestinal absorption properties of VB_{12} after nanoencapsulation have not been evaluated.

The purpose of this study was therefore to investigate the impacts of particle properties on VB_{12} transport efficiency and related mechanism across the small intestinal epithelium, which was simulated by Caco-2 cell monolayer. Paracellular transport was investigated by monitoring the opening of tight junctions between Caco-2 cells. Transcellular transport was investigated by blocking the transcytosis pathways using various inhibitors. Subsequently, the intracellular trafficking and biofate of nanoparticles inside Caco-2 cells were discussed based on their transport mechanisms. Finally, the particle that demonstrated highest VB_{12} transport efficiency was applied on *ex vivo* model to study its intestinal absorption capacity using the Ussing chamber tests.

6.2 Materials and Methods

6.2.1 Materials

SPI PRO-FAM® 646 was kindly provided by Archer Daniels Midland Company (ADM, Decatur, IL, USA). It contained 94.4% protein on a dry basis as determined by combustion with a nitrogen analyzer (Leco Corporation, St. Joseph, MI, USA); it was calibrated with analytical reagent grade EDTA and caffeine using a conversion factor of 6.25. Cobalt reference standard solution, low molecular chitosan and sodium alginate were purchased from Fisher Scientific (Toronto, ON, Canada). Caco-2 cells (HTB®-37™) were purchased from the American Type Culture Collection (ATCC, Manassas, VA, USA). Dimethyl sulfoxide (DMSO), Coumarin 6 (COUM-6), 4', 6-diamidino-2-phenylindole (DAPI), flilipin III (FLI), colchicine (COL), chlorpromazine hydrochloride (CPZ) and cytochalasin D (CyD) were purchased from Sigma-Aldrich (Oakville, ON, Canada). Dulbecco's modified eagle medium (DMEM), fetal bovine serum (FBS), trypsin-EDTA, 4-(2-hydroxyethyl)-1-piperazineethanesulfonic acid (HEPES) and 1% antibiotic-antimycotic were purchased from Invitrogen (Burlington, ON, Canada). All other chemicals were of reagent grade.

6.2.2 Preparation of Nanoparticles

As demonstrated in Chapter 5 (Section 5.2.2.2), SPI nanoparticles of three different sizes 30, 100 and 180 nm were prepared and defined as SPI-NP-1, SPI-NP-2 and SPI-NP-3, respectively. These nanoparticles had a similar average surface charge of -17 mV.

Surface modifications to SPI nanoparticles with chitosan and sodium alginate were performed according to Chapter 5 (Section 5.2.2.3). Two particle systems of SPI-NP-1 and SPI-NP-2 were selected for surface modification because they demonstrated higher cellular uptake efficiency in Chapter 5, compared with SPI-NP-3. The positively charged nanoparticles (22 mV), that were similar in size to the original SPI-NP-1 and SPI-NP-2 nanoparticles, were successfully prepared when the ratio of SPI original nanoparticles to 0.2% chitosan solution came to 9:1 (v/v). These were coded as CS-SPI-NP-1 and CS-SPI-NP-2, respectively. The alginate coating on optimized chitosan nanoparticles was applied by quickly introducing the sodium alginate solution into the CS-SPI-NP-1 and CS-SPI-NP-2 nanoparticles solutions (freshly prepared) at different ratios (Bagre, et al., 2013). The negatively charged nanoparticles (around -40 mV) that were similar in size to the original SPI nanoparticles were successfully generated when their ratio came to 1:1. The alginate modified CS-SPI-NP-1 and CS-SPI-NP-2 nanoparticles were coded as AL-CS-SPI-NP-1 and AL-CS-SPI-NP-2, respectively.

6.2.3 Preparation of Caco-2 Cell Monolayers

Caco-2 cells were seeded in a 75 cm^2 flask at a density of 1×10^6 cells/flask and were then harvested at 80% confluence, with trypsin-EDTA and seeded onto polyester membrane filters (0.45 μm pore size, 1.12 cm^2 growth area) inside Transwell® chambers (Costar, Corning, NY, USA) at a density of 1×10^5 cells/insert. The culture medium (0.5 ml per insert and 1.5 ml per well) was replaced every other day. Cells were allowed to grow and differentiate for 21 days in 12-transwell plates. The integrity of the monolayers was monitored by measuring the transepithelial electrical resistance (TEER) values in an HBSS buffer using an epithelial tissue voltohmmeter (EVOM^2, World Precision Instruments, Sarasota, FL, USA). Only cell monolayers with TEER values above 500 $\Omega\cdot cm^2$ was used for the transport studies. During the transport study, the integrity of cell monolayers was monitored by recording the TEER value. To evaluate TEER reversibility, the nanoparticles were incubated with Caco-2 cells for 2 h. After removing the nanoparticle samples, the monolayer was gently washed with a fresh HBSS buffer and allowed to recover in a complete culture medium under culture conditions. Monolayer integrity was monitored in an HBSS buffer by recording the TEER value for up to 24 h. The TEER value was calculated according to (Déat-Lainé, et al., 2013):

$$\text{TEER } (\Omega\cdot cm^2) = (R_{total} - R_{filter}) * A \quad (6\text{-}1)$$

where R_{total} is the resistance of the filter with cells (Ω), R_{filter} is the resistance of the filter without cells (Ω), and A is the surface of the Transwell® insert (cm^2).

6.2.4 Transport Efficiency of VB_{12}

Caco-2 cell monolayers were rinsed with an HBSS buffer and allowed to equilibrate at 37 ^{o}C for 30 min. Experiments were conducted by replacing the apical buffer (0.5 ml) with either nanoparticle suspension or VB_{12} solution. The basolateral buffer was replaced with a fresh HBSS buffer (1.5 ml). The concentration of VB_{12} in each apical chamber was 1.5 μg/ml. After 22 h, the sample in each basolateral chamber was collected into a centrifuge tube. The collected samples were concentrated at 25 ^{o}C until dry using a Vacufuge® vacuum concentrator (Eppendorf AG, Barkhausenweg 1, Hamburg, Germany). SDS (0.05%, w/v) was added to each sample to dissociate nanoparticles and release VB_{12}. The amount of VB_{12} transported across Caco-2 cell monolayer was measured by Reverse-phase high performance liquid chromatography (RP-HPLC). RP-HPLC was performed with a Kinetex^{TM} C_{18} column (4.6×150 mm), with a 1200 Series Binary HPLC System (Agilent Technologies, Waldbronn, Germany) equipped with a G1312A bin pump, a G1315D DAD detector. Flow rate was set at 1.0 ml/min, the injection volume was 50 μl and the detector was set at 360 nm. VB_{12} standards were prepared ranging from 0.5 ng/ml-50 μg/ml in MilliQ water. Each experiment was performed in triplicate. Linear gradient elution with aqueous acetonitrile was done according to Hugenschmidt, et al. (2011).

6.2.5 Transport Mechanism across Caco-2 Cell Monolayers

To study the transport mechanism of nanoparticles, Caco-2 cell monolayers were rinsed with HBSS for 3 times and allowed to equilibrate at 37 ^{o}C for 30 min. HBSS in apical and basolateral compartments was replaced with HBSS (as a control) or HBSS containing various inhibitors, including COL (5 μg/ml), CPZ (5 μg/ml), FLI (5 μg/ml), and CyD (10 μg/ml) (Beloqui, et al., 2013). These inhibitors were incubated with Caco-2 cells for 30 min at 37 ^{o}C. Afterwards, solutions in both compartments were removed and gently rinsed 3 times with the HBSS buffer. Subsequently, 0.75 ml nanoparticle suspensions containing 1.6 μg/ml VB_{12} and 1.5 ml HBSS were applied to apical and basolateral compartments, respectively. Following 6 h incubation at 37 ^{o}C, solutions in basolateral compartments were collected and subjected to a similar treatment, prior to quantification of VB_{12} by RP-HPLC, as indicated in Section 6.2.4.

A temperature block was also applied. Caco-2 cell monolayers were washed 3 times with pre-cooled HBSS (4 ^{o}C) and pre-incubated with HBSS at 4 ^{o}C for 30 min, to reach equilibrium. After removing HBSS, the pre-cooled nanoparticle suspensions (0.75 ml) containing 1.6 μg/ml VB_{12} and HBSS (1.5 ml) were applied to the apical and basolateral compartments, respectively. Following a 6-h incubation at 4 ^{o}C, solutions in the basolateral compartments were collected. A similar experiment conducted at 37 ^{o}C was used as the corresponding control. The collected samples were subjected to the same treatment as illustrated in Section 6.2.4, prior to the RP-HPLC quantification of VB_{12}.

6.2.6 TEM Observation of Nanoparticles

Caco-2 cell monolayers were washed 3 times with HBSS and pre-incubated at 37 ^{o}C for 30 min. Then 0.75 ml of either SPI-NP-1 nanoparticle suspension or VB_{12} (a control) were applied to apical compartments. The VB_{12} concentration was 1.6 μg/ml (w/v) in each sample. After a 2 or 4 h incubation at 37 ^{o}C, solutions in each compartment were collected and prepared for TEM observation. Briefly, a drop of 1% phosphotungstic acid (PTA, w/v) was dipped on the carbon-coated copper grid for 1 min, then a drop of nanoparticle solution was added to react with the 1% PTA for 45 s. The extra solution was drawn off using filter paper. The samples were allowed to air dry thoroughly and observed under the Philips-FEI transmission electron microscope (Morgagni 268, FEI co., Hillsboro, OR, USA) at an accelerating voltage of 140 kV.

Caco-2 cell monolayers were also washed gently 3 times with HBSS to remove non-attached nanoparticles. Subsequently, cell monolayers were pre-fixed with 2.5% glutaraldehyde and 2% paraformaldehyde solution overnight at 4 ^{o}C, followed by washing 4 times with phosphate buffered saline (PBS, 0.1 M, pH 7.4) for 10 min per change. The cells were post-fixed with 1% osmium tetroxide (OxO_4 in 0.12 M cacodylate buffer, pH 7.2) for 1 h, washed with PBS for 10 min per change. Samples were dehydrated in 50%, 70% and 90% ethanol, for 15 min in each solution and 3 times in 100% ethanol. The cell monolayers were infiltrated twice, for 2 h each time, firstly by replacing the 100% ethanol with an ethanol:spur mixture (1:1, v/v) and then with a pure spur resin. The cell monolayers, together

with a polyester membrane, were then carefully cut into small pieces and carefully placed in molds filled with spur resin. The molds were incubated at 70^{o}C overnight to allow the polymerization of resin. The resin sample block was trimmed, thin-sectioned to a thickness of 70 nm using a microtome (Ultracut E Ultramicrotome, Reichert-Jung, Germany) and collected on Formvar-coated copper grids. These grids were stained by 4% uranyl acetate for 30 min and lead citrate for 7 min in a CO_2 free chamber. The samples were then blotted with a filter paper and air-dried. Samples were observed under the TEM at 140 kV.

6.2.7 *Ex Vivo* Studies

The *ex vivo* study of the intestinal absorption of VB_{12}-nanoparticles was performed on a modified Ussing chamber model (Vine, et al., 2002). The animal care and experimental procedures were conducted in accordance with the Canadian Council on Animal Care and approved by the University of Alberta Animal Care and Use Committee (Livestock). Male 10-week old Sprague Dawley rats were purchased from Charles River Laboratories (Wilmington, MA, USA) and fed a standard chow diet (Laboratory chow 5001). Animals were given free access to food and water. On the day of the experiment, animals were anesthetized with isoflurance-oxygen mix (3.5%) and sacrificed by exsanguination. The jejunum was removed distal to the ligament of the Treitz and immediately placed in an ice-cold Krebs buffer supplemented with sodium L-glutamate (4.9 mM), disodium fumarate (5.4 mM), sodium pyruvate (4.9 mM) and D-glucose (11.5 mM) and continuously

bubbled with O_2/CO_2 (95%/5%). Individual segments were cut from the jejunum and mounted in modified Ussing chambers (Harvard Apparatus Inc, Holliston, MA, USA). Each mounted area available for permeation was 1.15 cm^2. Tissues were allowed to equilibrate in 6 ml oxygenated Krebs buffer at 37 °C for 30 min for the following experiments.

6.2.7.1 Ex Vivo Absorption of Nanoparticles in Rat Jejunum

Followed by the above equilibration of tissue in Krebs buffer, 3 ml of buffer in mucosal chambers was replaced by 3 ml solutions of SPI-NP-1 nanoparticles containing 1.13 and 2.50 μg/ml VB_{12}. VB_{12} alone was used as a control. After incubating for 2 h, the jejunum tissues were carefully removed from the Ussing chamber and frozen in liquid N_2. The tissues were weighed and ground into a homogenous suspension in PBS solution. The suspensions were treated by ultrasonication for 1 h. Then samples were centrifuged at 10, 000 g for 30 min and the supernatant was collected. The pellet was suspended with 1.0 ml of PBS solution, treated by ultrasonication for 4 h and centrifuged again. All the supernatants were pooled together after washing the pellet twice and then dried by a Vacufuge® vacuum concentrator at 25 °C. The residue was suspended in 200 μl of PBS containing 0.05% SDS solution and subjected to ultrasonication for 10 min, then centrifuged at 10,000g for 20 min. The supernatant was filtered through a 0.45 μm PVDF syringe filter. A 50 μl filtered sample was loaded into RP-HPLC to quantify the amount of VB_{12} in the tissue according to Section 6.2.4. The amount of

VB_{12} in the jejunum was expressed as μg VB_{12} per g jejunum segment. 15 pieces of jejunum segments were used in the group of SPI-NP-1 nanoparticles, obtained from 5 rats, whereas 9 pieces of jejunum segments were used in the VB_{12} group, obtained from 3 rats.

The particles in donor and acceptor chambers were observed under TEM as indicated in Section 6.2.6.

6.2.7.2 Histological Observation of Nanoparticles

The tissue was left in 6 ml of oxygenated Krebs buffer for 30 min. Upon equilibration, 3 ml of buffer in mucosal chambers was replaced by 3 ml solutions of COUM-6 labeled SPI-NP-1 nanoparticles and free VB_{12}. The average concentration of VB_{12} in each given sample was 1.6 μg/ml. After incubating for 2 h, solutions from mucosal and serosal chambers were collected. Tissues were carefully removed for histological observation. A small piece was cut from each segment and immediately mounted in OCT embedding media (Thermo Scientific, Toronto, ON, Canada) on dry ice. Upon frozen, tissue blocks were stored at -20 °C until cryosectioning. The sectioned tissues were mounted on glass slides using Prolong® Gold Anitfade reagent with DAPI staining and then observed with a CLSM 510 Meta (Carl Zeiss, Jena, Germany) equipped with a diode at 405 nm of excitation, an argon laser (providing the excitation at 488 nm) and a helium/neon laser (providing the excitation at 543 nm). An oil immersion objective (40 ×) was used to visualize samples. Images were processed with ZEN

2009 LE software (Carl Zeiss MicroImaging GmbH, Oberkochen, Germany). The number of jejunum segments for SPI-NP-1 and VB_{12} was 3, obtained from 1 rat.

6.2.1 Statistical Analysis

All transport experiments were performed in triplicate samples in at least three independent batches. Data were represented as mean ± standard deviation (SD). Student's t-test was used for comparisons between two samples and one-way ANOVA for more than two samples.

6.3 Results and Discussion

6.3.1 Integrity of Caco-2 Cell Monolayers

The most widely established *in vitro* model of human intestinal absorption is the Caco-2 cell line, which is derived from a human colorectal adenocarcinoma. When cultured on permeable inserts, Caco-2 cells are able to spontaneously differentiate and polarize, forming a continuous monolayer that exhibits the phenotype of mature enterocytes, including the presence of microvilli, tight junctions, dome formation, and production of brush border enzymes and transporters (Hidalgo, et al., 1989). Therefore, Caco-2 cell monolayers have been widely used for evaluating the transport and transport mechanisms of nanoparticles across the small intestinal epithelium for nutraceutical delivery.

In this study, Caco-2 cells were seeded on permeable inserts at a density of 1×10^5 cells/insert cultured at 37 ^oC. This insert separated the apical and basolateral compartment, which corresponded to the intestinal lumen and serosal side, respectively. The formation of the permeable barrier was assessed by monitoring the TEER value of the Caco-2 cell monolayers (Ghaffarian, et al., 2012). The TEER values vary from laboratory to laboratory, which mainly depend on passage number. The TEER values are higher for older passages (Delie & Rubas, 1997). In this study, the time-course of TEER values of the Caco-2 cell monolayer was shown in Figure 6-1. The TEER values slowly increased from day 1 to 5 and then increased rapidly until day 17 reaching a plateau with a maximum TEER value of 803 ± 12 $\Omega\cdot cm^2$. This value was consistent with that of passages 20-40 indicating the formation of intact epithelial junctions (Déat-Lainé, et al., 2013; Delie & Rubas, 1997).

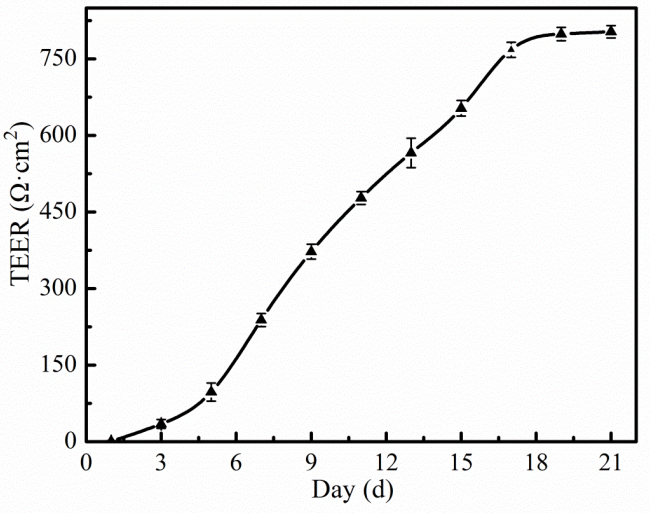

Figure 6-1. Transepithelial electrical resistance (TEER) of Caco-2 cell monolayers at different stages of confluence and differentiation.

6.3.2 VB_{12} Transport Efficiency across Caco-2 Cell Monolayers

Once an intact cell monolayer was acheived, the cumulative transport of VB_{12} in various nanoformulations across the epithelial barrier moving from the apical to the basolateral side was evaluated, and VB_{12} was used as a control. The size and surface charge of nanoparticles, above other physicochemical characteristics, determine the transport efficiency as well as the related mechanisms across the small intestine barrier (He, et al., 2012; He, et al., 2010). Thereby, the impacts of these parameters on VB_{12} transport efficiency were studied.

6.3.2.1 Impact of Particle Size

The effect of particle size on the accumulative transport of VB_{12} across Caco-2 cell monolayers was firstly studied. The results were displayed in Figure 6-2. The transport of VB_{12} without encapsulation was 0.25 ± 0.015 μg/cm^2 at 22 h at 37 °C. After nanoencapsulation, its transport increased to 0.80 ± 0.012 μg/cm^2, 0.61 ± 0.016 μg/cm^2, and 0.48 ± 0.033 μg/cm^2 for the particles of SPI-NP-1 (30 nm), SPI-NP-2 (100 nm) and SPI-NP-3 (180 nm), respectively. These findings indicated that SPI nanoparticles significantly enhanced VB_{12} transport, compared with VB_{12} solution. In addition, SPI nanoparticles with smaller size had a higher permeability through Caco-2 cell monolayers, which were in agreement with previous findings (He, et al., 2012; Lin, et al., 2011). Smaller nanoparticles have a larger surface to mass ratio and hence have more contact with the Caco-2 cell monolayers. This fact led to a higher transport of VB_{12} (Lin, et al., 2011). Interestingly, the results in

Chapter 4 showed that 30 nm particles exhibited a significantly lower cellular uptake efficiency compared with 100 nm ($p < 0.05$). This can be explained by the fact that particles less than 50 nm could effectively transport through paracellular spaces by opening the tight junctions, instead of being taken up inside Caco-2 cells (Yin Win & Feng, 2005). Also, even after being internalized inside Caco-2 cells, there are two transport directions for nanoparticles: apical-to-basolateral transport (absorption) and basolateral-to-apical transport (secretion). More VB_{12} in 100 nm particles may be delivered back to the apical chamber via exocytosis pathway instead of being transported across the basolateral membrane. This statement however needs to be tested in the future by evaluating the basolateral-to-apical transport of VB_{12}.

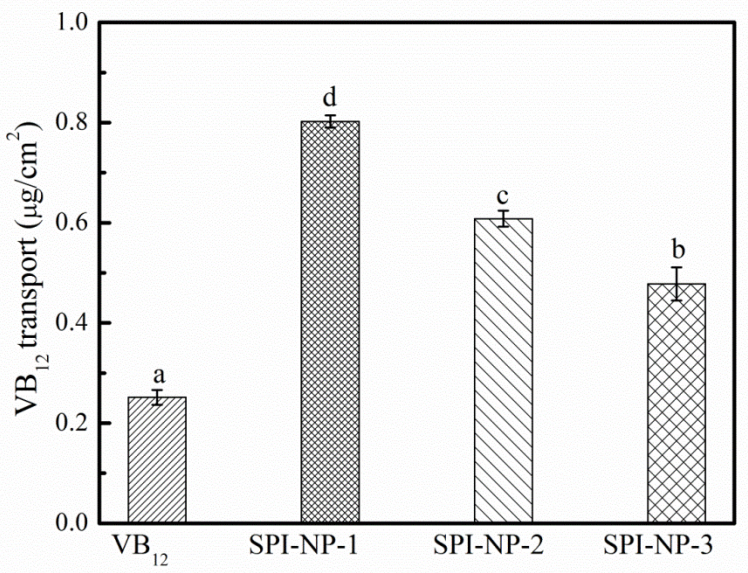

Figure 6-2. The impact of particle size on the accumulative transport of VB_{12} in SPI nanoparticle systems across Caco-2 cell monolayers from the apical to basolateral chamber at 37 ^{o}C for 22 h. Significant difference was expressed as ^{a,b,c,d} at $p < 0.05$.

6.3.2.2 Impact of Particle Surface Charge

In addition to particle size, the surface properties impact the particle transport efficiency. Therefore, the surface of nanoparticles was modified with mucoadhesive polymers including cationic chitosan and anionic alginate. These two polymer-based nanoparticles have shown promising potential in oral delivery of bioactives due to their biocompatible, low toxicity, mucoadhesive and permeability enhancing properties (Bagre, et al., 2013). As SPI-NP-1 and SPI-NP-2 demonstrated significantly higher VB_{12} transport efficiency compared with SPI-NP-3, these two samples (SPI-NP-1 and SPI-NP-2) were chosen to be coated with a thin layer of chitosan, on which a second layer of alginate was applied, achieving nanoparticles with the zeta-potential of 22 mV (CS-SPI-NP-1 and CS-SPI-NP-2) and -40 mV (AL-CS-SPI-NP-1 and AL-CS-SPI-NP-2) respectively, but still maintaining their original sizes.

As shown in Figures 6-3 and 6-4, surface modification of SPI nanoparticles with chitosan (CS-SPI-NP-1 or CS-SPI-NP-2) significantly decreased the transport of VB_{12} across Caco-2 cell monolayers ($p < 0.05$), compared with the original SPI nanoparticles (SPI-NP-1 or SPI-NP-2). This finding was in accordance with the previous report that the negatively charged nanoparticles demonstrated a higher permeability across Caco-2 cell monolayers compared with the positively charged ones (Lin, et al., 2011). However, our finding in Chapter 5 showed that positively charged CS-SPI-NP-2 nanoparticles had similar uptake efficiency by Caco-2 cells to that of negatively charged SPI-NP-2 nanoparticles. In this case, a similar amount

of VB_{12} in these systems would presumedly to be transported across Caco-2 cell monolayers. However, CS-SPI-NP-2 formulation demonstrated a lower transport efficiency for VB_{12} in the present study. It was probably caused by the strong electrostatic interactions between the positively charged particles and negatively charged basolateral membrane of Caco-2 cells that may prevent particles from passing through this barrier (Lin, et al., 2011). Variation in VB_{12} transport efficiency may also be caused by the different transport mechanisms.

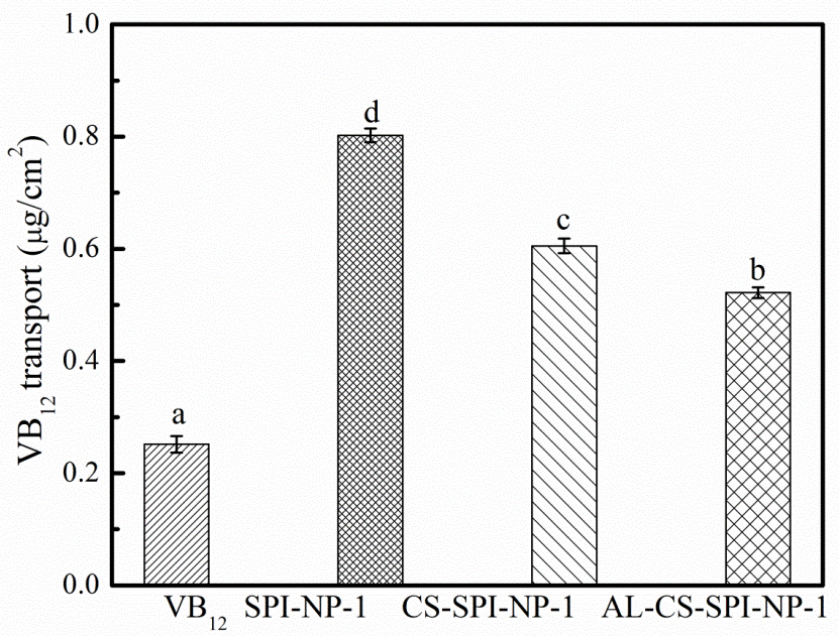

Figure 6-3. The impact of particle surface charge on the cumulative transport of VB_{12} in 30 nm nanoparticles across Caco-2 cell monolayers from the apical to the basolateral chamber at 37 ^{o}C for 22 h. Significant difference was expressed as ^{a,b,c,d} at $p < 0.05$.

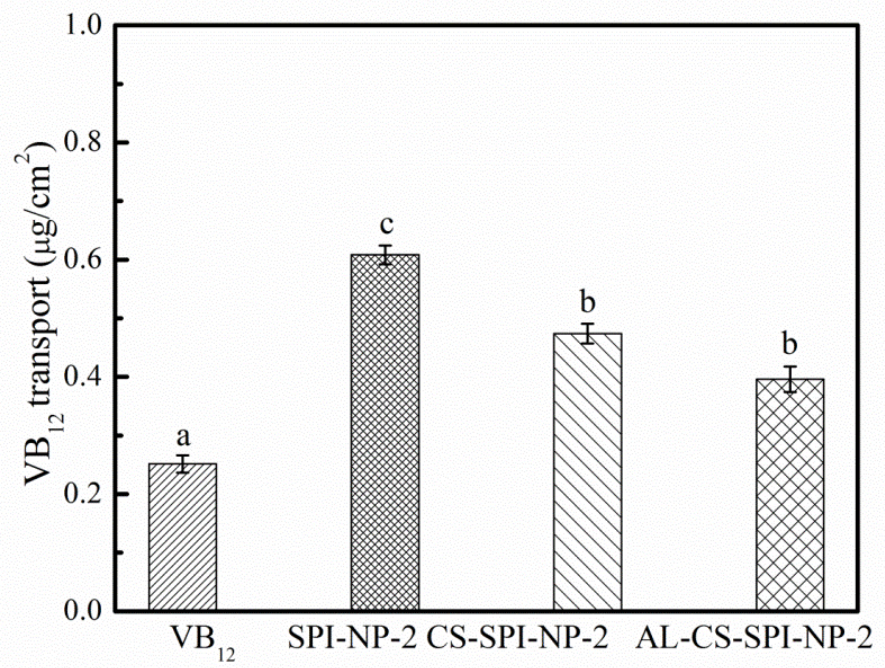

Figure 6-4. The impact of particle surface charge on the accumulative transport of VB_{12} in 100 nm nanoparticles across Caco-2 cell monolayers from the apical to basolateral chamber at 37 ^{o}C for 22 h. Significant difference was expressed as ^{a,b,c} at $p < 0.05$.

Similarly, negatively charged alginate and chitosan modified nanoparticles (AL-CS-SPI-NP-1 and AL-CS-SPI-NP-2) led to a decreased VB_{12} transport compared with the original chitosan nanoparticles (CS-SPI-NP-1 and CS-SPI-NP-2) respectively, as shown in Figures 6-3 and 6-4. The transport of VB_{12} by AL-CS-SPI-NP-1 was significantly lower than that by CS-SPI-NP-1 ($p < 0.05$, Figure 6-3), while the VB_{12} transport by AL-CS-SPI-NP-2 was similar to that by CS-SPI-NP-2 ($p > 0.05$, Figure 6-4). The decreased transport could be caused by the strong energy barrier between negatively charged alginate/chitosan modified nanoparticles and the negatively charged Caco-2 cell membrane. This repulsion

force would prevent the nanoparticles from attaching to the apical membranes thus resulting in lower transport efficiency (He, et al., 2010).

In terms of negatively charged nanoparticles, AL-CS-SPI-NP-1 and AL-CS-SPI-NP-2 nanoparticles (-44 mV) demonstrated significantly lower transport efficiency for VB_{12} than that of SPI-NP-1 (Figure 6-3, $p < 0.01$) and SPI-NP-2 (Figure 6-4, $p < 0.01$) nanoparticles (-17 mV), respectively. This finding was in good agreement with our previous result that AL-CS-SPI-NP-2 nanoparticles had significantly lower uptake efficiency by Caco-2 cells than that of SPI-NP-2 nanoparticles ($p < 0.05$). The lower transport efficiency in the more negatively charged particles was due to the stronger repulsive forces between these nanoparticles and the Caco-2 cell apical membrane. This stronger energy barrier would consequently prevent AL-CS-SPI-NP-1 and AL-CS-SPI-NP-2 nanoparticles from adhering to apical membrane of Caco-2 cells and being internalized inside cells, thus leading to the lower transport efficiency (He, et al., 2010).

In addition, the data in Figures 6-3 and 6-4 also indicated that particle size of surface modified nanoparticles determined VB_{12} transport efficiency. For instance, VB_{12} transport efficiency for the 30 nm CS-SPI-NP-1 and 100 nm CS-SPI-NP-2 particles was 0.605 ± 0.013 and 0.474 ± 0.017 $\mu g/cm^2$, respectively. Transport efficiency for the 30 nm AL-CS-SPI-NP-1 and 100 nm AL-CS-SPI-NP-2 particles was 0.522 ± 0.095 and 0.396 ± 0.022 $\mu g/cm^2$, respectively. In both cases, 30 nm nanoparticles exhibited a significantly higher transport efficiency for VB_{12} than that of the 100 nm nanoparticles ($p < 0.05$). Again, the transport efficiency of

nanoparticles was size-dependent and smaller particles demonstrated a better effect over the larger ones.

To sum up, encapsulation of VB_{12} in SPI nanoparticles enhanced VB_{12} transport across Caco-2 cell monolayers. Transport of SPI nanoparticles was dependent on particle size and surface charge. The smaller the size of SPI nanoparticles, the higher the transport efficiency of VB_{12} was achieved. SPI nanoparticles (-17 mV) demonstrated a higher VB_{12} transport efficiency compared with chitosan (22 mV) and alginate/chitosan (-40 mV) modified ones, though chitosan and alginate are well-known for their permeability enhancing properties (Bagre, et al., 2013). The optimized VB_{12} transport efficiency in SPI nanoparticles may attribute to the multifunctional groups on their surface such as balanced hydrophilic/hydrophobic groups, the cooperation of the surface charge and hydrophobicity (des Rieux, et al., 2006). These groups could probably facilitate the interactions between SPI nanoparticles and Caco-2 cells, as well as the transport of VB_{12} across Caco-2 cell monolayers. Besides, certain peptides on the protein particle surface may be able to activate the transport mechanisms in Caco-2 cells (Luo, et al., 2013). Variations in VB_{12} transport efficiency would be caused by different transport mechanisms as well; these were studied in the following sections. The findings suggested that SPI nanoparticles alone possess a high potential to improve the intestinal absorption of VB_{12}. In addition, SPI nanoparticles being mild negatively charged (-17 mV) are more favorable for drug/nutraceutical delivery, considering positively charged particles tend to be

toxic and immunogenic due to the strong interactions between positively charged particles and negatively charged cell membranes or serum proteins (Bajaj, et al., 2009).

6.3.3 Transport Mechanism of Nanoparticles across Caco-2 Cell Monolayers

Intestinal transport is a complex transfer process. Research into absorptive mechanisms is best conducted in a model that contains only absorptive cells in the absence of the confounding contribution of mucus, the lamina propria and muscularis mucosa (Mehra, 2012). Therefore, much attention is paid to epithelial cell culture to study the transport mechanisms of nanoparticles for drug delivery. Increasing our understanding of the mechanisms and processes of nanoparticle transport across the small intestinal barrier and the parameters restricting their transport efficiency could help us modify nanoformulations and then achieve the optimized absorption of encapsulated compounds (Beloqui, et al., 2013).

Having demonstrated that nanoparticles were able to enhance VB_{12} transport across Caco-2 cell monolayers, their underlying transport pathways were studied. Theoretically, nanoparticles can cross the epithelium by: 1) the paracellular pathway via tight junctions; 2) the transcellular pathway (passive or active) via the intestinal cells, being the most commonly studied; and 3) lymphatic pathway (phagocytosis) via micro-fold (M) cells of Peyer's patches (Jung, et al., 2000; Rieux, et al., 2005). The lymphatic pathway was not discussed in this study

considering the M cells only contribute less than 1% of the human intestinal epithelial cells.

6.3.3.1 Paracellular Transport of VB_{12}-SPI Nanoparticles

The intestinal epithelium is a major barrier to the absorption of hydrophilic macromolecules, since they cannot diffuse across the epithelial cells through the lipid-bilayer of cell membranes to the blood stream. In addition, the hydrophilic macromolecules cannot diffuse through the tight junctions (Lin, et al., 2007). Paracellular spaces, sealed by the tight junctions, contribute less than 1% of the mucosal surface area and the pore size of the junctions is less than 1 nm. Paracellular transport is passive and based on diffusion (Yun, et al., 2012). The paracellular transport of nanoparticles is limited by the tightness and tiny pore size of junctions between the epithelial cells (Jung, et al., 2000). A decrease of TEER value reflects the enhancement of paracellular permeability, due to ion passage through the paracellular pathway (Yamashita, et al., 2000).

After exposure of nanoparticles to the Caco-2 cell monolayers, a remarkable decrease of TEER value was detected, indicating the increase of paracellular permeability (Figure 6-5). No obvious change of the TEER value, on the contrary, was detected with the incubation of the VB_{12} solution. The progressive decline in TEER values with the increased incubation time indicated the prolonged interactions of nanoparticles with the epithelial surface (El-Sayed, et al., 2002). The integrity and function of tight junctions depend on the extracellular Ca^{2+} and Mg^{2+}

(Delie & Rubas, 1997), which can be chelated by free carboxyl groups at the C-terminal of polypeptide chains or acidic amino acids (aspartate and glutamate) in soy protein. Consequently, the structure of tight junctions was reorganized and thus leading to the enhancement of nanoparticle transport through the paracellular spaces (Delie & Rubas, 1997; Rekha & Sharma, 2009). This decreasing trend was more remarkable in the nanoparticles with the smaller size (Figure 6-5 (A)), which was in accordance with previous findings (Lin, et al., 2011). SPI nanoparticles were formed by using Ca^{2+} as a salt-bridge between two carboxyl groups, and less Ca^{2+} was introduced in smaller sized SPI-NP-1 (2.5 mM), compared with larger sized SPI-NP-2 (5 mM), to interact with carboxyl groups (Chapter 3). Accordingly, more free carboxyl groups was left on smaller particles, which might chelate more Ca^{2+}/Mg^{2+}, thus accounting for a dramatic decrease in TEER (Figure 6-5 (A)). This study suggested that negatively charged SPI nanoparticles were able to modulate the tight junctions by reducing the free extracellular Ca^{2+}/Mg^{2+} concentration, thus facilitating the paracellular transport of particles. Previous research also demonstrated that both negatively and positively charged dendrimers could lead to the reorganization of the tight junctions, thus enhancing the paracellular permeability of ^{14}C-mannitol across Caco-2 cell monolayers (Kitchens, et al., 2006). The underlying mechanisms of paracellular transport of negatively dendrimer particles, however, were unknown (Kitchens, et al., 2006). It was generally believed that only positively charged nanoparticles such as chitosan and lectins nanoparticles could facilitate the paracellular transport of particles (Lin, et

al., 2007; Roger, et al., 2009). Nevertheless, the findings in the present study and other studies (Déat-Lainé, et al., 2013; Kitchens et al., 2006) shed light on the capability of negatively charged particles to open the tight junctions of Caco-2 cells.

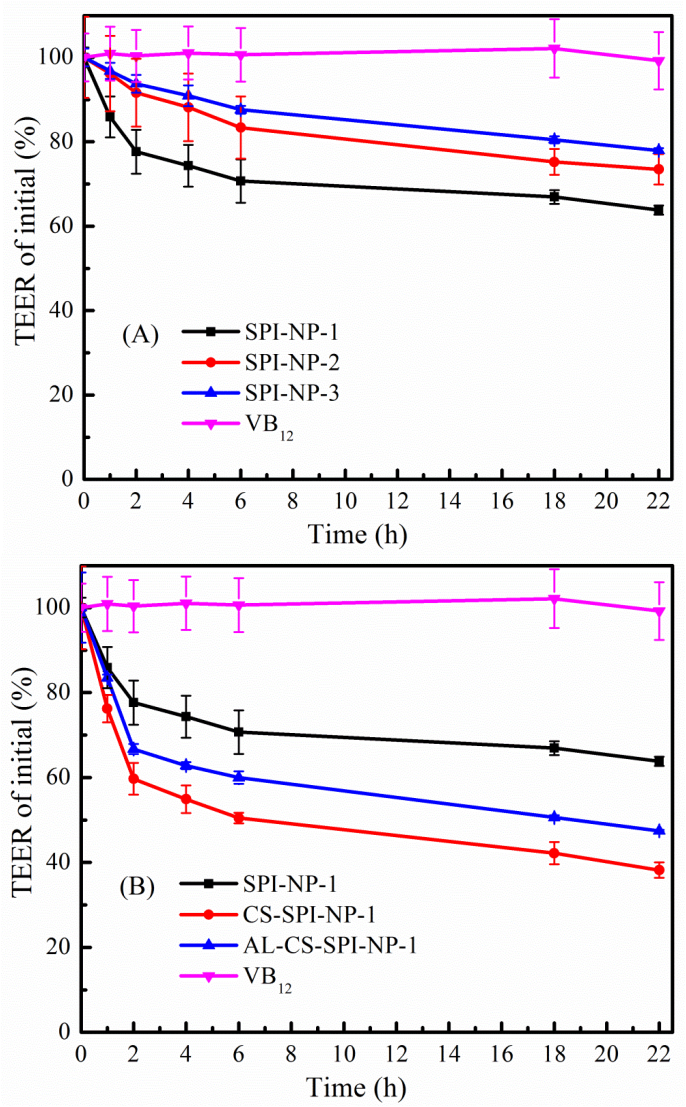

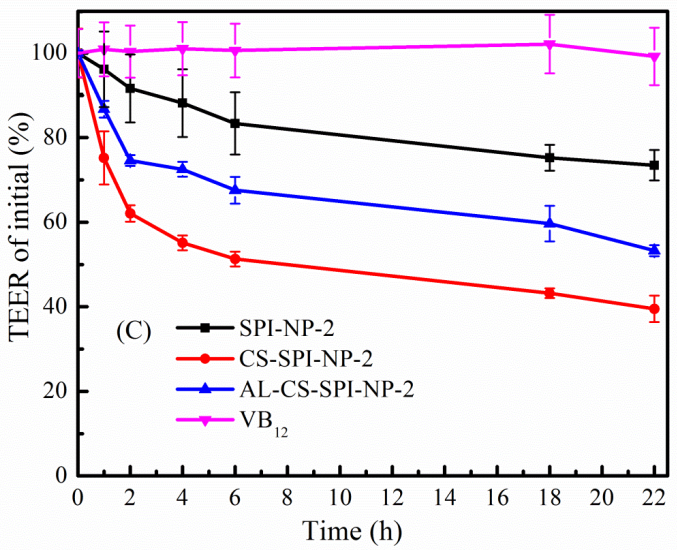

Figure 6-5. The impacts of (A) particle size and (B)-(C) surface charge/coating on the transepithelial electrical resistance (TEER) values of Caco-2 cell monolayers as a function of time. Data were expressed as mean ± SD of n=3.

Chitosan modified nanoparticles (CS-SPI-NP-1 and CS-SPI-NP-2) showed a more remarkable decrease in the TEER value, than that of the original SPI nanoparticles (SPI-NP-1 and SPI-NP-2) in Figure 6-5 (B)-(C), respectively. The opening of tight junctions was caused by the structural reorganization of the tight junction-associated proteins, which was induced by the electrostatic interactions between negatively charged sites of these proteins and positively charged chitosan nanoparticles (Lin, et al., 2007). The paracellular permeability of nanoparticles consequently improved. However, the particle size of chitosan modified nanoparticles did not have a significant difference on decreasing the TEER values. The TEER values, for example, decreased to 38.191 ± 1.821% and 39.499 ± 3.114% of the initial values with the treatment of 30 nm CS-SPI-NP-1 and 100 nm

CS-SPI-NP-2 nanoparticles for 22 h. This may indicate that the transport efficiency of these two particles via paracellular pathway was on the same level.

Alginate and chitosan modified nanoparticles (AL-CS-SPI-NP-1 and AL-CS-SPI-NP-2) also triggered the decline of TEER values with increased incubation time as shown in Figure 6-5 (B)-(C) by reversibly interacting with junctional proteins between Caco-2 cells (Déat-Lainé, et al., 2013). The decline of TEER values in the particles of AL-CS-SPI-NP-1 and AL-CS-SPI-NP-2 was slower than that in the positively charged ones CS-SPI-NP-1 and CS-SPI-NP-2, but faster than that in the lesser negatively charged ones SPI-NP-1 and SPI-NP-2, respectively. The results again indicated that negatively charged nanoparticles had a lesser ability to open tight junctions, compared with positively charged ones. Accordingly, chitosan modified nanoparticles would have a higher paracellular permeation of VB_{12}. In terms of capability of opening the tight junctions, larger sized AL-CS-SPI-NP-2 nanoparticles (100 nm) had a slightly stronger ability over the smaller sized AL-CS-SPI-NP-1 nanoparticles (30 nm). For instance, the TEER values dropped to 53.274 ± 1.316% (Figure 6-5 (B)) and 47.448 ± 0.249% (Figure 6-5 (C)) of the initial values with the treatment of 100 nm AL-CS-SPI-NP-2 and 30 nm AL-CS-SPI-NP-1 nanoparticles for 22 h.

Decreasing TEER values also gives an indication of the toxic effects induced by nanoparticles, since damage to the tight junctions would allow the leakage of potentially toxic substances or allergenic compounds through the epithelial barrier into system tissues or circulation, consequently leading to inflammatory or

immunological responses (Deitch, 1992). Therefore, the recovery of the integrity of the monolayers, after removal of the nanoparticles, is of great importance to maintain the function of the epithelial barrier. As shown in Figure 6-6, the TEER values recovered nearly completely in 24 h after removal of nanoparticles, suggesting that the enhanced paracellular permeability of nanoparticles across Caco-2 cell monolayers was not mediated by completely destroying tight junctions, but by transiently and reversibly opening the tight junctions. The paracellular pathways were beneficial for bioactive compound absorption, due to the absence of the proteolytic enzymes in the intercellular spaces, thus making it possible to maintain its bioactivity (Gaumet, et al., 2009). The transport efficiency of nanoparticles, however, via the paracellular pathway is severely restricted by the limited surface area (<1% of the mucosal surface area) and tightness of the junctions between the epithelial cells (Nellans, 1991).

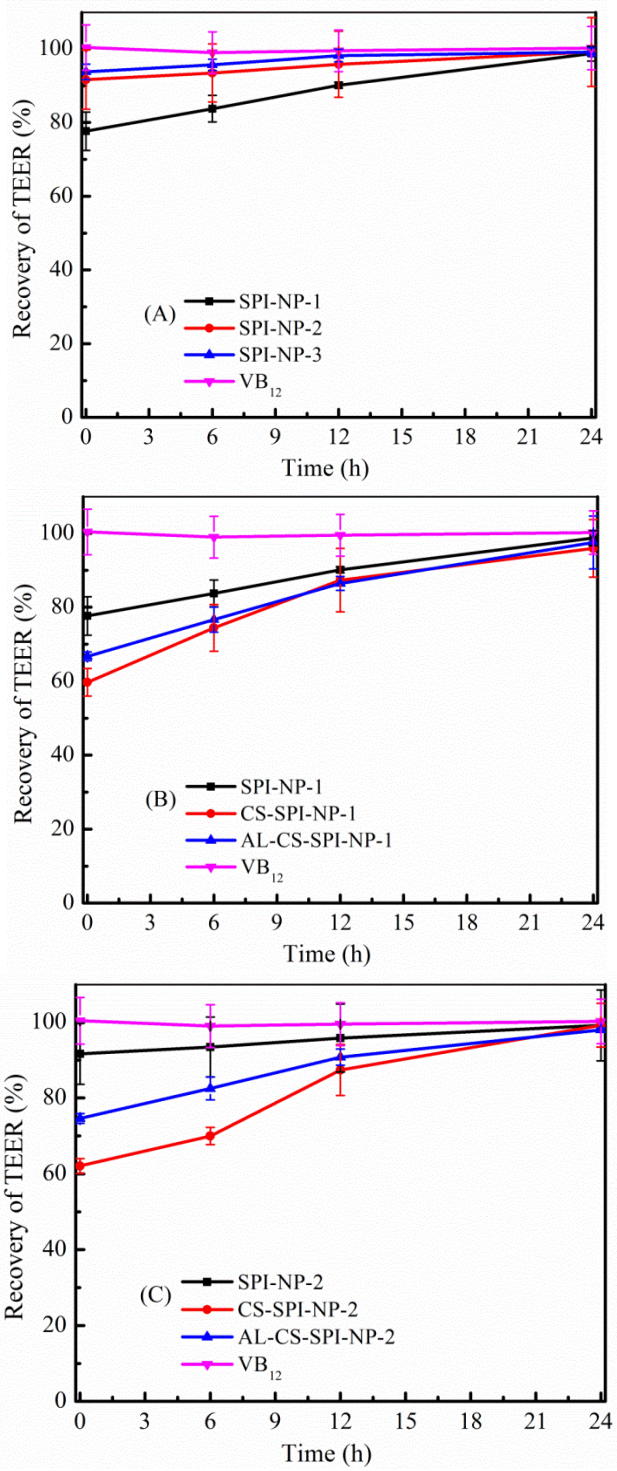

Figure 6-6. The impacts of (A) particle size and (B)-(C) surface charge/coating on the recovery of transepithelial electrical resistance (TEER) values of Caco-2 cell monolayers as a function of time.

6.3.3.2 Transcytosis and Transcytosis Mechanisms of Nanoparticles

The cell membrane of enterocytes is the most efficient targeting area for nanoparticle delivery, as it contributes more than > 90% epithelial spaces. During the transport across the epithelial membrane, nanoparticles need to experience the whole journey from the apical to basolateral membrane. In general, it involves cell surface binding, entry into cytoplasm via endocytosis, transport intracellularly, and final exit from the basolateral membrane via exocytosis (He, et al., 2013). Therefore, the comprehensive understanding of transcytosis of nanoparticles is of great importance.

The results in Figures 6-2, 6-3 and 6-4 indicated VB_{12} transport efficiency was in the increasing order of SPI-NP-1 > SPI-NP-2 > CS-SPI-NP-1 > AL-CS-SPI-NP-1 > SPI-NP-3 > CS-SPI-NP-2 > AL-CS-SPI-NP-2 > VB_{12}. Therefore, the transcellular mechanisms of the top 4 samples, including SPI-NP-1, SPI-NP-2, CS-SPI-NP-1, and AL-CS-SPI-NP-1, were explored. In transcellular transport pathways, nanoparticles can pass the cell membrane barriers by passive diffusion or active transcytosis. The active transcytosis of nanoparticles can be blocked by setting up the incubation temperature at 4 ^{o}C (Tomoda, et al., 1989). As shown in Figure 6-7, the transport efficiency of VB_{12} in all the nanoparticles, crossing Caco-2 cell monolayers, decreased significantly at this temperature compared with the corresponding control at 37 ^{o}C. This suggested that active transcytosis was the predominant transcellular pathway for the transport of SPI nanoparticles rather than passive diffusion (Beloqui, et al., 2013). However,

nearly 20% VB_{12} in all the particles passed through Caco-2 cell monolayers at 4 ^{o}C, which was through paracellular transport as discussed above and passive diffusion, due to the change of membrane structure/fluidity under this temperature (Verma, et al., et al., 2008). The passive diffusion was probably driven by a concentration gradient of VB_{12} in the apical and basolateral chambers of the Caco-2 cell monolayers.

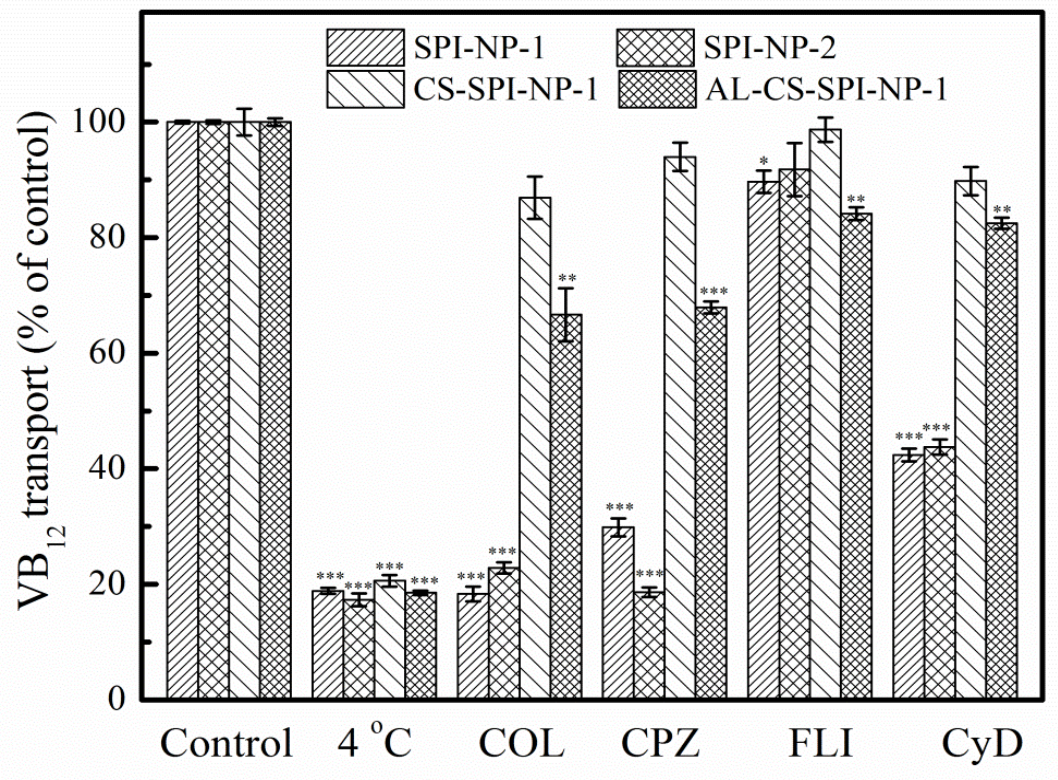

Figure 6-7. The impacts of temperature and inhibitors on the transport of VB_{12} across Caco-2 cell monolayers. Significant difference versus corresponding control was expressed as *: $p < 0.05$; **: $p < 0.01$; ***: $p < 0.001$.

The active transcytosis mechanisms could be subdivided into clathrin-mediated, caveolae-mediated, clathrin-/caveolae-independent, and

macropinocytosis pathways (Hillaireau & Couvreur, 2009). The transcytosis of SPI nanoparticles for VB_{12} delivery were studied by applying several inhibitors. COL is an inhibitor of caveolae-mediated and/or clathrin-mediated endocytosis. It inhibits actin polymerization and rearrangement for the formation and invagination of coated pits and caveosomes (He, et al., 2010). CPZ blocks clathrin-mediated endocytosis via a mechanism, where adaptor complex 2 (AP2) and clathrin are redistributed away from the plasma membrane, making clathrin unavailable for assembly at the cell surface (Jiang, et al., 2012). FLI interacts with 3-β-hydroxysterol in the plasma membrane to form filipin-sterol complexes. The complexes consequently disassemble the caveolae-1 coat leading to a block of the caveolin-mediated pathway but without blocking the clathrin-mediated pathway (Jiang, et al., 2012). CyD inhibits the macropinocytosis/phagocytosis by blocking the F-actin polymerization and membrane ruffling (Lien, et al., 2012; Lien, et al., 2012). Since Caco-2 cell lines are considered to be non-phagocytic cells (Harley, et al., 1997), the inhibition of VB_{12} transport by CyD would only reflect the role of macropinocytosis.

As shown in Figure 6-7, treatment of Caco-2 cell monolayers with COL led to a significant reduction in VB_{12} transport in SPI-NP-1 and SPI-NP-2 systems ($p < 0.001$), indicating that clathrin- and/or caveolae-mediated pathways were involved in the transcytosis of these nanoparticles. In order to determine the specific pathway, preincubation of CPZ and FLI with Caco-2 monolayers was also applied to block clathrin-mediated and caveolae-mediated transcytosis pathway

respectively. It was observed that preincubation with CPZ induced a significant decrease in VB_{12} transport ($p < 0.001$) in the samples of SPI-NP-1 and SPI-NP-2, suggesting that the clathrin-mediated pathway played a main role in the transcytosis of both 30 and 100 nm SPI nanoparticles. The FLI treatment, however, only led to 10% reduction in the VB_{12} transport in SPI-NP-1 nanoparticles compared with the control, though this decreased level was statistically significant ($p < 0.05$). This result pointed that the caveolae-mediated route played a minor role in the transcytosis of 30 nm nanoparticles. In addition, the VB_{12} transport dropped off remarkably with the treatment of CyD ($p < 0.001$). This indicated that macropinocytosis also played a main role in the transcytosis of SPI-NP-1 and SPI-NP-2 nanoparticles. In summary, the transcytosis of 30 and 100 nm SPI nanoparticles was mainly regulated by clathrin-mediated transcytosis and macropinocytosis routes. Caveolae-mediated transcytosis was only slightly involved in the transcytosis of 30 nm nanoparticles. In Chapter 5, our findings indicated that clathrin- and/or caveolae-mediated transport and macropinocytosis were the main mechanisms involved in the endocytosis of SPI-NP-1 and SPI-NP-2 nanoparticles. By comparison, the transcytosis pathways of SPI-NP-1 and SPI-NP-2 nanoparticles were similar to their endocytosis pathways. This finding was consistent with a previous report that endocytosis and transcytosis in epithelial cells shared the same mechanisms (Simionescu, et al., 2009). It was documented that clathrin- and caveolae-mediated internalization of

paclitaxel-loaded lipid nanoparticles was also involved in the transcellular transport of the paclitaxel across Caco-2 cells (Roger, et al., 2009).

In order to study the impacts of particle surface charge/coating on its transport mechanism, SPI-NP-1 was selected for surface modification by chitosan and alginate/chitosan due to its optimized transport efficiency (Figure 6-1). Interestingly, as shown in Figure 6-7, pre-incubation with all these inhibitors did not induce a significant reduction in the VB_{12} transport in positively charged CS-SPI-NP-1 nanoparticles ($p > 0.05$). This indicated that clathrin-mediated, caveolae-mediated and macropinocytosis routes were excluded from the transcytosis of CS-SPI-NP-1 nanoparticles across Caco-2 cell monolayers. The transport of CS-SPI-NP-1 nanoparticles was predominantly mediated by the active-transcytosis route, as VB_{12} transport efficiency in this sample significantly decreased at 4 ^{o}C ($p < 0.001$). It can therefore be concluded that the clathrin- and caveolae-independent pathways played major roles in the transcytosis of chitosan modified nanoparticles (CS-SPI-NP-1). The uptake of the larger sized CS-SPI-NP-2 nanoparticles, as indicated in Chapter 5, was mainly regulated by clathrin-/caveolae-independent pathways as well. The clathrin- and caveolae-independent pathways appear to require specific lipid compositions and are dependent on cholesterol rather than clathrin and caveolin-1 proteins (Sahay, et al., 2010). However, the mechanisms that govern these pathways remain poorly understood (Conner & Schmid, 2003).

In contrast to the positively charged CS-SPI-NP-1, all the inhibitors induced a remarkable decrease in VB_{12} transport in the highly negatively charged AL-CS-SPI-NP-1 nanoparticles (Figure 6-7). It suggested that clathrin-/caveolae-mediated pathway and macropinocytosis contributed to the transcytosis of AL-CS-SPI-NP-1 nanoparticles. Amongst all the inhibitors, CPZ blocked approximately 32% of the VB_{12} transport, while FLI and CyD only blocked 16% and 18% of the VB_{12} transport, respectively. Hence, it can be concluded that the clathrin-dependent pathway played a more important role than caveolae-dependent and macropinocytosis pathways in the transcytosis of AL-CS-SPI-NP-1 nanoparticles.

To sum up, the transcytosis of 30 and 100 nm SPI nanoparticles was mainly regulated by clathrin-mediated transcytosis and macropinocytosis. Caveolae-mediated transcytosis was slightly involved in the transcytosis of 30 nm nanoparticles. However, surface modification using chitosan changed the transcytosis of 30 nm nanoparticles into clathrin- and caveolae-independent pathways. Applying a second layer over chitosan modified 30 nm nanoparticles switched the trancytosis pathways back to a clathrin-dependent pathway, together with a small degree of caveolae-dependent and macropinocytosis pathways. Variation in particle transcytosis mechanisms would probably contribute to the different transport efficiency for VB_{12}. Further studies using specific co-localization markers for caveolin and clathrin proteins as well as using a

combination of inhibitors, would shed more light on the endocytosis and transcytosis of the SPI nanoparticles.

6.3.3.3 Intracellular Trafficking of Nanoparticles

Intracellular trafficking of SPI nanoparticles was studied by monitoring SPI nanoparticles inside Caco-2 cells at different time intervals using TEM imaging. Upon growing for 21 days, Caco-2 cells progressively differentiated to polarized monolayers with well-defined microvilli on the apical side and tight junctions between cells, which could be reflected by the continuously increasing TEER value with its highest value at day 21 in Figure 6-1. After 2 and 4 h incubation with nanoparticles at 37 ^{o}C, non-adsorptive nanoparticles were washed off prior to preparation of the cross-section of Caco-2 cell monolayers for TEM observation. From the cross-section of Caco-2 cells, particles with a diameter of approximately 20-25 nm were observed at a high density inside cells at the time of 2 and 4 h (Figures 6-8 (B)-(C)); however, few similarly sized particles were detected in cells at the time of 0 h (Figure 6-8 (A)). Accordingly, it could be concluded that these high density particles were mostly from the exogenous SPI-NP-1 nanoparticles. This finding again indicated that nanoparticles could be internalized into Caco-2 cells. Interestingly, the entrapping vesicles of nanoparticles varied in size, up to 1000 nm in diameter (red arrow, Figure 6-8 (B)), which bore resemblance to the macropinosomes (Lin, et al., 2011) based on the facts that macropinosomes are heterogenous in size and have no apparent coat structures (Hewlett, et al., 1994;

Jones, 2007; Swanson & Watts, 1995; Xiang, et al., 2012). Furthermore, nanoparticles with a lower density was observed at 4 h, compared with that at 2 h, suggesting nanoparticles were either degraded inside the lysosome or transported through the basolateral membrane (exocytosis). The bio-fate of nanoparticles was further evaluated by monitoring the solutions in the basolateral chamber.

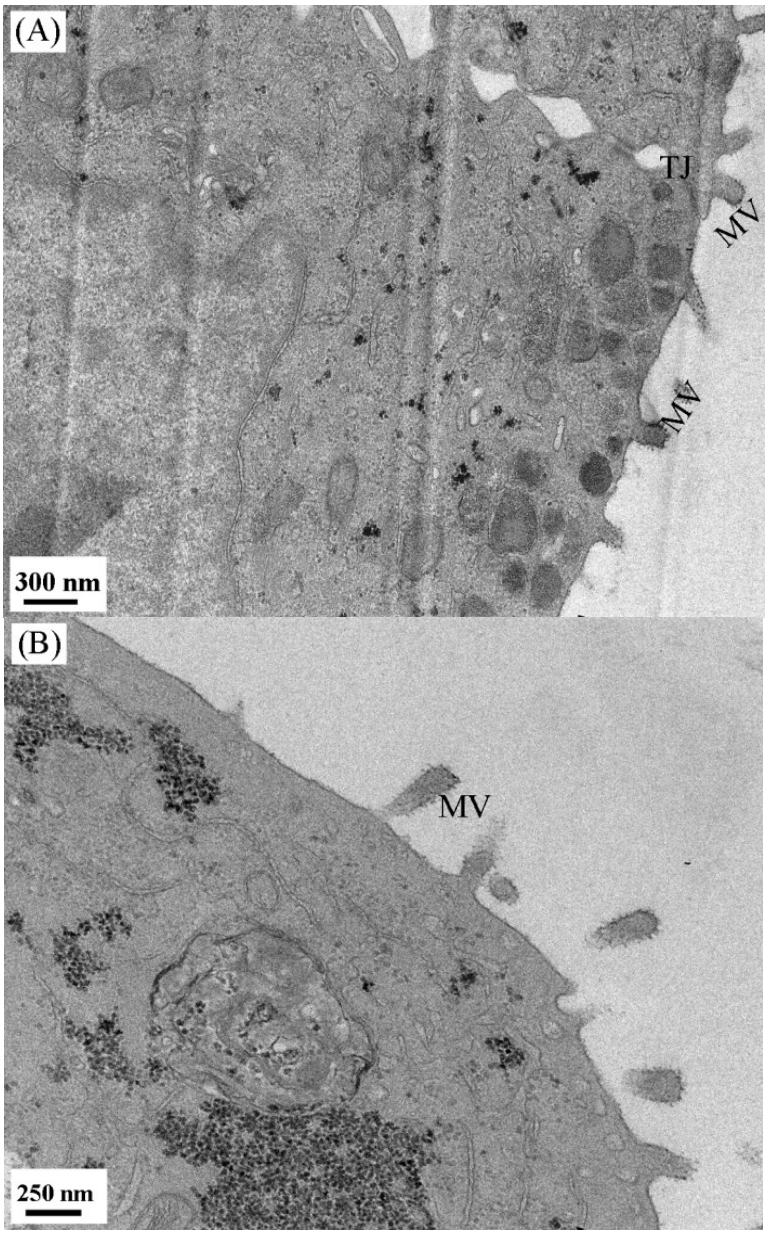

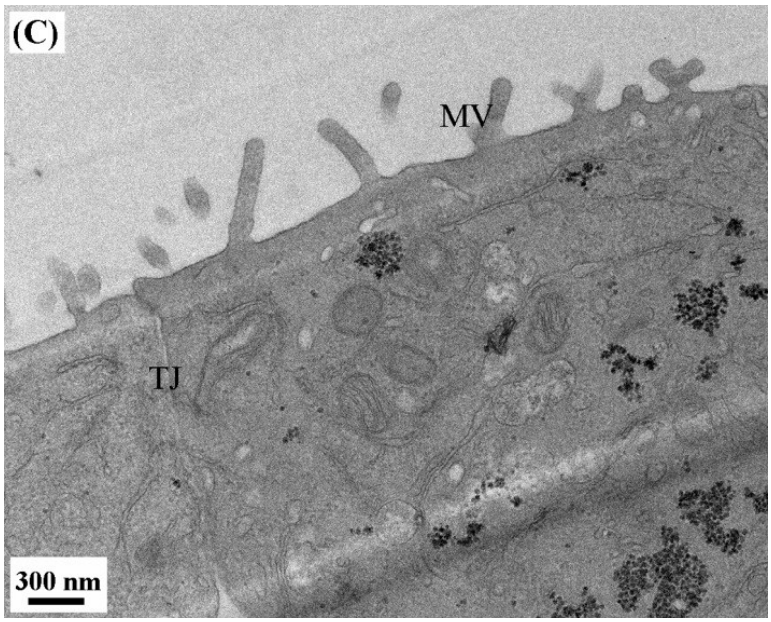

Figure 6-8. TEM micrographs of Caco-2 cell monolayers on Transwell inserts incubated with SPI-NP-1 for (A) 0 h, (B) 2 h and (C) 4 h at 37 ^{o}C. Arrow heads show nanoparticles accumulated within cells. TJ: tight junction; MV: microvilli.

6.3.3.4 Exocytosis and Biofate of Nanoparticles: TEM

In order to track the existence of nanoparticles after transport, the basolateral medium was observed by TEM after 4 h of incubation with SPI-NP-1 nanoparticles, VB_{12} solution was used as a control. As displayed in Figure 6-9, on the apical side, particles ranged in size from 10-50 nm (average: 25 nm) and some tiny fragments in the SPI-NP-1 sample were observed, which were detected on the basolateral side as well. However, in the control chamber, only fragments could be visualized. This result indicated the existence of direct exocytosis of nanoparticles. Nonetheless, the percentage of intact nanoparticles in basolateral chambers was not able to be

quantified in the current study. The exocytosis of nanoparticles to the basolateral chamber could be explained by their transport pathways.

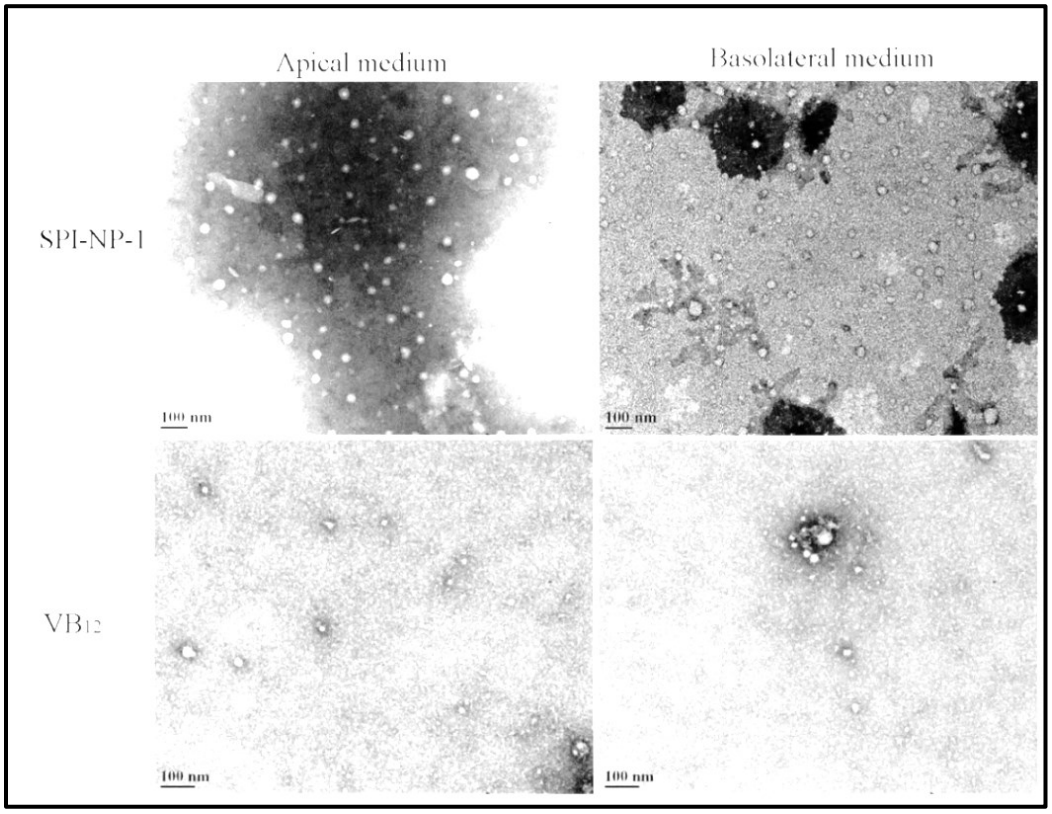

Figure 6-9. TEM images of apical and basolateral media of Caco-2 cells incubated with SPI-NP-1 and VB_{12} solutions at 37 ^{o}C for 4 h.

In small intestine, majority of SPI-NP-1 and SPI-NP-2 nanoparticles were transported across the basolateral membrane by clathrin-mediated and macropinocytosis routes. The internalization of nanoparticles by these pathways would typically end up in the endolysosomal path, which serves as a scaffold for intracellular trafficking of nanoparticles. Consequently, nanoparticles would be fused with lysosomes, where nanoparticles would probably be broken down by acid

hydrolase enzymes (Bareford & Swaan, 2007). In this case, VB_{12} was finally released to the cytoplasm, where it would be further reduced to active coenzymes, methylcobalamin or *S*-adenosylcobalamin and be ready to function (Petchkrua, et al., 2003). Instead of being sorted to late lysosomes for degradation, there were other possible fates of nanoparticles via the clathrin-dependent pathway. Nanoparticles could be sorted to the recycling endosomes to be transported back to the plasma membrane (Rappoport, 2008) or to the trans-Golgi network where they could get packed into secretory vesicles before fusing with the basolateral membrane for exocytosis (Reix, et al., 2012).

In addition to clathrin-mediated pathway and macropinocytosis, the caveolae-mediated route played a considerable role in the transcytosis of SPI-NP-1 and AL-CS-SPI-NP-1 nanoparticles. In contrast to the clathrin-mediated route, the caveolae-mediated one is generally regarded as a non-acidic and non-digestive pathway. This means it does not experience a drop in pH (neutral pH) and thus most of the nanoparticles can be directly transported to the Golgi and/or endoplasmic reticulum, thus avoiding the normal lysosomal degradation (Bengali, et al., 2007). There are some exceptions, where caveosomes fused with lysosomes and this consequently lead to the degradation of the contents (Kiss & Botos, 2009; Roger, et al., 2009; Schnitzer, et al., 1994).

In the case of transcytosis of positively charged CS-SPI-NP-1 nanoparticles, this was regulated by the clathrin-/caveolae-independent pathway. By this pathway, CS-SPI-NP-1 nanoparticles experience cellular internalization and vesicular

trafficking to the non-lysosomal subcellular compartment to achieve a non-degradative intracellular delivery (Bareford & Swaan, 2007).

Besides the transcellular pathway, paracellular transport could keep nanoparticles intact because the paracellular spaces lack major metabolic enzymes, such as proteases, to break down protein nanoparticles (Delie & Rubas, 1997). Yet its efficiency is restricted by the limited spaces of tight junctions and the tightness of these junctions (Nellans, 1991).

However, in terms of the intact nanoparticles, their biological behaviors after they enter the blood flow and the release kinetics in the systematic circulation have been rarely studied. More work is needed in order to study the intracellular trafficking of nanoparticles and monitor their *in vivo* distribution and destination. The intracellular trafficking of particles can be done by colocalization of nanoparticles with specific probes. For instance, LysoTracker (red) and cell light (green or red) could be applied to stain the lysosomes and early endosomes respectively (Xiang, et al., 2012). Combined with confocal imaging technology, the colocation of nanoparticles and intracellular compartments can be visualized directly.

6.3.4 *Ex Vivo* Intestinal Absorption

Small intestinal barriers are mainly composed of a mucus layer and a compact epithelial cell lining. Although the Caco-2 cell monolayer is an excellent *in vitro* model of intestinal epithelium, it lacks the mucus layer (Legen, et al., 2005). The

mucus of the small intestine is composed of anionic glycoprotein mucins that form a continuous adherent gel layer over the underlying epithelial cells (Yun, et al., 2012). Nanoparticles have the potential to adhere to mucosa and pass through this barrier to interact with the intestinal epithelium, subsequently, delivering the incorporated compound into the blood circulation. Therefore, the absorption of nanoparticles by intestinal tissues is of great importance in determining the delivery efficacy of nanoparticles. The intestinal absorption of SPI nanoparticles was studied on the rat jejunum model using the *ex vivo* Ussing chamber technique. The SPI-NP-1 nanoparticle was applied on this test because of its optimized efficiency for VB_{12} transport across Caco-2 cell monolayers (Figures 6-2 and 6-3).

In order to visualize particles in the jejunum tissue, SPI-NP-1 nanoparticles were first labeled with COUM-6 prior to incubation with the mucosal side of the jejunum. After 2 h, the segments of jejunum tissue were collected and sectioned for CLSM observation. The green SPI-NP-1 nanoparticles can be distinguished from the blue nuclei in Figure 6-10, indicating that SPI nanoparticles could be absorbed by intestinal tissue.

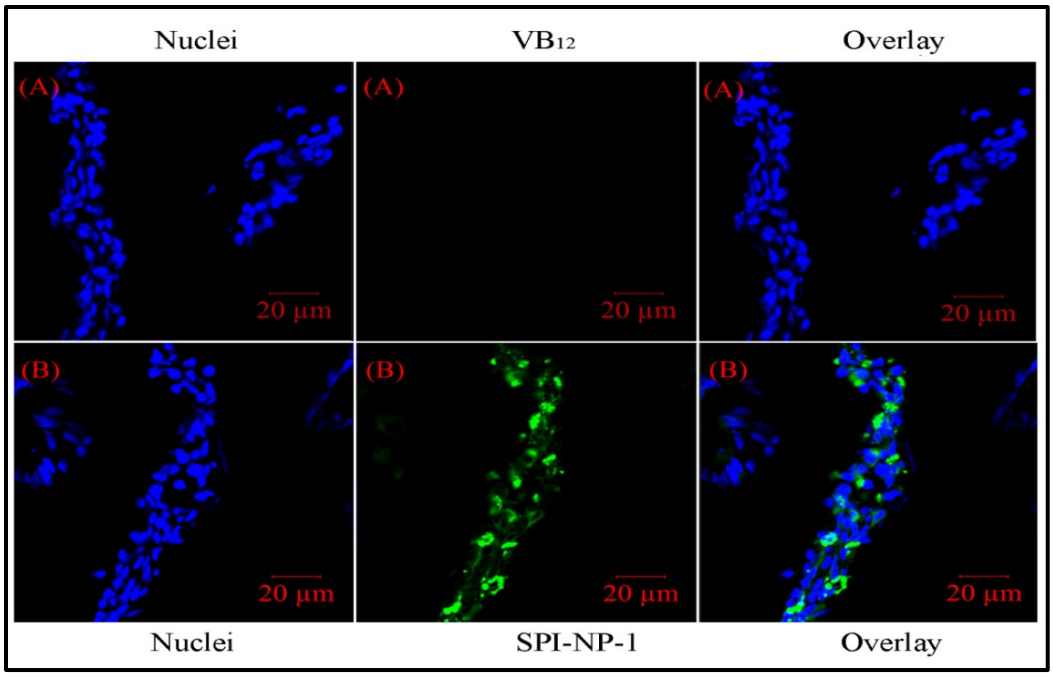

Figure 6-10. Confocal images of rat jejunum incubated with (A) VB_{12} (a control) and (B) SPI-NP-1 nanoparticles for 2 h 37 ^{o}C using Ussing chamber model.

In order to study the absorption enhancement of nanoparticles, the amount of VB_{12} in the jejunum tissue was measured by RP-HPLC after incubation with SPI-NP-1 nanoparticles for 2 h at 37 ^{o}C, with VB_{12} alone as a control. The similar sized segments of jejunum that were left untreated, were collected and submitted to the same procedure for VB_{12} extraction. After deducting the amount of VB_{12} in blank tissue, the absorption of VB_{12} by the jejunum tissue was shown in Figure 6-11. The absorption of VB_{12} by the jejunum incubated with SPI-NP-1 nanoparticles, was significantly higher than that with the VB_{12} solution ($p < 0.01$). The more VB_{12} was taken up by the jejunum tissues, the more would probably enter into the blood circulation. When the given dose of VB_{12} was at 2.5 μg/ml,

incubation with VB_{12} solution led to the absorption of 0.08 ± 0.13 μg per g jejunum, whereas incubation with SPI-NP-1 nanoparticles led to the absorption of 0.42 ± 0.24 μg VB_{12} per g of jejunum. In other words, SPI-NP-1 nanoparticles increased the absorption of VB_{12} by 0.34 μg per g jejunum. In this study, the surface area of jejunum mounted on the Ussing chamber was slightly over 1.15 cm^2, whereas the absorption area of small intestine in human body is approximately 25,000 cm^2. The recommended dietary amount of VB_{12} is around 2.4 μg daily for adults (FDA). Accordingly, SPI-NP-1 nanoparticles have the great potential to meet this requirement.

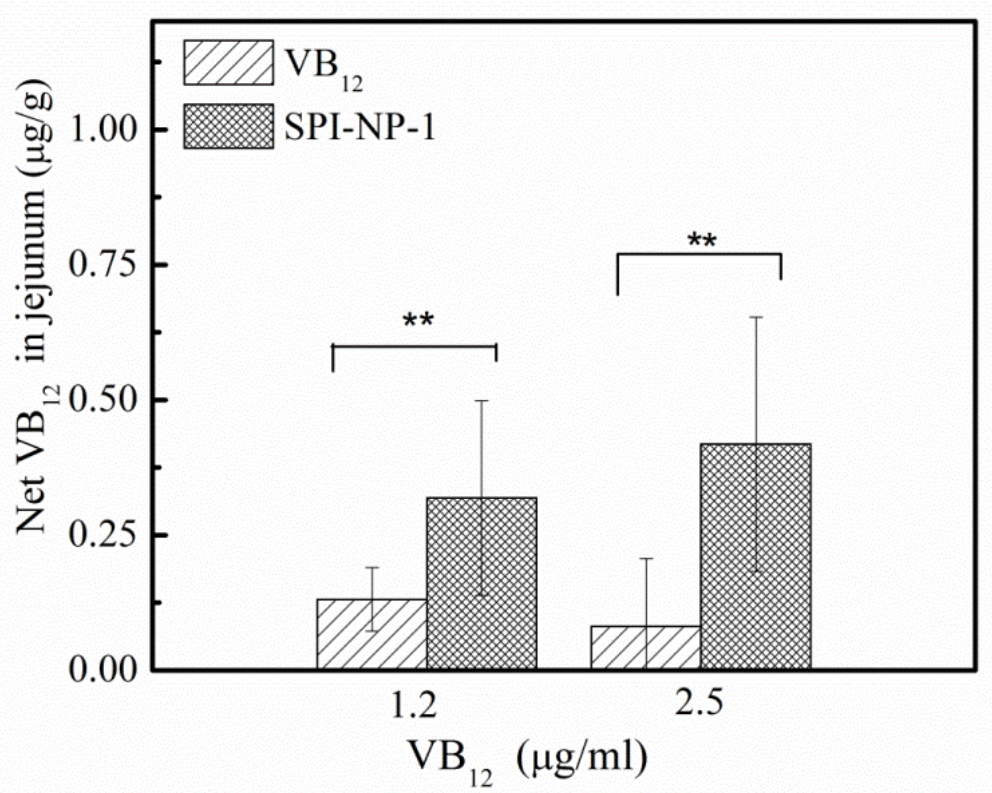

Figure 6-11. The absorption of VB_{12} by rat jejunum in 2 h at 37 ^oC. Indicated value was mean ± SD (n=15 and 9 of SPI-NP-1 and VB_{12}, respectively); $^{**}p < 0.01$.

This absorption of SPI nanoparticles by the jejunum tissues could probably be triggered by non-specific interactions such as hydrogen-bonding, van der Waal interactions and hydrophobic interactions. These interactions could be affected by particle size, surface properties and so on (Galindo-Rodriguez, et al., 2005; Shakweh, et al., 2005). Generally, smaller nanoparticles had a higher permeability through rat intestine (Sonavane, et al., 2008). Positively charged nanoparticles had a better mucoadhesive ability than that of negatively and non-ionized ones due to the electrostatic interactions between positively charged particles and the negatively charged mucus gel layer (Galindo-Rodriguez, et al., 2005); however, strong electrostatic interactions may consequently slow down the progression and penetration of particles toward the epithelium, leading to less uptake of nanoparticles by epithelial cells (Galindo-Rodriguez, et al., 2005). The SPI-NP-1 nanoparticles used in this study with a surface charge of -17 mV, there was an electrostatic repulsion between negatively charged particles and mucus layer. Though this energy barrier would not facilitate the adhesion of SPI nanoparticles on the mucus layer, the hydrogen-bonding, hydrophobic interactions and van der Waal forces would probably favor the adhesion of SPI nanoparticles. It is well-known that soy proteins have a high density of hydrogen-bonding groups such as $-NH_2$, $-COOH$,$-OH$, and $-SH$, which would be able to interact with the mucin glycoproteins. Mucins have hydrophobic groups on the protein backbone chains and thus they have a strong affinity to the hydrophobic surface of particles (Rekha & Sharma, 2009; Shi & Caldwell, 2000). SPI-NP-1 nanoparticles (30 nm)

have a relatively larger surface area and stronger surface hydrophobicity (Chapter 3). This larger surface area would provide nanoparticles with more space to interact with the intestinal surface and the hydrophobic interactions, hydrogen bonding and van der Waal forces would favor the further adhesion and penetration of particles toward the epithelium. The next step for SPI nanoparticles was to interact with the epithelial surface. According to the *in vitro* transport mechanisms, the majority of the SPI-NP-1 nanoparticles passed through this epithelial barrier using the clathrin-mediated transcytosis and macropinocytosis processes. Few of them passed through via caveolae-mediated transcytosis and paracellular pathway by conversely opening the tight junctions. The *ex vivo* absorption mechanism of SPI nanoparticles for VB_{12} delivery could be further investigated by applying inhibitors on the mucosal tissues.

The media in the donor and acceptor chambers were observed under the TEM after incubation with SPI-NP-1 nanoparticles and VB_{12} (control) for 2 h. As displayed in Figure 6-12, after 2 h of incubation with SPI-NP-1 nanoparticles, particles with the diameter ranging from 10 to 40 nm (about 20 nm on average) and from 15 to 50 nm (around 40 nm on average) were observed in the mucosal and serosal medium, respectively. However, only some tiny fragments were observed with the incubation of VB_{12}, which were also present with the incubation of SPI-NP-1 nanoparticles. These tiny fragments may have come from the "noisy" background. The existence of nanoparticles in the serosal chamber suggested that some of the nanoparticles were able to cross the jejunum barrier for VB_{12} delivery.

This finding again supported the statements of some of SPI-NP-1 nanoparticles could pass through the epithelial barrier via clathrin- and caveolae-mediated routes together with paracellular transport. Particle labeling for TEM, such as labeling with positively charged nanogold, could be applied in future test for better observation. To date, it is not possible to detect whether VB_{12} remained encapsulated inside the SPI nanoparticles after crossing the jejunum barrier.

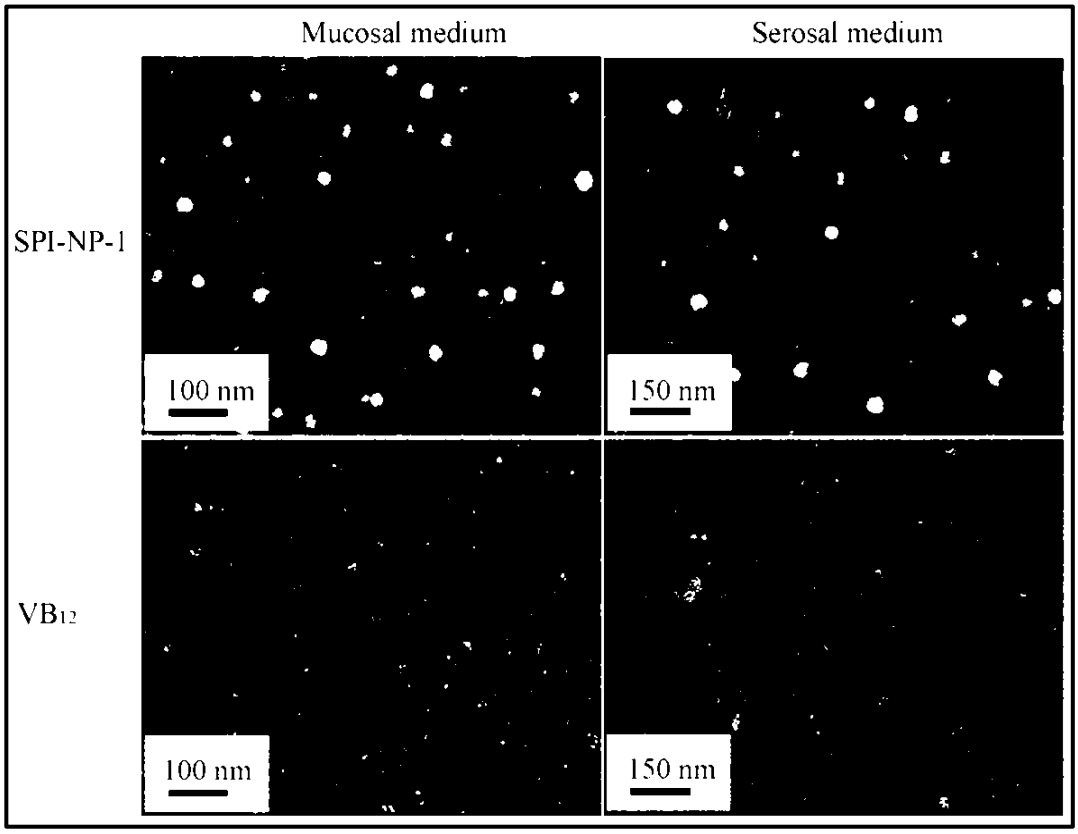

Figure 6-12. TEM Images of mucosal and serosal media of rat jejunum on Ussing chamber after incubating with SPI-NP-1 and VB_{12} for 2 h at 37 °C.

6.4 Conclusions

Understanding the transport of nanocarriers as well as their modulation by particle properties is important for rational design of optimal delivery carriers for nutraceuticals. This study provided insight into the impacts of particle size and surface charge/modification on their transport efficiency and associated mechanisms. All nanoparticles demonstrated a significantly higher efficiency of VB_{12} transport across the Caco-2 cell monolayers compared with VB_{12} without nanoencapsulation. The transport efficiency of VB_{12} was dependent on particle size and surface charge, in the order of 30 > 100 > 180 nm and -17 > 22 > -40 mV. The transport mechanisms of nanoparticles were dependent on the particles surface charge/coating. In general, the transport of 30 and 100 nm SPI nanoparticles was mainly through clathrin-mediated and macropinocytosis routes. In addition to these pathways, caveolae-mediated transcytosis was involved in the transport of 30 nm SPI nanoparticles. The transcytosis of chitosan modified SPI nanoparticles was regulated by clathrin- and caveolae-mediated pathways, while the transcytosis of alginate/chitosan modified nanoparticles was mainly regulated by clathrin-mediated routes together with caveolae-mediated pathway and macropinocytosis. Paracellular pathways were, in part, involved in the transport of all nanoparticles. Nanoparticles were observed in the basolateral and serosal media, indicating that some of the nanoparticles could carry VB_{12} and directly transport it across the epithelial cells without being degraded in the lysosomes. This is

beneficial to some vulnerable compounds. SPI nanoparticles (30 nm) also demonstrated a significantly higher intestinal absorption of VB_{12} compared with the VB_{12} solution. The findings in this study suggested that SPI nanoparticles could be a promising carrier for VB_{12} delivery by oral administration.

Chapter 7. General Discussion and Conclusions

7.1 Significance of the Research

Various nanoparticlate systems have been successfully developed using synthetic polymers. These nanoparticles, however, cannot be used in food products, where generally recognized as safe (GRAS) ingredients are required. Natural polymers such as SPI have been considered as a good candidate for nutraceutical delivery. The bioavailability of nutraceuticals can be improved by the formation of stable protein-nutraceutical complexes. Their interactions can be triggered by hydrophobic interactions, hydrogen bond, van der Waal interactions, electrostatic interactions and/or covalent bonding (Kroll, et al., 2003). In this thesis research, VB_{12} was bound inside the three-dimensional protein network by forming soy protein-VB_{12} complexes through hydrophobic interactions. This provided a fundamental basis to design soy protein nanoparticles for VB_{12} delivery (De Wolf & Brett, 2000). More VB_{12} was absorbed in jejunum after nanoencapsulation; it reflected that SPI nanoparticles could interact with mucus layer probably through hydrophobic interactions, hydrogen bonding, or van der Waal interactions. Once nanoparticles pass through mucus layers and reach epithelial lining. The high cellular uptake efficiency of particles revealed the SPI nanoparticles could interact with epithelial cell membranes and be internalized inside Caco-2 cells. Compared with VB_{12} alone, SPI nanoencapsulation led to a higher VB_{12} transport efficiency across simulated epithelial lining. It indicated that SPI nanoparticles could

potentially enhance the translocation of VB_{12} across intestinal epithelial barrier to the systemic circulations.

The absorption of VB_{12} is a complex process as described in Section 2.2.1 (Chapter 2), which only occurs in the distal ileum. SPI nanoparticles could potentially carry VB_{12} across the intestinal barriers mainly via clathrin-mediated and macropinicytosis pathways compared to its original complex pathway, thus leading to alternative absorption in the whole small intestine. Since SPI nanoparticles could significantly improve VB_{12} transport across the simulated epithelial barrier and enhance its intestinal absorption, these nanoparticles could potentially improve the oral bioavailability of VB_{12}. Using SPI nanoparticles as VB_{12} carrier is especially beneficial to the people who are suffering VB_{12} deficiency problem.

Besides, understanding of nanoparticle formation mechanism in relation to the release, uptake and transport properties could enable us to design an ideal encapsulating carrier at molecular level to optimize particle delivery efficacy.

Considering SPI nanoparticles were prepared at ambient temperature without using organic reagents, these nanoparticles would provide a promising opportunity to serve as novel delivery systems for various nutraceuticals even for heat labile ingredients. Novel functional foods could be developed by incorporating SPI nanoparticles into the food matrices aiming to enhance the oral bioavailability and health promoting benefits of bioactive compounds, without impacting food sensory properties.

7.2 Summary and Conclusions

SPI nanoparticles (30-180 nm) were successfully prepared by adapting a cold gelation method with a minor modification. A primary alkaline/heat treatment improved SPI solubility and enabled protein unfolding to expose reactive amino acids, followed by a cooling step and the adjustment of pH to 7-9. Calcium was then added to induce nano-scale network formation. The obtained nanoparticles demonstrated spherical shape and uniform size distribution. Nanoparticle characteristics such as size, surface charge and hydrophobicity could be modulated by modifying environmental pH and calcium concentration. The protein conformation study and nanoparticle dissociation test both suggested that calcium shielded the negative charges on polypeptide chains and served as a salt-bridge to facilitate SPI aggregation. These aggregates were then associated to form SPI nano-networks through hydrophobic interactions.

In order to study the feasibility of using SPI nanoparticles to encapsulate VB_{12}, the molecular interactions of VB_{12} with two major soy protein fractions, β-conglycinin (7S) and glycinin (11S) were studied using fluorescence and far-UV circular dichroism spectroscopic techniques. The results showed that the fluorescence of 7S and 11S was quenched by VB_{12} through binding-related quenching after correcting the inner-filter effect. Both 7S and 11S had a good affinity to VB_{12} as indicated by their high binding constant 1.252 (± 0.085) × 10^4 M^{-1} for 7S and 0.952 (± 0.04) × 10^4 M^{-1} for 11S at 292 K, respectively. Such binding

induced a more organized protein conformation with increased β-sheet and β-turn structural components and a more folded tertiary structure. It suggested that VB_{12} was bound in the interior of soy protein three-dimensional network mainly through hydrophobic interactions to form 7S-VB_{12} and 11S-VB_{12} binding complexes.

VB_{12} was subsequently loaded into SPI nanoparticles before the addition of calcium as a crosslinker. Surface modifications were performed by coating chitosan over original SPI nanoparticles (100 nm, -17 mV) to obtain positively charged nanoparticles (100 nm, 22 mV). Alginate was also coated over the chitosan modified SPI nanoparticles to achieve negatively charged nanoparticles (100 nm, -40 mV). Afterwards, the *in vitro* release, cytotoxicity and cellular uptake properties of nanoparticles were studied. The release of VB_{12} significantly decreased after nanoencapsulation in the simulated GI tract. Surface modified nanoparticles exhibited a slower VB_{12} release than that of original SPI nanoparticles. All nanoparticles demonstrated low cytotoxicity to Caco-2 cells in 6 h as indicated by their high cell viability. It was observed that around 14-37% nanoparticles were taken up by Caco-2 cells in 4 h at 37 °C. Their uptake was dependent on particle size and surface charge, in the increasing order of 100 nm > 30nm > 180 nm or 22 mV ≥ -17 mV > -44 mV. The internalization of nanoparticles was saturable and dependent on incubation time and temperature as well as particle dose, suggesting an active endocytosis pathway. Further inhibition study indicated that multiple endocytosis pathways including clathrin- and/or caveolae-mediated endocytosis and macropinocytosis were involved in uptake of

nanoparticles. The transport efficiency of VB_{12} across Caco-2 cell monolayers significantly increased after nanoencapsulation, which was depedent on particle size and surface charge. Nanoparticles with smaller size and lower negatively charge led to a significantly higher VB_{12} transport, compared with the other particles. The VB_{12} transport was significantly higher in SPI nanoparticles than that in chitosan and alginate/chitosan modified ones ($p < 0.05$). Moreover, the transport mechanisms of nanoparticles were dependent on particles surface charge/coating. Generally, the transport of SPI nanoparticles was mainly mediated by clathrin-mediated and macropinocytosis routes. Besides, the caveolae-mediated trancytosis was also involved in the transport of 30 nm nanoparticles. Chitosan modified 30 nm SPI nanoparticles used clathrin-/caveolae-independent transcytosis pathways; whereas, alginate-chitosan modified nanoparticles used clathrin-/caveolae-mediated and macropinocytosis routes.

In addition, paracellular pathways were in part involved in the transport of all nanoparticles. Nanoparticles were observed in the basolateral and serosal media, indicating that some of nanoparticles could carry VB_{12} and directly transport it across the epithelial cells without being degraded in the lysosomes. This is beneficial to some sensitive compounds.

Since 30 nm SPI nanoparticles demonstrated the optimized VB_{12} transpot efficiency across the simulated epithelial lining, this particle is the optimal carrier for VB_{12} delivery. This particle was futher applied on the rat jejunum to study test

the intestinal absorption enhancement of VB_{12}. In comparison to VB_{12} alone, 30 nm SPI nanoparticles demonstrated significantly greater intestinal absorption by the rat jejunum, up to 4 times. It again suggested that 30 nm SPI nanoparticles could be a promising carrier for VB_{12} delivery by oral administration.

7.3 Originality of the Research Investigations Presented in this Thesis

In the field of nutraceutical/drug delivery, there has been exciting achievement in the development of nanoparticles to enhance the oral bioavailability of poorly water-soluble compounds by increasing their solubility and stability in GI fluids (Livney, 2010). However, developing nanocarriers for the compounds such as VB_{12} that are soluble in GI fluids but have low permeability across intestinal barriers has been barely reported. The bioavailability of these compounds can be improved by enhancing their intestinal absorption.

The following investigations presented in this thesis fill the research gap that exists in the literature:

1). A fundamental investigation of the impacts of preparation processes on particle features and formation mechanisms was performed (Chapter 3). This could help us to optimize particle properties in order to achieve optimal delivery efficiency.

2). The molecular interactions between soy protein and VB_{12} were explored using fluorescence spectroscopy technique. Their interaction provided a driving force of using SPI nanoparticles to encapsulate VB_{12} (Chapter 4).

3). The particle uptake and transport properties were evaluated with respect to particle size and surface charge. The outcome of these studies is helpful to better engineer particle properties so as to achieve optimal delivery efficiency (Chapters 5 and 6).

4). The intestinal absorption of VB_{12} after nanoencapsulation was evaluated using the *ex vivo* model. This adavantage of this model is that the intestinal absorption behavior of SPI nanoparticles can be directly evaluated (Chapter 6).

7.4 Recommendations for Future Work

The cellular uptake and intestinal absorption of SPI nanoparticles for VB_{12} delivery have been evaluated in this research; the oral bioavailability of VB_{12} after nanoencapsulation needs to be evaluated using the animal model. Such a study will reflect the effectiveness of SPI nanoparticles for VB_{12} delivery.

In order to address the safety concern of nanoparticles, *in vivo* examination of the distribution and accumulation of SPI nanoparticles in animal organs and tissues is necessary. This can be done by labeling SPI nanoparticles with fluorescence dyes such as Cy5 prior to the observation of particles inside animal body under the confocal microscopy (Hoshino, et al., 2012).

References

Abbasi, A., Emam-Djomeh, Z., Mousavi, M. A. E., & Davoodi, D. (2014). Stability of Vitamin D_3 Encapsulated in Nanoparticles of Whey Protein Isolate. *Food Chemistry, 143*(0), 379-383.

Acosta, E. (2009). Bioavailability of Nanoparticles in Nutrient and Nutraceutical Delivery. *Current Opinion in Colloid and Interface Science, 14*(1), 3-15.

Agüeros, M., Ruiz-Gatón, L., Vauthier, C., Bouchemal, K., Espuelas, S., Ponchel, G., & Irache, J. (2009). Combined Hydroxypropyl-β-Cyclodextrin and Poly (Anhydride) Nanoparticles Improve the Oral Permeability of Paclitaxel. *European Journal of Pharmaceutical Sciences, 38*(4), 405-413.

Akbari, B., Tavandashti, M. P., & Zandrahimi, M. (2011). Particle Size Characterization of Nanoparticles-a Practical Approach. *Iranian Journal of Materials Science and Engineering, 8*(2), 48-56.

Alishahi, A., Mirvaghefi, A., Tehrani, M., Farahmand, H., Shojaosadati, S., Dorkoosh, F., & Elsabee, M. Z. (2011). Shelf Life and Delivery Enhancement of Vitamin C Using Chitosan Nanoparticles. *Food Chemistry, 126*(3), 935-940.

Allaoua, A., & Wang, Z. (2001). Effect of Succinylation on the Physicochemical Properties of Soy Protein Hydrolysate. *Food Research International*, *34*, 507-514.

Allémann, E., Leroux, J. C., Gurny, R., & Doelker, E. (1993). *In Vitro* Extended-Release Properties of Drug-Loaded Poly(DL-Lactic Acid) Nanoparticles Produced by a Salting-out Procedure. *Pharmaceutical Research, 10*(12), 1732-1737.

Allémann, E., Rousseau, J., Brasseur, N., Kudrevich, S. V., Lewis, K., & Van Lier, J. E. (1996). Photodynamic Therapy of Tumours with Hexadecafluoro Zinc Phthalocyanine Formulated in PEG-Coated Poly (Lactic Acid) Nanoparticles. *International Journal of Cancer, 66*(6), 821-824.

Allen, A. (1989). Gastrointestinal Mucus. *Comprehensive Physiology*.

Allen, A., & Garner, A. (1980). Mucus and Bicarbonate Secretion in the Stomach and Their Possible Role in Mucosal Protection. *Gut, 21*(3), 249-262.

Allen, R. H., Seetharam, B., Podell, E., & Alpers, D. H. (1978). Effect of Proteolytic Enzymes on the Binding of Cobalamin to R Protein and Intrinsic Factor: *In Vitro* Evidence That a Failure to Partially Degrade Protein is Responsible for Cobalamin Malabsorption in Pancreatic Insufficiency. *Journal of Clinical Investigation, 61*(1), 47.

Anal, A. K., Tobiassen, A., Flanagan, J., & Singh, H. (2008). Preparation and Characterization of Nanoparticles Formed by Chitosan-Caseinate Interactions. *Colloids and Surfaces B: Biointerfaces, 64*(1), 104-110.

Anderson, J. W., Johnstone, B. M., & Cook-Newell, M. E. (1995). Meta-Analysis of the Effects of Soy protein Intake on Serum Lipids. *New England Journal of Medicine, 333*(5), 276-282.

Andrès, E., Federici, L., Affenberger, S., Vidal-Alaball, J., Loukili, N. H., Zimmer, J., & Kaltenbach, G. (2007). B12 Deficiency: A Look Beyond Pernicious Anemia. *Journal of Family Practice, 56*(7), 537-544.

Andrès, E., Loukili, N. H., Noel, E., Ka ltenbach, G., Abdelgheni, M. B., Perrin, A. E., Noblet-Dick, M., Maloisel, F., Schlienger, J. L., & Blicklé, J. F. (2004). Vitamin B_{12} (Cobalamin) Deficiency in Elderly Patients. *Canadian Medical Association Journal, 171*(3), 251-259.

Anton, N., Benoit, J. P., & Saulnier, P. (2008). Design and Production of Nanoparticles Formulated From Nano-Emulsion Templates-a Review. *Journal of Controlled Release, 128*(3), 185-199.

Arangoa, M. A., Campanero, M. A., Renedo, M. J., Ponchel, G., & Irache, J. M. (2001). Gliadin Nanoparticles as Carriers for the Oral Administration of Lipophilic Drugs. Relationships Between Bioadhesion and Pharmacokinetics. *Pharmaceutical Research*, *18*(11*)*, 1521-1527.

Arrondo, J. L. R., Muga, A., Castresana, J., & Goni, F. M. (1993). Quantitative Studies of the Structure of Proteins in Solution by Fourier-Transform Infrared Spectroscopy. *Progress in Biophysics and Molecular Biology*, *159*, 23-56.

Artursson, P., Ungell, A. L., & Löfroth, J. E. (1993). Selective Paracellular Permeability in Two Models of Intestinal Absorption: Cultured Monolayers of Human Intestinal Epithelial Cells and Rat Intestinal Segments. *Pharmaceutical Research, 10*(8), 1123-1129.

Atuma, C., Strugala, V., Allen, A., & Holm, L. (2001). The Adherent Gastrointestinal Mucus Gel Layer: Thickness and Physical State i*n Vivo*. *American Journal of Physiology-Gastrointestinal and Liver Physiology, 280*(5), G922-G929.

Augustin, M. A., Sanguansri, L., & Bode, O. (2006). Maillard Reaction Products as Encapsulants for fish Oil Powders. *Journal of Food Science, 71*(2), E25-E32.

Bagheri, L., Madadlou, A., Yarmand, M., & Mousavi, M. E. (2013). Nanoencapsulation of Date Palm Pit Extract in Whey Protein Particles Generated via Desolvation Method. *Food Research International*, *51* (2), 866-871.

Bagre, A. P., Jain, K., & Jain, N. K. (2013). Alginate Coated Chitosan Core Shell Nanoparticles for Oral Delivery of Enoxaparin: *In Vitro* and *in Vivo* Assessment. *International Journal of Pharmaceutics, 456*(1), 31-40.

Bajaj, A., Samanta, B., Yan, H., Jerry, J., & Rotello, V. M. (2009). Stability, Toxicity and Differential Cellular Uptake of Protein Passivated-Fe_3O_4 Nanoparticles. *Journal of Materials Chemistry, 19*(35), 6328-6331.

Bandekar, J. (1992). Amide Modes and Protein Conformation. *Biochimica et Biophysica Acta-Protein Structure and Molecular Enzymology*, *1120*(2), 123-143.

Bareford, L. M., & Swaan, P. W. (2007). Endocytic Mechanisms for Targeted Drug Delivery. *Advanced Drug Delivery Reviews, 59*(8), 748-758.

Barthe, L., Woodley, J., & Houin, G. (1999). Gastrointestinal Absorption of Drugs: Methods and Studies. *Fundamental & Clinical Pharmacology, 13*(2), 154-168.

Basu, S. K., Thomas, J. E., & Acharya, S. N. (2007). Prospects for Growth in Global Nutraceutical and Functional Food Markets: a Canadian Perspective. *Australian Journal of Basic and Applied Sciences, 1*(4), 637-649.

Bedine, M. S. (2000). Textbook of Gastroenterology. *Gastroenterology, 118*(5), 984.

Behrens, I., Pena, A. I. V., Alonso, M. J., & Kissel, T. (2002). Comparative Uptake Studies of Bioadhesive and Non-bioadhesive Nanoparticles in Human Intestinal Cell Lines and Rats: The Effect of Mucus on Particle Adsorption and Transport. *Pharmaceutical Research, 19*(8), 1185-1193.

Belatik, A., Hotchandani, S., Bariyanga, J., & Tajmir-Riahi, H. A. (2012). Binding Sites of Retinol and Retinoic Acid with Serum Albumins. *European Journal of Medicinal Chemistry, 48*, 114-123.

Bell, L. (2001). Stability Testing of Nutraceuticals and Functional Foods. *Handbook of Nutraceuticals and Functional Foods*, 501-516.

Beloqui, A., Solinís, M. Á., Gascón, A. R., del Pozo-Rodríguez, A., des Rieux, A., & Préat, V. (2013). Mechanism of Transport of Saquinavir-Loaded Nanostructured Lipid Carriers across the Intestinal Barrier. *Journal of Controlled Release*, *166*(2), 115-123.

Bengali, Z., C Rea, J., & Shea, L. D. (2007). Gene Expression and Internalization Following Vector Adsorption to Immobilized Proteins: Dependence on Protein Identity and Density. *The Journal of Gene Medicine, 9*(8), 668-678.

Berlin, H., Berlin, R., & Brante, G. (1968). Oral Treatment of Pernicious Anemia with High Doses of Vitamin B_{12} Without Intrinsic Factor. *Acta Medica Scandinavica, 184*(1-6), 247-258.

Bernkop-Schnürch, A. (2013). Reprint of: Nanocarrier Systems for Oral Drug Delivery: Do We Really Need Them? *European Journal of Pharmaceutical Sciences, 50*(1), 2-7.

Bi, S., Ding, L., Tian, Y., Song, D., Zhou, X., Liu, X., & Zhang, H. (2004). Investigation of the Interaction Between Flavonoids and Human Serum Albumin. *Journal of Molecular Structure, 703*(1), 37-45.

Bi, S., Song, D., Kan, Y., Xu, D., Tian, Y., Zhou, X., & Zhang, H. (2005). Spectroscopic Characterization of Effective Components Anthraquinones in Chinese Medicinal Herbs Binding with Serum Albumins. *Spectrochimica Acta Part A: Molecular and Biomolecular Spectroscopy, 62*(1–3), 203-212.

Björk, E., Isaksson, U., Edman, P., & Artursson, P. (1995). Starch Microspheres Induce Pulsatile Delivery of Drugs and Peptides Across the Epithelial Barrier by Reversible Separation of the Tight Junctions. *Journal of Drug Targeting, 2*(6), 501-507.

Borges, O., Cordeiro-da-Silva, A., Romeijn, S. G., Amidi, M., de Sousa, A., Borchard, G., & Junginger, H. E. (2006). Uptake Studies in Rat Peyer's Patches, Cytotoxicity and Release Studies of Alginate Coated Chitosan Nanoparticles for Mucosal Vaccination. *Journal of Controlled Release, 114*(3), 348-358.

Bouchemal, K., Briançon, S., Perrier, E., & Fessi, H. (2004). Nano-Emulsion Formulation Using Spontaneous Emulsification: Solvent, Oil and Surfactant Optimisation. *International Journal of Pharmaceutics, 280*(1), 241-251.

Boye, J. I., Ma, C. Y., Ismail, A., & Alli, I. (1996). Effects of Physicochemical Factors on the Secondary Structure of β-Lactoglobulin. *Journal of Dairy Research*, *63*, 97-109.

Bradford, M. M. (1976). A Rapid and Sensitive Method for the Quantization of Microgram Quantities of Protein Utilizing the Principle of Protein Dye Binding. *Analytical Biochemistry*, *172*, 248-254.

Brannon-Peppas, L. (1995). Recent Advances on the Use of Biodegradable Microparticles and Nanoparticles in Controlled Drug Delivery. *International Journal of Pharmaceutics, 116*(1), 1-9.

Byler, D. M., & Susi, H. (1986). Examination of the Secondary Structure of Proteins by Deconvoluted FTIR Spectra. *Biopolymers*, *25*, 469-487.

Calvo, P., Remunan-Lopez, C., Vila-Jato, J., & Alonso, M. (1997). Novel Hydrophilic Chitosan-polyethylene Oxide Nanoparticles as Protein Carriers. *Journal of Applied Polymer Science, 63*(1), 125-132.

Campbell, I. (2009). The Mouth, Stomach and Intestines. *Anaesthesia & Intensive Care Medicine, 10*(7), 336-338.

Canada Health (1998). Policy Paper on Nutraceutical/Functional Foods and Health Claims on Food.

Carroll, K. K. (1991). Review of Clinical-Studies on Cholesterol-Lowering Response to Soy Protein. *Journal of the American Dietetic Association, 91*(7), 820-827.

Casso, D., White, E., Patterson, R. E., Agurs-Collins, T., Kooperberg, C., & Haines, P. S. (2000). Correlates of Serum Lycopene in Older Women. *Nutrition and Cancer, 36*(2), 163-169.

Catizone, A., Medolago Albani, L., Reola, F., & Alescio, T. (1993). A Quantitative Assessment of Non-specific Pinocytosis by Human Endothelial Cells Surviving in Vitro. *Cellular and Molecular Biology, 39*(2), 155-169.

Charbonneau, D. M., & Tajmir-Riahi, H. A. (2010). Study on the Interaction of Cationic Lipids with Bovine Serum Albumin. *Journal of Physical Chemistry B, 114*(2), 1148-1155.

Charve, J. P., & Reineccius, G. A. (2009). Encapsulation Performance of Proteins and Traditional Materials for Spray Dried Flavors. *Journal of Agricultural and Food Chemistry, 57*(6), 2486-2492.

Chau, C. F., Wu, S. H., & Yen, G. C. (2007). The Development of Regulations for Food Nanotechnology. *Trends in Food Science & Technology, 18*(5), 269-280.

Chaudhry, Q., George, C., & Watkins, R. (2007). Nanotechnology Regulation: Developments in the United Kingdom. *New Global Frontiers in Regulation: The Age of Nanotechnology*, 212.

Chavda, H. V., & Patel, C. N. (2011). Preparation and In Vitro Evaluation of a Stomach Specific Drug Delivery System Based on Superporous Hydrogel Composite. *Indian Journal of Pharmaceutical Sciences, 73*(1), 30-37.

Chen, L. Y., & Subirade, M. (2006). Alginate-Whey Protein Granular Microspheres as Oral Delivery Vehicles for Bioactive Compounds. *Biomaterials, 27*(26), 4646-4654.

Chen, L. Y., & Subirade, M. (2009). Elaboration and Characterization of Soy/Zein Protein Microspheres for Controlled Nutraceutical Delivery. *Biomacromolecules, 10*(12), 3327-3334.

Chen, L. Y., Hebrard, G., Beyssac, E., Denis, S., & Subirade, M. (2010). *In Vitro* Study of the Release Properties of Soy-Zein Protein Microspheres with a Dynamic Artificial Digestive System. *Journal of Agricultural and Food Chemistry, 58*(17), 9861-9867.

Chen, L. Y., Remondetto, G. E., & Subirade, M. (2006). Food Protein-Based Materials as Nutraceutical Delivery Systems. *Trends in Food Science & Technology, 17*(5), 272-283.

Chen, L. Y., Remondetto, G., Rouabhia, M., & Subirade, M. (2008). Kinetics of the Breakdown of Cross-Linked Soy Protein Films for Drug Delivery. *Biomaterials, 29*(27), 3750-3756.

Chen, L., & Subirade, M. (2005). Chitosan/β-Lactoglobulin Core-Shell Nanoparticles as Nutraceutical Carriers. *Biomaterials, 26*(30), 6041-6053.

Chen, L., & Subirade, M. (2006). Alginate-Whey Protein Granular Microspheres as Oral Delivery Vehicles for Bioactive Compounds. *Biomaterials, 27,* 4646-4654.

Chen, L., & Subirade, M. (2008). Food-Protein-Derived Materials and Their Use as Carriers and Delivery Systems for Active Food Components. In N. Garti (Ed.), *Delivery and Controlled Release of Bioactives in Foods and Nutraceuticals* (pp. 251-278). Cambridge: Woodhead Publishing Ltd.

Chen, L., & Subirade, M. (2009). Elaboration and Characterization of Soy/Zein Protein Microspheres for Controlled Nutraceutical Delivery. *Biomacromolecules*, *10*, 3327-3334.

Chen, M. C., Wong, H. C., Lin, K. J., Chen, H. L., Wey, S. P., Sonaje, K., Lin, Y. H., Chu, C. Y., & Sung, H. W. (2009). The Characteristics, Biodistribution and Bioavailability of a Chitosan-Based Nanoparticulate System for the Oral Delivery of Heparin. *Biomaterials, 30*(34), 6629-6637.

Cheng, J. J., Teply, B. A., Sherifi, I., Sung, J., Luther, G., Gu, F. X., Levy-Nissenbaum, E., Radovic-Moreno, A. F., Langer, R., & Farokhzad, O. C. (2007). Formulation of Functionalized PLGA-PEG Nanoparticles for *in Vivo* Targeted Drug Delivery. *Biomaterials, 28*(5), 869-876.

Chiu, Y. W., & Tan, C. S. (2001). Regeneration of Supercritical Carbon Dioxide by Membrane at Near Critical Conditions. *The Journal of Supercritical Fluids, 21*(1), 81-89.

Chu, B. S., Ichikawa, S., Kanafusa, S., & Nakajima, M. (2007). Preparation of Protein-Stabilized β-Carotene Nanodispersions by Emulsification-Evaporation Method. *Journal of the American Oil Chemists' Society, 84*(11), 1053-1062.

Chung, H. E., Park, D. H., Choy, J. H., & Choi, S. J. (2012). Intracellular Trafficking Pathway of Layered Double Hydroxide Nanoparticles in Human Cells: Size-Dependent Cellular Delivery. *Applied Clay Science, 65*, 24-30.

Congdon, R. W., Muth, G. W., & Splittgerber, A. G. (1993). The Binding Interaction of Coomassie Blue with Proteins. *Analytical Biochemistry, 213*(2), 407-413.

Conner, S. D., & Schmid, S. L. (2003). Regulated Portals of Entry into the Cell. *Nature, 422*(6927), 37-44.

Couvreur, P., & Puisieux, F. (1993). Nano- and Microparticles for the Delivery of Polypeptides and Proteins. *Advanced Drug Delivery Reviews, 10*(2), 141-162.

Couvreur, P., Dubernet, C., & Puisieux, F. (1995). Controlled Drug Delivery with Nanoparticles: Current Possibilities and Future Trends. *European Journal of Pharmaceutics and Biopharmaceutics, 41*(1), 2-13.

Dali-Youcef, N., & Andrès, E. (2009). An Update on Cobalamin Deficiency in Adults. *QJM, 102*(1), 17-28.

Damodaran, S., & Kinsella, J. E. (1981). Interaction of Carbonyls with Soy Protein-Conformational Effects. *Journal of Agricultural and Food Chemistry, 29*(6), 1253-1257.

Danhier, F., Ansorena, E., Silva, J. M., Coco, R., Le Breton, A., & Préat, V. (2012). PLGA-based Nanoparticles: An Overview of Biomedical Applications. *Journal of Controlled Release, 161*(2), 505-522.

Dausend, J., Musyanovych, A., Dass, M., Walther, P., Schrezenmeier, H., Landfester, K., & Mailänder, V. (2008). Uptake Mechanism of Oppositely Charged Fluorescent Nanoparticles in HeLa Cells. *Macromolecular Bioscience, 8*(12), 1135-1143.

Davda, J., & Labhasetwar, V. (2002). Characterization of Nanoparticle Uptake by Endothelial Cells. *International Journal of Pharmaceutics, 233*(1), 51-59.

de Britto, D., de Moura, M. R., Aouada, F. A., Mattoso, L. H. C., & Assis, O. B. G. (2012). N,N,N-Trimethyl Chitosan Nanoparticles as a Vitamin Carrier System. *Food Hydrocolloids, 27*(2), 487-493.

De Wolf, F. A., & Brett, G. M. (2000). Ligand-Binding Proteins: Their Potential for Application in Systems for Controlled Delivery and Uptake of Ligands. *Pharmacological Reviews, 52*(2), 207-236.

Deitch, E. (1992). Nutrition and the Gut Mucosal Barrier. *Current Opinion in General Surgery,* 85-91.

del Pozo-Rodriguez, A., Pujals, S., Delgado, D., Solinís, M. A., Gascón, A. R., Giralt, E., & Pedraz, J. L. (2009). A Proline-Rich Peptide Improves Cell Transfection of Solid Lipid Nanoparticle-Based Non-Viral Vectors. *Journal of Controlled Release, 133*(1), 52-59.

del Pozo-Rodriguez, A., Pujals, S., Delgado, D., Solinís, M., Gascón, A., Giralt, E., & Pedraz, J. (2009). A proline-rich Peptide Improves Cell Transfection of Solid Lipid Nanoparticle-based Non-viral Vectors. *Journal of Controlled Release, 133*(1), 52-59.

Delie, F., & Rubas, W. (1997). A Human Colonic Cell Line Sharing Similarities with Enterocytes as a Model to Examine Oral Absorption: Advantages and Limitations of the Caco-2 Model. *Critical Reviews™ in Therapeutic Drug Carrier Systems, 14*(3), 221-286.

des Rieux, A., Fievez, V., Garinot, M., Schneider, Y. J., & Préat, V. (2006). Nanoparticles as Potential Oral Delivery Systems of Proteins and Vaccines: A Mechanistic Approach. *Journal of Controlled Release, 116*(1), 1-27.

Desai, M. P., Labhasetwar, V., Amidon, G. L., & Levy, R. J. (1996). Gastrointestinal Uptake of Biodegradable Microparticles: Effect of Particle Size. *Pharmaceutical Research, 13*(12), 1838-1845.

Desai, M. P., Labhasetwar, V., Walter, E., Levy, R. J, & Amidon, G. L. (1997). The Mechanism of Uptake of Biodegradable Microparticles in Caco-2 Cells is Size Dependent. *Pharmaceutical Research*, *14*, 1568-1573.

Diarrassouba, F., Liang, L., Remondetto, G., & Subirade, M. (2013). Nanocomplex Formation Between Riboflavin and β-Lactoglobulin: Spectroscopic Investigation and Biological Characterization. *Food Research International, 52*(2), 557-567.

Ding, F., Han, B. Y., Liu, W., Zhang, L., & Sun, Y. (2010). Interaction of Imidacloprid with Hemoglobin by Fluorescence and Circular Dichroism. *Journal of Fluorescence, 20*(3), 753-762.

Dixon, D. J., Johnston, K. P., & Bodmeier, R. A. (1993). Polymeric Materials Formed by Precipitation with a Compressed Fluid Antisolvent. *American Institute of Chemical Engineers Journal, 39*(1), 127-139.

Dragicevic-Curic, N., Gräfe, S., Gitter, B., Winter, S., & Fahr, A. (2010). Surface Charged Temoporfin-Loaded Flexible Vesicles: *In Vitro* Skin Penetration Studies and Stability. I*nternational Journal of Pharmaceutics*, *384*(1-2), 100-108.

Dube, A., Nicolazzo, J. A., & Larson, I. (2010). Chitosan Nanoparticles Enhance the Intestinal Absorption of the Green Tea Catechins (+)-Catechin and (-)-Epigallocatechin Gallate. *European Journal of Pharmaceutical Sciences, 41*(2), 219-225.

Dunne, M., Corrigan, O., & Ramtoola, Z. (2000). Influence of Particle Size and Dissolution Conditions on the Degradation Properties of Polylactide-co-glycolide Particles. *Biomaterials, 21*(16), 1659-1668.

Eldridge, J. H., Hammond, C. J., Meulbroek, J. A., Staas, J. K., Gilley, R. M., & Tice, T. R. (1990). Controlled Vaccine Release in the Gut-Associated

Lymphoid Tissues. I. Orally Administered Biodegradable Microspheres Target the Peyer's Patches. *Journal of Controlled Release, 11*(1), 205-214.
El-Sayed, M., Ginski, M., Rhodes, C., & Ghandehari, H. (2002). Transepithelial Transport of Poly (Amidoamine) Dendrimers Across Caco-2 Cell Monolayers. Journal of Controlled Release, 81(3), 355-365.
Elvassore, N., Bertucco, A., & Caliceti, P. (2001). Production of Insulin-Loaded Poly (Ethylene Glycol)/Poly (L-Lactide)(PEG/PLA) Nanoparticles by Gas Antisolvent Techniques. *Journal of Pharmaceutical Sciences, 90*(10), 1628-1636.
Elzoghby, A. O., Abo El-Fotoh, W. S., & Elgindy, N. A. (2011). Casein-Based Formulations as Promising Controlled Release Drug Delivery Systems. *Journal of Controlled Release, 153*(3), 206-216.
Elzoghby, A. O., Samy, W. M., & Elgindy, N. A. (2012). Protein-Based Nanocarriers as Promising Drug and Gene Delivery Systems. *Journal of Controlled Release, 161*(1), 38-49.
Ermens, A. A. M., Vlasveld, L. T., & Lindemans, J. (2003). Significance of Elevated Cobalamin (Vitamin B_{12}) Levels in Blood. *Clinical Biochemistry, 36*(8), 585-590.
Ezpeleta, I., Irache, J. M., Stainmesse, S., Chabenat, C., Gueguen, J., Popineau, Y., & Orecchioni, A. M. (1996). Gliadin Nanoparticles for the Controlled Release of all-Trans-Retinoic Acid. *International Journal of Pharmaceutics, 131*(2), 191-200.
Feng, X. Z., Lin, Z., Yang, L. J., Wang, C., & Bai, C. L. (1998). Investigation of the Interaction Between Acridine Orange and Bovine Serum Albumin. *Talanta, 47*(5), 1223-1229.
Florence, A. T. (2005). Nanoparticle Uptake by the Oral Route: Fulfilling its Potential? *Drug Discovery Today: Technologies, 2*(1), 75-81.
Foged, C., Brodin, B., Frokjaer, S., & Sundblad, A. (2005). Particle Size and Surface Charge Affect Particle Uptake by Human Dendritic Cells in an *in Vitro* Model. *International Journal of Pharmaceutics, 298*(2), 315-322.
Förster, C. (2008). Tight Junctions and the Modulation of Barrier Function in Disease. *Histochemistry and Cell Biology, 130*(1), 55-70.
Förster, T. (1965). *Delocalized Excitation and Excitation Transfer*: Florida State University.
Franzen, K. L., & Kinsella, J. E. (1976). Functional Properties of Succinylated and Acetylated Soy Protein. *Journal of Agricultural and Food Chemistry, 24*(4), 788-795.
Fukushima, D. (1968). Internal Structure of 7S and 11S Globulin Molecules in Soybean Proteins. *Cereal Chemistry, 45*(3), 203-224.
Fukushima, D. (1991). Recent Progress of Soybean Protein Foods: Chemistry, Technology, and Nutrition. *Food Reviews International, 7*(3), 323-351.
Gabor, F., Bogner, E., Weissenboeck, A., & Wirth, M. (2004). The Lectin-Cell Interaction and its Implications to Intestinal Lectin-Mediated Drug Delivery. *Advanced Drug Delivery Reviews, 56*(4), 459-480.

Galindo-Rodriguez, S. A., Allemann, E., Fessi, H., & Doelker, E. (2005). Polymeric Nanoparticles for Oral Delivery of Drugs and Vaccines: a Critical Evaluation of in Vivo Studies. *Critical Reviews™ in Therapeutic Drug Carrier Systems, 22*(5), 419-464.

Gamboa, J. M., & Leong, K. W. (2013). *In Vitro* and *in Vivo* Models for the Study of Oral Delivery of Nanoparticles. *Advanced Drug Delivery Reviews*, *65*(6), 800-810.

Gaumet, M., Gurny, R., & Delie, F. (2009). Localization and Quantification of Biodegradable Particles in an Intestinal Cell Model: the Influence of Particle Size. *European Journal of Pharmaceutical Sciences, 36*(4), 465-473.

George, M., & Abraham, T. E. (2006). Polyionic Hydrocolloids for the Intestinal Delivery of Protein Drugs: Alginate and Chitosan-A Review. *Journal of Controlled Release, 114*(1), 1-14.

Ghaffarian, R., Bhowmick, T., & Muro, S. (2012). Transport of Nanocarriers Across Gastrointestinal Epithelial Cells by a New Transcellular Route Induced by Targeting ICAM-1. *Journal of Controlled Release, 163*(1), 25-33.

Ghosh, K. S., Sen, S., Sahoo, B. K., & Dasgupta, S. (2009). A Spectroscopic Investigation into the Interactions of 3′-O-Carboxy Esters of Thymidine with Bovine Serum Albumin. *Biopolymers, 91*(9), 737-744.

Giannasca, P. J., Giannasca, K. T., Leichtner, A. M., & Neutra, M. R. (1999). Human Intestinal M Cells Display the Sialyl Lewis a Antigen. *Infection and immunity, 67*(2), 946-953.

Girard, M., Turgeon, S. L., & Gauthier, S. F. (2002). Interbiopolymer Complexing Between β-Lactoglobulin and Low-and High-Methylated Pectin Measured by Potentiometric Titration and Ultrafiltration. *Food Hydrocolloids, 16*(6), 585-591.

Giroux, H. J., & Britten, M. (2011). Encapsulation of Hydrophobic Aroma in Whey Protein Nanoparticles. *Journal of Microencapsulation, 28*(5), 337-343.

Giroux, H. J., Houde, J., & Britten, M. (2010). Preparation of Nanoparticles from Denatured Whey Protein by pH-Cycling Treatment. *Food Hydrocolloids, 24*(4), 341-346.

Gülseren, İ., Fang, Y., & Corredig, M. (2012). Zinc Incorporation Capacity of Whey Protein Nanoparticles Prepared with Desolvation with Ethanol. *Food Chemistry, 135*(2), 770-774.

Guo, M., Que, C. L., Wang, C. H., Liu, X. Z., Yan, H. S., & Liu, K. L. (2011). Multifunctional Superparamagnetic Nanocarriers with Folate-Mediated and pH-Responsive Targeting Properties for Anticancer Drug Delivery. *Biomaterials*, *32*, 185-194.

Guo, Y., Yue, Q., Gao, B., & Zhong, Q. (2010). Spectroscopic Studies on the Interaction Between Disperse Blue SBL and Bovine Derum Albumin. *Journal of Luminescence, 130*(8), 1384-1389.

Hamman, J. H., Enslin, G. M., & Kotzé, A. F. (2005). Oral Delivery of Peptide Drugs. *BioDrugs, 19*(3), 165-177.

Han, X., Gelein, R., Corson, N., Wade-Mercer, P., Jiang, J., Biswas, P., Finkelstein, J. N., Elder, A., & Oberdörster, G. (2011). Validation of an LDH Assay for Assessing Nanoparticle Toxicity. *Toxicology, 287*(1), 99-104.

Harley, V. S., Dance, D. A., Drasar, B. S., & Tovey, G. (1997). Effects of Burkholderia Pseudomallei and Other Burkholderia Species on Eukaryotic Cells in Tissue Culture. *Microbios, 96*(384), 71-93.

Harush-Frenkel, O., Debotton, N., Benita, S., & Altschuler, Y. (2007). Targeting of Nanoparticles to the Clathrin-Mediated Endocytic Pathway. *Biochemical and Biophysical Research Communications, 353*(1), 26-32.

Hasler, C. M. (2000). The Changing Face of Functional Foods. *Journal of the American College of Nutrition, 19*(sup5), 499S-506S.

Hattori, M., Watabe, A., & Takahashi, K. (1995). β-Lactoglobulin Protects β-Ionone Related Compounds from Degradation by Heating, Oxidation, and Irradiation. *Bioscience, Biotechnology, and Biochemistry, 59*(12), 2295-2297.

He, B., Jia, Z. R., Du, W. W., Yu, C., Fan, Y. C., Dai, W. B., Yuan, L., Zhang, H., Wang, X. Q., & Wang, J. C. (2013). The Transport Pathways of Polymer Nanoparticles in MDCK Epithelial Cells. *Biomaterials*, *34* (17), 4309-4326.

He, C. B., Hu, Y. P., Yin, L. C., Tang, C., & Yin, C. H. (2010). Effects of Particle Size and Surface Charge on Cellular Uptake and Biodistribution of Polymeric Nanoparticles. *Biomaterials, 31*(13), 3657-3666.

He, C., Hu, Y., Yin, L., Tang, C., & Yin, C. (2010). Effects of Particle Size and Surface Charge on Cellular Uptake and Biodistribution of Polymeric Nanoparticles. *Biomaterials, 31*(13), 3657-3666.

He, C., Yin, L., Tang, C., & Yin, C. (2012). Size-Dependent Absorption Mechanism of Polymeric Nanoparticles for Oral Delivery of Protein Drugs. *Biomaterials, 33*(33), 8569-8578

He, W., Li, Y., Xue, C., Hu, Z., Chen, X., & Sheng, F. (2005). Effect of Chinese Medicine Alpinetin on the Structure of Human Serum Albumin. *Bioorganic & Medicinal Chemistry, 13*(5), 1837-1845.

Health-Canada. (1998). Policy Paper: Nutraceuticals/Functional Foods and Health Claims on Foods. *Government of Canada: Therapeutic Products Program and the Food Directorate from the Health Protection Branch*.

Helms, V. (2008). *Principles of Computational Cell Biology*: Wiley. com.

Hewlett, L. J., Prescott, A. R., & Watts, C. (1994). The Coated Pit and Macropinocytic Pathways Serve Distinct Endosome Populations. *Journal of Cell Biology, 124,* 689-689.

Hidalgo, I. J., Raub, T. J., & Borchardt, R. T. (1989). Characterization of the Human Colon Carcinoma Cell Line (Caco-2) as a Model System for Intestinal Epithelial Permeability. *Gastroenterology, 96*(3), 736-749.

Hillaireau, H., & Couvreur, P. (2009). Nanocarriers' Entry into the Cell: Relevance to Drug Delivery. *Cellular and Molecular Life Sciences, 66*(17), 2873-2896.

Holick, M. F. (2007). Vitamin D Deficiency. *New England Journal of Medicine, 357*(3), 266-281.

Hoshinoa, Y., Koide, H., Furuya, K., Haberaecker W. W., Lee, S. H., Kodama, T., Kanazawa, H., Oku, N., & Sheab, K. J. (2012). The rational design of a synthetic polymer nanoparticle that neutralizes a toxic peptide *in vivo*. *Proceedings of the National Academy of Sciences of the United States of America, 109* (1), 33-38.

Hou, H. N., Qi, Z. D., OuYang, Y. W., Liao, F. L., Zhang, Y., & Liu, Y. (2008). Studies on Interaction Between Vitamin B_{12} and Human Serum Albumin. *Journal of Pharmaceutical and Biomedical Analysis, 47*(1), 134-139.

Hu, J. H., Johnston, K. P., & Williams III, R. O. (2004). Nanoparticle Engineering Processes for Enhancing the Dissolution Rates of Poorly Water Soluble Drugs. *Drug Development and Industrial Pharmacy, 30*(3), 233-245.

Huang, M., Ma, Z. S., Khor, E., & Lim, L. Y. (2002). Uptake of FITC-Chitosan Nanoparticles by A549 Cells. *Pharmaceutical Research, 19*(10), 1488-1494.

Huang, Q. R., Yu, H. L., & Ru, Q. M. (2010). Bioavailability and Delivery of Nutraceuticals Using Nanotechnology. *Journal of Food Science, 75*(1), R50-R57.

Hugenschmidt, S., Schwenninger, S. M., & Lacroix, C. (2011). Concurrent High Production of Natural Folate and Vitamin B_{12} Using a Co-culture Process with Lactobacillus Plantarum SM39 and Propionibacterium Freudenreichii DF13. *Process Biochemistry, 46*(5), 1063-1070.

Hussain, N., Jaitley, V., & Florence, A. T. (2001). Recent Advances in the Understanding of Uptake of Microparticulates Across the Gastrointestinal Lymphatics. *Advanced Drug Delivery Reviews, 50*(1), 107-142.

Hwang, D. C., & Damodaran, S. (1996). Chemical Modification Strategies for Synthesis of Protein-Based Hydrogel. *Journal of Agricultural and Food Chemistry*, *44*(3), 751-758.

Issa, M. M., Köping-Höggård, M., & Artursson, P. (2005). Chitosan and the Mucosal Delivery of Biotechnology Drugs. *Drug Discovery Today: Technologies, 2(*1), 1-6.

Jani, P., Halbert, G. W., Langridge, J., & Florence, A. T. (1989). The Uptake and Translocation of Latex Nanospheres and Microspheres after Oral Administration to Rats. *Journal of Pharmacy and Pharmacology, 41*(12), 809-812.

Jayabharathi, J., Thanikachalam, V., & Venkatesh Perumal, M. (2011). Mechanistic Investigation on Binding Interaction of Bioactive Imidazole with Protein Bovine Serum Albumin-A Biophysical Study. *Spectrochimica Acta Part A: Molecular and Biomolecular Spectroscopy, 79*(3), 502-507.

Jenkins, D. J. A., Kendall, C. W. C., Vuksan, V., Vidgen, E., Parker, T., Faulkner, D., Mehling, C. C., Garsetti, M., Testolin, G., & Cunnane, S. C. (2002). Soluble Fiber Intake at a Dose Approved by the US Food and Drug Administration for a Claim of Health Benefits: Serum Lipid Risk Factors for Cardiovascular Disease Assessed in a Randomized Controlled Crossover Trial. *The American Journal of Clinical Nutrition, 75*(5), 834-839.

Jiang, J., Chen, J., & Xiong, Y. L. (2009). Structural and Emulsifying Properties of Soy Protein Isolate Subjected to Acid and Alkaline pH-Shifting Processes. *Journal of Agricultural and Food Chemistry*, *57*, 7576-7583.

Jiang, L., Li, X., Liu, L., & Zhang, Q. (2013). Cellular Uptake Mechanism and Intracellular Fate of Hydrophobically Modified Pullulan Nanoparticles. *International Journal of Nanomedicine, 8,* 1825-1834.

Jiang, M., Gan, L., Zhu, C., Dong, Y., Liu, J., & Gan, Y. (2012). Cationic Core–shell Liponanoparticles for Ocular Gene Delivery. *Biomaterials, 33*(30), 7621-7630.

Jiang, W., Kim, B. Y., Rutka, J. T., & Chan, W. C. (2008). Nanoparticle-Mediated Cellular Response is Size-Dependent. *Nature Nanotechnology, 3*(3), 145-150.

Jin, H., Heller, D. A., Sharma, R., & Strano, M. S. (2009). Size-dependent Cellular Uptake and Expulsion of Single-walled Carbon Nanotubes: Single Particle Tracking and a Generic Uptake Model for Nanoparticles. *ACS Nano, 3*(1), 149-158.

Jo, G. H., Yu, J. H., Yun, J. H., Hwang, S. J., & Woo, J. S. (2002). Preparation of Amorphous Form of Cefuroxime Axetil Using Supercritical Fluid Processing. In *Controlled Release Society 29th Annual Meeting Proceedings*, (pp. 20-25).

Jones, A. T. (2007). Macropinocytosis: Searching for an Endocytic Identity and Role in the Uptake of Cell Penetrating Peptides. *Journal of Cellular and Molecular Medicine, 11*(4), 670-684.

Jun, J. Y., Nguyen, H. N., Paik, S. Y. R., Chun, H. S., Kang, B. C., & Ko, S. (2011). Preparation of Size-Controlled Bovine Serum Albumin (BSA) Nanoparticles by a Modified Desolvation Method. *Food Chemistry*, *127*(4), 1892-1898.

Jung, J., & Perrut, M. (2001). Particle Design Using Supercritical Fluids: Literature and Patent Survey. *The Journal of Supercritical Fluids, 20*(3), 179-219.

Jung, T., Kamm, W., Breitenbach, A., Kaiserling, E., Xiao, J., & Kissel, T. (2000). Biodegradable Nanoparticles for Oral Delivery of Peptides: Is There a Role for Polymers to Affect Mucosal Uptake? *European Journal of Pharmaceutics and Biopharmaceutics, 50*(1), 147-160.

Junginger, H. (1996). Drug Absorption Enhancement, Concepts, Possibilities, Limitations and Trends. *Journal of Drug Targeting, 4*(1), 51-52.

Kalra, E. K. (2003). Nutraceutical-Definition and Introduction. *American Association of Pharmaceutical Scientists, 5*(3), 27-28.

Kawashim, Y. (2001). Preface Nanoparticulate Systems for Improved Drug Delivery. *Advanced Drug Delivery Reviews*, *47*(1), 1-2.

Kelly, S. M., Jess, T. J., & Price, N. C. (2005). How to Study Proteins by Circular Dichroism? *Biochimca et Biophysica Acta*, *1751*, 119-139.

Kerč, J., Srčič, S., Knez, Ž., & Senčar-Božič, P. (1999). Micronization of Drugs Using Supercritical Carbon Dioxide. *International Journal of Pharmaceutics, 182*(1), 33-39.

Kerss, S., Allen, A., & Garner, A. (1982). A Simple Method for Measuring Thickness of the Mucus Gel Layer Adherent to Rat, Frog and Human Gastric

Mucosa: Influence of Feeding, Prostaglandin, N-Acetylcysteine and Other Agents. *Clinical Science, 63*, 187-195.

Kesisoglou, F., Panmai, S., & Wu, Y. (2007). Application of Nanoparticles in Oral Delivery of Immediate Release Formulations. *Current Nanoscience, 3*(2), 183-190.

Kikic, I., Moneghini, M., Perissutti, B., & Voinovich, D. (2000). Improvement of Carbamazepine Dissolution Characteristics Using Supercritical Carbon Dioxide. In *Proceedings of the Seventh Meeting on Supercritical Fluids, Tome*, vol. 1 (pp. 95-100).

Kim, D., & Cho, G. (2006). Nanofood and its Materials as Nutrient Delivery System (NDS). *Agricultural Chemistry and Biotechnology, 49*(2), 39-47.

Kim, Y. D., & Morr, C. V. (1996). Microencapsulation Properties of Gum Arabic and Several Food Proteins: Spray-Dried Orange Oil Emulsion Particles. *Journal of Agricultural and Food Chemistry, 44*(5), 1314-1320.

Kinsella, J. E. (1979). Functional Properties of Soy Proteins. *Journal of the American Oil Chemists' Society, 56*(3), 242-258.

Kiss, A. L., & Botos, E. (2009). Endocytosis via Caveolae: Alternative Pathway with Distinct Cellular Compartments to Avoid Lysosomal Degradation? J*ournal of Cellular and Molecular Medicine, 13*(7), 1228-1237.

Kitchens, K. M., Kolhatkar, R. B., Swaan, P. W., Eddington, N. D., & Ghandehari, H. (2006). Transport of Poly (Amidoamine) Dendrimers Across Caco-2 Cell Monolayers: Influence of Size, Charge and Fluorescent Labeling. *Pharmaceutical Research, 23*(12), 2818-2826.

Klajnert, B., & Bryszewska, M. (2002). Fluorescence Studies on PAMAM Dendrimers Interactions with Bovine Serum Albumin. *Bioelectrochemistry, 55*(1), 33-35.

Ko, S., & Gunasekaran, S. (2006). Preparation of Sub-100-nm β-Lactoglobulin (BLG) Nanoparticles. *Journal of Microencapsulation, 23*(8), 887-898.

Kompella, U. B., & Lee, V. H. L. (2001). Delivery Systems for Penetration Enhancement of Peptide and Protein Drugs: Design Considerations. *Advanced Drug Delivery Reviews, 46*(1), 211-245.

Korsmeyer, R. W., & Peppas, N. A. (1983). Macromolecular and Modeling Aspects of Swelling-Controlled Systems. *Controlled Release Delivery Systems. New York: Marcel Dekker*, 77-90.

Kozyraki, R., & Cases, O. (2013). Vitamin B_{12} Absorption: Mammalian Physiology and Acquired and Inherited Disorders. *Biochimie, 95*, 1002-1007.

Kratz, F. (2008). Albumin as a Drug Carrier: Design of Prodrugs, Drug Conjugates and Nanoparticles. *Journal of Controlled Release, 132*(3), 171-183.

Krause, H. J., Schwarz, A., & Rohdewald, P. (1985). Polylactic Acid Nanoparticles, a Colloidal Drug Delivery System for Lipophilic Drugs. *International Journal of Pharmaceutics, 27*(2), 145-155.

Kris-Etherton, P. M., Harris, W. S., & Appel, L. J. (2003). Fish Consumption, Fish Oil, Omega-3 Fatty Acids, and Cardiovascular Disease. *Arteriosclerosis, Thrombosis, and Vascular Biology, 23*(2), e20-e30.

Kristinsson, H. G., & Hultin, H. O. (2004). Changes in Trout Hemoglobin Conformations and Solubility after Exposure to Acid and Alkali pH. *Journal of Agricultural and Food Chemistry*, *52*, 3633-3643.

Kroll, J., Rawel, H. M., & Rohn, S. (2003). Reactions of Plant Phenolics with Food Proteins and Enzymes Under Special Consideration of Covalent Bonds. *Food Science and Technology Research, 9*(3), 205-218.

Kuo, S. C., Yeh, C. B., Yeh, Y. W., & Tzeng, N. S. (2009). Schizophrenia-like Psychotic Episode Precipitated by Cobalamin Deficiency. *General Hospital Psychiatry, 31*(6), 586-588.

Kuzminski, A. M., Del Giacco, E. J., Allen, R. H., Stabler, S. P., & Lindenbaum, J. (1998). Effective Treatment of Cobalamin Deficiency with Oral Cobalamin. *Blood, 92*(4), 1191-1198.

Lai, L. F., & Guo, H. X. (2011). Preparation of New 5-Fluorouracil-Loaded Zein Nanoparticles for Liver Targeting. *International Journal of Pharmaceutics, 404*(1), 317-323.

Lai, S. K. , Hida, K., Chen, C., Hanes, J. (2008). Characterization of the Intracellular Dynamics of a Non-degradative Pathway Accessed by Polymer Nanoparticles. *Journal of Controlled Release, 125* (2),107–111.

Lai, S. K., Wang, Y. Y., & Hanes, J. (2009). Mucus-Penetrating Nanoparticles for Drug and Gene Delivery to Mucosal Tissues. *Advanced Drug Delivery Reviews, 61*(2), 158-171.

Lai, S. K., Wang, Y. Y., Hida, K., Cone, R., & Hanes, J. (2010). Nanoparticles Reveal That Human Cervicovaginal Mucus is Riddled with Pores Larger than Viruses. *Proceedings of the National Academy of Sciences, 107*(2), 598-603.

Lakowicz, J. R. (2009). *Principles of Fluorescence Spectroscopy*: Springer.

Lamprecht, A., Saumet, J. L., Roux, J., & Benoit, J. P. (2004). Lipid Nanocarriers as Drug Delivery System for Ibuprofen in Pain Treatment. *International Journal of Pharmaceutics*, *278*, 407-414.

Lavelle, E. C. (2001). Targeted Delivery of Drugs to the Gastrointestinal Tract. *Critical Reviews™ in Therapeutic Drug Carrier Systems, 18*(4), 341-386.

Lee, K. D., Nir, S., & Papahadjopoulos, D. (1993). Quantitative Analysis of Liposome-cell Interactions in Vitro: Rate Constants of Binding and Endocytosis with Suspension and Adherent J774 Cells and Human Monocytes. *Biochemistry, 32*(3), 889-899.

Lefèvre, T., & Subirade, M. (1999). Structural and Interaction Properties of β-Lactoglobulin as Studied by FTIR Spectroscopy. *International Journal of Food Science and Technology*, *34*, 419-428.

Lefèvre, T., & Subirade, M. (2000). Molecular Differences in the Formation and Structure of Fine-Stranded and Particulate Beta-Lactoglobulin Gels. *Biopolymers*, *54*, 578-586.

Legen, I., Salobir, M., & Kerč, J. (2005). Comparison of Different Intestinal Epithelia as Models for Absorption Enhancement Studies. *International Journal of Pharmaceutics, 291*(1), 183-188.

Lehr, C. M., Bouwstra, J. A., Kok, W., Boer, A. G., Tukker, J. J., Verhoef, J., Breimer, D. D., & Junginger, H. E. (1992). Effects of the Mucoadhesive Polymer Polycarbophil on the Intestinal Absorption of a Peptide Drug in the Rat. *Journal of Pharmacy and Pharmacology, 44*(5), 402-407.

Lehr, C. M., Bouwstra, J. A., Tukker, J. J., & Junginger, H. E. (1990). Intestinal Transit of Bioadhesive Microspheres in an in Situ Loop in the Rat-a Comparative Study with Copolymers and Blends Based on Poly (Acrylic Acid). *Journal of Controlled Release, 13*(1), 51-62.

Lennernäs, H., Palm, K., Fagerholm, U., & Artursson, P. (1996). Comparison Between Active and Passive Drug Transport in Human Intestinal Epithelial (Caco-2) Cells *in Vitro* and Human Jejunum *in Vivo*. *International Journal of Pharmaceutics, 127*(1), 103-107.

Levine, R. R., McNary, W. F., Kornguth, P. J., & LeBlanc, R. (1970). Histological Reevaluation of Everted Gut Technique for Studying Intestinal Absorption. *European Journal of Pharmacology, 9*(2), 211-219.

Lewinski, N., Colvin, V., & Drezek, R. (2008). Cytotoxicity of Nanoparticles. *Small, 4*(1), 26-49.

Li, D. J., Yang, Y. M., Cao, X. X., Xu, C., & Ji, B. M. (2012). Investigation on the pH-Dependent Binding of Vitamin B_{12} and Lysozyme by Fluorescence and Absorbance. *Journal of Molecular Structure, 1007*, 102-112.

Li, D. J., Zhang, T., Xu, C., & Ji, B. M. (2011). Effect of pH on the Interaction of Vitamin B12 with Bovine Serum Albumin by Spectroscopic Approaches. *Spectrochimica Acta Part a-Molecular and Biomolecular Spectroscopy, 83*(1), 598-608.

Li, Q. Y., Zhu, Q. C., Deng, X. Q., He, W. N., Zhao, T. F., & Zhang, B. Y. (2012). Binding Interactions of Water-Soluble Camptothecin Derivatives with Bovine Serum Albumin. *Spectrochimica Acta Part A: Molecular and Biomolecular Spectroscopy, 86*, 124-130.

Li, X. Y., Kong, X. Y., Shi, S., Zheng, X. L., Wei, T. Q., & Qian, Z. Y. (2008). Preparation of Alginate Coated Chitosan Microparticles for Vaccine Delivery. *BMC Biotechnology, 8* (89), 1-11.

Li, X., Jin, L., McAllister, T. A., Stanford, K., Xu, J., Lu, Y., Zhen, Y., Sun, Y., & Xu, Y. (2007). Chitosan-Alginate Microcapsules for Oral Delivery of Egg Yolk Immunoglobulin (IgY). *Journal of Agricultural and Food Chemistry, 55*(8), 2911-2917.

Liang, L., & Subirade, M. (2012). Study of the Acid and Thermal Stability of β-Lactoglobulin-Ligand Complexes Using Fluorescence Quenching. *Food Chemistry, 132*(4), 2023-2029.

Liang, L., Tajmir-Riahi, H. A., & Subirade, M. (2008). Interaction of Beta-Lactoglobulin with Resveratrol and its Biological Implications. *Biomacromolecules, 9*(1), 50-56.

Liang, L., Tremblay-Hébert, V., & Subirade, M. (2011). Characterisation of the β-Lactoglobulin/α-Tocopherol Complex and its Impact on α-Tocopherol Stability. *Food Chemistry, 126*(3), 821-826.

Liang, Y., & Kristinsson, H. G. (2007). Structural and Foaming Properties of Egg Albumen Subjected to Different pH-Treatments in the Presence of Calcium Ions. *Food Research International*, *40*, 668-678.

Lien, Z. Y., Hsu, T. C., Liu, K. K., Liao, W. S., Hwang, K. C., & Chao, J. I. (2012). Cancer Cell Labeling and Tracking Using Fluorescent and Magnetic Nanodiamond. *Biomaterials, 33*(26), 6172-6185.

Lin, I. C., Liang, M. T., Liu, T. Y., Ziora, Z. M., Monteiro, M. J., & Toth, I. (2011). Interaction of Densely Polymer-Coated Gold Nanoparticles with Epithelial Caco-2 Monolayers. *Biomacromolecules, 12*(4), 1339-1348.

Lin, W., Coombes, A., Davies, M., Davis, S., & Illum, L. (1993). Preparation of Sub-100 nm Human Serum Albumin Nanospheres Using a pH-coacervation Method. *Journal of Drug Targeting, 1*(3), 237-243.

Lin, Y. H., Chen, C. T., Liang, H. F., Kulkarni, A. R., Lee, P. W., Chen, C. H., & Sung, H. W. (2007). Novel Nanoparticles for Oral Insulin Delivery via the Paracellular Pathway. *Nanotechnology, 18*(10), 105102.

Lin, Y. H., Mi, F. L., Chen, C. T., Chang, W. C., Peng, S. F., Liang, H. F., & Sung, H. W. (2007). Preparation and Characterization of Nanoparticles Shelled with Chitosan for Oral Insulin Delivery. *Biomacromolecules, 8*(1), 146-152.

Lin, Y. H., Sonaje, K., Lin, K. M., Juang, J. H., Mi, F. L., Yang, H. W., & Sung, H. W. (2008). Multi-Ion-Crosslinked Nanoparticles with pH-Responsive Characteristics for Oral Delivery of Protein Drugs. *Journal of Controlled Release, 132*(2), 141-149.

Liu, G., Li, J., Shi, K., Wang, S., Chen, J., Liu, Y., & Huang, Q. (2009). Composition, Secondary Structure, and Self-Assembly of Oat Protein Isolate. *Journal of Agricultural and Food Chemistry*, *57*, 4552-4558.

Liu, M. X., Lee, D. S., & Damodaran, S. (1999). Emulsifying Properties of Acidic Subunits of Soy 11S Globulin. *Journal of Agricultural and Food Chemistry, 47*(12), 4970-4975.

Liu, X. M., Sun, Q. S., Wang, H. J., Zhang, L., & Wang, J. Y. (2005). Microspheres of Corn Protein, Zein, for an Ivermectin Drug Delivery System. *Biomaterials, 26*(1), 109-115.

Liu, Y., Wang, P., Sun, C., Feng, N., Zhou, W., Yang, Y., Tan, R., Chen, Z., Wu, S., & Zhao, J. (2010). Wheat Germ Agglutinin-Grafted Lipid Nanoparticles: Preparation and *in Vitro* Evaluation of the Association with Caco-2 Monolayers. *International Journal of Pharmaceutics, 397*(1), 155-163.

Livney, Y. D. (2010). Milk Proteins as Vehicles for Bioactives. *Current Opinion in Collid and Interface Science*, *15*, 73-83.

Lodhia, J., Mandarano, G., Ferris, N. J., Eu, P., & Cowell, S. F. (2010). Development and Use of Iron Oxide Nanoparticles (Part 1): Synthesis of Iron Oxide Nanoparticles for MRI. *Biomedical Imaging and Intervention Journal*, *6*(2), 1-11.

Loveday, S. M., & Singh, H. (2008). Recent Advances in Technologies for Vitamin A Protection in Foods. *Trends in Food Science & Technology, 19*(12), 657-668.

Lu, W., Zhang, Y., Tan, Y. Z., Hu, K. L., Jiang, X. G., & Fu, S. K. (2005). Cationic Albumin-conjugated Pegylated Nanoparticles as Novel Drug Carrier for Brain Delivery. *Journal of Controlled Release, 107*(3), 428-448.

Lukowski, G., Müller, R. H., Miiller, B. W., & Dittgen, M. (1992). Acrylic acid Copolymer Nanoparticles for Drug Delivery: I. Characterization of the Surface Properties Relevant for *in Vivo* Organ Distribution. *International Journal of Pharmaceutics*, *84*, 23-31.

Luo, Y., Teng, Z., Wang, T. T., & Wang, Q. (2013). Cellular Uptake and Transport of Zein Nanoparticles: Effects of Sodium Caseinate. *Journal of Agricultural and Food Chemistry, 61*(31), 7621-7629.

Ma, Z. S., Lim, T. M., & Lim, L. Y. (2005). Pharmacological Activity of Peroral Chitosan-Insulin Nanoparticles in Diabetic Rats. *International Journal of Pharmaceutics, 293*(1), 271-280.

Malik, N., Wiwattanapatapee, R., Klopsch, R., Lorenz, K., Frey, H., Weener J. W., Meijer, E. W., Paulus, W., & Duncan, R. (2000). Dendrimers: Relationship Between Structure and Biocompatibility *in vitro*, and Preliminary Studies on the Biodistribution of I^{125}-Labelled Polyamidoamine Dendrimers *in Vivo*. *Journal of Controlled Release*, *65*, 133-148.

Maltais, A., Remondetto, G. E., & Subirade, M. (2008). Mechanisms Involved in the Formation and Structure of Soya Protein Cold-Set Gels: A Molecular and Supramolecular Investigation. *Food Hydrocolloids*, *22*, 550-559.

Marieb, E., & Hoehn, K. (2010). Human Anatomy & Physiology (8e). In: Boston, Massachusetts: Pearson Benjamin Cummings.

Martirosyan, A., Polet, M., Bazes, A., Sergent, T. R. S., & Schneider, Y. J. (2012). Food Nanoparticles and Intestinal Inflammation: A Real Risk? Chapter 8.

Maruyama, N., Adachi, M., Takahashi, K., Yagasaki, K., Kohno, M., Takenaka, Y., Okuda, E., Nakagawa, S., Mikami, B., & Utsumi, S. (2001). Crystal Structures of Recombinant and Native Soybean Beta-Conglycinin Beta Homotrimers. *European Journal of Biochemistry, 268*(12), 3595-3604.

Maruyama, N., Katsube, T., Wada, Y., Oh, M. H., Barba De La Rosa, A. P., Okuda, E., Nakagawa, S., & Utsumi, S. (1998). The Roles of the N-Linked Glycans and Extension Regions of Soybean β-Conglycinin in Folding, Assembly and Structural Features. *European Journal of Biochemistry, 258*(2), 854-862.

Matalanis, A., Jones, O. G., & McClements, D. J. (2011). Structured Biopolymer-Based Delivery Systems for Encapsulation, Protection, and Release of Lipophilic Compounds. *Food Hydrocolloids, 25*(8), 1865-1880.

Matson, D. W., Fulton, J. L., Petersen, R. C., & Smith, R. D. (1987). Rapid Expansion of Supercritical Fluid Solutions: Solute Formation of Powders, Thin Films, and Fibers. *Industrial & Engineering Chemistry Research, 26*(11), 2298-2306.

Matsuo, K., Yonehara, R., & Gekko, K. (2004). Secondary-Structure Analysis of Proteins by Vacuum-Ultraviolet Circular Dichroism Spectroscopy. *Journal of Biochemistry, 135*(3), 405-411.

McClements, D. J. (1999). *Food Emulsions: Principles, Practices and Techniques* (Vol. 5): CRC Press.
McClements, D. J. (2010). Emulsion Design to Improve the Delivery of Functional Lipophilic Components. *Annual Review of Food Science and Technology, 1*, 241-269.
McClements, D. J. (2013). Edible Lipid Nanoparticles: Digestion, Absorption, and Potential Toxicity. *Progress in lipid research, 52,* 409-423.
McMahon, H. T., & Boucrot, E. (2011). Molecular Mechanism and Physiological Functions of Clathrin-Mediated Endocytosis. *Nature Reviews Molecular Cell Biology, 12*(8), 517-533.
Mehra, R. (2012). Approaches to Improve the Solubility and Bioavailability of Poorly Soluble Drugs and Different Parameter to Screen Them. *Novel Science International Journal of Pharmaceutical Sciences, 1*(4).
Mellman, I. (1996). Endocytosis and Molecular Sorting. *Annual Review of Cell and Developmental Biology, 12*(1), 575-625.
Mendanha, D. V., Molina Ortiz, S. E., Favaro-Trindade, C. S., Mauri, A., Monterrey-Quintero, E. S., & Thomazini, M. (2009). Microencapsulation of Casein Hydrolysate by Complex Coacervation with SPI/Pectin. *Food Research International, 42*(8), 1099-1104.
Meshulam, T., Levitz, S. M., Christin, L., & Diamond, R. D. (1995). A Simplified New Assay for Assessment of Fungal Cell Damage with the TetrazoliumDye,(2,3)-bis-(2-Methoxy-4-Nitro-5-Sulphenyl)-(2H)-Tetrazoliu m-5-Carboxanilide (XTT). *Journal of Infectious Diseases, 172*(4), 1153-1156.
Mikos, A. G., Mathiowitz, E., Langer, R., & Peppas, N. A. (1991). Interaction of Polymer Microspheres with Mucin gels as a Means of Characterizing Polymer Retention on Mucus. *Journal of Colloid and Interface Science, 143*(2), 366-373.
Miriani, M., Keerati-u-rai, M., Corredig, M., Iametti, S., & Bonomi, F. (2011). Denaturation of Soy Proteins in Solution and at the Oil-Water Interface: A Fluorescence Study. *Food Hydrocolloids, 25*(4), 620-626.
Mitri, K., Shegokar, R., Gohla, S., Anselmi, C., & Müller, R. H. (2011). Lutein Nanocrystals as Antioxidant Formulation for Oral and Dermal Delivery. *International Journal of Pharmaceutics, 420*(1), 141-146.
Mohanraj, V. J., & Chen, Y. (2007). Nanoparticles-A Review. *Tropical Journal of Pharmaceutical Research, 5*(1), 561-573.
Muzzarelli, R. A. A. (2009). Genipin-Crosslinked Chitosan Hydrogels as Biomedical and Pharmaceutical Aids. *Carbohydrate Polymers, 77*(1), 1-9.
Nam, H. Y., Kwon, S. M., Chung, H., Lee, S. Y., Kwon, S. H., Jeon, H., Kim, Y., Park, J. H., Kim, J., & Her, S. (2009). Cellular Uptake Mechanism and Intracellular Fate of Hydrophobically Modified Glycol Chitosan Nanoparticles. *Journal of Controlled Release, 135*(3), 259-267.
Nardone, R., & Tezzon, F. (2010). Neurological Disorders in Vitamin B_{12} Deficiency *Horizons in Neuroscience Research, Vol 2*, 119-136.

Nel, A., Xia, T., Mädler, L., & Li, N. (2006). Toxic Potential of Materials at the Nanolevel. *Science, 311*(5761), 622-627.

Nellans, H. N. (1991). (B) Mechanisms of Peptide and Protein Absorption:(1) Paracellular Intestinal Transport: Modulation of Absorption. *Advanced Drug Delivery Reviews, 7*(3), 339-364.

Nesterenko, A., Alric, I., Silvestre, F., & Durrieu, V. (2012). Influence of Soy Protein's Structural Modifications on Their Microencapsulation Properties: α-Tocopherol Microparticle Preparation. *Food Research International, 48*(2), 387-396.

Nielsen, M. J., Rasmussen, M. R., Andersen, C. B. F., Nexø, E., & Moestrup, S. K. (2012). Vitamin B_{12} Transport from Food to the Body's Cells-a Sophisticated, Multistep Pathway. *Nature Reviews Gastroenterology and Hepatology, 9*(6), 345-354.

Nobs, L., Buchegger, F., Gurny, R., & Allémann, E. (2003). Surface Modification of Poly (Lactic Acid) Nanoparticles by Covalent Attachment of Thiol Groups by Means of Three Methods. *International Journal of Pharmaceutics, 250*(2), 327-337.

Nyholm, E., Turpin, P., Swain, D., Cunningham, B., Daly, S., Nightingale, P., & Fegan, C. (2003). Oral vitamin B12 Can Change Our Practice. *Postgraduate Medical Journal, 79*(930), 218-219.

Ohama, H., Ikeda, H., & Moriyama, H. (2006). Health Foods and Foods with Health Claims in Japan. *Toxicology, 221*(1), 95-111.

O'Neill, M. J., Bourre, L., Melgar, S., & O'Driscoll, C. M. (2011). Intestinal Delivery of Non-Viral Gene Therapeutics: Physiological Barriers and Preclinical Models. *Drug Discovery Today, 16*(5), 203-218.

O'Neill, T. E., & Kinsella, J. E. (1987). Binding of Alkanone Flavors to Beta-Lactoglobulin: Effects of Conformational and Chemical Modification. *Journal of Agricultural and Food Chemistry, 35*(5), 770-774.

Pan, X. R., Qin, P. F., Liu, R. T., & Wang, J. (2011). Characterizing the Interaction between Tartrazine and Two Serum Albumins by a Hybrid Spectroscopic Approach. *Journal of Agricultural and Food Chemistry, 59*(12), 6650-6656.

Pan, X., Yu, S., Yao, P., & Shao, Z. (2007). Self-assembly of β-casein and Lysozyme. Journal of Colloid and Interface *Science, 316*(2), 405-412.

Panyam, J., Dali, M. M., Sahoo, S. K., Ma, W., Chakravarthi, S. S., Amidon, G. L., Levy, R. J., & Labhasetwar, V. (2003). Polymer Degradation and *in Vitro* Release of a Model Protein from Poly (d, l-lactide-co-glycolide) Nano-and Microparticles. *Journal of Controlled Release, 92*(1), 173-187.

Pappenheimer, J. R. (1987). Physiological Regulation of Transepithelial Impedance in the Intestinal Mucosa of Rats and Hamsters. *The Journal of Membrane Biology, 100*(1), 137-148.

Park, J. M., Muhoberac, B. B., Dubin, P. L., & Xia, J. (1992). Effects of Protein Charge Heterogeneity in Protein-Polyelectrolyte Complexation. *Macromolecules, 25*(1), 290-295.

Park, K. (2012). Albumin: A Versatile Carrier for Drug Delivery. *Journal of Controlled Release, 157*(1), 3.

Patel, A., Hu, Y. C., Tiwari, J. K., & Velikov, K. P. (2010). Synthesis and Characterisation of Zein-Curcumin Colloidal Particles. *Soft Matter*, *6*, 6192-6199.

Peppas, L. B. (1995). Recent Advances on the Use of Biodegradable Microparticles and Nanoparticles in Controlled Drug Delivery. *International Journal of Pharmaceutics*, *116*(1), 1-9.

Pérez, M. D., & Calvo, M. (1995). Interaction of β-Lactoglobulin with Retinol and Fatty Acids and Its Role as a Possible Biological Function for This Protein: A Review. *Journal of Dairy Science, 78*(5), 978-988.

Perrut, M., & Clavier, J. Y. (2003). Supercritical Fluid Formulation: Process Choice and Scale-up. *Industrial & Engineering Chemistry Research, 42*(25), 6375-6383.

Perumal, O. P., Inapagolla, R., Kannan, S., & Kannan, R. M. (2008). The Effect of Surface Functionality on Cellular Trafficking of Dendrimers. *Biomaterials, 29*(24), 3469-3476.

Perumal, O. P., Podaralla, S. K., & Seefeldt, T. M. (2009). Doxorubicin Loaded Zein Nanoparticles. *AAPS Annual Meeting and Exposition*.

Petchkrua, W., Burns, S. P., Stiens, S. A., James, J. J., & Little, J. W. (2003). Prevalence of Vitamin B_{12} Deficiency in Spinal Cord Injury. *Archives of Physical Medicine and Rehabilitation, 84*(11), 1675-1679.

Petrelli, F., Borgonovo, K., & Barni, S. (2010). Targeted delivery for breast cancer therapy: the history of nanoparticle-albumin-bound paclitaxel. *Expert Opinion on Pharmacotherapy, 11*(8), 1413-1432.

Petruccelli, S., & Anon, M. C. (1995). Soy protein Isolate Components and Their Interactions. *Journal of Agricultural and Food Chemistry, 43*(7), 1762-1767.

Picot, A., & Lacroix, C. (2003). Encapsulation of Bifidobacteria in Whey Protein-Based Microcapsules and Survival in Simulated Gastrointestinal Conditions and in Yoghurt. *Journal of Food Science, 68*(9), 2693-2700.

Pinto Reis, C., Neufeld, R. J., Ribeiro, A. J., & Veiga, F. (2006). Nanoencapsulation I. Methods for Preparation of Drug-Loaded Polymeric Nanoparticles. *Nanomedicine: Nanotechnology, Biology and Medicine, 2*(1), 8-21.

Plumb, J. A., Burston, D., Baker, T. G., & Gardner, M. L. G. (1987). A Comparison of the Structural Integrity of Several Commonly Used Preparations of Rat Small Intestine *in Vitro*. *Clinical Science, 73*(1), 53-59.

Postgård, P., Himmelman, J., Lindencrona, U., Bhogal, N., Wiberg, D., Berg, G., Jansson, S., Nyström, E., Forssell-Aronsson, E., & Nilsson, M. (2002). Stunning of Iodide Transport by 131I Irradiation in Cultured Thyroid Epithelial Cells. *Journal of Nuclear Medicine, 43*(6), 828-834.

Potter, S. M. (1995). Overview of Proposed Mechanisms for The Hypocholesterolemic Effect of Soy *Journal of Nutrition, 125*(3), S606-S611.

Primard, C., Rochereau, N., Luciani, E., Genin, C., Delair, T., Paul, S., & Verrier, B. (2010). Traffic of Poly (Lactic Acid) Nanoparticulate Vaccine Vehicle from

Intestinal Mucus to Sub-Epithelial Immune Competent Cells. *Biomaterials, 31*(23), 6060-6068.

Puyol, P., Perez, M. D., Ena, J. M., & Calvo, M. (1991). Interaction of Bocine Beta-Lactoglobulin and Other Bovine And Human Whey Proteins with Retinol and Fatty-Acids *Agricultural and Biological Chemistry, 55*(10), 2515-2520.

Quintanilla-Carvajal, M. X., Camacho-Díaz, B. H., Meraz-Torres, L. S., Chanona-Pérez, J. J., Alamilla-Beltrán, L., Jimenéz-Aparicio, A., & Gutiérrez-López, G. F. (2010). Nanoencapsulation: a New Trend in Food Engineering Processing. *Food Engineering Reviews, 2*(1), 39-50.

Rajaonarivony, M., Vauthier, C., Couarraze, G., Puisieux, F., & Couvreur, P. (1993). Development of a New Drug Carrier Made from Alginate. *Journal of Pharmaceutical Sciences, 82*(9), 912-917.

Rang, M. J., & Miller, C. A. (1999). Spontaneous Emulsification of Oils Containing Hydrocarbon, Nonionic Surfactant, and Oleyl Alcohol. *Journal of Colloid and Interface Science, 209*(1), 179-192.

Rappoport, J. (2008). Focusing on Clathrin-Mediated Endocytosis. *Biochemistry Journal, 412*, 415-423.

Rashba, E., & Gamota, D. (2003). Anticipatory Standards and the Commercialization of Nanotechnology. *Journal of Nanoparticle Research, 5*(3-4), 401-407.

Ray, J. G., & Cole, D. E. C. (2005). Cobalamin Deficiency in Elderly Patients. *Canadian Medical Association Journal, 172*(4), 448-450.

Reix, N., Parat, A., Seyfritz, E., Van Der Werf, R., Epure, V., Ebel, N., Danicher, L., Marchioni, E., Jeandidier, N., & Pinget, M. (2012). *In Vitro* Uptake Evaluation in Caco-2 Cells and *in Vivo* Results in Diabetic Rats of Insulin-Loaded PLGA Nanoparticles. *International Journal of Pharmaceutics, 437* (1-2), 213-220.

Rekha, M., & Sharma, C. P. (2009). Synthesis and Evaluation of Lauryl Succinyl Chitosan Particles Towards Oral Insulin Delivery and Absorption. *Journal of Controlled Release, 135*(2), 144-151.

Ren, C. R., Tang, L., Zhang, M., & Guo, S. T. (2009). Structural Characterization of Heat-Induced Protein Particles in Soy Milk. *Journal of Agricultural and Food Chemistry*, *57*, 1921-1926.

Renkema, J. M. S., Knabben, J. H. M., & van Vliet, T. (2001). Gel Formation by β-Conglycinin and Glycinin and Their Mixtures. *Food Hydrocolloids*, *15*, 407-414.

Rieux, A. d., Ragnarsson, E. G., Gullberg, E., Préat, V., Schneider, Y. J., & Artursson, P. (2005). Transport of Nanoparticles Across an *in Vitro* Model of the Human Intestinal Follicle Associated Epithelium. *European Journal of Pharmaceutical Sciences, 25*(4), 455-465.

Rodrigues, M., Peirico, N., Matos, H., Gomes de Azevedo, E., Lobato, M., & Almeida, A. (2004). Microcomposites Theophylline/Hydrogenated Palm Oil

from a PGSS Process for Controlled Drug Delivery Systems. *The Journal of Supercritical Fluids, 29*(1), 175-184.
Roger, E., Lagarce, F., Garcion, E., & Benoit, J. P. (2009). Lipid Nanocarriers Improve Paclitaxel Transport Throughout Human Intestinal Epithelial Cells by Using Vesicle-Mediated Transcytosis. *Journal of Controlled Release, 140*(2), 174-181.
Ross, P. D., & Subramanian, S. (1981). Thermodynamics of Protein Association Reactions: Forces Contributing to Stability. *Biochemistry, 20*(11), 3096-3102.
Rubas, W., Cromwell, M. E. M., Shahrokh, Z., Villagran, J., Nguyen, T. N., Wellton, M., Nguyen, T. H., & Mrsny, R. J. (1996). Flux Measurements Across Caco-2 Monolayers May Predict Transport in Human Large Intestinal Tissue. *Journal of Pharmaceutical Sciences, 85*(2), 165-169.
Russell-Jones, G. J., Veitch, H., & Arthur, L. (1999). Lectin-Mediated Transport of Nanoparticles Across Caco-2 and OK Cells. *International Journal of Pharmaceutics, 190*(2), 165-174.
Sahay, G., Alakhova, D. Y., & Kabanov, A. V. (2010). Endocytosis of Nanomedicines. *Journal of Controlled Release, 145*(3), 182-195.
Sahay, G., Alakhova, D. Y., & Kabanov, A. V. (2010). Endocytosis of Nanomedicines. *Journal of Controlled Release, 145*(3), 182-195.
Saifer, A., & Goldman, L. (1961). The Free Fatty Acids Bound to Human Serum Albumin. *Journal of Lipid Research, 2*(3), 268-270.
Saio, K., & Watanbe, T. (1978). Differences in Functional Properties of 7S and 11S Soybean Proteins. *Journal of Texture Studies, 9*(1-2), 135-157.
Sanderson, I. R., & Walker, W. A. (1993). Uptake and Transport of Macromolecules by the Intestine: Possible Role in Clinical Disorders (an Update). *Gastroenterology, 104*(2), 622-639.
Sanguansri, P., & Augustin, M. A. (2006). Nanoscale Materials Development-a Food Industry Perspective. *Trends in Food Science & Technology, 17*(10), 547-556.
Santipanichwong, R., Suphantharika, M., Weiss, J., & McClements, D. J. (2008). Core-Shell Biopolymer Nanoparticles Produced by Electrostatic Deposition of Beet Pectin onto Heat-Denatured β-Lactoglobulin Aggregates. *Journal of Food Science*, *73*(6), N23-N30.
Sarmento, B., Ribeiro, A. J., Veiga, F., Ferreira, D. C., & Neufeld, R. J. (2007). Insulin-Loaded Nanoparticles are Prepared by Alginate Ionotropic Pre-Gelation Followed by Chitosan Polyelectrolyte Complexation. *Journal of Nanoscience and Nanotechnology, 7*(8), 2833-2841.
Sarmento, B., Ribeiro, A., Veiga, F., Sampaio, P., Neufeld, R., & Ferreira, D. (2007). Alginate/chitosan Nanoparticles Are Effective for Oral Insulin Delivery. *Pharmaceutical Research, 24*(12), 2198-2206.
Schachter, H., & Williams, D. (1982). Biosynthesis of Mucus Glycoproteins. In *Mucus in Health and Disease-II*, (pp. 3-28): Springer.
Schachter, H., & Williams, D. (1982). Biosynthesis of mucus glycoproteins. *In Mucus in Health and Disease-II, (pp. 3-28)*: Springer.

Schipper, N. G. M., Olsson, S., Hoogstraate, J. A., Vårum, K. M., & Artursson, P. (1997). Chitosans as Absorption Enhancers for Poorly Absorbable Drugs 2: Mechanism of Absorption Enhancement. *Pharmaceutical Research, 14*(7), 923-929.

Schnitzer, J. E., Oh, P., Pinney, E., & Allard, J. (1994). Filipin-Sensitive Caveolae-Mediated Transport in Endothelium: Reduced Transcytosis, Scavenger Endocytosis, and Capillary Permeability of Select Macromolecules. *The Journal of Cell Biology, 127*(5), 1217-1232.

Scudiero, D. A., Shoemaker, R. H., Paull, K. D., Monks, A., Tierney, S., Nofziger, T. H., Currens, M. J., Seniff, D., & Boyd, M. R. (1988). Evaluation of a Soluble Tetrazolium/Formazan Assay for Cell Growth and Drug Sensitivity in Culture Using Human and Other Tumor Cell Lines. *Cancer Research, 48*(17), 4827-4833.

Shakweh, M., Besnard, M., Nicolas, V., & Fattal, E. (2005). Poly (Lactide-co-Glycolide) Particles of Different Physicochemical Properties and Their Uptake by Peyer's Patches in Mice. *European Journal of Pharmaceutics and Biopharmaceutics, 61*(1), 1-13.

Shewry, P. R. (1995). Plant Storage Proteins. *Biological Reviews, 70*(3), 375-426.

Shi, L., & Caldwell, K. D. (2000). Mucin Adsorption to Hydrophobic Surfaces. *Journal of Colloid and Interface Science, 224*(2), 372-381.

Shimomura, M., & Sawadaishi, T. (2001). Bottom-up Strategy of Materials Fabrication: a New Trend in Nanotechnology of Soft Materials. *Current Opinion in Colloid and Interface science, 6*(1), 11-16.

Shinoda, K., & Saito, H. (1968). The Effect of Temperature on the Phase Equilibria and the Types of Dispersions of the Ternary System Composed of Water, Cyclohexane, and Nonionic Surfactant. *Journal of Colloid and Interface Science, 26*(1), 70-74.

Shutava, T. G., Balkundi, S. S., Vangala, P., Steffan, J. J., Bigelow, R. L., Cardelli, J. A., O'Neal, D. P., & Lvov, Y. M. (2009). Layer-by-layer-coated Gelatin Nanoparticles as a Vehicle for Delivery of Natural Polyphenols. *ACS Nano*, *3*(7), 1877-1885.

Shutov, A. D., Kakhovskaya, I. A., Bastrygina, A. S., Bulmaga, V. P., Horstmann, C., & Muntz, K. (1996). Limited Proteolysis of Beta-Conglycinin and Glycinin, the 7S and 11S Storage Globulins from Soybean Glycine Max (L) Merr-Structural and Evolutionary Implications. *European Journal of Biochemistry, 241*(1), 221-228.

Siepmann, J., & Peppas, N. A. (2011). Higuchi Equation: Derivation, Applications, Use and Misuse. *International Journal of Pharmaceutics, 418*(1), 6-12.

Sievers, R. E., Sellers, S. P., & Carpenter, J. F. (2003). Supercritical Fluid-Assisted Nebulization and Bubble Drying. In): Google Patents.

Silva, H. D., Cerqueira, M. Â., & Vicente, A. A. (2012). Nanoemulsions for Food Applications: Development and Characterization. *Food and Bioprocess Technology, 5*(3), 854-867.

Simionescu, M., Popov, D., & Sima, A. (2009). Endothelial Transcytosis in Health and Disease. *Cell and Tissue Research, 335*(1), 27-40.

Siro, I., Kapolna, E., Kapolna, B., & Lugasi, A. (2008). Functional Food. Product Development, Marketing and Consumer Acceptance-A Review. *Appetite, 51*(3), 456-467.

Solans, C., Izquierdo, P., Nolla, J., Azemar, N., & Garcia-Celma, M. J. (2005). Nano-Emulsions. *Current Opinion in Colloid and Interface science, 10*(3), 102-110.

Sonaje, K., Chen, Y. J., Chen, H. L., Wey, S. P., Juang, J. H., Nguyen, H. N., Hsu, C. W., Lin, K. J., & Sung, H. W. (2010). Enteric-Coated Capsules Filled with Freeze-Dried Chitosan/Poly (γ-Glutamic Acid) Nanoparticles for Oral Insulin Delivery. *Biomaterials, 31*(12), 3384-3394.

Sonaje, K., Lin, K. J., Tseng, M. T., Wey, S. P., Su, F. Y., Chuang, E. Y., Hsu, C. W., Chen, C. T., & Sung, H. W. (2011). Effects of Chitosan-Nanoparticle-Mediated Tight Junction Opening on the Oral Absorption of Endotoxins. *Biomaterials, 32*(33), 8712-8721.

Sonaje, K., Lin, Y. H., Juang, J. H., Wey, S. P., Chen, C. T., & Sung, H. W. (2009). *In Vivo* Evaluation of Safety and Efficacy of Self-Assembled Nanoparticles for Oral Insulin Delivery. *Biomaterials, 30*(12), 2329-2339.

Sonavane, G., Tomoda, K., Sano, A., Ohshima, H., Terada, H., & Makino, K. (2008). *In Vitro* Permeation of Gold Nanoparticles Through Rat Skin and Rat Intestine: Effect of Particle Size. Colloids and Surfaces B: *Biointerfaces, 65*(1), 1-10.

Stan, D., Matei, I., Mihailescu, C., Savin, M., Matache, M., Hillebrand, M., & Baciu, I. (2009). Spectroscopic Investigations of the Binding Interaction of a New Indanedione Derivative with Human and Bovine Serum Albumins. *Molecules, 14*(4), 1614-1626.

Sundar, S., Kundu, J., & Kundu, S. (2010). Biopolymeric Nanoparticles. *Science and Technology of Advanced Materials*, *11*, 1-13.

Swanson, J. A., & Watts, C. (1995). Macropinocytosis. *Trends in Cell Biology, 5*(11), 424-428.

Sze, K. W. C., Kshirsagar, H. H., Venkatachalam, M., & Sathe, S. K. (2007). A Circular Dichroism and Fluorescence Spectrometric Assessment of Effects of Selected Chemical Denaturants on Soybean (Glycine max L.) Storage Proteins Glycinin (11S) and Beta-Conglycinin (7S). *Journal of Agricultural and Food Chemistry, 55*(21), 8745-8753.

Szentkuti, L. (1997). Light Microscopical Observations on Luminally Administered Dyes, Dextrans, Nanospheres and Microspheres in the Pre-epithelial Mucus Gel Layer of the Rat Distal Colon. *Journal of Controlled Release, 46*(3), 233-242.

Tadros, T., Izquierdo, P., Esquena, J., & Solans, C. (2004). Formation and Stability of Nano-Emulsions. *Advances in Colloid and Interface Science, 108*, 303-318.

Takeuchi, H., Yamamoto, H., Niwa, T., Hino, T., & Kawashima, Y. (1996). Enteral Absorption of Insulin in Rats from Mucoadhesive Chitosan-Coated Liposomes. *Pharmaceutical Research, 13*(6), 896-901.

Tang, H. D., Murphy, C. J., Zhang, B., Shen, Y. Q., Van Kirk, E. A., Murdoch, W. J., & Radosz, M. (2010). Curcumin Polymers as Anticancer Conjugates. Biomaterials, 31(27), 7139-7149.

Tang, V. W., & Goodenough, D. A. (2003). Paracellular Ion Channel at the Tight Junction. *Biophysical Journal, 84*(3), 1660-1673.

Teng, Z., Luo, Y., & Wang, Q. (2012). Nanoparticles Synthesized from Soy Protein: Preparation, Characterization, and Application for Nutraceutical Encapsulation. *Journal of Agricultural and Food Chemistry, 60*(10), 2712-2720.

Teng, Z., Luo, Y., & Wang, Q. (2013). Carboxymethyl Chitosan-Soy Protein Complex Nanoparticles for the Encapsulation and Controlled Release of Vitamin D_3. *Food Chemistry, 141*(1), 524-532.

Teng, Z., Luo, Y., Wang, T., Zhang, B., & Wang, Q. (2013). Development and Application of Nanoparticles Synthesized with Folic Acid Conjugated Soy Protein. *Journal of Agricultural and Food Chemistry, 61*(10), 2556-2564.

Tomczykiewicz, K., Tutaj, A., & Janda, R. (1998). Neurological Disorders of Vitamin B12 Deficiency. *Neurologia I Neurochirurgia Polska, 32*(6), 1473.

Tomita, M., Shiga, M., Hayashi, M., & Awazu, S. (1988). Enhancement of Colonic Drug Absorption by the Paracellular Permeation Route. *Pharmaceutical Research, 5*(6), 341-346.

Tomoda, H., Kishimoto, Y., & Lee, Y. (1989). Temperature Effect on Endocytosis and Exocytosis by Rabbit Alveolar Macrophages. *Journal of Biological Chemistry, 264*(26), 15445-15450.

Torres, G., Sergio, Martinez, A., Antonio, Ocio, M. J., & Lagaron, J. M. (2010). Stabilization of a Nutraceutical Omega-3 Fatty Acid by Encapsulation in Ultrathin Electrosprayed Zein Prolamine. *Journal of Food Science, 75*(6), N69-N79.

Uson, N., Garcia, M. J., & Solans, C. (2004). Formation of Water-in-Oil (W/O) Nano-Emulsions in a Water/Mixed Non-Ionic Surfactant/Oil Systems Prepared by a Low-Energy Emulsification Method. *Colloids and Surfaces A: Physicochemical and Engineering Aspects, 250*(1), 415-421.

Van Damme, E. J., Peumans, W. J., Pusztai, A., & Bardocz, S. (1998). *Handbook of Plant Lectins: Properties and Biomedical Applications*: Wiley. com.

Van De Weert, M. (2010). Fluorescence Quenching to Study Protein-Ligand Binding: Common Errors. *Journal of Fluorescence, 20*(2), 625-629.

Van de Weert, M., & Stella, L. (2011). Fluorescence Quenching and Ligand Binding: a Critical Discussion of a Popular Methodology. *Journal of Molecular Structure, 998*(1), 144-150.

Verma, A., Uzun, O., Hu, Y. h., Hu, Y., Han, H. S., Watson, N., Chen, S. L., Irvine, D. J., & Stellacci, F. (2008). Surface-Structure-Regulated Cell-Membrane

Penetration by Monolayer-Protected Nanoparticles. *Nature Materials, 7*(7), 588-595.

Vine, D., Charman, S., Gibson, P., Sinclair, A., & Porter, C. (2002). Effect of Dietary Fatty Acids on the Intestinal Permeability of Marker Drug Compounds in Excised Rat Jejunum. *Journal of Pharmacy and Pharmacology, 54*(6), 809-819.

Vogel, S., Contois, J. H., Tucker, K. L., Wilson, P., Schaefer, E. J., & Lammi-Keefe, C. J. (1997). Plasma Retinol and Plasma and Lipoprotein Tocopherol and Carotenoid Concentrations in Helderly Participants of the Framingham Heart Study. *The American Journal of Clinical Nutrition, 66*(4), 950-958.

Wallace, B. A., & Janes, R. W. (2003). Circular Dichroism and Synchrotron Radiation Circular Dichroism Spectroscopy: Tools for Drug Discovery. *Biochemical Society Transactions*, *31*, 631-633.

Walter, E., Janich, S., Roessler, B. J., Hilfinger, J. M., & Amidon, G. L. (2000). HT29-MTX/Caco-2 Cocultures as an in vitro Model for the Intestinal Epithelium: *In Vitro-in Vivo* Correlation with Permeability Data from Rats and Humans. *Journal of Pharmaceutical Sciences, 85*(10), 1070-1076.

Wang, H., Wang, T., & Johnson, L. A. (2006). Mechanism for Refunctionalizing Heat-Denatured Soy Protein by Alkaline Hydrothermal Cooking. *Journal of the American Oil Chemists' Society*, *83*(1), 39-45.

Wang, M. S., Zhang, Y., Feng, J., Gu, T. J., Dong, Q. G., Yang, X., Sun, Y. N., Wu, Y. G., Chen, Y., & Kong, W. (2013). Preparation, Characterization, and *in Vitro* and *in Vivo* Investigation of Chitosan-Coated Poly (d, l-Lactide-co-Glycolide) Nanoparticles for Intestinal Delivery of Exendin-4. *International Journal of Nanomedicine, 8*, 1141.

Wang, Q. W., Allen, J. C., & Swaisgood, H. E. (1997). Binding of Vitamin D and Cholesterol to β-Lactoglobulin. *Journal of Dairy Science, 80*(6), 1054-1059.

Watanabe, F. (2007). Vitamin B_{12} Sources and Bioavailability. *Experimental Biology and Medicine, 232*(10), 1266-1274.

Weiss, J., Decker, E. A., McClements, D. J., Kristbergsson, K., Helgason, T., & Awad, T. (2008). Solid Lipid Nanoparticles as Delivery Systems for Bioactive Food Components. *Food Biophysics, 3*(2), 146-154.

Whitesides, G. M., & Grzybowski, B. (2002). Self-Assembly at all Scales. *Science, 295*(5564), 2418-2421.

Wikman-Larhed, A., & Artursson, P. (1995). Co-cultures of Human Intestinal Goblet (HT29-H) and Absorptive (Caco-2) Cells for Studies of Drug and Peptide Absorption. *European Journal of Pharmaceutical Sciences, 3*(3), 171-183.

Win, K. Y., & Feng, S. S. (2005). Effects of Particle Size and Surface Coating on Cellular Uptake of Polymeric Nanoparticles for Oral Delivery of Anticancer Drugs. *Biomaterials*, *26*, 2713-2722.

Wolf, W. J., Babcock, G. E., & Smith, A. K. (1961). Ultracentrifugal Differences in Soybean Protein Composition. *Nature, 191*, 1395-1396.

Wu, W., Zhang, C. M., Kong, X. Z., & Hua, Y. F. (2009). Oxidative Modification of Soy Protein by Peroxyl Radicals. *Food Chemistry*, *116*, 295-301.

Xiang, S., Tong, H., Shi, Q., Fernandes, J. C., Jin, T., Dai, K., & Zhang, X. (2012). Uptake Mechanisms of Non-Viral Gene Delivery. *Journal of Controlled Release, 158*(3), 371-378.

Xing, J., Deng, L., & Dong, A. (2010). Chitosan/Alginate Nanoparticles Stabilized by Poloxamer for the Controlled Release of 5-fluorouracil. *Journal of Applied Polymer Science, 117*(4), 2354-2359.

Yamashita, S., Furubayashi, T., Kataoka, M., Sakane, T., Sezaki, H., & Tokuda, H. (2000). Optimized Conditions for Prediction of Intestinal Drug Permeability Using Caco-2 Cells. *European Journal of Pharmaceutical Sciences, 10*(3), 195-204.

Ye, A., Flanagan, J., & Singh, H. (2006). Formation of Stable Nanoparticles via Electrostatic Complexation Between Sodium Caseinate and Gum Arabic. *Biopolymers, 82*(2), 121-133.

Ye, S., Wang, C., Liu, X., & Tong, Z. (2005). Multilayer Nanocapsules of Polysaccharide Chitosan and Alginate Through Layer-by-Layer Assembly Directly on PS Nanoparticles for Release. *Journal of Biomaterials Science, Polymer Edition, 16*(7), 909-923.

Yeh, P. Y., Smith, P. L., & Ellens, H. (1994). Effect of Medium-Chain Glycerides on Physiological Properties of Rabbit Intestinal Epithelium *in Vitro*. *Pharmaceutical Research, 11*(8), 1148-1154.

Yeo, S. D., & Kiran, E. (2005). Formation of Polymer Particles with Supercritical Fluids: A Review. *The Journal of Supercritical Fluids, 34*(3), 287-308.

Yin Win, K., & Feng, S. S. (2005). Effects of Particle Size and Surface Coating on Cellular Uptake of Polymeric Nanoparticles for Oral Delivery of Anticancer Drugs. *Biomaterials, 26*(15), 2713-2722.

Yin, Y., Chen, D., Qiao, M., Wei, X., & Hu, H. (2007). Lectin-Conjugated PLGA Nanoparticles Loaded with Thymopentin: Ex Vivo Bioadhesion and *in Vivo* Biodistribution. *Journal of Controlled Release, 123*(1), 27-38.

Yu, C. Y., Wang, W., Yao, H., & Liu, H. J. (2007). Preparation of Phospholipid Microcapsule by Spray Drying. *Drying Technology, 25*(4), 695-702.

Yuan, T., Weljie, A. M., & Vogel, H. J. (1998). Tryptophan Fluorescence Quenching by Methionine and Selenomethionine Residues of Calmodulin: Orientation of Peptide and Protein Binding. *Biochemistry, 37*(9), 3187-3195.

Yun, Y., Cho, Y. W., & Park, K. (2012). Nanoparticles for Oral Delivery: Targeted Nanoparticles with Peptidic Ligands for Oral Protein Delivery. *Advanced Drug Delivery Reviews, 65* (6), 822-832.

Zabaleta, V., Ponchel, G., Salman, H., Agüeros, M., Vauthier, C., & Irache, J. M. (2012). Oral Administration of Paclitaxel with Pegylated Poly (Anhydride) Nanoparticles: Permeability and Pharmacokinetic Study. *European Journal of Pharmaceutics and Biopharmaceutics, 81*(3), 514-523.

Zhao, F., Zhao, Y., Liu, Y., Chang, X. L., Chen, C. Y., & Zhao, Y. L. (2011). Cellular Uptake, Intracellular Trafficking, and Cytotoxicity of Nanomaterials. *Small, 7*(10), 1322-1337.

Zhong, Q., Tian, H., & Zivanovic, S. (2009). Encapsulation of Fish Oil in Solid Zein Particles by Liquid-Liquid Dispersion. *Journal of Food Processing and Preservation, 33*(2), 255-270.

Zittoun, J., & Zittoun, R. (1999). Modern Clinical Testing Strategies in Cobalamin and Folate Deficiency. In *Seminars in Hematology*, 36, 35-46.